HYBRID POWDER METALLURGY PROCESSING FOR HIGH TEMPERATURE STRENGTH NI-BASE SUPERALLOY INCONEL 718

by

Rachel Elizabeth Jennings

A thesis submitted to The University of Birmingham for the degree of

DOCTOR OF PHILOSOPHY

Department of Metallurgy and Materials
College of Engineering and Physical Sciences
The University of Birmingham
December 2020

ABSTRACT

Additive layer manufacturing (ALM) processes such as powder bed fusion (PBF) provide an opportunity for the manufacture of new more complex designs of Ni-base superalloy components, which have the potential to extend the operating temperatures and efficiencies of gas turbine engines. There are however challenges to the industrial implementation of ALM, in particular the slow production times associated with these processes and required post-processing. In recent years hybrid additive manufacturing has been proposed as a way of increasing ALM production efficiency. The most popular hybrid concept to date combines additive and subtractive manufacturing in the direct laser deposition process.

In this work an alternative approach to hybrid manufacturing- the in-situ shelling process- is proposed for the production of Ni-base superalloy Inconel 718. This method combines PBF with Powder Metallurgy Hot Isostatic Pressing (PM HIPping). The HIPping canister is manufactured and filled in-situ during PBF, followed by consolidation of the powders inside the canister by HIPping.

Powder characteristics and their interaction with PBF and HIPping processes are examined extensively and the importance of control of powder packing densities and powder chemistry for the success of each processing route is highlighted. Parametric studies are presented for laser and electron PBF, with the aim to optimise conditions to meet the property requirements of HIPping canisters. In-situ shelling components are manufactured and the strength of bonding across the laser PBF-PM HIPped interface is examined by tensile testing. Two mechanisms for improving bond strength are proposed and tested.

Throughout this work scanning electron microscopy (SEM), electron backscattered diffraction (EBSD) and energy dispersive and wave dispersive spectroscopy (EDS & WDS) have been implemented to evaluate microstructures, grain morphologies and chemistries.

The in-situ shelling process shows promise as a production route for the manufacture of Inconel 718 when electron PBF is implemented at the shelling stage. The use of laser PBF for shelling resulted in significant oxide formation at the PBF- PM HIPped interface leading to poor bonding and a substantial diminishment in tensile properties. Yet, initial results suggest that through manipulation of the LPBF surface, improved bonding may be achievable. It is suggested that chromia oxide forming Ni-base superalloys may be better candidates for in-situ shelling owing to chromia being less stable than alumina.

The overall novelty of this work lies in the examination of Inconel 718 for the in-situ shelling process, however throughout investigations into different aspects of the in-situ shelling process, several additional novel research outcomes emerged. The diffusion zone in state-of-the-art PM HIPped material was found to result in a diminishment of tensile properties as it created a Nb concentration gradient, reducing Nb available for strengthening phases. Surface optimisation studies in in-situ shelling work showed minimising continuous oxides and increasing point contacts between power particles and the LPBF surface to result in an increase in grain growth across LPBF-PM HIPped interfaces owing to an increase in recrystallisation. Oxide chemistry was suggested to influence whether PPB formation was dictated by the oxygen content of the powder or by powder particle size in state-of-the-art PM HIPping.

For my mother who made me promise to finish this

For my dear friend Dr Richard Firn who taught me to question everything

And for my Grandfather with whom I shared a love of engineering

ACKNOWLEDGEMENTS

I would like to acknowledge the financial support provided by the Engineering and Physical Sciences Research Council (EPSRC) through EPSRC Centre for Doctoral Training in Innovative Metal Processing [grant number EPL016206]. I would also like to thank my industrial sponsor, IHI Corporation, for providing additional funds and materials.

I would like to acknowledge the support of my academic supervisory team. Firstly, my primary supervisor, Professor Moataz Attallah, for his guidance and expertise in the area of powder metallurgy. Secondly, I would like to thank Dr Mark Ward for sparking my interest in research and giving me the idea to do a PhD in the first place. Finally, a special thank you goes to Dr Luke Carter for sharing his expertise in laser powder fusion and providing unwavering support and humorous conversation when it was most needed.

I am extremely grateful for the support provided by Dr Noriko Read, in her capacity as a research fellow at The University of Birmingham, as an industrial supervisor for IHI Corporation and as a colleague and friend. Without her this work would not have been possible. I would also like to thank Dr Akihiro Sato for providing industrial supervision in the first year of this work and Dr Tomomichi Ozaki for taking over the role when Dr Sato changed positions.

I express my gratitude to all technical staff within the Department of Metallurgy and Materials who have aided me in performing experiments. Additional I would like to thank the members of IHI's additive manufacturing team for assisting me in performing EPBF experiments and providing me with samples for analysis.

Finally, for their never-ending moral support, I would like to thank my friends Dr Amanda Field and Miles Fan and Jennifer Kirk as well as my father and sisters, without whom I would not have made it this far.

TABLE OF CONTENTS

LIST OF FIGURES

LIST OF TABLES

Chapter 1
Introduction

1.1 Ni-base superalloys

1.1.1 A brief history

The creation of the Ni-base superalloy was one of happy convenience, as it happened to coincide with the development of gas turbine engines (GTEs) for jet aircraft. In 1929 additions of Al and Ti were made to Nichrome; an alloy already extensively in use for its high temperature corrosion resistance. These alloying additions were found to result in a significant increase in the strength of the alloy. During the same period of time, aircraft design was evolving, with engines transitioning from the internal combustion engine to the GTE. It was already well known that higher temperatures were necessary to increase efficiency of the GTE, creating a demand for materials that could maintain their properties at elevated temperature (ET). The recently modified Nichrome was a promising new candidate, and thus began the close relationship of the superalloy and the GTE.

Since 1940 the advancement of GTEs has continued to fuel superalloy development (figure 1-1) in a mission to go to higher temperatures and increase efficiency further. Beyond alloy development much work has gone into optimising manufacturing processes to yield the very best performance from the materials. The most prominent example of this is the evolvement of casting techniques for turbine blades. The creation of methods for casting directionally solidified and single crystal material, has allowed for a reduction in material grain boundaries and an improvement in superalloy properties at ET.

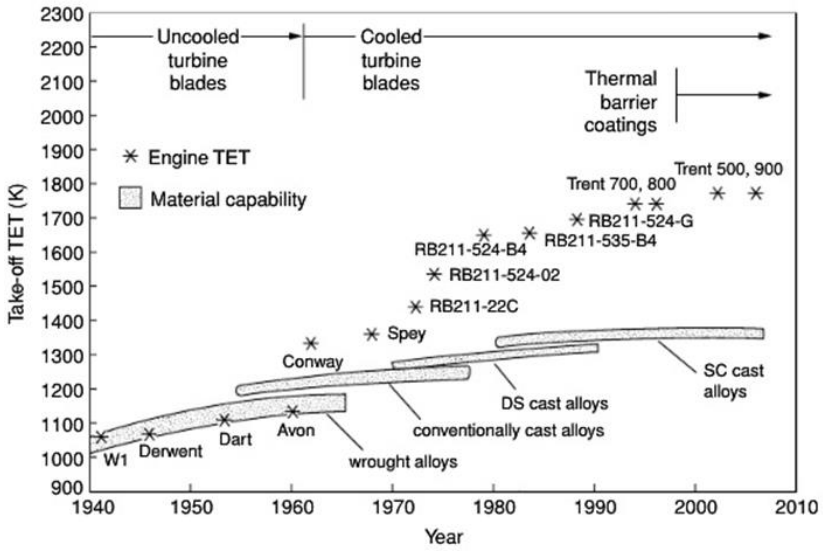

Figure 1-1: Evolution of the turbine blade material, processing route, surface finish and design, and the resulting increase in turbine entry temperature. Taken from [1].

1.1.2 An introduction to Ni-base superalloy metallurgy

As a consequence of the large number of alloying additions, Ni-base superalloys possess complex microstructures with numerous phases present. The majority of phases can be classified into five categories: the gamma (γ) matrix, geometrical close packed (GCP) phases, topologically close packed (TCP) phases and carbides and borides [2]. Table 1-1 highlights the phases belonging to each of these categories, along with possible elemental compositions and material properties resulting from the precipitation of each phase type.

Table 1-1: Categories of phases present in Ni-base superalloys along with phase descriptions, compositions, and positive and negative attributes imparted to the alloys. Information on phases obtained primarily from [1, 2]

Sub-category of phase	Phases & compositions	Positive attributes	Negative attributes
GCP	γ' (Ni_3(Al/Ti) γ''(Ni_3Nb) δ (Ni_3Nb) η (Ni_3Ti)	γ' and γ'' contribute to precipitation strengthening. In small quantities δ can act as a grain refiner improving tensile properties.	η precipitation can result in a reduction in tensile elongation. δ can have detrimental effects on tensile yield strength and creep properties (time to 0.2% strain and rupture strength).
TCP	Laves (Fe_2(Nb/Ti/Mo) σ (CrCo / FeCr/Mo) μ ($(Fe/Co)_7(Mo/W)_6$)		Brittle phases whose precipitation leads to a reduction in ductility.
Carbides	MC (Hf/Mo/Nb/Ta/Ti/W) M_7C_3 (Cr) $M_{23}C_6$ (Cr/Mo/W) M_6C (Mo/Nb/W)	Discrete carbides can pine grain boundaries and refine grain size improving multiple mechanical properties.	Closely spaced discrete carbides, carbides of script morphology and carbide films encourage intergranular fracture under loading.
Borides	M_3B_2 (Cr/Zr)	Improve creep rupture strength.	No data is available for quantities of precipitation that may cause detrimental effects to mechanical properties.

i. Gamma prime- γ'

As discussed in section 1.1.1 Ni-base superalloys were born from the addition of Al and Ti to Nichrome. While it was known that these alloying additions increased strength, the mechanism by which they did this was not discovered until some many years later, when the γ' phase was finally observed by electron microscopy [3]. Today γ' is the dominant strengthening precipitate in most Ni-base superalloys. Figure 1-2 (a) illustrates the ordered $L1_2$ crystal structure of γ' while figure 1-2 (b) shows a SEM image depicting the cubic morphology of the γ' precipitate.

a) **b)**

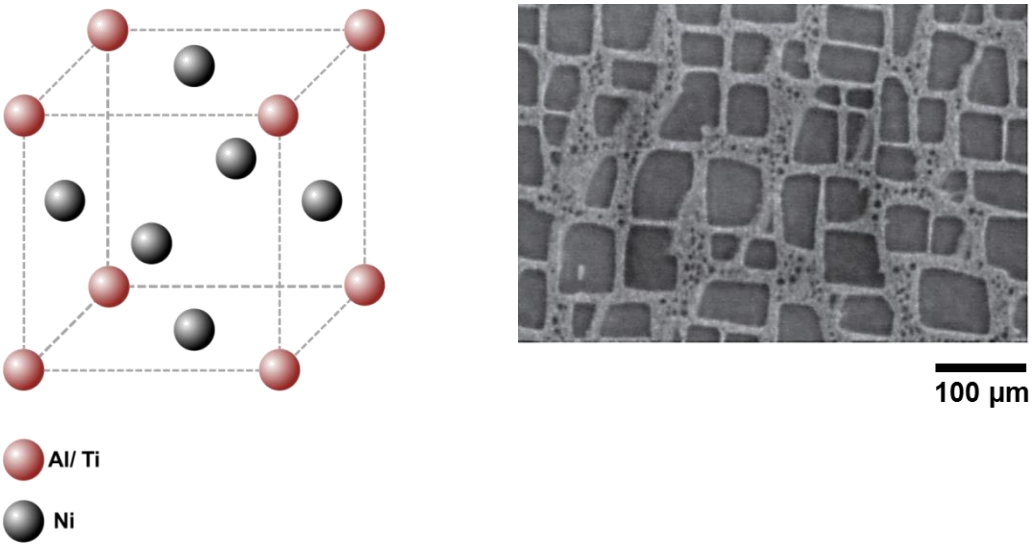

Figure 1-2: a) Illustration of γ' crystal structure and b) BSE SEM image of primary cuboidal γ' interspersed with spherical secondary γ', adapted from [4].

The mechanism by which γ' strengthens results from the difference in crystal structure and variation in allowable lattice vectors between the γ matrix and γ'. Dislocations in the FCC γ

matrix can be quantified by the lattice vector $\frac{a}{2}$<110>; this lattice vector however does not exist in the $L1_2$ γ' structure. Upon transitioning from the γ matrix into the γ', such a dislocation results in a reconfiguration of stacking sequence in the {111} planes of the $L1_2$ crystal structure leading to the formation of forbidden Ni-Ni and Al-Al bonds; in order that these bonds, be tolerated an anti-phase boundary (APB) must be introduced. The increase in APB energy within the {111} planes is thought to create favourable conditions for cross-slip of dislocation to the {100} planes, where the APB energy is significantly lower. Once in the {100} planes dislocations become immobile, as their glide is not possible within these planes [5]. This inhibition of dislocation movement results in a significant increase in strength.

Going back to the {111} planes, once an APB has formed it can be removed by a second dislocation of the same burgers vector; it is therefore energetically favourable for dislocations to move in pairs. Dislocation pairs can be weakly or strongly coupled. Weakly coupled dislocations are spaced such that the distance between them is greater than the diameter of the precipitates within their path. Strongly coupled dislocations on the other hand do not have much distance between them, allowing both parts of the dislocation pair to exist within a single precipitate simultaneously. To cut through the γ', the energy associated with the APB formed by the first dislocation, must be overcome by the second dislocation. The shear stresses required to do this differ depending on the coupling behaviour of the dislocations. For weakly coupled dislocations, equation one (Eq.1) can be utilised to estimate the shear stress required, whereas for strongly coupled dislocation equation two (Eq.2) is used. From the equations, the influence of γ' particle size is clarified, with the critical shear stress required being a direct function of the precipitate variables, particle radius and volume fraction. Particle radius is of course influenced by volume fraction, with increasing volume fractions limiting the growth of precipitates.

$$\tau_c = \frac{Y_{APB}}{2b}\left[\frac{6\,Y_{APB} \times f_r \times r}{\pi\, T}\right]^{\frac{1}{2}} - f_r \qquad \text{Eq. 1}$$

$$\tau c = \sqrt{\frac{3}{2}}\left(\frac{Gb}{r}\right) f_r^{\frac{1}{2}} \times \frac{W}{\pi^{\frac{3}{2}}}\left(\frac{2\pi \times Y_{APB} \times r}{W \times Gb^2} - 1\right)^{\frac{1}{2}} \qquad \text{Eq. 2}$$

Where, **Y_{APB}** is antiphase boundary energy

b is the burgers vector of the dislocation

T is line tension

f_r is volume fraction of γ'

r is the radius of the γ'

G is the shear modulus of the material

W represents the elastic repulsion of the dislocation within the γ'

ii. Gamma double prime- γ''

While γ' is the primary strengthening phase of most Ni-base superalloys, there are a select few alloys that achieve their strength through the precipitation of the γ" phase. The γ'' phase is an ordered body centred tetragonal (BCT) phase denoted $D0_{22}$, typically of the composition Ni_3Nb (figure 1-3). The γ'' is generally considered coherent with the γ matrix, however some coherency strain does exist parallel to the c axis of the lattice unit. This difference in coherency strain, leads to an increase in precipitate growth in one direction, resulting in the formation of disc shaped morphology. Precipitates typically have a length to width ratio of 3:1 or less [6] and are reported as being in the nm size range.

a) **b)**

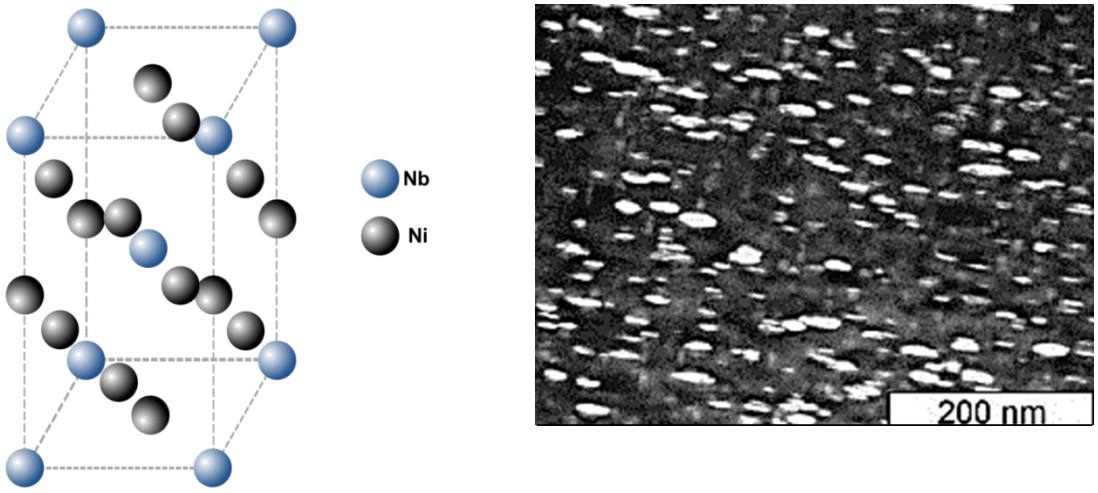

Figure 1-3: a) Illustration of the structure of the γ" precipitate and b) TEM dark field image of γ'' in γ matrix adapted from [7].

The strengthening mechanism of the γ'' is attributed to the coherency strains introduced in the γ matrix by the elongated precipitate. The stress fields created around the precipitate interact with the stress fields of moving dislocations impeding dislocation movement, strengthening the material. Coherency strains, such as that produced by γ", can be quantified by the following equation:

$$\Delta\tau \approx 1.7\mu|\varepsilon|^{\frac{3}{2}}\left(\frac{h^2 f}{bR}\right)^{\frac{1}{2}} \qquad \text{Eq. 3}$$

Where, **μ** is the shear modulus of the material
ε is the tetragonal distortion
R is the minor radius of precipitate
h is the major diameter of the precipitate
b is the burgers vector of the dislocation
f is the volume fraction of precipitates

As the γ'' coarsens, the coherent interface transforms into a semi-coherent interface with the nucleation of dislocations at the interface boundary, reducing the strain energy around the precipitate.

1.2 Near-net shape (NNS) manufacture of Ni-base superalloys

As industry is becoming increasingly competitive, the drive for shorter product to market times is strengthening. The majority of traditional manufacturing routes – forging, stamping, and machining etc.-all involve multiple stages of processing, adding time to the manufacturing process. Net shape (NS) manufacturing is the concept of producing a part that is of final component geometry, or close to final geometry (NNS), in one manufacturing step. At present Ni-base superalloy components commonly employ two NNS processes, casting and powder metallurgy (PM) hot isostatic pressing (HIPping).

Casting is the oldest NS/NNS processes known to man and has been used for the production of Ni-base superalloy blades since the mid 1950's. Excellent mechanical properties can be achieved through casting; however, they do not stand up to the demanding environment of GTEs without improvement by substantial machining of the castings post-process. In addition, improvement in performance of blades produced by casting has plateaued (figure 1-1); to address this issue a change in material, manufacturing process or both, is required.

PM HIPping was introduced to Ni-base superalloy production to address challenges presented by forging of evolving disc alloys. The development of higher strength alloys reduced hot workability making forging ever more difficult. PM HIPping was capable of processing such

alloys and provided the additional benefit of a reduction in processing time and improved material yield (figure 1-4).

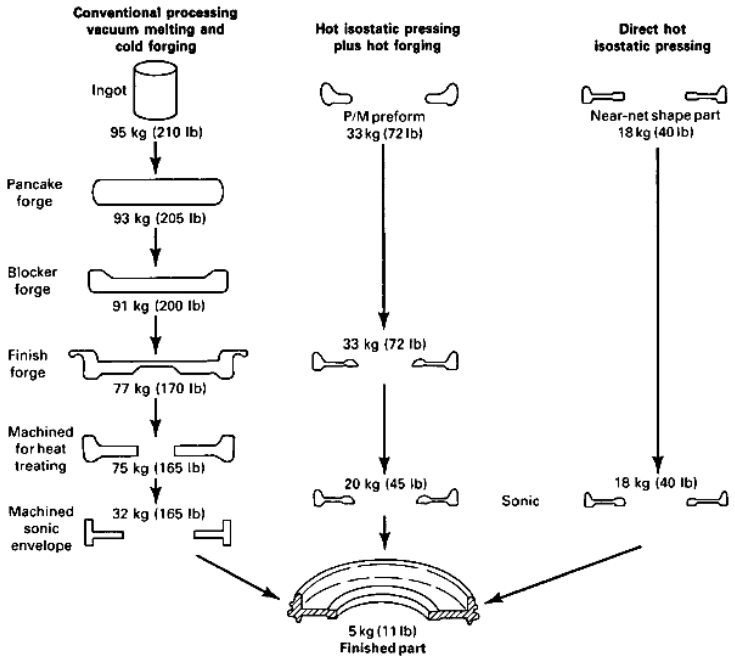

Figure 1-4: Possible processing sequences for a gas turbine compressor disk illustrating the input weight reductions possible with P/M superalloy technology. Taken from [2].

1.2.1 PM HIPping

Powder HIPping is a process by which metal powders are compacted by the application of high temperature and pressure. Powders are encapsulated in a canister, which is then outgassed and sealed. The canister is then placed into a pressure vessel (figure 1-5), which is then filled with an inert gas and heated until a desired pressure and temperature is achieved. The pressure and heat applied to the canister is transferred to the powders as the canister deforms. By using gas, equal heat and pressure is applied across the entire canister

making the process isostatic. The other advantage of gas applied pressure is its ability to apply pressure to small, hard to reach places in complex geometries. The applied heat and pressure are held for a length of time until the powders are fully consolidated.

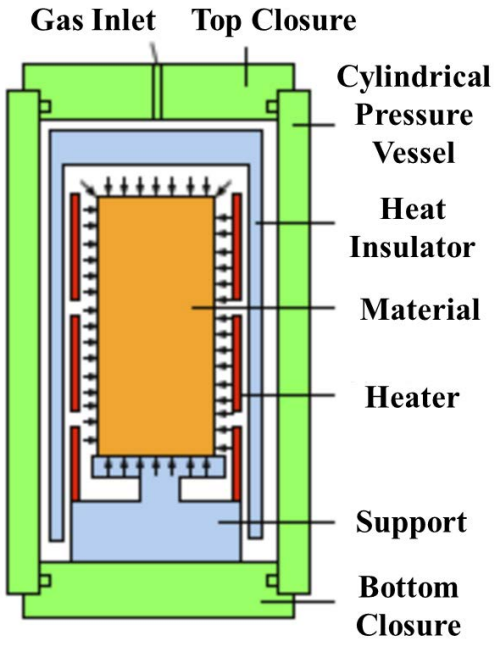

Figure 1-5: Illustration of a cross-section through a HIPping vessel. Taken from [8].

PM HIPping can offer advantages in multiple areas, including, part quality, cost and environmental impact [8]. In regards to part quality, HIPping has the ability to produce fine homogeneous microstructures resulting in improved mechanical properties. In addition complex parts can be produced without the need for multiple joints that act as points of weakness within the component. Economic advantages are gained due to PM HIPping being a leaner manufacturing route with relatively short production times. Such lean manufacturing is also of environmental benefit as with most NNS techniques the material yield is higher for PM HIPping compared to more traditional manufacturing routes.

Despite its advantages some challenges still exist for PM HIPping. Firstly, the time associated with production of HIPping canisters for large and complex parts, means that producing large quantities of such parts is not cost effective. Secondly, the canister material often differs from the powder material being compacted and hence needs removal after HIPping, adding another processing step to the component manufacture. Removal of the canister can be done by machining or etching. For complex geometries, etching is the preferred method, as some component areas may be hard to reach in machining. Relative to machining however, etching is more hazardous as it poses multiple health risks to the user as well as environmental risks if not disposed of appropriately.

1.2.2 Powder bed fusion (PBF) processes

Over the course of the last two decades, there has been growing interest in utilising PBF processes for production of Ni-base superalloy components. While powder HIPping was found to be the NNS solution to challenges posed by forging of superalloy components, PBF may just provide the answer for addressing challenges posed by casting [9]. PBF belongs to a group of additive manufacturing (AM) processes employing a layerwise approach to production. Such an approach is of interest for Ni-base superalloy components, as it has the potential to create more complex structures that yield improved performance relative to castings.

Simply framed, the PBF process is comprised of two steps, spreading a layer of powder across a metal substrate, followed by localised melting of the powder with a high energy beam. These two steps are repeated for hundreds to thousands of layers resulting in the building of a 3-dimensional component. PBF processes are categorised by the energy beam used for melting, with both laser (LPBF) and electron (EPBF) beam systems being available.

At present the LPBF market is substantially larger than EPBF. While there are tens of manufacturers of LPBF systems, only a handful of manufacturers offer sales of EPBF systems. This is in principal due to the relatively large capital investment needed to acquire an EPBF machine, which results from an increase in the cost of technology production for EPBF systems. This cost is of course accompanied by an improvement in performance capability.

Table 1-2 offers a comparison of each PBF technology. EPBF uses larger powders relative to LPBF, resulting in thicker build layers and faster build times on average. The downside of this is that EPBF has reduced resolution and significantly rougher surface finish. EPBF is carried out in vacuum, while LPBF is typically performed in an inert gas environment, making the former process much cleaner overall. LPBF is generally performed at room temperature (RT); however, in recent years systems have been introduced that carry out processing at higher temperatures (200-500°C). Even more recently, Aconity3D have developed LPBF systems capable of processing at 1200°C. Processing at ET reduces the magnitude of the thermal gradient between the weld pool and surrounding area reducing residual stresses in the build part. In addition to faster build rates resulting from greater layer thicknesses, EPBF also benefits from faster scan speeds due to the beam being deflected via electro-magnetic coils as opposed to LPBF which directs the laser beam mechanically by galvanometers.

Table 1-2: Comparison of LPBF and EPBF capabilities.

	LPBF	**EPBF**
Powder size range (µm)	15-45	45-105
Layer thickness range (µm)	20-60	50-100
Processing environment	Inert gas	Vacuum
Processing temperature	RT - 1200°C	Elevated (> $0.5T_m$)
Maximum power (KW)	1	3
Maximum scan speed (ms^{-1})	8	8000

1.3 Hybrid NNS manufacturing

Layerwise production methods are relatively slow when compared to other NNS processes such as PM HIPping. Increasing production rates is of critical importance for making the industrialisation of layerwise AM techniques economically favourable, and thus, has received substantial focus from the research community. In the last decade the concept of hybrid NS manufacturing has emerged. These techniques combine two or more manufacturing methods in a way that each process addresses the challenges of the other. The most prominent hybrid concept to date combines additive and subtractive manufacturing. After a layer of material is melted by direct laser deposition (DLD) – a blown powder AM technique- the edges and contour of the NNS layer are machined such that the layer becomes NS. This process allows the manufacture of complex parts to a high degree of tolerance with overall reduced production time and material waste. Machining in-situ is however not viable for PBF processes, therefore other methods of reducing component production time must be considered. One such process is in-situ shelling.

1.3.1 An introduction to in-situ shelling

Approximately a decade before hybrid manufacturing was a concept, Das et al. [10] proposed a production method combining LPBF and HIPping- the in-situ shelling process. The method consists of the shell of a component melted and its core sintered by LPBF, followed by HIPping to eliminate the core porosity and create a fully dense part. Figure 1-6 illustrates the process. By only partially melting the core of the component, significant time can be saved during the LPBF stage. As the HIPping canister and internal powders are of the same material, the canister no longer needs to be removed as with traditional HIPping. Several advantages can be gained by not removing the HIPping canister. Firstly there is a reduction in post-processing time. Secondly, less material waste is created; and finally complex shapes can be made without the need for hazardous etching processes to remove the canister.

c

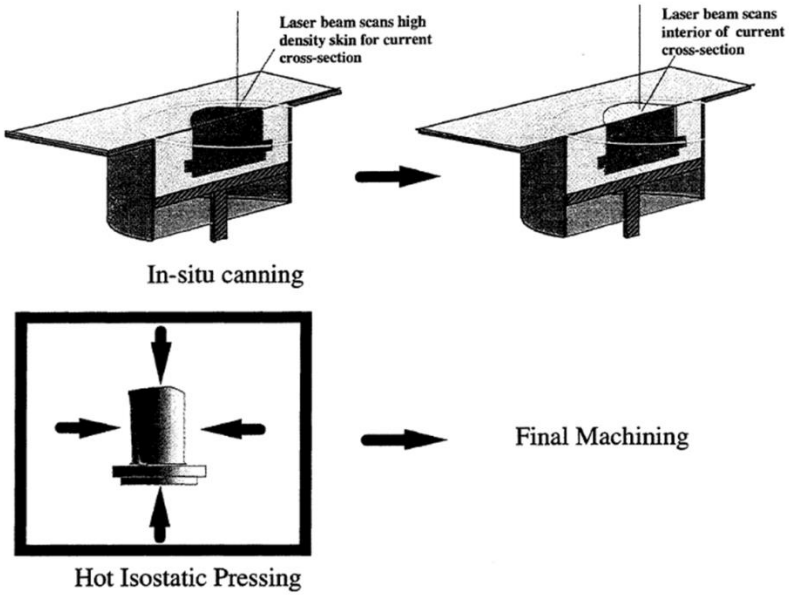

Figure 1-6: Illustration of the in-situ shelling process. Adapted from [10].

1.4 Research motivation

It is believed that the in-situ shelling process presents a possible means for incorporation of PBF technology into the mass manufacture of Ni-base superalloy components. By utilising this technology, parts of increased complexity can be manufactured without sacrificing production time and cost. As such the potential to yield performance improvements from existing superalloy components becomes increasingly viable. This work will therefore seek to provide proof of concept for in-situ shelling of Ni-base superalloys through the investigation of the process fundamentals.

Chapter 2
Literature Review

2.1 In-situ shelling

As discussed in chapter 1, the in-situ shelling method utilises LPBF to melt a dense skin around a partially sintered powder core, making it suitable for porosity closure by HIPping; the novelty of the technique being the simultaneous creation of green part and HIPping vessel. The original work by Das et al. in which the method was first examined [10, 11] studies two alloys- Ti-6Al-4V and Inconel 625. In the first stage of process development, the influence of HIPping on cylindrical coupons sintered to 98.5% density during the LPBF stage is examined. In both material cases HIPping was found to increase the density of the coupons. In the second stage of process development, coupons were sintered with gradually decreasing density from surface to core, the surface having above 98.5% density and the very centre of the core approximately 60%. HIPping in this instance was reported to be successful for the Ti-6Al-4V alloy, with very little porosity observed after HIPping. Microstructural examination however showed differences in the shell of the cylinder and core (figure 2-1), with the shell presenting a more prominent lamella structure. Results of the second stage Inconel 625 study were not discussed in detail, concluding remarks however suggest that initial trials were unsuccessful and requiring further investigation.

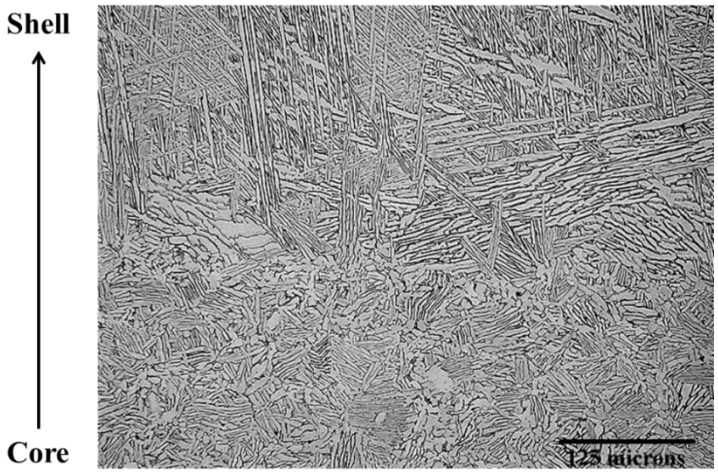

Figure 2-1: The interface between skin and core in SLS/HIP processed Ti-6Al-4V adapted from [11].

Almost 20 years after the last work was published by Das et al.[11] on the in-situ shelling method, a new body of work appeared, with the publication of work from researchers at the University of Birmingham[12, 13]. Given the ability of AM to build tailored geometries with little additional cost, Qiu et al.[12] combined the in-situ shelling method with modelling to build Ti-6Al-4V HIPping canisters with geometries that would result in uniform cylindrical canisters post HIPping. Figure 2-2 shows the canisters before and after HIPping. In addition to optimising canister geometries, Qiu et al.[12] also modified the in-situ shelling method, choosing not to sinter the powers in the centre of the canisters during LPBF; by doing this further time savings could be made during production. The disadvantage of this however, was that the mismatch in microstructure observed by Das et al.[11] between canister and core, was more exaggerated (figure 2-3) with the HIPped powder microstructure being significantly finer than the LPBF canister post HIPping.

Figure 2-2: Photographs showing several canister designs (a) before and (b) after HIPing. Taken from [12].

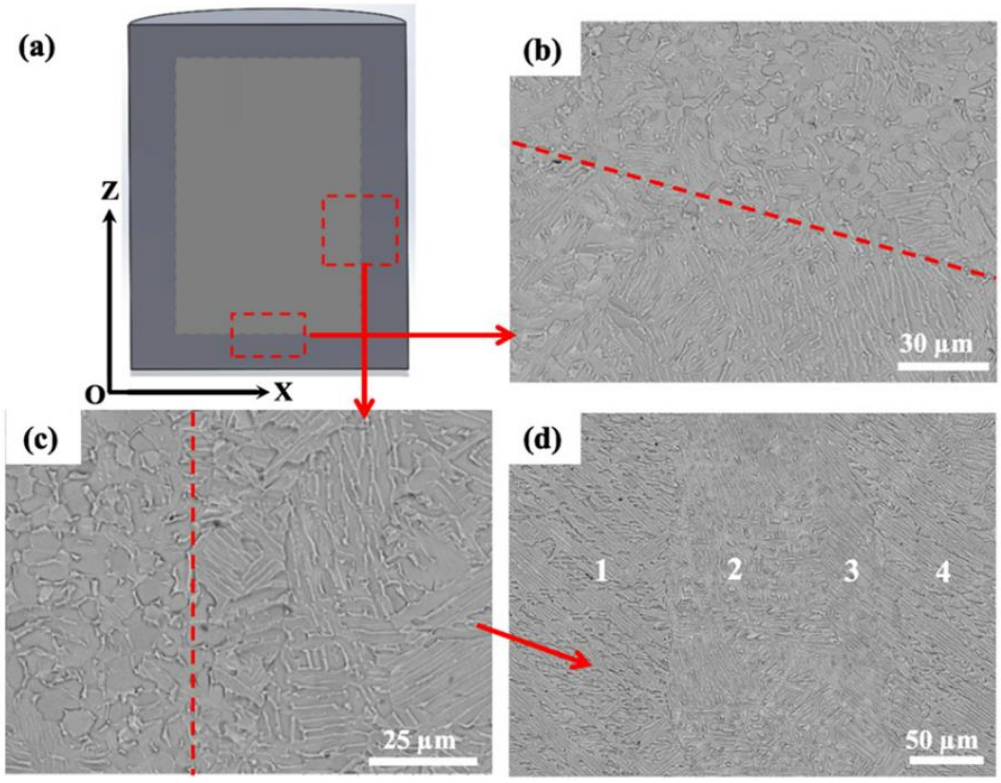

Figure 2-3: (a) Schematic illustration of a vertical section (XZ plane) for SEM characterisation; (b) microstructure at the interface between the bottom wall and HIPed powder;(c) microstructure at the interface between a lateral wall and HIPed powder; (d) microstructure within the LPBF + HIPed canister. The numbers in (d) represent several different columnar grains. Taken from [12].

While Das et al.[11] examined the tensile strength of the HIPped LPBF pre-sintered material, Qiu et al.[12] went one step further, performing tensile tests across the bond interface. They built canisters with the bottom half fully melted by LPBF and the top half, powders densified in the HIP, placing the bond interface at the centre of the tensile gauge length. Tensile specimens did not fail at the bond suggesting a perfect bond to exist between LPBF and powder HIPped material. Specimens failed in the LPBF side of the tensile specimen, owing to the coarser microstructure.

Further work examining production of Ti-6Al-4V by the in-situ shelling method, investigated the influence of HIPping temperature on microstructural homogeneity across the HIPped powder and LPBF canister tooling. Cai et al.[14] examined three different HIPping temperatures -950℃, 1000℃ and 1050℃. In addition to studying HIP temperature, they also opted to change the size of powder particles HIPped inside the canister, removing the LPBF powders (dia. 20-60 μm) and adding powders with an average diameter of 120 μm. Comparing the different HIPping temperatures, it was observed that as HIPping temperature increased, variation in HIPped powder and LPBF microstructures decreased (figure 2-4). Tensile and fatigue testing was also performed across the interface. For both tensile and fatigue testing, all of the samples failed within the LPBF canister, indicating a strong bond between HIPped powder and LPBF material. Tensile properties were significantly better in samples HIPped at 1000℃ and 1050℃; however, fatigue properties were improved in the sample HIPped at 950℃ owing to the more ductile basketweave structure relative to the Widmanstatten present in the LPBF canister material.

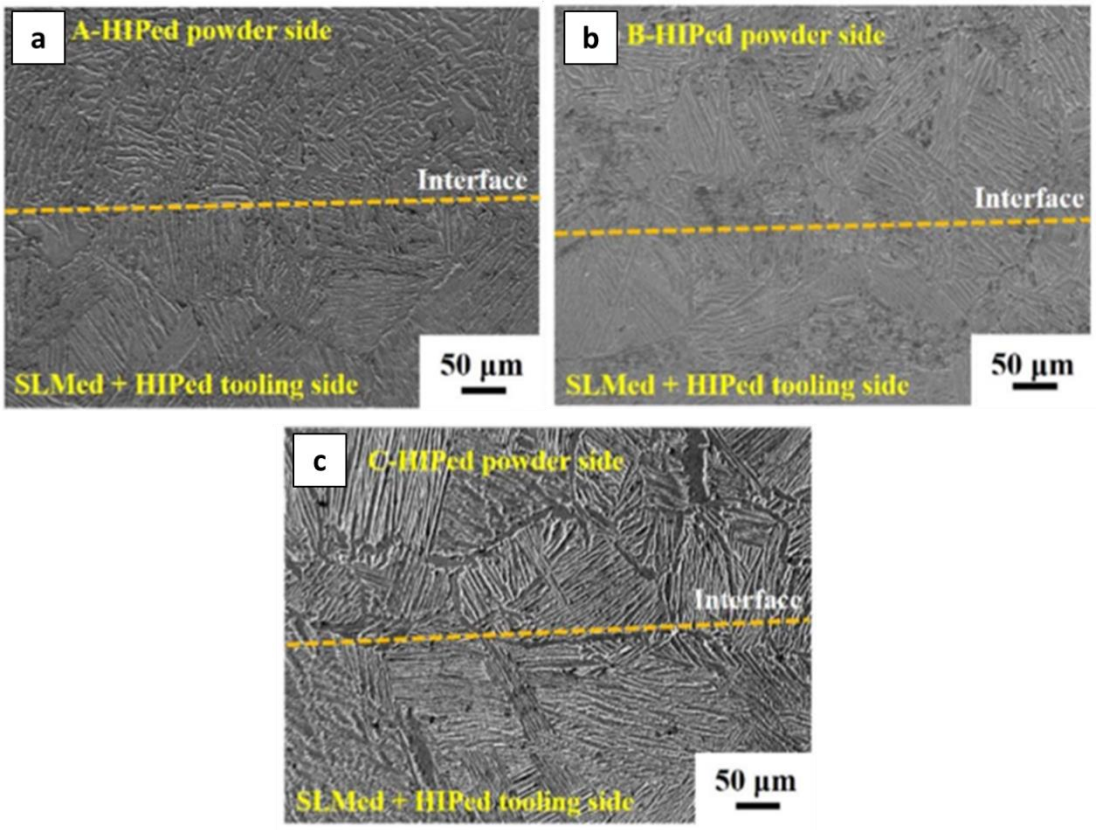

Figure 2-4: Microstructure at the interface between as-HIPped powder and LPBF canister: a) specimen HIPped at 950°C; b) specimen HIPped at 1000°C and c) specimen HIPped at 1050°C. Adapted from [14].

Leicht et al.[15] and Frisk et al.[16] took an alternative approach to the in-situ shelling method, opting to use EPBF at the AM stage of process. As the EPBF process already involves partial sintering of the power prior to melting, no productivity gains can be made by leaving the powder loose as with LPBF; however relative to EPBF small gains can be made due to not melting the entire component. Ti-6Al-4V in-situ shelling samples were produced with six different wall thicknesses ranging between 0.5 and 1.5 mm. As EPBF is performed in vacuum, samples were sealed in process. Figure 2-5 shows photographs of the samples. Cylinders with wall thicknesses 1.1 mm and greater were all found to show significant radial shrinkage during HIPping and to be fully dense. Cylinders with wall thickness of 0.9 mm

showed variable densification during HIPping, with some being fully dense and others showing no shrinkage at all. All specimens with wall thicknesses less than 0.9 mm failed to reach full density. Consequently, critical wall thickness for preventing surface connected porosity was deemed to be greater than 0.9 mm. Samples dimensions were measured before and after HIPping. Wall thickness was found to influence the levels of radial shrinkage in fully dense samples, with thinner wall thickness leading to an increase in radial shrinkage.

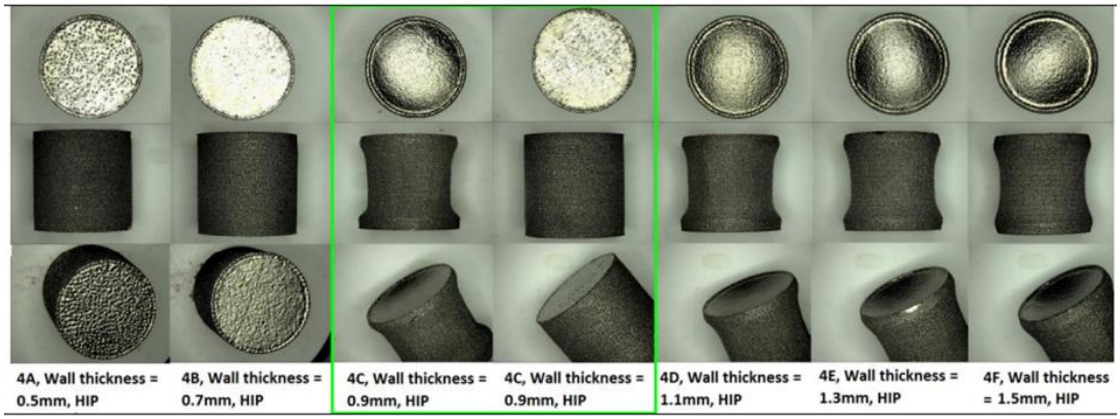

Figure 2-5: Overview of the EBM fabricated cylinders with different wall sizes, after HIP. The marked green square shows the critical wall thickness, 0.9mm, that need to be exceeded to obtain compaction during HIP. Taken from [16].

Microstructural examination of the EPBF in-situ samples showed no clean lines between EBPF + HIP shell and sintered + HIPped powder suggesting good bonding across the interface. As with LPBF samples, microstructure differed between the shell and core, however some regions of the sintered + HIPped powder showed similar microstructure to the EPBF + HIP shell (figure 2-6), likely resulting from the partial sintering of the powder.

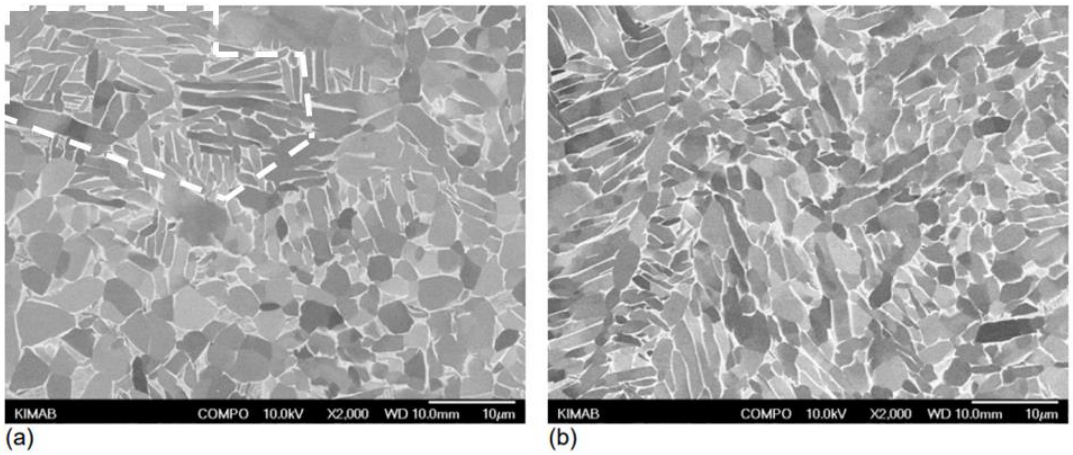

Figure 2-6: Microstructure in the shelled sample with 1.3mm wall thickness after HIP in the center (a) and in the surface (b). White dashed line in (a) indicates region of similar microstructure to EPBF shell. Adapted from [16].

The majority of work relating to in-situ shelling since the publication of Das et al.[11] has been conducted in Ti-6Al-4V. Follow up work to the in-situ shelling of Inconel 625 is almost non-existent with only one patent loosely relating to the in-situ shelling process being found[17]. The patent comprised of a method for process crack susceptible Ni-base superalloys, whereby the following steps were performed:

1. Conventional LPBF of the component.
2. Raising the temperature of the component to temperatures in excess of the operating temperature of material.
3. While at elevated temperature, re-melting the surface of the component by laser.
4. HIPping the component ton remove internal voids including cracks and pores.

The lack of work relating to Ni-base superalloys is most likely to stem from the difficulty in achieving good bonding between the core and the shell of the component. Ni-base superalloys produce relatively stable surface oxides. The disadvantage of this for a process such as in-situ

shelling is that these oxides can form on the surfaces of voids within the partially densified core, preventing bonding across voids formed at the interface between fully dense shell and partially densified core. Analogies can be drawn with the solid-state diffusion bonding process (SSDB). SSDB of Ni-base superalloys has been extensively researched, with the formation of stable oxides on faying surfaces reported as a common problem [18]. Studies have implemented multiple methods to improve surface conditions, predominantly focused on reducing surface oxides [18, 19], including use of filler materials and nickel surface plating, and simple polishing and chemical cleaning of surfaces. By significantly reducing the oxidation at the surface bonding between two Ni-alloy surfaces and dissimilar material can be achieved [18].

2.2 Oxidation of Ni-base superalloys

Due to the aggressive nature of the environments in which superalloy components operate, it is extremely important for the alloys to possess high temperature oxidation resistance. Such resistance is imparted by the formation of a continuous protective oxide film. Figures 2-7 and 2-8 show examples of oxide scales formed in two different Ni-base superalloys. For the majority of Ni-base superalloys, films are predominantly composed of Chromia (Cr_2O_3) and/or Alumina (Al_2O_3). Chromia is primarily induced to impart hot corrosion resistance and alumina high temperature oxidation resistance [20, 21]. Additions of transient oxides NiO and TiO_2 may also be observed within the external scale, though in relatively small quantities [21-24]. Also typically observed is a γ' depleted zone (figure 2-8) between the oxide scale and bulk material, resulting from a localised reduction in Al concentration as a consequence of Al_2O_3 formation.

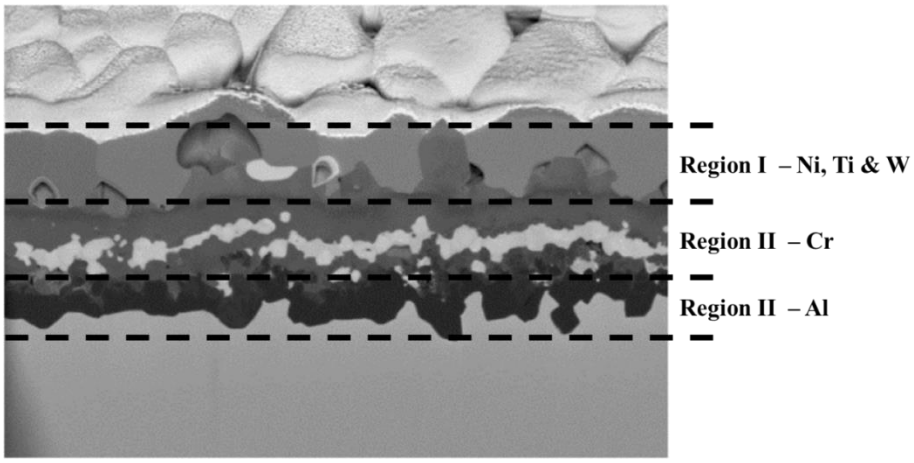

Figure 2-7: BSE micrograph of surface cross-section of oxidised CMSX-4 Ni-base superalloy, following oxidation at 1135 °C for 960 seconds in air. Adapted from [23].

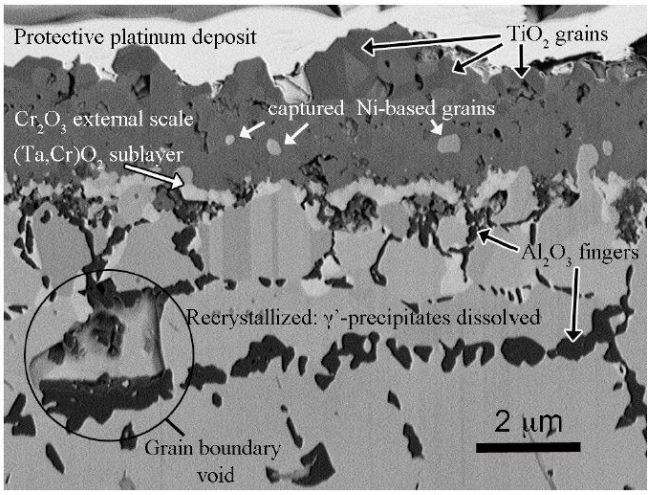

Figure 2-8: BSE micrograph of surface cross-section of oxidised ME3 Ni-base superalloy, following isothermal oxidation at 815 °C for 440 hours in air. Taken from [22].

2.2.1 Formation mechanisms of oxide scales in Ni-base superalloys

It is generally accepted that the nucleation and growth of both transient and stable oxides occurs simultaneously in the first stages of oxidation [21, 24, 25]. The growth rate of the transient oxides is significantly faster than that of the more stable oxides and thus forms the initial external oxide layer. As the more stable oxides continue to grow below the transient

oxides, they form continuous films, cutting off the supply of metal ions to the external oxides slowing their growth rate. When supplies of Ti and Ni ions are significantly reduced their oxides will begin to decompose, eventually leaving only trace grains of NiO and TiO_2 visible within the new stable external scale of Cr_2O_3 or Al_2O_3.

2.2.2 Influence of alloy composition on oxide scale composition

The composition of a Ni-base superalloy's outer most oxide scale is predominantly dependent on the concentrations of Cr and Al in the alloy. Less than 10 wt-% of Cr is insufficient for formation of a continuous external oxide scale of chromia [24] with the majority of Chromia forming superalloys having typically greater than 13 wt-% Cr [26]. Generally Al concentrations of greater than 6 wt-% are required to promote establishment of an external alumina scale in binary Ni-Al systems, however with additions of Cr (approximately 15 wt-% or greater) external alumina can be formed at Al concentrations as low as 3 wt-% [24], with its formation as an external scale often more favourable than chromia [20, 27].

In addition to the Cr-Al balance, concentrations of other minor alloying elements such as Ti, Co, W and Mn [21, 24, 28, 29] can also influence the composition and quality of the external scale. Cruchley et al. [28] examined the oxidation kinetics of Ni-base superalloy RR1000 with the objective of understanding the influence of Ti doping on the quality of protective Chromia scales. They found chromia growth rate to be significantly higher in the superalloy when compared to chromia forming steels and simpler Ti-free alloys. This increase in growth rate was attributed to an increase in Cr vacancies within the existing scale created by the presence of Ti. The growth rates seen in this study would suggest that Ti acts to destabilise chromia scales, encouraging the formation of alternative oxides in the outermost region of the scale; conclusive with earlier studies in which oxides such as NiO, TiO_2 and alumina are the

dominant constituents of the external scale [20, 30, 31] despite Cr and Al concentrations and oxidation conditions suggesting chromia formation should be more thermodynamically favourable.

2.2.3 Influence of oxidation environment on oxide scale composition

In addition to the influence of alloying constituents on oxide scale composition, the oxidation environment- temperature, oxygen partial pressure and exposure time- also plays a key role. Increasing temperature will of course increase the diffusion rate of oxide forming elements, resulting in an increase in oxide growth rate and in some cases transformation of the oxide species. Three polymorphs of alumina exist, Θ-Al_2O_3, γ-Al_2O_3 and α-Al_2O_3. At lower temperatures and with short exposure times alumina presents as the metastable polymorphs of Θ and γ; as temperature increases the alumina scale transforms into the stable stoichiometric α polymorph [32], which is stable to approximately 1400 °C. Chromia on the other hand transforms into the volatile CrO_3 species at a temperature of approximately 900 °C.

According to Sieverts law the concentration of oxygen dissolved in a metal is proportional to the partial pressure of oxygen in the surrounding atmosphere. Consequently the critical concentration of protective oxide forming elements such as Cr and Al, decreases with decreasing oxygen partial pressure [31], leading to earlier nucleation and growth of protective oxide films. Jung et al. [23] investigated the influence of oxygen partial pressure on oxide scales formed by CMSX-4. Samples were sealed in a vacuum environment, 99.999 % oxygen at 2 atm. and 99.998 % argon at 860 mbar, equating to oxygen partial pressures of $2x10^{-11}$, $2x10^{-1}$ and $2x10^{-9}$ respectively. Samples were then heated to 1135 °C and then immediately withdrawn to cool, resulting in a total of just 960 seconds above 100 °C. At the highest partial pressure of oxygen, it was found that a complex multi-layered scale formed, consisting of an

outer layer of NiO, a middle layer composed of both chromia and alumina and an inner alumina layer. Conversely samples heated in vacuum, produced only a single layer of alumina.

2.2.4 Influence of material surface condition on oxide formation and stability

The starting surface condition of a material undergoing oxidation plays a key role in its oxidation behaviour. Characteristics such as surface roughness and stress state have been shown to influence rates of oxide scale formation and even the composition of the scales that are formed [26]. Very few studies have looked at the influence of surface roughness on oxidation behaviour of Ni-base superalloys [33-35]; of these the most comprehensive was presented by Nowak et al. [35]. Thickness and composition of oxide scales produced by Mar M 247 exposed to isothermal and fast and slow cyclic oxidation conditions were examined for three different surface roughness, spanning a range of average surface roughness values from 0.096 to 0.925 μm. Under isothermal conditions- 1000 °C for 48 hrs- oxide thickness, homogeneity and composition varied between high and low surface roughness. Low surface roughness produced highly homogeneous external scales of NiO, whereas high surface roughness resulted in heterogeneous scales of Θ-Al_2O_3. Glow discharge optical emission spectroscopy (GD-OES) along with cross-sectioning of the samples (figure 2-9) revealed multi-layered scales for both surface conditions; however, thickness and composition varied significantly. Thickness of the oxide scale formed on samples with high surface roughness was approximately half that of those formed on samples with low surface roughness. Furthermore, low surface roughness samples produced both chromia and alumina whereas high surface roughness samples produced only the latter.

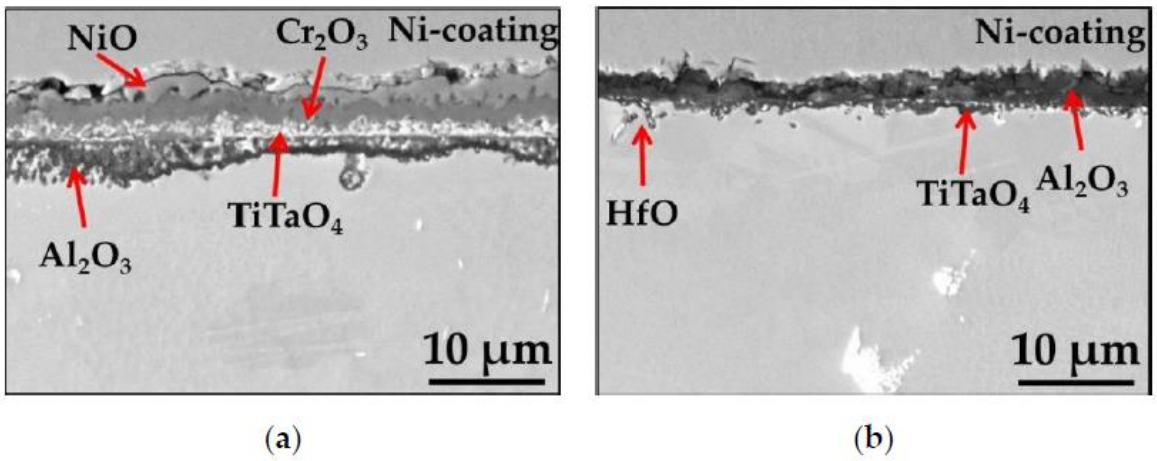

Figure 2-9: SEM/BSE images performed on cross-sections of Mar M 247 after isothermal air oxidation test at 1000 °C up to 48 h showing oxide scale formation on: a) Polished surface (Ra = 0.096 µm) ; b) Ground surface (Ra = 0.925 µm). Taken from [35].

To investigate the mechanisms responsible for the observed discrepancies in oxide formation behaviour resulting from differences in surface roughness, Nowak et al. studied the oxidation behaviour, surface stress state and quantity of defects in a simpler ternary alloy of Ni-14Cr-4Al. Oxidation behaviour was similar to that observed in Mar M 247, in that, samples with rougher surface finish produced predominantly alumina as an external oxide and smoother samples NiO. Rougher samples were found to possess a greater number of surface defects as well as exhibiting a higher level of compression at the surface. It was concluded that the dominant mechanisms driving the oxidation behaviour were quantity of surface defect and surface stress state, and not in fact surface roughness itself. Similar results have been observed in steels that had undergone shot peening, in which external scales of chromia were established earlier relative to samples that had not had compressive stresses induced in the surface [36].

2.2.5 Failure of oxide scales

For Ni-base superalloy components in service, failure of existing stable oxide scales would result in further oxidation and significant degradation of the component. Failure of the oxide scale occurs in one of two ways, either the oxide scale cracks or spalls. Generally cracking in the oxide layer occurs when the oxide is subjected to tensile stresses. Surface connected cracks provide new pathways for inward diffusion of oxygen, locally increasing the rate of oxidation. While further oxidation of a component in service is not desirable in any form, relative to spalling, failure by tensile cracking is not so detrimental. Very little of the component bulk surface is exposed to the environment through the cracks and due to the increase in localised oxidation rate, cracks can heal relatively quickly [37].

Spalling is the process by which relatively large pieces of the oxide scale break away and occurs when compressive stresses are induced in the oxide scale. Spalling can occur by one of two mechanisms depending on the strength of the bond between oxide scale and bulk metal [37]. When the strength of the oxide-metal interface exceeds the compressive strength of the oxide, shear cracks can form at the oxide surface and grow towards the oxide-metal interface. Once at the interface, tensile cracks can nucleate from the shear crack tip, penetrating along the oxide-metal interface removing sections of oxide scale as they progress. Figure 2-10 illustrates the mechanism of spallation when the oxide-metal interface strength is less than that of the compressive strength of the oxide. Compressive stresses induced in the oxide scale led to decohesion and buckling of the oxide scale; at a critical stress, cracks develop at the boundaries of the buckling oxide and a large piece of the oxide scale breaks away.

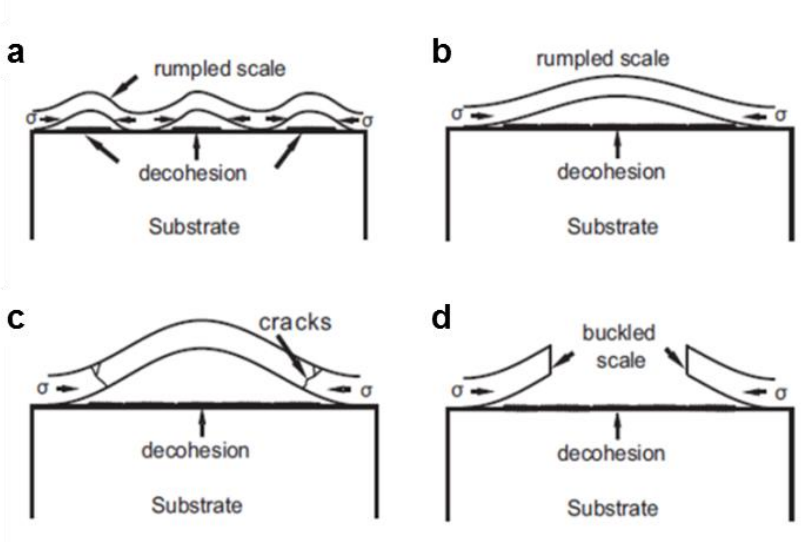

Figure 2-10: Schematic illustration of oxide decohesion, cracking and spalling. a) rumpled scale induced by compressive internal stress and decohesion of oxides scale from scale/substrate interface; b) large area of decohesion formed by connecting small ones; c) cracking due to further rumpling and growing of oxides scale; d) spalling of oxides scale from the scale/substrate interface and the buckled scale after spalling. Adapted from [38].

2.3 Powder Metallurgy of Ni-base superalloys

PM processing of Ni-base superalloys has typically been reserved for those alloys utilised in turbine disk applications and those employing oxide dispersive strengthening (ODS) as one of their primary strengthening mechanisms. Historically such alloys have been difficult to process, even more so as alloys have developed to become stronger by the addition of new, often harder, alloying elements. Increased alloy complexity and hardness, resulted in challenges for both casting of ingots, in the form of elemental segregation, and forging of components due to reduced workability [2]. PM processes could be used to address both challenges presented by conventional processing. Firstly, rapid solidification of melt during

powder production reduced segregation of alloying elements. Secondly, components could be made NNS eliminating the need for forging and reducing the extent of machining.

2.3.1 Production of Ni-base superalloy powders

Nickel-base superalloys go through three stages of melting prior to being formed into powder- vacuum induction melting (VIM), electro-slag refining (ESR) and vacuum arc re-melting (VAR) [1]. In the first stage (VIM) an electromagnetic field is used to heat and melt raw and scrap metal (charge). An illustration of the induction furnace can be seen in figure 2-11. The crucible is commonly lined with an oxide such as Al_2O_3, MgO or CaO [39]. A current is passed through the copper heating coils, creating a magnetic field within the crucible. This induces a current in the charge, heating it. Once the charge is molten the electromagnetic field acts as a stirrer, mixing the alloy elements [39]. When the molten charge has been stirred for a sufficient time, it is poured into a mould ready for the next melting stage.

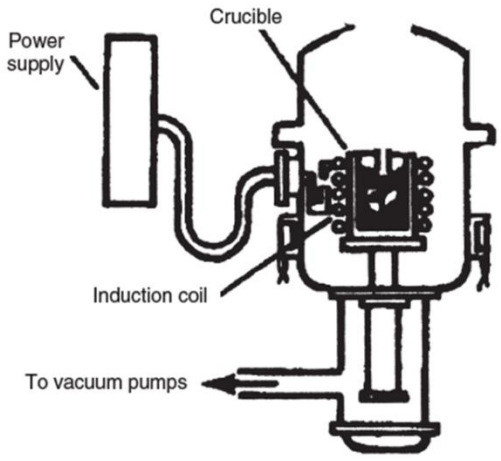

Figure 2-11: Illustration of vacuum induction furnace adapted from [39].

Following VIM, the solidified alloy is then re-melted by the ESR process to remove impurities such as oxides, nitrides and sulphides. The material produced by VIM is re-melted through a slag, usually composed of CaF_2, CaO, MgO and Al_2O_3 [1]. As the molten droplets pass through the slag, the slag reacts with the alloy droplets picking up any impurities and refining the melt chemistry. Finally, the solidified casting from the ESR process is transferred to the VAR process, in which it is again re-melted, this time in a vacuum environment, allowing for further removal of impurities by volatilisation. VAR like VIM, also uses an electromagnetic stirring process, creating a more homogeneous microstructure relative to the starting electrode.

Proceeding alloy production and refining atomisation of the superalloy is performed to create powders for use in PM processes. Several methods of atomisation exist, including but not limited to, water atomisation (WA), gas atomisation (GA), plasma rotating electrode process (PREP) and plasma atomisation. GA and WA processes begin by melting of the superalloy ingot produced in the refining stages. The melt is then transferred to a melt chamber fixed above an atomisation chamber (figure 2-12-b), connected by an atomisation nozzle (figure 2-12-a). As the molten metal flows through the nozzle orifice, high pressure fluid (water or gas) is directed at the melt stream, breaking the flow of melt creating powder particles. The atomisation chamber typically has two collectors. A cyclone separator draws finer particles which are then collected in the secondary collector, leaving larger denser particles to be collected by the primary.

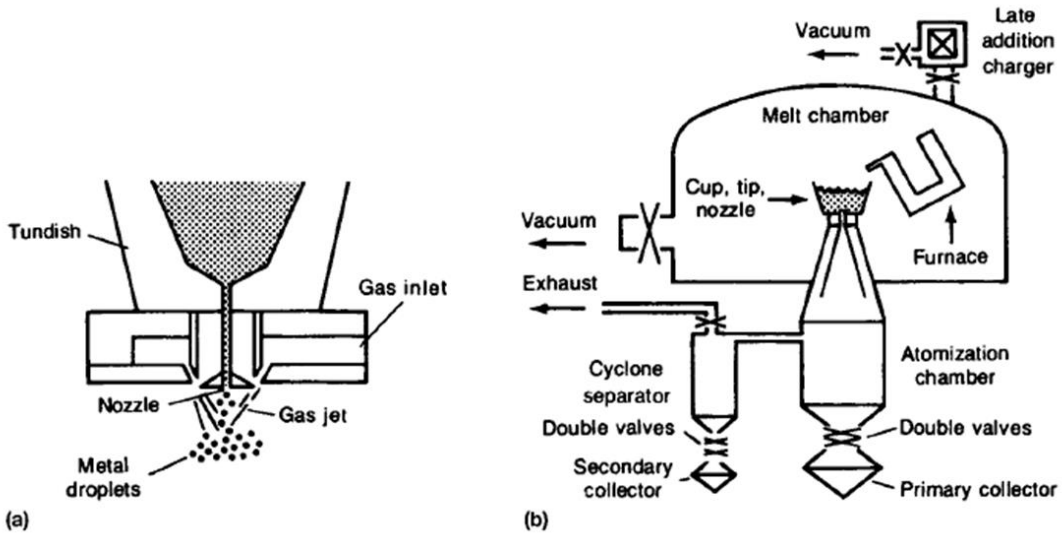

Figure 2-12: GA system for producing superalloy powder. a) Nozzle detail; b) System. Taken from [2].

Unlike the melt spray techniques described above, PREP and plasma atomisation utilise a solid wire for the powder feedstock material. The PREP process (figure 2-13) atomises powders by rotating a wire electrode at high speed while melting its rotating face with an arc plasma gun [40]; the centrifugal force created by the rapid rotation throws the melt material away from the electrode creating metallic powder particles. The plasma atomisation process (figure 2-14) works by pre-heating a wire feedstock which is then fed into an atomisation chamber and through the apex of three plasma torches [41]. The force of the plasma torches creates a spray of molten metal from the wire tip. Recycled powders can also be used as a feedstock material for the plasma atomisation process.

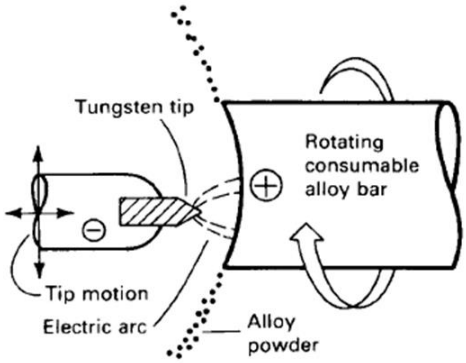

Figure 2-13: Schematic of the plasma rotating electrode process (PREP). Taken from [2].

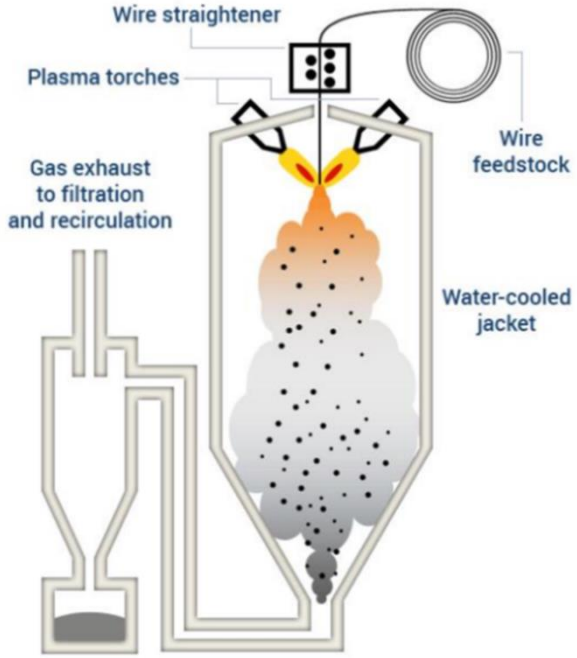

Figure 2-14: Schematic of plasma atomiser employed by AP&C. Taken from [42].

2.3.2 Powder morphology and microstructure

The morphology and microstructure of Ni-base superalloy powders has a significant influence on the microstructure that results from each PM processing route. It is highly dependent on the atomisation techniques employed in production, as well as the conditions

implemented in each technique. Here, only the resulting morphologies and microstructures of each atomisation technique will be presented, as the mechanisms of how these are achieved is outside the scope of this thesis.

Figure 2-15 illustrates the morphologies typical of Ni-base superalloys produced by a range of atomisation techniques. Powders produced by plasma atomisation techniques (figure 2-15-c and -d) possess significantly more sphericity than those produced by melt spray techniques (figure 2-15-a and -b). This is the result of several factors; firstly, surface oxide formation is more prominent in melt spray techniques, with the presence of these oxides lowering surface tension and increasing spheroidisation time, such that solidification completes before spheroidisation. Secondly, the rotational force exerted on the solidifying melt during PREP promotes spheroidisation of the melt prior to solidification. Finally, in plasma atomisation, the gradation of temperature from the core of the plasma arc to the outermost region provides time for spheroidisation prior to melt particles solidifying upon exiting the plasma.

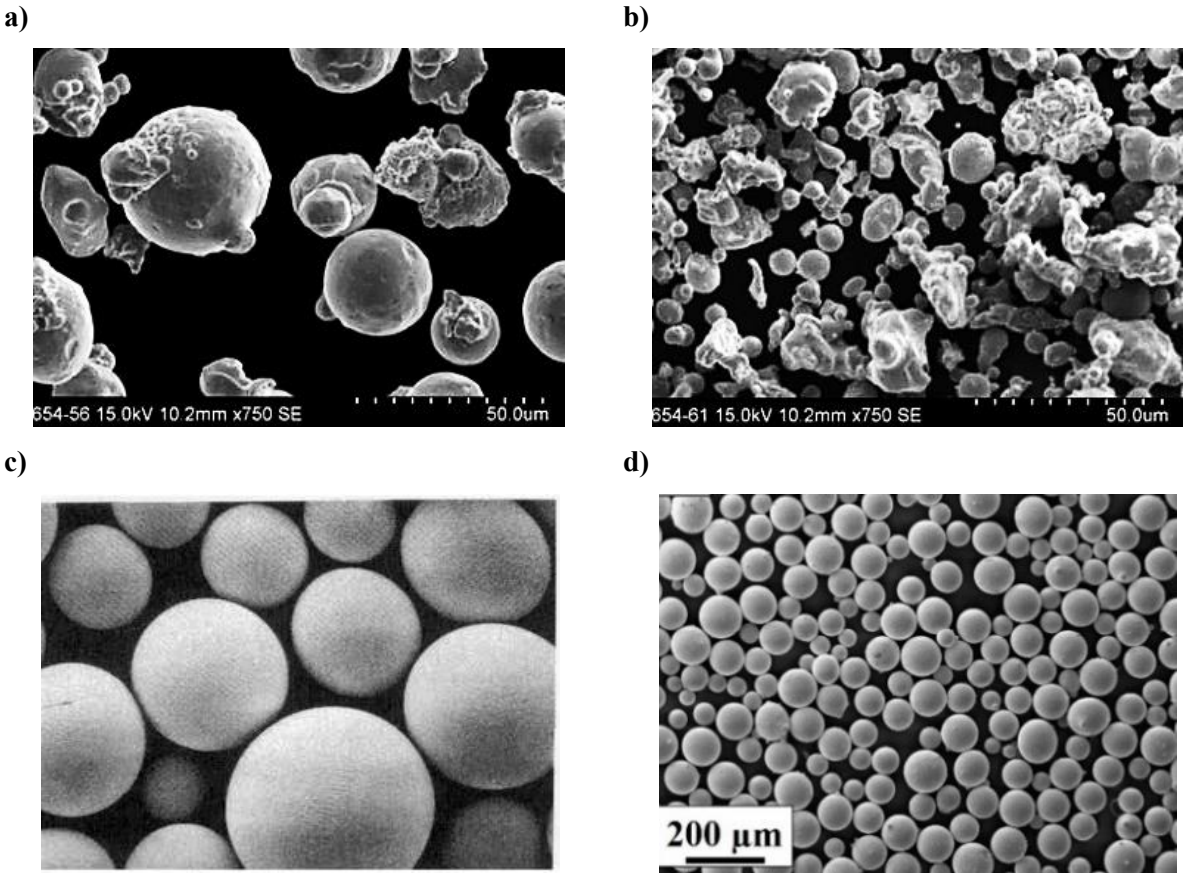

Figure 2-15: SE SEM images of powder particles. a) GA IN625[43]; b) WA IN625[43]; c) PREP Rene 95[44] and d) plasma atomised IN718[45] .

The solidification times and consequently microstructures of powders, while influenced by powder size, is primarily dictated by atomization media. GA powders are typically subjected to cooling rates of 10^2 Ks^{-1}, WA, 10^4 Ks^{-1} and plasma $10^5 Ks^{-1}$ [46]. Figure 2-16 shows micrographs of cross-sections of Ni-base superalloy powders produced by GA and plasma atomisation. The slower solidification rates undergone by GA powders are clearly defined by coarser dendritic structures and reduced solute trapping relative to plasma atomised powders.

a) b)

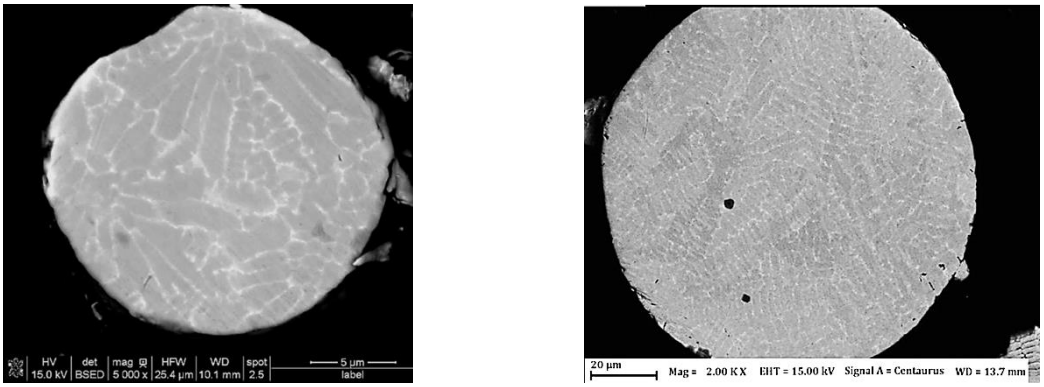

Figure 2-16: BSE SEM micrographs of IN718 powder cross-sections yielded by: a) GA[47] and b) Plasma atomisation[48].

2.4 PM HIPping of Ni-base superalloys

PM HIPping has been an established manufacturing process for Ni-base superalloys for near 70 years having first been employed for the production of ODS alloys in the 1950's [2]. In the following decade PM HIPping alloys were expanded to include γ' strengthened Ni-base superalloys. Initial results from these alloys were however poor, owing to the presence of prior particle boundaries (PPBs). It wasn't until several years later when alloys were adapted to have lower carbon content, effectively reducing PPBs that HIPping was re-popularised. Today HIPping is an integral part of PM processing of Ni-base superalloys; whether for direct component production by PM HIPping or for ensuring the integrity of AM parts.

2.4.1 PM HIPping Process

PM HIPping consists of five main processing stages: HIP canister design and construction, powder filling, canister outgassing and sealing, HIPping and canister removal.

i) **The HIPping canister**

The European HIP group (EuroHIP) specify a HIPping canister must have the following requirements in order for powder HIPping to be successful [8]:

1. The canister must be strong enough to maintain shape and dimensional control during HIPping.
2. The canister must be malleable at HIP temperature.
3. The canister must not react with the powder being processed.
4. The canister must be leak proof as any surface connected porosity will prevent densification.
5. The canister must be weldable for secure sealing.
6. The canister must be removable.

Several materials exist capable of fulfilling these requirements, the most popular of which for HIPping of metallic powders are low carbon steel (mild steel) and stainless steel. Canisters are commonly constructed by Tungsten Inert Gas (TIG) welding of cut steel sheet and/or pipe. TIG welding tends to provide higher precision relative to other welding techniques suitable for steels; important as, despite the isotropic nature of pressure applied by the HIP vessel, the location and quality of weld seems can influence densification behaviour during HIPping. Figure 2-17 illustrates the influence of such parameters on the deformation behaviour of a simple canister. To maintain uniformity during shrinkage, a canister with rounded corners and a centre weld seam is suggested. Considering design 1, it has also been suggested that the proximity of the weld seams to the centre plane of the canister affects the homogeneity of densification, with weld seams positioned further from the middle plane resulting in more uniform shrinkage [49].

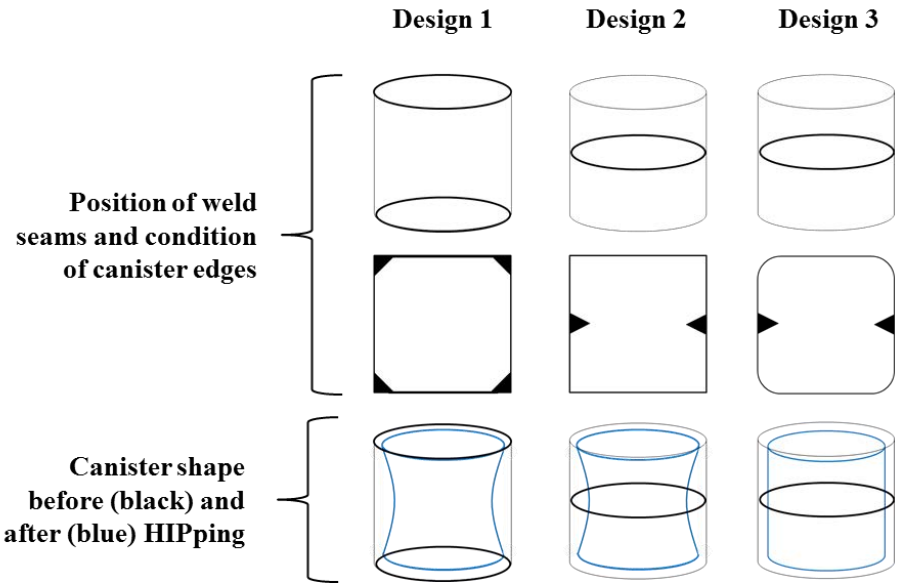

Figure 2-17: Illustration of three simple cylindrical canister designs and their influence on uniformity of densification during HIPping. Adapted from [8].

For netshape PM HIPping the canister geometry is similar to the geometry of the final PM part. Modelling and simulation is quite often conducted to predict the starting canister geometry based on the differences in shrinkage that may occur owing to characteristics such as weld placement as discussed prior.

In addition to canister geometry and assembly procedures, canister thickness plays an important role in maintaining dimensional control during densification [8]. Besson et al. [50] demonstrated that the difference in axial and radial stress tensors tends towards zero, when the ratio of canister radius to wall thickness is greater than 1. Consequently, as canister wall thickness is decreased for a constant canister diameter, uniformity of densification improves. The proof presented by Besson et al. was performed for a constant temperature, however later studies examining the influence of temperature [51, 52] mostly show the relationship to hold true. Modelling presented by Van Nguyen et al. [52] shows the exception to the rule to be inhomogeneity in the powder packing within the canister; while anisotropy of shrinkage is

still less for a thin walled canister, the influence of canister wall thickness is less impactful when significant discrepancies exist in the powder distribution.

ii) Filling and outgassing of the HIP canister

Following assembly of the HIPping canister, the canister is filled with the powders. Figure 2-18 shows an example of a HIPping canister with filling tube and funnel attached. The filling tube is welded to the canister assembly and is also used for outgassing. To ensure high powder packing densities inside the canister, the canister is often shaken or vibrated, followed by filling of additional powders. Shaking and filling is repeated until tap density of the powders is reached.

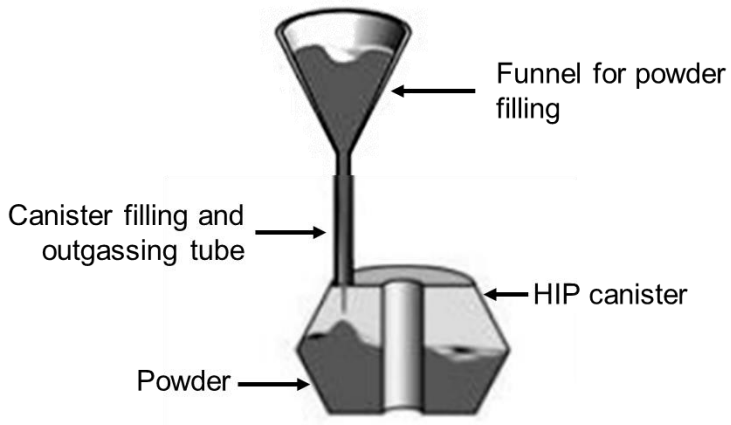

Figure 2-18: Illustration of HIP canister being filled with powder. Adapted from [53].

Figure 2-19 shows a schematic of canister outgassing and sealing. Outgassing of the canister is performed to remove residual gasses from the canister. Reactive gases such as oxygen and nitrogen would form undesirable oxides and precipitates at powder surfaces preventing diffusion between powder particles during HIPping. Under the high pressures and temperature of HIP non-reactive gases such as argon are forced into solution with the powders. However, if high temperature heat treatments are later applied to the powder component, without added

pressure, such gasses will come out of solution forming new porosity within the part; so-called thermally induced porosity (TIP). TIP can act as a stress initiator when components are subjected to mechanical stresses, and hence can be detrimental to the properties of PM HIPped parts[54]. Outgassing can be performed at RT or ET. ET conditions may be used where moisture is a concern. To perform ET outgassing the entire HIP canister is encased in a vertical tube furnace while being evacuated. The influence of ET outgassing on HIP microstructure is discussed in section 2.4.3-i.

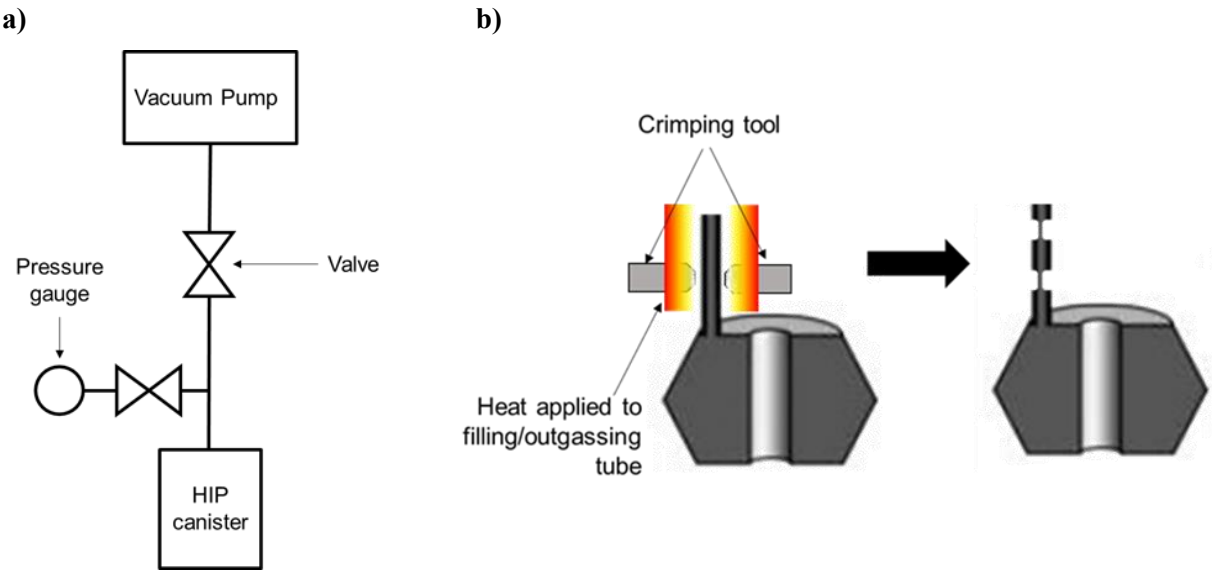

Figure 2-19: Schematic of canister outgassing (a) and sealing by hot crimping (b). Adapted from {Gamil, 2016 #433}

iii. HIPping

Following outgassing and sealing of the HIP canister, the canister is placed in the HIP vessel (figure 2-20). Multiple canisters can be placed in a single vessel side by side and/or stacked. The isostatic pressure and temperature applied to the HIP canisters is created by the

application of hot gas, typically argon. The HIP vessel once sealed is evacuated and then filled with the gas either being heated during its introduction to the vessel or after a specified pressure is reached. The canister is held at pressure and temperature for a period that allows for full densification of the powders by diffusion and creep mechanisms (section 2.4.2). During densification the voids between powder particles will close, leading to shrinkage of the entire component.

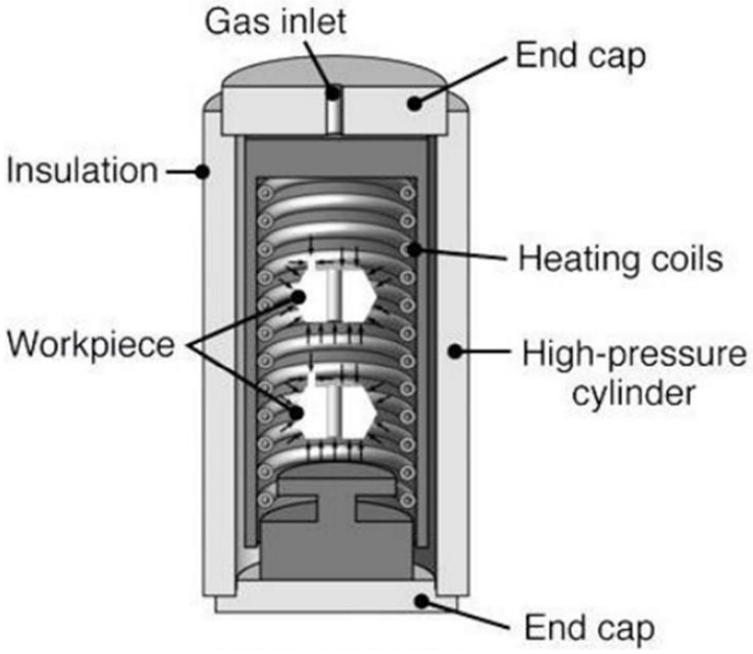

Figure 2-20: Illustration of coil heated HIPping vessel. Adapted from {Gamil, 2016 #433}

iv. Canister removal

As the canister is commonly a dissimilar material to the powders it should be removed post HIPping. Canister removal can be performed by machining or by acid pickling. For more complex geometries with inaccessible surface areas acid pickling is more likely to be used. Pickling involves the emersion of the entire HIP canister in a bath of acid, which gradually

corrodes away the HIP canister material; for stainless steels this is usually a mixture of nitric acid, hydrofluoric acid and water [55]. Due to the nature of the acids involved, pickling poses hazards to both the process operator and environment. Table 2-1 summarises the hazard statements and ecological information associated with nitric and hydrofluoric acid. As can be seen hydrofluoric acid can be fatal and consequently extremely careful handling of the substance is required. Specialised disposal methods are required for the pickling liquid after canister removal and will consequently add to the cost of the HIPping process.

Table 2-1: Hazard statements associated with hydrofluoric and nitric acid [56, 57].

Hazard Statements	
Hydrofluoric acid	Fatal if swallowed, in contact with skin or if inhaled.
	Causes severe skin burns and eye damage
	May cause respiratory irritation
Nitric acid	Causes severe skin burns and eye damage
	Toxic if inhaled
	Corrosive to respiratory tract
Ecological Information	
Hydrofluoric acid	Do not empty into drain. Fatal to freshwater fish at concentrations of 660 mg/L.
	Will likely be mobile in the environment due to its water solubility.
Nitric acid	Do not empty into drain. Large quantities will affect pH and harm aquatic organisms.
	Will likely be mobile in the environment due to its water solubility.

In addition to the hazards associated with pickling, it can also be an extremely time-consuming process. Wang et al. [58] reported a pickling time of six days for removal of a pure Fe canister from CM247LC PM blisk component using Nitric acid. Furthermore, nitric acid concentrations had to be adjusted three times during the process increasing the health and safety risk.

2.4.2 Mechanisms of densification

As discussed, the densification of powders by HIPping is achieved by the application of hot pressurised gas to the surface of a canister containing powders, which in turn transmits the pressure and heat across the contacts of the powders. Heat transfer between the canister and powders and powder contacts occurs by conduction. The effective contact conductivity between two spherical particles can be estimated by the Reimann-Webber equation (Eq. 2-1).

$$\lambda_e = \lambda \left(\frac{1}{x} + \frac{1}{\pi}\ln\frac{2}{x}\right)^{-1} \qquad \text{Eq. 2-1}$$

Where, λ is the conductivity of the solid material and x is the ratio of the contact spot radius to the radius of the particle. The contact spot radius is the radius of the neck between two particles. For a given particle diameter, as necking increases between particles the effective conductivity increases. Conductivity is significantly affected by the packing density of the powders within the canister. Gusarov et al. [59] utilised the Reimann-Webber equation to describe the effective conductivity of randomly packed spheres by equation 2-2.

$$\frac{\lambda_e}{\lambda} = \frac{\rho n}{\pi} x \qquad \text{Eq. 2-2}$$

Where, λ_e is the effective contact conductivity given by the Reimann-Weber equation, ρ is the relative density and n is the mean coordination number of the structure. It can be seen from the equation that for a given contact size, effective conductivity increases with increasing density and mean coordination number. Therefore, the closer packed the structure the greater the conductivity between particles.

Three key stages of powder densification occur as temperature and pressure are increased [60]. Powders first undergo elastic deformation until their compressive yield stress is reached and

they transition into a regime of plastic deformation. During plastic yielding powder contact areas increase up to a point where yielding is no longer energetically favourable; at this stage the time-dependent processes of diffusion and power-law creep take over.

Whether diffusion creep or power-law creep dominates is dependent on the conditions of temperature and stress. At high temperature and stress power-law creep dominates, however as stress decreases diffusion creep becomes increasingly prevalent [61]. The real stress experienced by powders undergoing HIP, is of course not equivalent to the applied external stress, and varies as a function of powder contact area. Initial point contacts between powders results in high levels of stress at the start of the HIP cycle, making power-law creep the dominant mechanism by which densification occurs. As part density increases diffusion creep mechanisms become responsible for final pore closure.

2.4.3 Microstructures and mechanical properties of HIPped Ni-base superalloy

i. Prior particle boundaries (PPBs)

One of the most defining features of a HIPped microstructure is the presence of PPBs. PPBs are characterised by the formation of secondary phases that trace boundaries of the powder particles. Not all materials are equally susceptible to formation of PPBs, though, due to numerous alloying additions, a significant number of Ni-base superalloys are [54, 62-64]. Figure 2-21 shows a micrograph of PPBs in the cross-section of a Ni-base superalloy. Superalloy PPBs are most commonly composed of oxide films, carbides, oxy-carbides and nitrides.

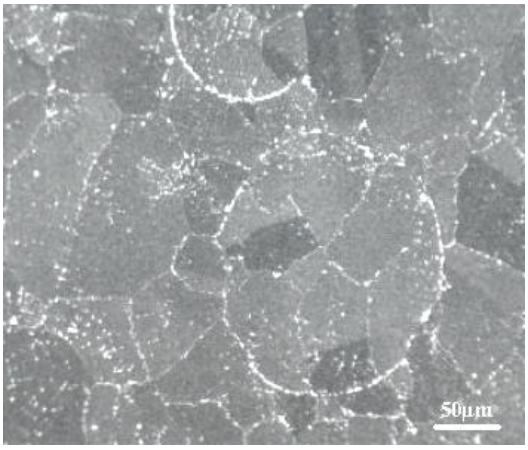

Figure 2-21: BSE micrograph of PPBs in Ni-base superalloy EP741NP. Taken from [64].

Oxide films and precipitates can form at the powder surfaces/ boundaries during powder atomisation and/or HIPping. As mentioned in section 2-3 surface oxides are more likely to form when melt spray techniques are utilised for atomisation, consequently PPBs would be more likely to form when gas and water atomised powders are used. If oxide films do not form during atomisation, they will likely form during HIPping, as the HIP temperature is raised. While canisters are outgassed prior to HIPping, some residual gas will remain in the canister providing low levels of oxygen for the formation of oxides (see sections 2.2.1 and 2.3.3). Following precipitation of oxides, conditions for nucleation and growth of other precipitates, including carbides, are more favourable, resulting in a chain of precipitation following the oxide and surface boundary of the powder. PPBs negatively impact the mechanical properties of the HIPped material for a number of reasons. Firstly, PPB precipitates are comprised of brittle phases that act as crack initiation sites and easy routes for crack propagation [64]. Figure 2-22 shows the fracture surface of a HIPped Ni-base superalloy, in which voids can be seen to follow the boundaries of powder particles. Secondly, precipitates following PPBs can impede the movement of dislocations, preventing creep of the material during HIPping [65] and effective closure of voids.

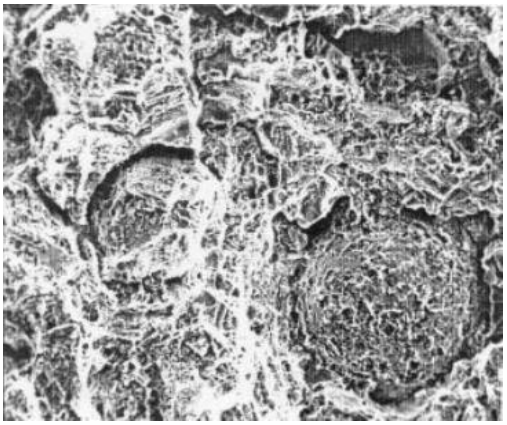

Figure 2-22: SE micrograph of PPBs in the fracture surface of Ni-base superalloy EP741NP. Taken from [64].

PPB formation and the resulting affect it has on mechanical properties of superalloy components, is commonly regarded as the main challenge preventing wider use of HIPping for processing of Ni-base superalloys [2, 64, 66]. Consequently, methods for prevention of PPB formation have been the focus of studies since the introduction of PM HIPping to superalloys. Some studies have investigated methods for removing PPBs after they have formed [67-69] while others aim to prevent their formation, focusing on either reducing oxide formation [70-72] and/or limiting the precipitation of carbides [2, 73].

Hot forging has been a standard post processing treatment employed in the production of turbine discs since the introduction of PM HIPping [2]. Thermomechanical working breaks up continuous chains of precipitates along PPBs by grain flow. As the grains align to the direction of applied stress so do the precipitates, opening up paths for migration of grain boundaries beyond PPBs [68]. The magnitude of the impact thermomechanical treatment can have, is of course limited by how much shape change can be tolerated for the PM component.

Consequently, such post processing may not be the best solution for addressing PPBs in NS/NNS components.

Controlling carbide precipitation by compositional adaptions has been one of the more traditional approaches to minimising PPB formation [2]. It has been reported that in order for PPBs to be entirely eliminated, carbon content must be reduced to less than 0.02 wt% [73] . Obviously at such low carbon levels the overall quantity of carbide precipitated is significantly lowered which may negatively impact mechanical properties such as creep. An alternative approach to controlling carbide precipitation is to make additions of stable carbide formers to the alloy [74]. Stable carbide formers, like oxide formers, have reduced diffusion rates and thus precipitation of their carbides is delayed. This provides time for grain growth to occur beyond PPBs before carbide precipitation happens. While control of carbide precipitation through alloy adaptations can be somewhat effective, studies have shown that carbides will still form at PPB boundaries if surface oxide films are present [73].

The presence of surface oxides on Ni-base superalloy powders is inevitable, yet there are steps that can be implemented to minimise their formation and consequently reduce PPBs. Rao et al. [70] investigated the influence of varying oxygen content on the quantity of PPBs. GA Inconel 718 powders were produced with three different oxygen concentrations, 140, 180 and 275 ppm, and then consolidated by PM HIPping. A higher number of PPBs were observed in samples produced with powders containing the highest concentration of oxygen. In addition, carbides were more likely to precipitate at PPBs, as opposed to grain boundaries, if oxygen content was high. It should be noted that powders with the highest ppm of oxygen had an average particle diameter of 50 μm, whereas those produced with the lowest ppm of oxygen had an average diameter of 85 μm. Oxygen content tends to be higher in smaller

powder particles, owing to the larger surface area for oxygen pick-up during atomisation. MacDonald et al. [74] studied the influence of powder particle size and oxygen concentration on the tensile properties of PM HIPped CM247LC. Studies were performed on powder supplied in three particle size ranges- 15-53 μm, 53-150 μm and 0-150 μm. Oxygen content of the virgin powders was found to be greatest in the particles with size range 15-53 μm and corresponded to a marked decrease in tensile elongation of the HIPped material owing to an increase in PPB formation. To determine if particle size or oxygen content had greater influence on tensile elongation, powders from the 0-150 μm size range were sieved into two new size distributions of 23-53 μm and 53-150 μm and HIPped for tensile testing. Elongation was found to be greater in PM HIPped material produced from the new size distributions relative to the original size distribution, with elongation greatest for the material produced with 23-53 μm size range of powders; thus, suggesting oxygen concentration to have a greater impact on PPB formation than particle size.

Earlier studies by Kissinger et al.[72] suggested PPB formation was influenced by powder size dependent deformation. They examined the influence of powder particle size distribution on PPB formation in Ni-base superalloy René 95. Three different powder sizes were studied- 33-35 μm, 75-90 μm and powders greater than 140 μm. HIPping temperature was constant at 1120°C, and different holding times (5 minutes to 180 minutes) and pressures (103 MPa and 10.3 MPa) were tested for each powder size. For the higher HIP pressure all powder sizes underwent deformation within the first 5 minutes of HIPping, however for the lower HIP pressure only the smaller particles deformed within the first 15 minutes of the HIP cycle. PPBs were predominantly observed to trace larger particles, leading to the conclusion that greater levels of deformation in the smaller particles resulted in the elimination of PPBs. It should be noted that oxygen content of each particle size range was not disclosed.

Few additional studies have been performed examining the influence of powder particle size on PPB formation and mechanical properties in Ni-base superalloys, however studies have been performed studying their influence in Al[75], steel[76] and Ti[77]. Studies in Ti were similar to those conducted by MacDonald et al.[74] with a single supplied powder lot being sieved into two new size distributions. Ti-6Al-4V powders with size distributions of 5-250 μm (as-supplied), 5-53 μm and 180-250 μm were HIPped and microstructural analysis and mechanical testing performed. PPBs could not be observed in any of the HIPped samples; however, the phase composition of each sample did differ. Samples produced with the finer powder lot showed a significant increase in equiaxed α grains, consequently improving tensile elongation. The increase in equiaxed α was attributed to a greater level of recrystallisation in samples produced with the finer powder, concurrent with René 95 studies by Kissinger et al.[72]. Similar results were observed in steel and Al alloys with PPBs being less prominent at the surfaces of small powder particles relative to large particles, irrespective of oxygen content.

As discussed in section 2.4.1-ii, HIP canister outgassing may be carried out at RT or ET; the purpose of performing at ET being to evaporate off any moisture that may be present on the powder particles, thus reducing oxygen and hydrogen contents and minimising PPBs. Aristizabal et al.[78] examined the influence of outgassing temperature on the oxygen content and PPB formation in HIPped IN718 powders. Three outgassing temperatures- RT, 800°C and 1100°C -were studied, with each canister being outgassed for 24 hours. The oxygen content of each canister, measured after HIP, was found to be almost equivalent to that of the virgin powders and did not differ between canisters. PPB formation also did not differ between canisters HIPped at the same temperature. Qiu et al.[54] studied the influence of outgassing temperature and time on oxygen, nitrogen and hydrogen contents of HIPped RR 1000

samples. Samples outgassed at ET (400°C) for 4 hours showed the lowest levels of nitrogen and oxygen, however not significantly so. Hydrogen levels did not differ between samples.

ii. Diffusion zone

Figure 2-23 shows the microstructure of a HIPped Ni-base superalloy in the region near the HIPping canister, referred to as the diffusion zone. The diffusion zone is characterised by an increase in carbide precipitation and subsequently an increase in PPBs. The high quantity of carbides is the result of diffusion of carbon from the steel HIPping canister into the powder being HIPped.

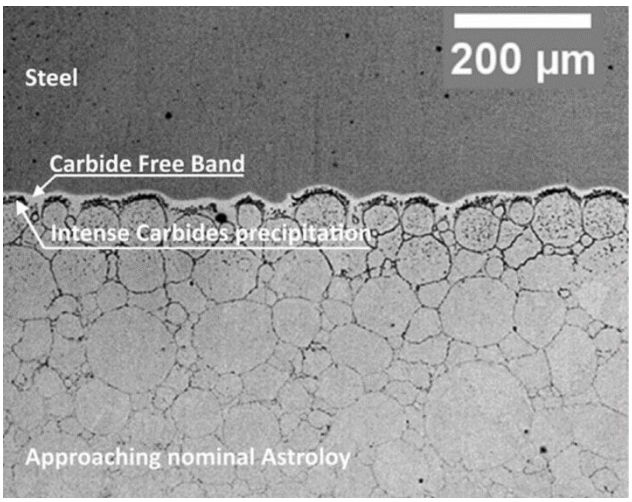

Figure 2-3: Optical image of diffusion zone in PM HIPped Astroloy. Adapted from [79].

Due to the increase in precipitation and PPB formation, the HIPped material lying within the diffusion zone has substantially different properties from the rest of the HIPped material; consequently, material in the diffusion zone must be removed along with the HIPping canister. In an effort to minimise material waste, some studies have examined alternative canister materials that minimise carbide precipitation [54, 80].

Qiu et al. [54] investigated the influence of different steel alloys on the depth of the formed diffusion zone in PM HIPping of Ni-base superalloy RR1000. Medium carbon steel and 1% Cr bearing steel were both found to result in the formation of a diffusion zone of approximately 300 μm in depth with sizeable carbide precipitates (1.2 μm); while the diffusion zone in powders HIPped inside ultra-low carbon steel was only 50 μm in depth. Using 316L stainless steel prevented the formation of a diffusion zone, which was attributed not just to the low carbon content but also to the higher quantities of alloying elements.

Glass HIPping canisters have traditionally been using for the HIPping of ceramics, but more recently have been investigated as an alternative for HIPping of stainless-steel powders and Ni-superalloy powders [80]. Not only did use of the glass canister prevent the formation of a diffusion zone, but relative to HIPping in a mild steel container, powders were HIPped to higher densities.

iii. Influence of HIPping parameters on microstructures of PM HIPped Ni-base superalloys

PM HIPping has been investigated for a range of Ni-base superalloys, though most extensively for turbine disc alloys, René95 [81, 82], Astroloy[83], Udimet720 [84-87], RR1000 [88, 89] and Inconel 718 [63, 70, 90, 91]. While HIPping pressure and dwell time are important parameters to consider for densification, they have been found to have little influence on the as-HIPped microstructure [82]. Temperature on the other hand has a significant effect on the precipitation and grain size. For all superalloys, higher temperatures are necessary for the elimination of PPBs [63, 82, 83, 86, 89, 91].

Chang et al. [63] studied the influence of five different HIPping temperatures in Inconel 718 above the γ', γ'' and δ solvus. Temperatures were above and below the laves incipient melting

temperature, 1180 and 1140°C respectively; below the temperature for onset of carbide dissolution, 1210°C, and, at and above the solidus temperature, 1260 and 1275°C respectively. Samples were HIPped at pressures between 150 and 160 MPa for a dwell time of 4 hours. Interdendritic laves precipitation was found to be present in samples HIPped both above and below the laves incipient melting point, and was thought to be inherited from the powder. PPBs remained in all samples, except for that HIPped at 1275°C. Carbide precipitation was still present in the sample HIPped at 1275°C, and it appeared as though grain boundaries migrated beyond PPBs without rearrangement of carbides, as curved chains of carbides could be observed intragranularly. Figure 2-24 shows an example of such precipitation in the sample HIPped at 1260°C. HIPping at higher temperatures did however come at a potential detriment to mechanical properties with significant coarsening of grains and high quantities of liquid trapping (figure 2-25).

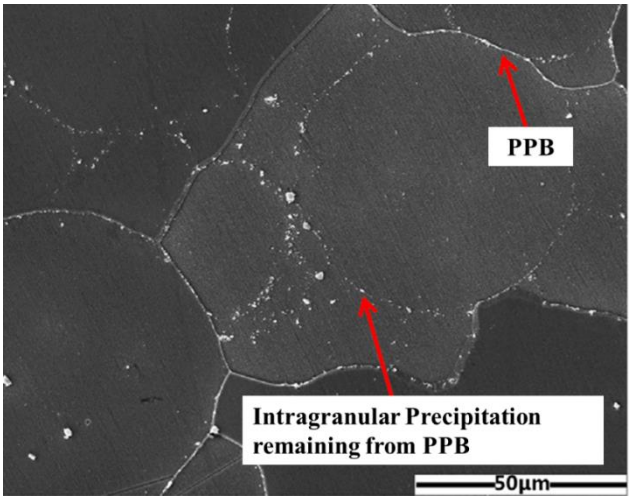

Figure 2-24: BSE micrograph of Inconel 718 powder HIPped at 1260°C with 150-160MPa for 4 hours. Highlighted are examples of PPB precipitation and intragranular precipitation remaining after grain boundary migration beyond the PPB. Adapted from [63].

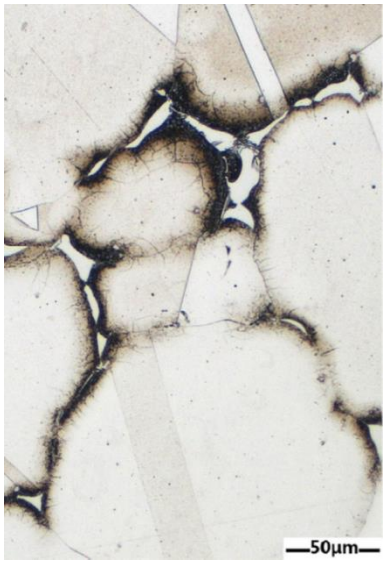

Figure 2-25: Optical image of etched sample of Inconel 718 powder HIPped at 1275°C with 150-160MPa for 4 hours. Adapted from [63].

Bartos et al. [82] studied the interacting effects of powder particle size, HIPping temperature and pressure on the microstructure of René 95. Smaller powder particles were fully recrystallised no matter the HIPping temperature, however larger powder particles were only partially recrystallised at lower temperatures (1037 and 1093°C) but fully recrystallised at 1121°C. Conversely, later studies by Chang et al. [81] utilising the same HIPping parameters as Bartos et al. (1121°C and 103 MPa) found the conditions to be insufficient for elimination of PPBs.

Couturier et al. [86] studied the influence of HIPping cycle parameters on the microstructure of PM HIPped Udimet720. Two cycles were examined, one where temperature and pressure were constant (1100°C and 140 MPa) and a second consisting of a two-step sequence with two different temperatures (1140 and 1170°) and pressures (10 and 100 MPa). PPBs could be observed in the microstructure of the single step HIPping cycle and very little γ' precipitation could be observed. On the other hand the two step heat treatment resulted in no PPBs and a

homogeneous distribution of γ'. $M_{23}C_6$ carbides could also be observed along grain boundaries. Figure 2-26 shows a TEM micrograph of the microstructure produced by the two-step HIPping cycle.

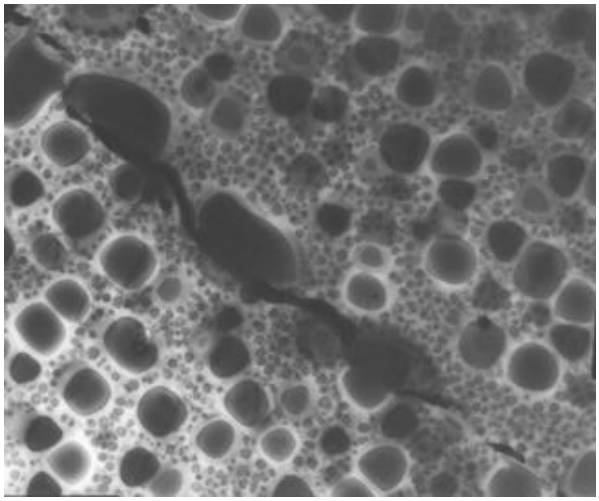

Figure 2-26: γ' distribution observed by TEM of PM Udimet720 consolidated by two-step HIPping cycle. Taken from [86].

iv. Tensile properties of PM HIPped Ni-base superalloys

Due to the brittle nature of PPBs it is expected that the quantity of PPBs would have an overriding influence on the tensile properties of PM HIPped Ni-base superalloys. Investigations on the influence of HIPping temperature on tensile properties of Inconel 718 conducted by Chang et al. [92] found increasing HIPping temperature to result in a diminishment in yield strength accompanied by an increase in UTS and elongation (figure 2-27). The increase in UTS and elongation was attributed to a decrease in PPB formation with increasing HIPping temperature. Investigations of grain boundary precipitation and γ' and γ'' precipitation revealed no significant differences between samples. What did differ however was the quantity of interdendritic precipitates, including laves and

carbides, with higher quantities observed in samples HIPped at 1140°C. A similar impact of PPB presence on tensile properties was observed for René95 [82]. At lower HIPping temperatures an increased number of PPBs was observed and the extent of grain recrystallisation was significantly less. This corresponded to a decrease in UTS and ductility in samples HIPped at low temperature verses those HIPped at higher temperatures.

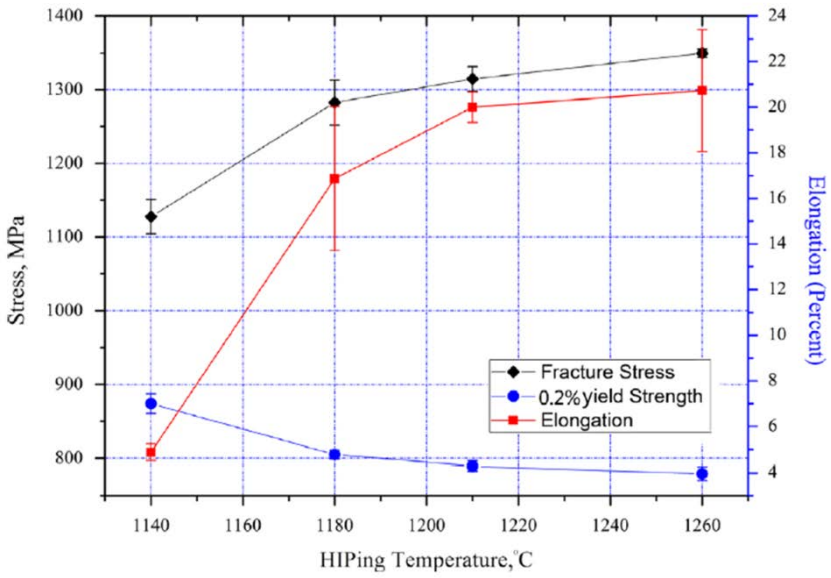

Figure 2-27: Results of elevated temperature (650°C) tensile testing of Inconel 718 powders HIPped at different temperatures. Pressure and dwell time were 150-160 MPa and4 hrs respectively. Taken from [92].

The NNS benefits of PM HIPping cannot be fully appreciated if desirable mechanical properties cannot be achieved without post-process thermomechanical working. Figures 2-28 and 2-29 summarise the RT tensile properties of two PM HIPped Ni-base superalloys compared with their forged counterparts. Tensile data for Ni-base superalloy Inconel 718 is for the as-HIPped condition, whereas data presented for RR1000 is in the HIPped + HT

condition. Inconel 718 Yield and UTS data are slightly lower for the as-HIPped material relative to the forged + HT, however this to be expected as precipitation of strengthening phases such as γ' and γ'' is limited in the as-HIPped samples. Elongation values however are more comparable, except in the case of Yao et al. [93] where elongation significantly exceeds that of other PM HIPped material and forged + HT material; though it should be noted that the strain rates used in the tensile testing performed by Yao et al. were half that of the strain rates used in other studies and consequently an increase in elongation would be expected.

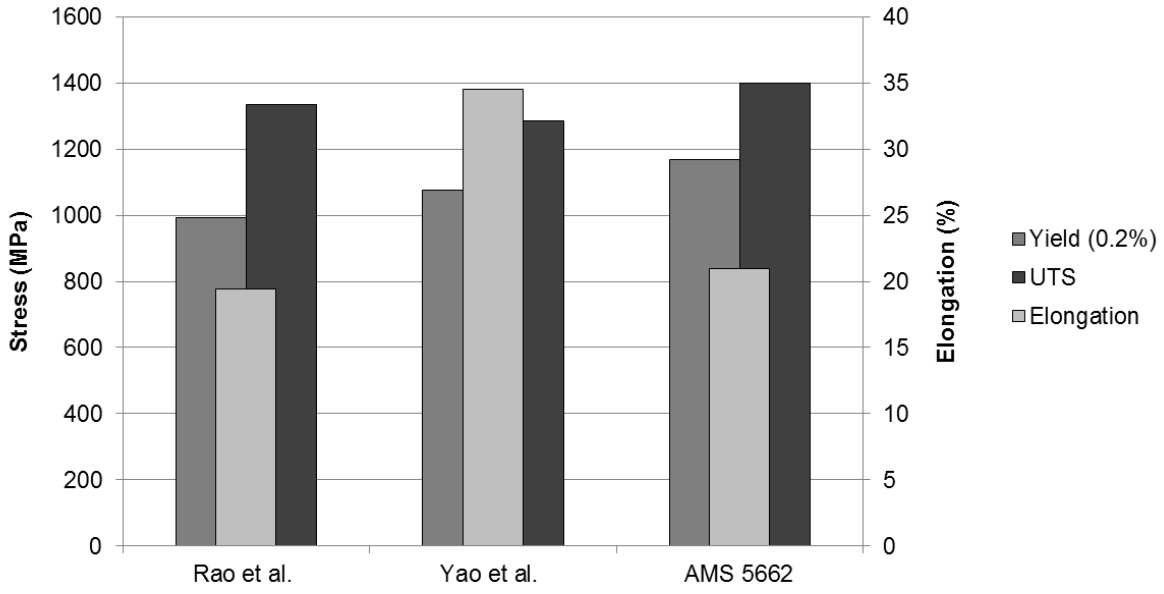

Figure 2-28: Comparison of RT tensile properties for PM HIPped Inconel 718 (Rao et al. [90] and Yao et al. [93]) and forged + HT Inconel 718 (AMS 5662 [94]).

PM HIPped + HT RR1000 samples show almost equivalent tensile yield and UTS values compared with forged + HT RR1000. In regard to elongation two things should be considered, firstly the value provided for the forged + HT state is the minimum required value, and within the studies of May et al. and Qiu et al. elongation properties have been described as being comparable to forged + HT material. Secondly comparing elongation

values presented by Qiu et al. with May et al., May et al. implemented a strain rate more than double that of Qiu et al. and consequently a reduction in elongation would be expected. Yet irrespective of this, the microstructures of samples from Qiu et al. are more likely to result in improved elongation, as the result of precipitation of finer γ' relative to the more coarse γ' observed in the microstructures of samples produced by May et al.

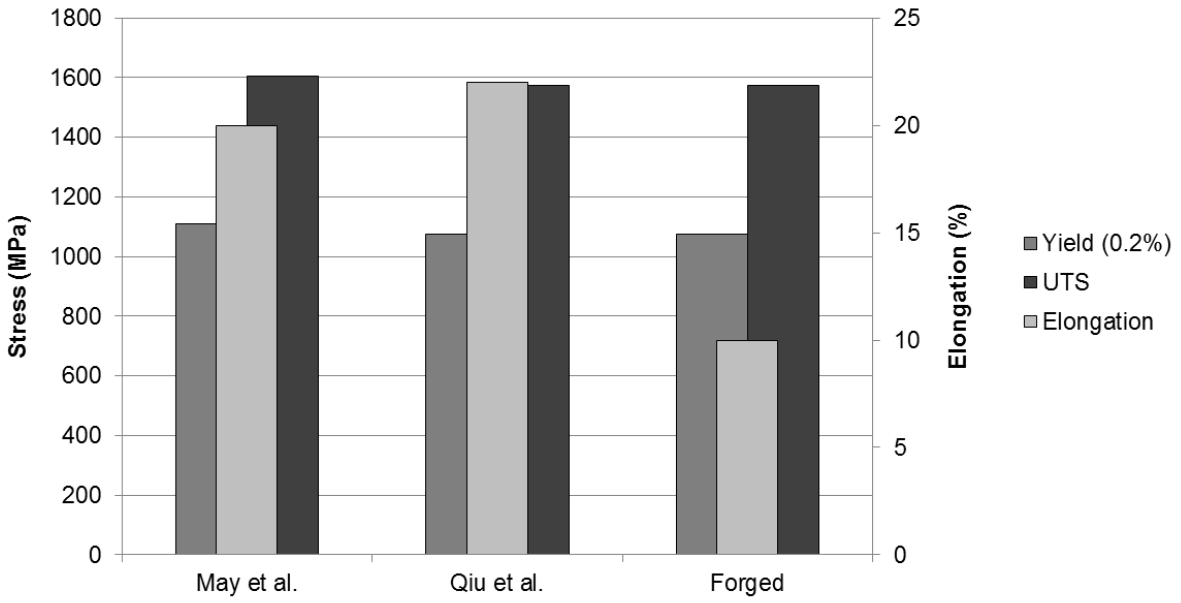

Figure 2-29: Comparison of RT tensile properties for PM HIPped + HT (May et al. [89] and Qiu et al. [88]) RR1000 and forged + HT RR1000. Forged + HT data was reported by Qiu et al.

2.5 PBF of Ni-base superalloys

Interest in AM of Ni-base superalloys grew from a need for more complex geometries required to improve component performance. Components of particular interest were low and high pressure turbine blades. By increasing the complexity of blade geometries, heat transfer could be enhanced and consequently turbine engines could operate at higher temperatures

increasing their efficiency. The higher resolution of PBF relative to other AM techniques, for example DLD, made it a more suitable AM process for the production of blades, which often have many small intricate geometries, such as cooling channels. Ni-base alloys investigated by PBF include but are not limited to, Inconel 718, Inconel 738LC, CM247LC and CMSX-4[95]. LPBF is the longest established PBF process and consequently there is a larger body of work relating to LPBF of Ni-base superalloys relative to EPBF.

i. Introduction to LPBF

Figure 2-30 shows examples of the layout of two LPBF systems. There are three commonly occurring differences in the technology of existing systems. Firstly, as discussed in the introduction, there is the difference in build plate heating capability, with some systems capable of operating at elevated temperature. The second difference is the mechanisms of how powder is fed to the build plate. In the Concept M2 Cusing system (figure 2-30-a), the powder tank is located next to the build tank. To feed a layer of powder, the powder tank moves up while the build tank moves down, the recoater then moves across pushing powder from the powder tank to the build area. In the second system, powder is fed from a hopper located above the build chamber and into another smaller hopper within the recoater blade system. Powder flows from this hopper in front of the recoater blade which then spreads the powder across the build plate. The final difference between systems resides in the gas flow. A constant flow of inert gas is used during processing to maintain a low level of oxygen, remove metal vapours and small melt spatter particles from the build area during processing. Some systems like the Concept M2 have the gas outlet and inlet located on the same side of the machine, creating a circular gas motion (figure 2-31-a). Other systems like the SLM solutions

system and most recent model of the Concept M2, have the gas inlet and outlet located on opposite sides creating a more laminar flow of gas across the build plate (figure 2-31-b).

a)

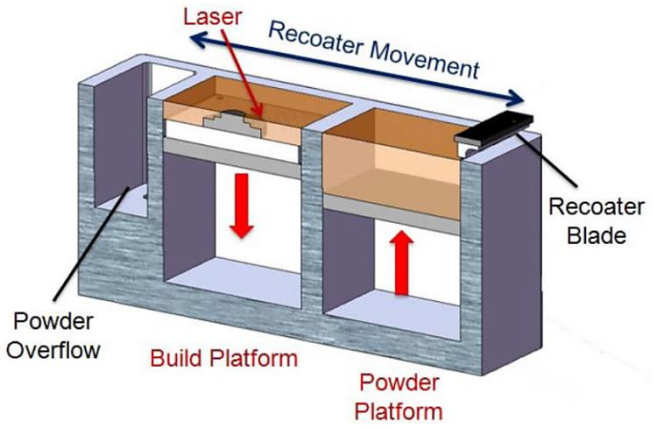

b)

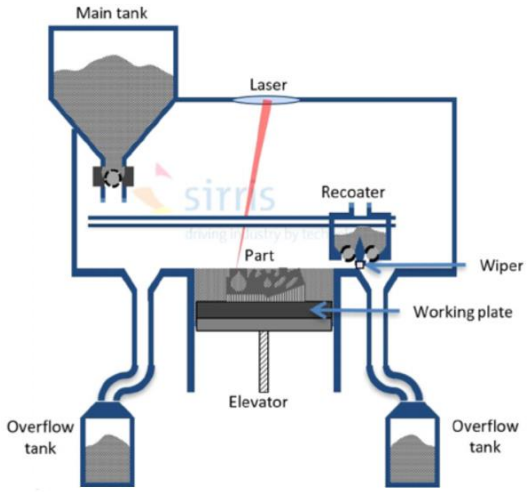

Figure 2-30: Schematic of LPBF systems currently available: a) Concept M2 Laser Cusing machine, taken from [96] and b) Schematic of system similar to SLM solution SLM 250HL, taken from [97].

a)

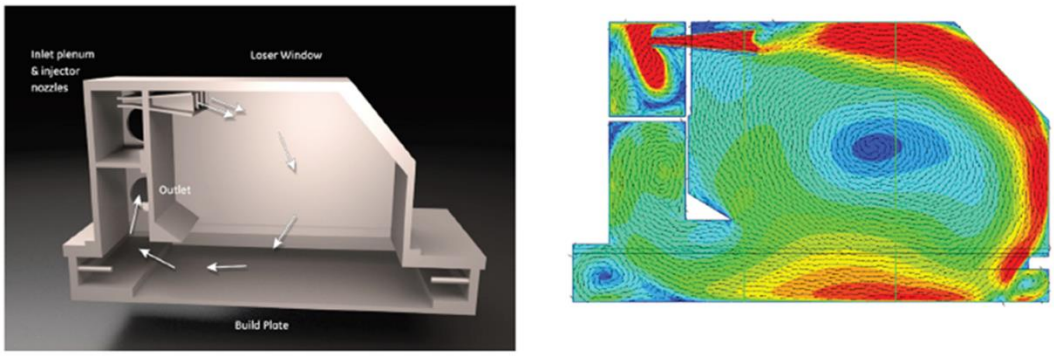

b)

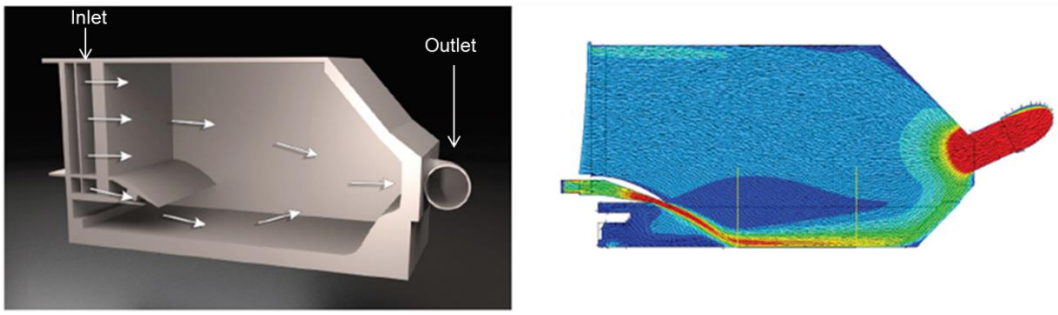

Figure 2-31: Influence of gas inlet and outlet locations on gas flow pressure and geometry in LPBF. Adapted from [98]. a) gas inlet and outlet on same side of the build plate and b) gas inlet and outlet on opposite sides of the build plate. Regions of high gas flow rate are indicated by red colouring and low flow rate blue.

ii. Introduction to EPBF

Figure 2-32 shows a schematic of the inside of an Arcam Q20 EPBF system. The powder feed system like the SLM 250HL employs hoppers to supply powder to the build area. A pile of powder forms under the hopper into which the recoater is pushed until power falls over the top of it and in front of the rake blades. The powder is then pushed across the

build plate and the recoater continues to the other hopper to retrieve more powder. As processing is carried out in vacuum it is assumed that no contamination will be induced in the powders and therefore there is no need for a power overflow as such powders may be pushed back and forth across the plate multiple times. The disadvantage of this, however, is that if optimal parameters are not used for processing, sections of powder sinter and potentially parts of melted components that have broken away from the build plate, could end up reincorporated into the build, resulting in component defects.

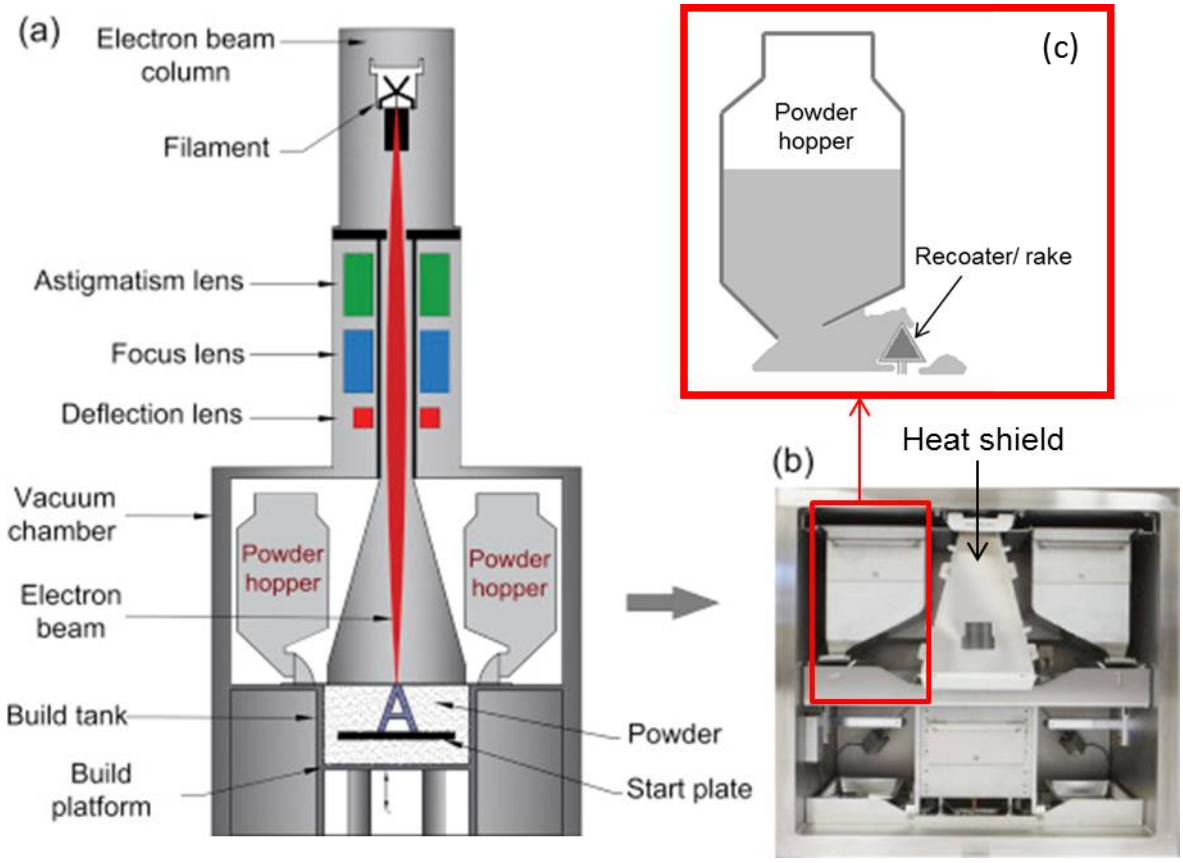

Figure 2-32: Arcam Q20 EPBF system: a) schematic of beam column and build area; b) photograph of build chamber and c) Schematic of powder rake system. Modified from [99].

Unlike in LPBF where powders are melted by the laser in a single processing step, in EPBF several stages of heating are used. Firstly, the build plate is heated to an elevated temperature; typically, in the region of 1000 °C for Ni-base superalloys. After the build plate has reached temperature and powder is spread, a fast scan with a defocused beam is performed across the powder bed, partially sintering the powders; this is referred to as preheat stage 1. Following the initial sinter there is the option to apply an additional sintering step (preheat stage 2) localised to the vicinity of the component melt area. Next the beam is refocused and melting of the component cross-section occurs. Finally, an optional post heat stage in which again a defocused beam is scanned at high speed (typically faster than the preheat stage) across the powder bed, can be implemented to help maintain the elevated build temperature. As a consequence of this multi-stage heating, EPBF part properties are not simply a function of their melt parameters, but also of preheat and post-heat parameters.

2.5.1 Heat transfer in PBF

Heat transfer in PBF differs depending on the energy beam used to heat the powder, the environment in which powder melting is performed and the characteristics of the powder itself.

i. Influence of energy beam

The physics of heating by energy beams is relatively simple. An energy carrier, such as an electron (EPBF) or photon (LPBF) penetrates atoms in the target material and their energy is absorbed by the atoms, increasing the atoms vibrational frequency, whose kinetic energy becomes heat. The likelihood of absorption of the energy carrier by the atoms increases with increasing penetration depth, which is dictated by the wavelength of the energy carrier. Shorter wavelengths can go to greater penetration depths relative to longer

wavelengths. Typically in LPBF, CO_2 and neodymium-doped yttrium aluminium garnet (Nd:YAG) lasers are used; their respective wavelengths are 10600 nm and 1064 nm. The wavelength of an electron is related to the velocity of the electron by the de Broglie relation (Eq. 2-3). For a typical EPBF system the acceleration voltage of the electron gun is 60 keV, which translate to a wavelength of 0.005 nm. The significantly shorter wavelength of the electron means energy is absorbed and consequently electron beam melting is substantially more efficient than laser melting.

$$\lambda = \frac{h}{p} \qquad \text{Eq. 2-3}$$

Where, λ is wavelength, h is Planck's constant and p is electron momentum as define by equation 2-4.

$$p = mV \qquad \text{Eq. 2-4}$$

Where m is electron mass and V is electron velocity.

ii. Influence of processing environment

The processing environment, like the energy beam influence the efficiency with which heat is transferred between powder particles. In LPBF processing is carried out in an inert gas environment and consequently all three mechanisms of heat transfer- conduction, radiation and convection- occur. EPBF on the other hand is performed in a vacuum environment and hence heat transfer between powder particles is dictated by conduction and radiation only. It should be noted however that in transfer of heat from the melt pool to the powder, convection does occur within the melt pool.

Radiation is most efficient in a vacuum as there are no particles with which it can collide attenuating its energy; consequently, radiation is a significant contributor to heat transfer in EPBF. Radiative heat transfer occurs not only between powder particles but between powders and the machine. As can be seen in figure 2-24 the Arcam Q20 build plate is surrounded by a heat shield, the purpose of which is twofold; firstly, to protect the machine from radiated heat transfer preventing machine elements from overheating and secondly to reflect heat radiated by the build plate back towards itself maintaining an elevated build temperature. Through a combination of heat transfer modelling and experimental temperature measurements Landau et al. [100] were able to approximate heat radiated from a stainless steel build plate to be 20 % of the total heat loss from the plate. Similar heat transfer studies conducted for LPBF, showed the sum of radiative and convective heat transfer from a single layer stainless steel powder bed to approximately 15 % of the total heat loss [101]. A comparison of the two highlights a significant reduction in radiative heat transfer in LPBF versus EPBF.

As discussed earlier, LPBF is carried out in an inert gas atmosphere which is constantly flowing across the powder bed and as a consequence transfers heat by convection. The thermal conductivity of the inert gas used will influence how much heat is transferred by convection. The two most common inert gases used in LPBF are argon and nitrogen, having thermal conductivity values of 0.018 and 0.026 W $m^{-1}K^{-1}$ respectively [102]. Bidare et al. [103] studied the influence of the type of inert gas used on melt pool behaviour. They compared argon and helium (thermal conductivity = 0.157 W $m^{-1}K^{-1}$), finding helium significantly reduced metal vapour plumes and spatter ejected from the melt pool, overall resulting in a more stable melt pool. They also found melt pool penetration depth to be greater in helium environments relative to argon.

iii. Influence of powder characteristics

Powder particle size distribution and morphology play an important role in heat transfer. As discussed in section 2.4.2-i of this chapter conductivity between particles is described by the Reimann-Webber equation with increased contact area increasing the effective thermal conductivity between particles. Consequently, higher packing densities- achieved by a spherical powder morphology and wider size distribution- result in better thermal conduction. The influence this has on melt pool formation has been studied in both LPBF and EPBF. Ning et al. [104] simulated the influence of packing density by modelling heat transfer in a solid with differing degrees of porosity. Melt pool dimensions were simulated for porosity ranging from zero to 60 %. The influence of porosity on conductivity was simulated by multiplying the material conductivity by the relative density. Melt pool depth was found to increase with increasing porosity, i.e., with decreasing thermal conductivity heat is held in the melt pool for longer leading to an increase in melt.

Powder packing density has also been shown to significantly influence laser absorption [105, 106]. Boley et al. [106] used a ray tracing model to calculate the magnitude of laser reflections and absorption resulting from those reflections, for two different packing densities with several different materials. In all material cases, increasing packing density increased the laser absorption. The factor by which laser absorption was increased was however dependent on material type, with more reflective materials seeing a greater increase in absorption for higher packing densities than less reflective materials. When comparing the absorption coefficient of spherical powders versus flat sheet for the same material, it was found that the absorption in powder could be increased by almost a factor of 2.

2.5.2 Process instabilities

LPBF and EPBF are well established technologies with decades of research behind them. There are however some less well understood aspects of the technologies that may lead to unpredictable behaviour during processing.

i. LPBF

As illustrated in section 2.5-i different LPBF systems have different configurations of gas flow systems resulting in variation in gas flow behaviour. The gas flow system should be optimised to remove metal vapour, melt spatter and soot particles from the build area and away from the laser optics. If this is not performed effectively then attenuation and diffraction of the laser beam can occur reducing the effective power delivered to the powder bed [107]. Figure 2-31 illustrated the influence of gas inlet and outlet position on localised gas pressure within the build chamber, highlighting the very turbulent nature of gas flow in systems that position inlet and outlet on the same side. The rotational nature of the gas flow can lead to the recirculation of process by-products, depositing them back into the powder bed where they can be incorporated into build parts leading to inclusions and the formation of other defects such as porosity. While many of the more recent systems utilise a laminar gas flow, variability in flow behaviour still occurs. The current challenge lies in adapting the gas inlet and extraction pressure throughout the build process to account or a reduction in gas flow rate resulting from build-up of soot particles in filtration systems [98].

ii. EPBF

The most prominent instability of the EPBF process is the phenomenon referred to as powder smoke [108]. It occurs as the result of a build of negative charge at the powder particles

surfaces by an accumulation of electrons. The negative charge of two adjacent powders creates a repulsive force between the powder particles. When this force exceeds the gravitational force holding the powders in place on the powder bed, the powders are ejected away from each other and the powder bed. This ejection of powder resembles the appearance of a puff of smoke, hence the name powder smoke.

The accumulation of electrons at the powder surface is predominantly due to the production of secondary electrons. When incident electrons collide with the atoms of the powder particles, they knock out electrons from atom shell; secondary electrons. These electrons have relatively low energy compared to the incident electrons and backscattered electrons (an incident electron sling shot out of the atom by the energy of the atom nucleus); consequently not all secondary electrons have the energy to leave the powder surface. If the powder is isolated from other powder particles and the substrate plate, by means of an oxide layer for example, there is no conduction path for the electrons and hence the electron charge builds [109].

There are several factors influencing the rate at which charge is accumulated in the powder. Firstly, as alluded to above, if some level of sintering and necking has occurred between the powder particles and the substrate plate, electrons can move through these conduction paths, dissipating charge. This is the reasoning behind the preheat stage of the EPBF process. Secondly, the energy with which the incident electrons are accelerated, and the number of incident electrons will affect the number of collision incidents within the atoms of the powder and as result will influence the number of secondary electron generated. Finally, the rate of charge dissipation is also influenced by the material properties, in particular the permittivity and resistivity of the powder surface [109]. Permittivity is defined as the ability of a material to

store an electric potential while under the influence of an electric field [110]. In the case of EPBF that electric field would be the incident electron beam. A materials permittivity relative to its capacitance is greater, meaning electrical discharge is less while under the influence of an electric field, therefore while the beam is over the powder, the rate at which the powder can dissipate charge is less than when the powder is not exposed to the beam. Considering all the above, the process parameters affecting powder smoke the most are beam power, beam spot size and scan speed. These processing parameters however can only control smoke to a certain extent, as powder characteristics still play a significant role. The extent to which powder recycling influences powder surface chemistry and consequently smoke behaviour is less known and random instances of smoke may still occur with reuse of powder, requiring re-optimisation of processing parameters.

2.5.3 Process induced defects

PBF is often described as being analogous to welding and as such typical welding defects are also expected to be observed in PBF processes. Pores and cracks are defects that commonly occur in the laser and electron beam welding of Ni-base superalloys [111].

i. Porosity

Three types of porosity can exist within the microstructure of PBF parts: gas porosity, keyhole porosity and lack of fusion (LoF) voids.

LoF voids result from insufficient melting of powder; this may be a consequence of insufficient beam energy, poor powder packing density and/ or powder surface chemistry. LoF voids are typified by their morphology. Figure 2-33 shows an optical micrograph of a LoF void in Inconel 718 formed by EPBF. LoF voids often possess irregular shapes formed

by the curvature of the un-melted powder particles. Smaller un-melted particles may sometimes be observed within the void.

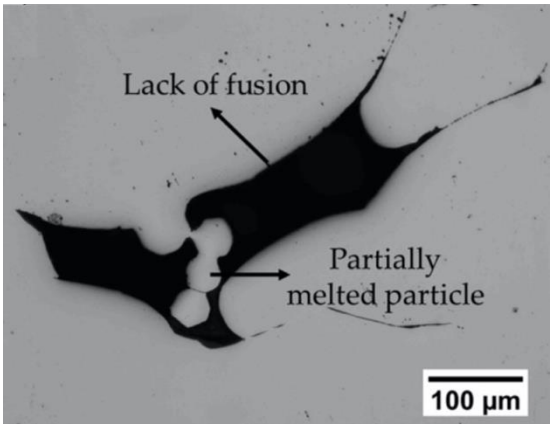

Figure 2-33: Optical micrograph showing LoF void in EPBF Inconel 718. Adapted from [112].

Carter et al. [113] examined the influence of area energy density (AED) (Eq. 2-5) on the area fraction of LoF voids in a range of Ni-base superalloys (figure 2-34), finding the onset of LoF voids to occur at a threshold value of approximately 1.75 J mm^{-2} for all five alloys studied. This was in spite of the fact that two of the superalloys were produced with a different scan strategy and that IN718 was built using 30 µm layers as opposed to the 20 µm layers used in the other studies.

$$\mathrm{AED} = \frac{\mathrm{P}}{\mathrm{V} \times \mathrm{h}} \qquad \text{Eq. 2-5}$$

Where, P is laser power in watts, V is beam velocity in mm s^{-1} and h is hatch distance in mm.

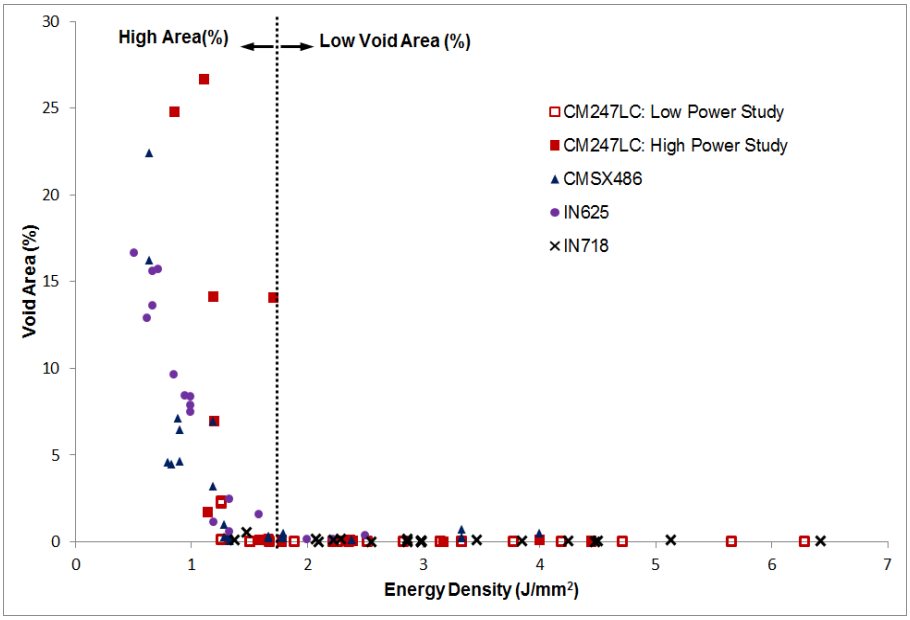

Figure 2-34: Relationship between area energy density and area fraction of voids. Taken from [113].

Gruber et al. [114] investigated the influence of powder recycling on defect formation in EPBF Inconel 718. Powders utilised for building were virgin and powder that had been recycled six, fourteen and thirty times. Build samples produced with the most recycled powder contained significantly more LoF voids compared to other builds. EDS analysis of the voids revealed relatively high concentrations of Al, Ti and occasionally Mg. Consequently, it was concluded that LoF occurred as the result of the presence of oxide films and inclusions.

Körner et al. [115] simulated heat transfer for different powder bed packing densities in EPBF, examining the influence on melt pool geometry. Lower powder packing densities lead to formation of irregular melt pool shapes and consequently were predicted to encourage the formation of porosity defect, predominantly LoF voids.

Gas pores tend to be small and spherical in morphology. They can be inherited from the powder or in the case of LPBF can form in process also. The majority of gas pores in powder are formed during the atomisation process and tend to be more prominent in melt spray techniques carried out in inert gas atmospheres. Smaller powder pores tend to result from the dissolution of inert gas in the powder while it is a melt droplet, followed by the subsequent expulsion of gas upon solidification of the powder particle. Larger powder porosity may form as the consequence of distortion of the melt during atomisation due to excessively high gas pressures [116]. Gas pores formed during the LPBF process occur much in the same way as the formation of smaller pores in the atomisation process; gas is dissolved in the melt pool during melting and upon solidification the gas is forced out of solution to form a small pore. If the solidification rate of the melt pool is relatively slow the gas pore may be able to diffuse to the top and out of the melt pool.

Keyhole pores form by the collapse of an unstable keyhole melt pool. Keyhole melt pools are formed when melt pool temperatures become high enough to vaporise the liquid metal within the melt pool; this creates a vapour filled cavity at the leading edge of the melt pool (figure 2-35). The metallic vapour encourages reflections of the laser beam between the walls of the cavity, increasing laser absorption and raising the temperature of the melt pool. This results in the formation of a deeply penetrating weld pool. The weld pool cavity is maintained by balance of the forces exerting outward pressure on the cavity, from the metal vapour, and forces exerting inward pressure on the cavity, hydrostatic pressure and surface tension of the melt [117]. When the forces exerted inward on the cavity exceed those working outwardly, the melt pool collapses and in doing so metal vapours, and in the case of LPBF atmospheric gases, can become entrapped leading to the formation of a pore.

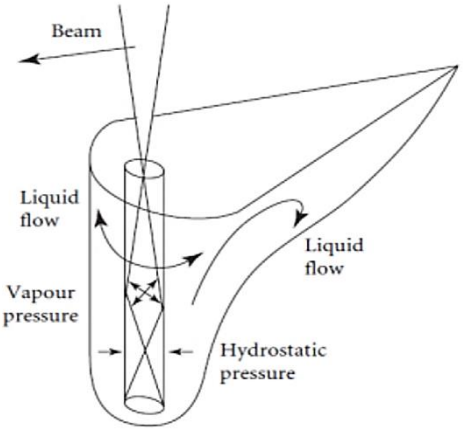

Figure 2-35: keyhole weld pool. Taken from [117].

Berger et al. [118] studied the mechanisms by which keyhole collapse occurs. Two mechanisms relating to the evolving melt pool shape during motion were proposed. In the first mechanism the tip of the melt pool collapses leading to a bulging of the backside of the melt pool; this bulge continues to grow until eventually the vapour condenses and a pore forms behind the melt pool. In the second mechanism the liquid at the top of the melt pool begins to extend toward the vapour cavity and when in close enough proximity causes a temperature change and sudden condensation of the vapour within the route of the cavity. This condensation lowers the pressure within the cavity pulling in atmospheric gases, such that the melt pool collapses on top of itself creating a pour at the tip of the melt pool. Figure 2-36 shows the process occurring in a series of photographs from high frame rate imaging.

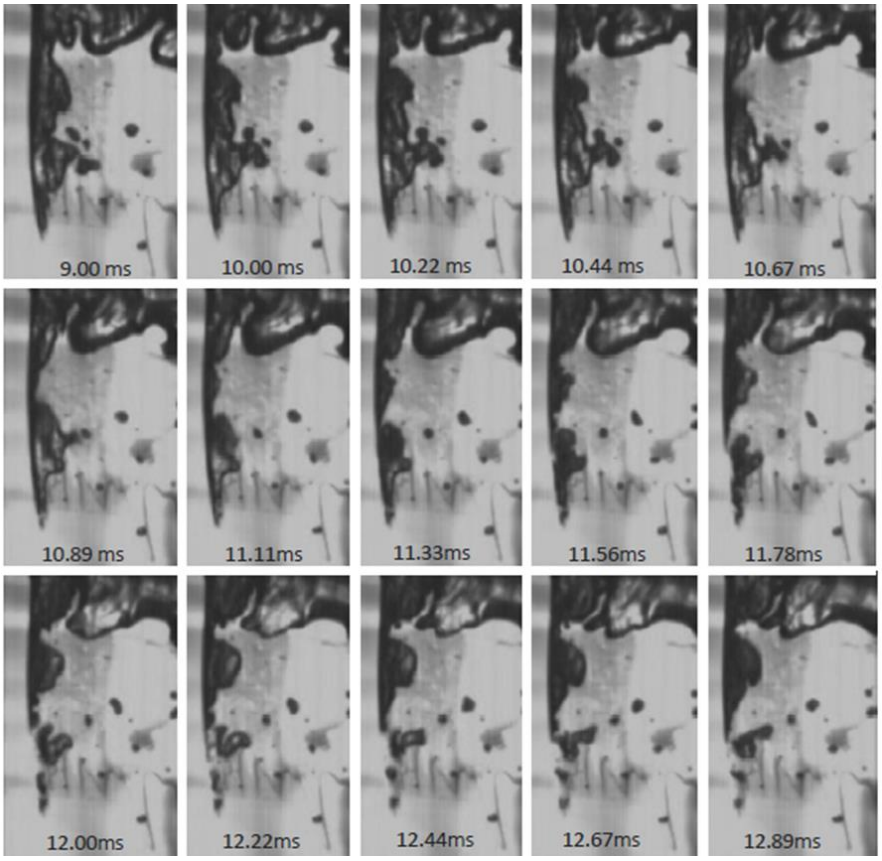

Figure 2-36: Photographs taken at different stages of keyhole pore formation at the tip of the melt pool. Taken from [118].

Keyhole porosity formation is quite common in the PBF of Ni-base superalloys. Temperatures in the melt pool often exceed the evaporation temperatures of lighter elements such as Al and as such vapour cavities are easily formed. Multiple studies performed for LPBF have shown increasing energy density and /or laser peak power results in an increase in keyhole pore formation [111]. EPBF is somewhat less affected by keyhole porosity due to the absence of atmospheric gases that can be pulled into the melt pool cavity and the tendency of metal vapours to be drawn up and out of the cavity by the vacuum. Nevertheless instances of keyhole pores can still occur and have been shown to be significantly influenced by the peak intensity of the electron beam, with higher peak intensities increasing the probability of keyhole pore formation [119].

ii. Cracking

Ni-base superalloys with high γ' content have been shown to be highly susceptible to weld cracking and hence are believed to be equally susceptible to cracking in PBF processing. Post weld heat treat cracking (PWHT) also referred to as strain-age cracking (SAC) occurs as a consequence of hardening and stress induced by γ' precipitation and growth in regions of existing high residual stress induced by the large thermal gradients experienced in welding [2]. Figure 2-37 shows the PWHT crack susceptibility of a range of Ni-base superalloys as a function of Ti and Al, and Cr and Co content. Higher quantities of Al and Ti result in the precipitation of higher volume fractions of γ', whereas higher Cr and Co content increases the coarsening rate of γ'[120].

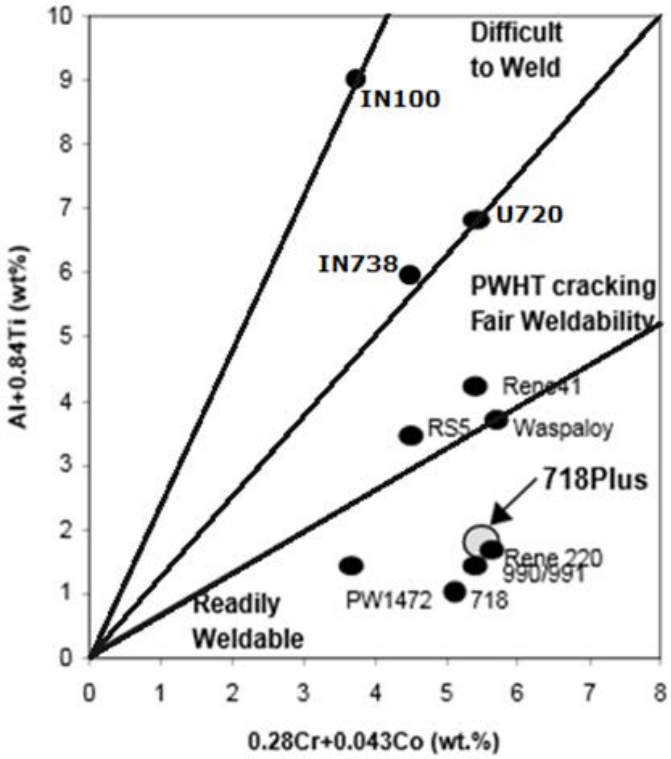

Figure 2-37: Relative weldability of Ni-base superalloys as a function of Al, Ti, Cr and Co content. Taken from [121].

In the case of welding, PWHT occurs during post process heat treatments; however, for PBF cracking in as-fabricated samples has been attributed to equivalent mechanisms [122-124]. It is believed that the thermal cycling that occurs due to the layerwise nature of PBF results in an in-situ heat treatment leading to a rise in the volume fractions of precipitated γ'.

Three additional mechanisms of cracking can be observed in the PBF of Ni-base superalloys; solidification cracking, liquation cracking and ductility dip cracking (DDC) [96]. Solidification cracking results from the trapping of solute rich liquid between the arms of solidifying dendrites, leading to the formation of interdendritic mushy regions. Thermal cycling, characteristic of the PBF process, creates localised mechanical stresses that tear and rupture these regions, producing jagged solidification cracks [125].

Liquation cracking is attributed to the precipitation of low melting point phases, for example metastable carbides and eutectics. These phases melt before the matrix and their liquid penetrates the grain boundaries, reducing the strength of the boundary. Coupled with high mechanical stresses, induced due to non-uniform relaxation from uneven cooling, this leads to micro fissuring and cracking [126]. A significant body of work investigating liquation cracking in welding found the size and quantity of liquation cracks to increase with increasing heating and cooling rates [126-129], suggesting liquation cracking would be prominent in PBF, though less so in EPBF due to processing at elevated temperature. Studies examining liquation cracking in welding and AM have found both high and low energy input conditions to result in an increase in liquation cracking, yet lower energy conditions would be expected to result in slower heating and cooling rates. Those presenting low energy input as the reason for liquation cracking [129-131] report mainly carbide and boride liquation and do not reach energy inputs anywhere near as high as those studying high energy liquation. Studies giving high

energy input and consequently rapid heating and cooling, as the reason for liquation cracking [126, 128] attribute cracking to the liquation of alternative low melting point phases other than carbides and borides. The minimum powers reached in these studies are still ten times greater than those reached in the low energy input studies.

DDC occurs when there is a localised drop in ductility, at temperatures in the region of the ageing temperature. There are two proposed mechanisms for the aforementioned phenomenon; firstly it is suggested that DDC occurs due to the formation of carbides in the grain boundary region, which are incoherent with the surrounding matrix [132]. Alternatively, some reports would suggest grain boundary shearing [133-135] as the mechanism for DDC. In the case of the latter, DDC always exhibits along regions of high-angle grain boundaries in Ni-base superalloys [136]. DDC and Liquation cracking often present in similar regions [137], and without the detectable presence of liquid films in the liquation cracks it can be difficult to distinguish the two. In consideration of the formation of DDC at high angle grain boundaries resulting from the grain boundary shearing mechanism, Carter et al. [138] created EBSD maps covering an area of 3 mm^2 to evaluate grain boundary characteristics in several areas where cracking was prominent in CM247LC samples produced by LPBF. Grain boundary angles were found to exceed 45° in the regions where cracking was present and consequently DDC was attributed as the cracking mechanism. The formation of these high angle grain boundaries in processing was suggested to be the result of the influence of the scanning strategy; a chess scan strategy was implemented (figure 2-38-a) with each square (island) scanned, shifted in the X and Y axis by +1 mm with each proceeding layer. Ever six layer the positions of islands realigned with the position of those in the first layer. High angle grain boundaries and cracks were found to be most prominent in the region defined by the edge of the islands in the first layer and those in the fifth layer before island positions realigned. A

simple raster scan (fig, 2-38-b) as opposed to the chess scan resulted in a reduction in cracking.

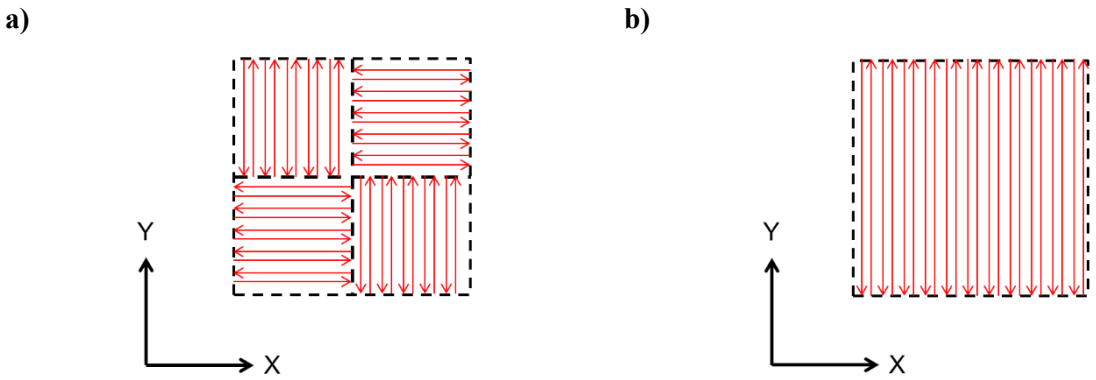

Figure 2-38: Different PBF scan strategies implemented in the work of Carter et al. [138]. a) chess scan strategy; b) raster scan strategy.

While the modification of some process parameters can target specific cracking mechanisms, such as beam power and speed for liquation cracking and scan strategy for DDC, generally control of cracking in PBF is achieved by adapting parameters to reduce residual stresses in build parts, minimising the mechanical forces acting to open cracks. Residual stresses develop by two mechanisms in PBF; the temperature gradient mechanism (TGM) and solidification shrinkage [139]. Figure 2-39 shows a schematic illustrating the mechanism of residual stress introduction in sheet material. In the first stage (TGM) as the top surface of the sheet is heated by the energy beam the area under the beam begins to melt, causing localised expansion of the material. The cooler surrounding material does not expand at the same rate and consequently compressive forces are induced in and around the melt pool. A similar mechanism occurs during PBF, as each new layer is melted, the previous layer acts to constrict the expansion of the melt in the new layer; as the build height and thermal gradients increase this become more pronounced [140]. Further residual stresses are then induced upon solidification of the material.

As the melt pool shrinks and cools it begins to contract; the outer edges of the melt pool will constrain the material at the centre of the pool as it cools and solidifies from the outer edge inward. This creates tensile stresses at the centre and top of the melt pool, resulting in the stress profile observed in figure 2-39.

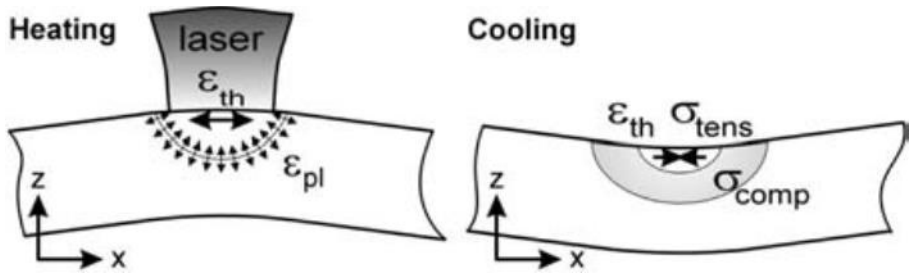

Figure 2-39: Schematic of the temperature gradient mechanism (TGM) introduces macroscopic residual stresses. Taken from [139].

Many strategies have been introduced to control the magnitude of residual stresses induced in Ni-base superalloys during PBF and other ALM processes. These include adapting of scan strategies, such as using shorter scan paths [139, 141, 142], re-orientation of build components to minimise part height and scan length [140] and in the case of LPBF introducing substrate preheating and/ or insulating the substrate plate [111, 143, 144]. Of course, EPBF is already carried at elevated temperature and consequently residual stresses are lower than in LPBF [145].

2.5.4 Influence of LPBF process parameters on the microstructure and mechanical properties of Ni-base superalloys

LPBF of Ni-base superalloys typically yields materials with fine columnar grains oriented in the build direction (figure 2-40) and spanning tens to hundreds of micrometres, resulting from partial remelting of previous layers leading to epitaxial growth of grains.

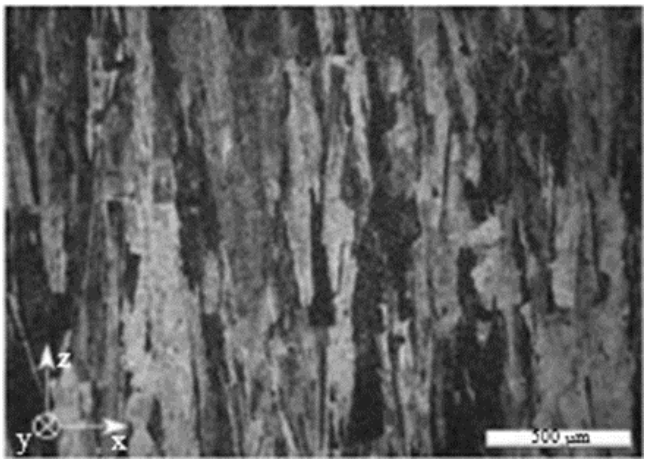

Figure 2-40: Epitaxial columnar grain growth in selective laser melted IN738LC. Build direction along Z axis. Taken from [146].

Alignment of the grains to the build direction is the result of a high temperature gradient created between the melt pool at the top of the build and the metal build substrate, which is acting as a heat sink. Thermal gradients can of course be influenced by processing parameters and component geometry and as such the columnar grain structure can be disrupted. Carter et al.[138] reported the influence of LPBF scanning strategy on grain morphology in CM247LC, comparing a chess scan strategy with a simple raster scanning strategy (figure 2-38). While both the simple and chess scan strategy were found to produce long columnar grains in the build direction (figure 2-41 -a and -c respectively), the columnar grains of the chess scan

strategy were interspersed with finer more equiaxed grains (figure 2-41-c). EBSD mapping of the XY cross-section also revealed a stronger grain texture in the samples produced with the simple scan strategy (figure 2-41-b) relative to those produced with the chess scan strategy (figure 2-41-d) suggesting a reduction in epitaxial grain growth.

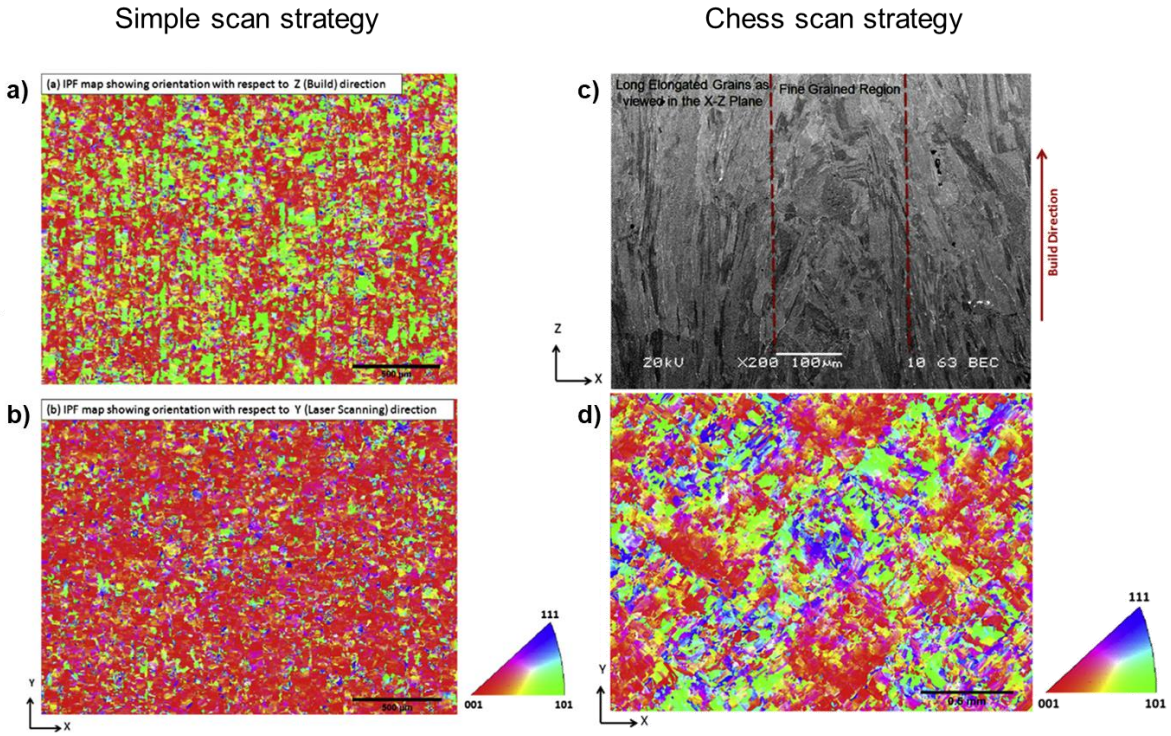

Figure 2-41: Grain structures for LPBF CM247LC produced with two different scanning strategies: a) EBSD map of XZ cross-section of simple scan strategy; b) EBSD map of XY cross-section of simple scan strategy; c) BSE micrograph of XZ cross-section of chess scan strategy & d) EBSD map of XY cross-section of chess scan strategy. Adapted from [138].

Wan et al.[147] studied the influence of scanning strategy on grain structure in Inconel 718. Two different scan strategies were trialled; a simple scan strategy with no interlayer rotation and a simple scan strategy whose scan direction rotated by 90° ever layer. They found rotating the scan strategy direction every layer to result in larger columnar grains relative to the scan

strategy in which scan direction was not rotated. Stronger grain texture was also observed in these samples. Later studies examined the influence of these microstructures on tensile properties[148] of specimens tested parallel to the build direction. They found that samples fabricated with rotating scan direction resulted in significantly poorer yield and UTS values relative to those produced with no rotation of scan direction. Differences in tensile properties were attributed predominantly to the difference in grain size between samples, with samples produced without rotation of scan direction having a more refined grain structure.

Due to the tendency for columnar grain growth along the build direction, LPBF samples typically yield anisotropic mechanical properties. Figures 2-42 -a and -b summarise the results of RT tensile testing of LPBF specimens with their longitudinal axis parallel (Z) and perpendicular (XY) to the build direction, before and after heat treatment. Tensile specimens with applied direction of stress perpendicular to the build direction have consistently better yield and UTS values relative to those with applied direction of stress in the build direction. Considering the typical microstructures observed in LPBF specimens, this can be attributed to the smaller grain diameter in the direction of applied stress. Comparing the anisotropy of tensile properties between studies, it appears that the difference between Z and XY samples is somewhat reduced in the work presented by Kuo et al.[149]. Tensile specimens in this work were produced on an EOS system, which utilises a unique scanning strategy, rotating the direction of scan by 66.5° every scan layer; this scan strategy has been shown to reduce the columnar grain structure in the build direction, though it is not eliminated entirely. Comparing tensile results before and after heat treatment[149, 150] it can be seen that the influence of build direction remains, suggesting little recrystallisation of grains to occur with HT. There is however a significant increase in the yield and UTS resulting from precipitation of strengthening phases.

a)

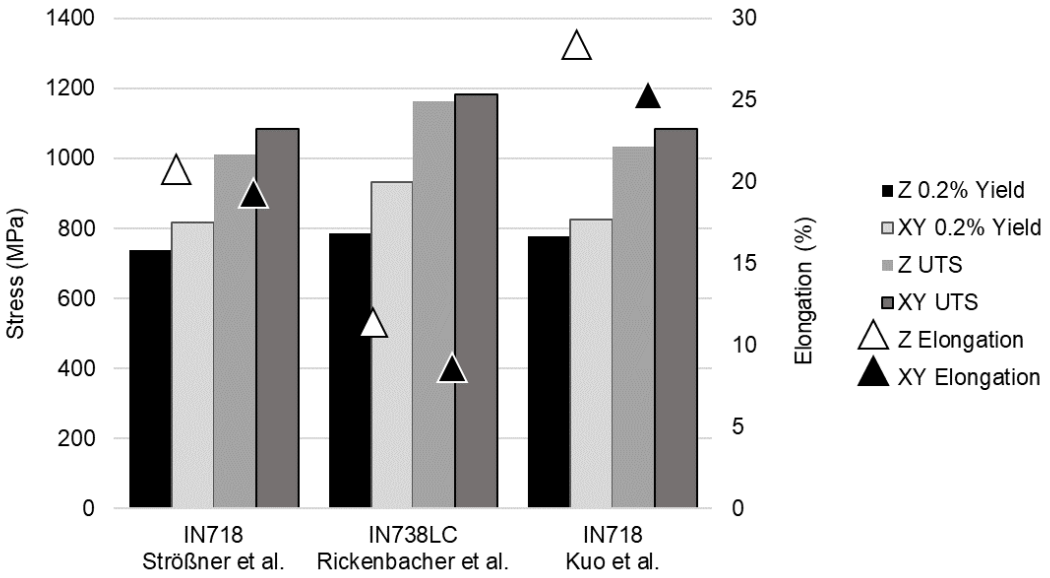

b)

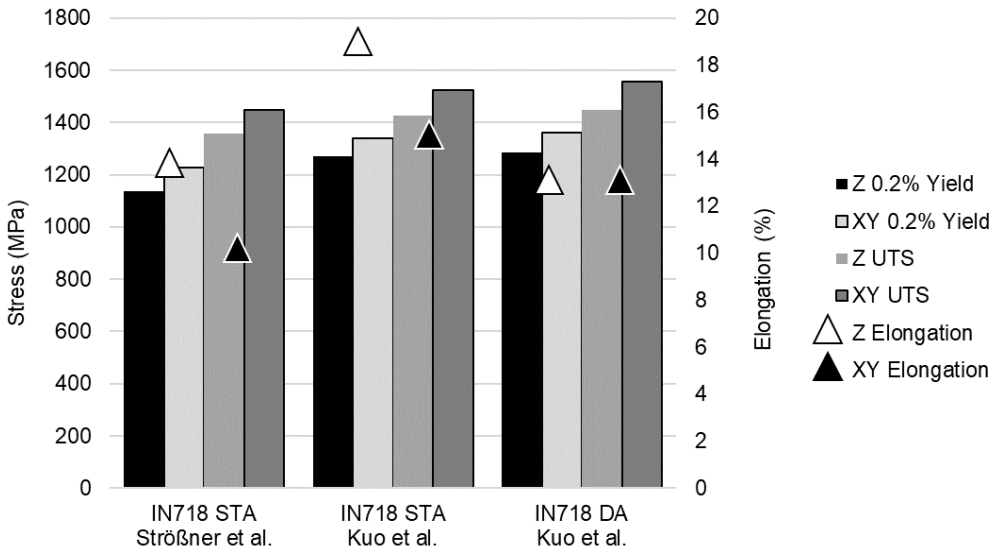

Figure 2-42: Tensile properties as a function of LPBF build direction: a) as-fabricated (Strößner et al.[150], Rickenbacher et al.[146] and Kuo et al.[149]) and b) in heat treated condition (Strößner et al.[150] and Kuo et al.[149]). STA and DA denote solutionising + Ageing HT and Direct Ageing HT respectively.

The microstructures of specimens produced by Strößner et al.[150] before HT exhibited almost no precipitation, with the exception of a few titanium carbonitrides observed by SEM.

Following standard HT δ precipitates could be observed at the grain boundaries and intragranularly. TEM imaging revealed the presence of γ" throughout, however quantities were found to be depleted in regions where δ precipitates had formed. Kuo et al.[149] examined the influence of two different HT on the microstructure and mechanical properties (figure 2-42). A standard solutionising + double ageing treatment (STA) and a direct ageing treatment (DA) were trialled. Prior to HT samples exhibited fine δ precipitates within interdendritic regions in the size range of 40-70 nm, resulting from high levels of Nb segregation. Following HT both STA and DA sample exhibited γ' and γ" in similar quantities, however δ size and morphology differed between the two HT conditions. STA resulted platelet like δ in the size range of 400 to 700 nm, however DA resulted in a combination of δ with platelet morphology and discrete blocky morphology in the size range of 50 to 100 nm. The slight improvement in mechanical properties of DA HT samples can be attributed to these more favourable δ morphologies.

2.5.5 Influence of EPBF process parameters on the microstructure and mechanical properties of Ni-base superalloys

While a wide range of Ni-base superalloys have been studies in LPBF, the majority of EPBF studies focus on Inconel 718. This is not necessarily due to its ease of weldability, but instead is likely a consequence of the requirements the machine manufacturer puts in place for qualification of powders for use in the machine. In order not to void the service agreement, only approved powders can be used; these include powders supplied by the manufacturer and powders that have gone through an approved qualification. To the best of the authors knowledge, the only Ni-base superalloys supplied by the machine manufacturer is Inconel 718.

EPBF microstructures like LPBF typically exhibit columnar grain structure owing to the thermal gradient created between the top and bottom of the build. However, due to being carried out at elevated temperature, for a constant set of beam parameters, grain morphology will vary from top to bottom of the build. Kirka et al.[151] classified the grain structure of Inconel 718 EPBF components into three regions (figure 2-43); at the top of the build a cored dendritic structure is observed resulting from the fast cooling rates formed by conduction of the previously deposited material and build substrate. Just below the coring, a diffuse dendritic structure is observed, in which very fine dendrites with secondary arm development can be observed; the size of dendrites increasing going down the build. Finally in the bottom of the build, grains are defined, and dendritic structures are no longer clearly visible; this resulting from the material in the bottom of the specimen being held at temperature for a number of hours.

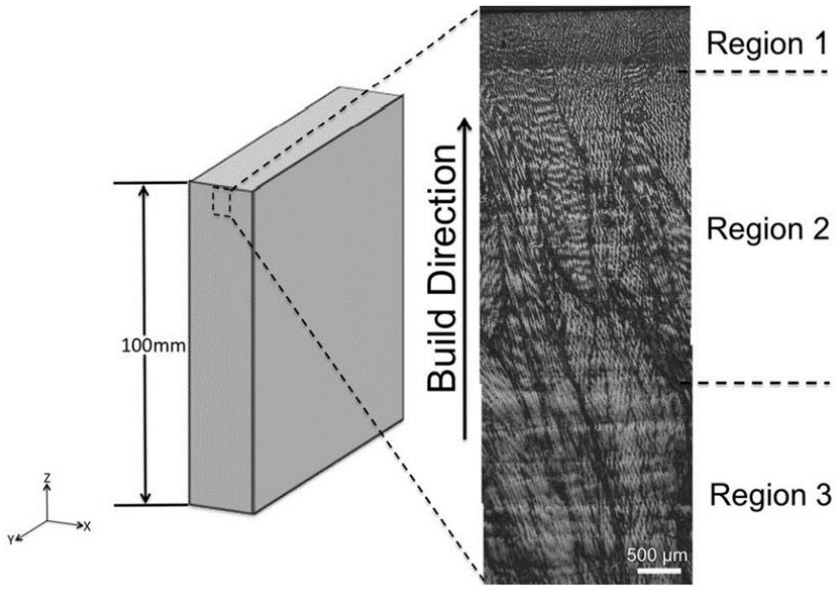

Figure 2-43: micrograph of the microstructure gradient observed at the top of EBM Inconel 718 block with the three distinct regions discernible. Taken from [151].

In addition to the graduating microstructure observed in EPBF specimens, precipitation also varies from the top to the bottom of the build. Types and quantities of precipitation will vary depending on total build time and the time it takes for the build to cool once finished. Build temperatures in EBM are typically measured at the build plate. As the build temperature is kept hot by heating each new layer with the electron beam, maintaining high temperatures at the build plate level means maintaining even higher temperatures at the top of the build. Figure 2-44 shows the time-temperature-transformation diagram for Inconel 718. Build temperatures commonly implemented for Inconel 718 are in excess of 950°C; depending on the height of the build, temperatures at the top of the build could easily reach 1050°C. Consequently, for a build time of just 1 hour, there would be no precipitation at the top of the build and delta precipitated towards the bottom of the build. If longer build time are considered, a more complex precipitation gradient is likely to occur.

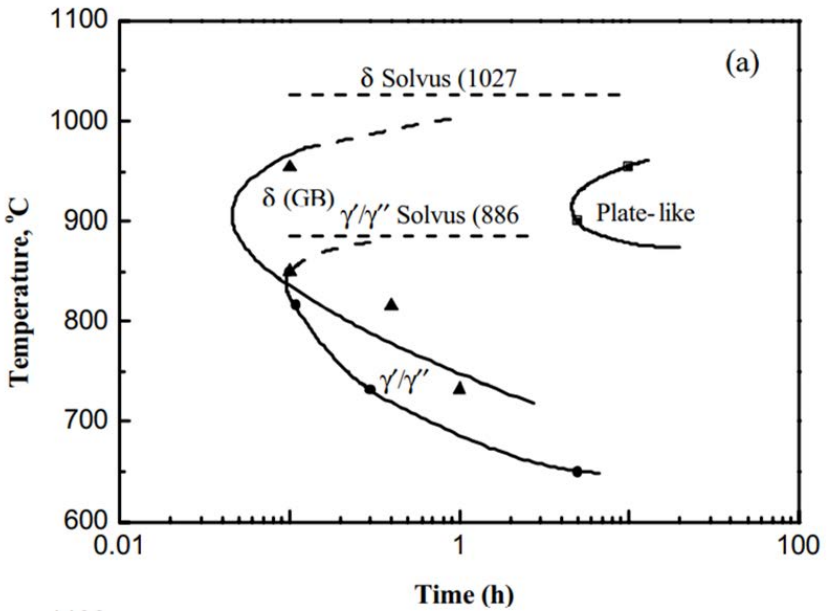

Figure 2-44: Time-Temperature-Transformation curve for Inconel 718. Adapted from [152].

The graduating microstructures observed in EPBF specimens would be expected to result in anisotropic mechanical properties. Kirka et al.[151] performed monotonic tensile tests with of Inconel 718 EPBF specimens with build height of 100 mm. Figure 2-45-a shows the variation in yield, UTS and elongation as a function of build height, and figure 2-45-b the corresponding stress-strain curves for RT measurements. Examining the stress behaviour from the top to the bottom of the build, yield and UTS depart from starting states 30 mm below the top of the build. Kirka et al. compared the tensile results with earlier observed microstructures (figure 2-43) finding the change in yield and UTS behaviour to occur well into the part of the EPBF build with fully developed grains, suggesting the tensile properties to be more dependent on precipitation than dendritic structure. Variation in tensile properties can also be seen at approximately half the build height suggesting a deviation in precipitation type or morphology at this point.

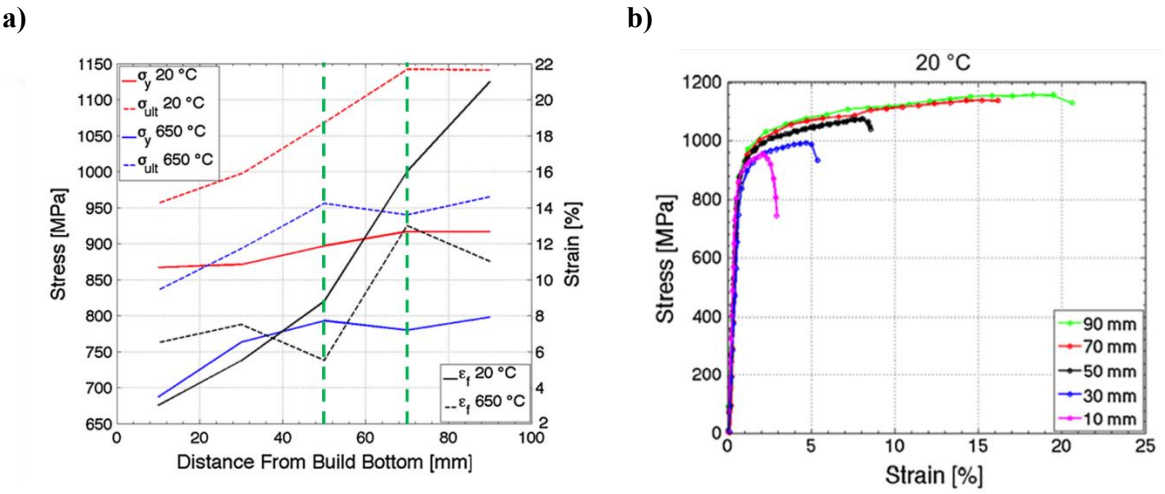

Figure 2-45: a) Results of room temperature monotonic tensile tests for EPBF Inconel 718 as a function of build height. The green dashed lines indicate the build heights at which stress conditions alter. b) Corresponding stress strain curves for RT measurements. Adapted from [151].

2.6 NNS PM Productivity comparison

One of the advantages of in-situ shelling highlighted in the literature is its increase in productivity relative to both PBF and HIPping processes. Regarding PBF, significant time can be saved by only scanning the shell of a component and partially melting the core. Compared to HIPping, in-situ shelling offers time saving advantages at the post-processing stage; the in-situ shelling canister, being of similar material to the powder, does not require removal. These claims should be carefully considered however, as productivity gains will differ depending on the geometry, quantity and material of the component being produced. For example, if the component is a stainless steel cylinder, the in-situ shelling process will only become more efficient than PM HIPping when the time to build the shell in PBF takes less time than welding the canister for HIPping. Relative to PBF of a cylinder, in-situ shelling only becomes more efficient when, the ratio of shell thickness to core diameter is such that the time taken to scan the shell plus HIP the un-sintered powders, is less than the time taken to melt the entire component to full density in PBF. Consequently, the in-situ shelling process is most suited to relatively large components of complex geometry and whose materials are not typically used for HIPping canisters.

2.7 Summary and concluding remarks

2.7.1 PM HIPping

A review of the literature relating to state-of-the-art PM HIPping of Ni-base superalloys, revealed the most defining microstructural feature to be PPBs. PPBs were observed to be influenced by powder chemistry, powder particle size and HIP cycle parameters. Conditions favouring recrystallisation of grains at the powder boundaries resulted in the elimination of PPBs and improved mechanical properties. Increased levels of

recrystallisation were observed in PM HIPped specimens produced with powders lower in oxygen and carbon and whose size were smaller. MacDonald et al.[74] however showed that for CM247LC powders, oxygen content was tied to powder particles size, with finer powders possessing higher levels of oxygen; in this case oxygen concentrations had a stronger influence on PPB formation than powder size. The use of powder particles sized for LPBF could consequently be either a benefit or hindrance to the properties of in-situ shelling parts depending on the oxygen content of the powders, both in their virgin state and after going through LPBF processing. Higher HIPping temperatures were observed to result in more recrystallisation and therefore may be more favourable for the in-situ shelling process.

2.7.2 PBF

PBF processing parameters were found to significantly influence the formation of porosity defects and cracks in Ni-base superalloys, necessitating parametric studies for the identification of processing windows. While a significant body of work has been conducted on the influence of beam power, scan speed, scan strategy and build part orientation, very few studies exist on the influence of layer thickness on defect formation. Studies optimising contour beam parameters for reduction of surface defects and improving surface finish also appear to be lacking. This could be an important factor regarding the bonding between PBF canisters and PM-HIPped material in in-situ shelling samples. When considering the mechanisms of bonding between the in-situ shelling canister and PM HIPped material, parallels may be drawn with the mechanisms of PPB elimination between powder particles. PM HIPping studies showed increasing the number of point contacts between particles to increase recrystallisation and reduce PPB formation. It is logical to assume that similar mechanisms can be taken advantage of when attempting to increase recrystallisation at in-situ shelling canister PM HIPped interface. An increase in point contacts at the interface may be

achieved by tailoring the surface roughness of the in-situ shelling canister, such that the distance between surface peaks is less than the average powder particle size.

Tensile properties of PBF specimens were observed to be anisotropic, resulting for the columnar grain structure produced by strong thermal gradients between the top of the build and the build substrate. This may influence the uniformity of deformation of in-situ shelling canisters. EPBF specimens showed even less isotropy relative to LPBF specimens owing to the gradient in microstructure from the bottom to the top of the build.

2.7.3 Inconel 718

Across all three PM processes investigated in the literature, Inconel 718 is the most common Ni-base superalloy studied. Its low susceptibility to cracking makes it a good candidate alloy for ensuring integrity of HIPping canisters in the in-situ shelling process. Furthermore Inconel 718 is the most widely used Ni-base superalloy and therefore a range of applications exist for which the in-situ shelling process might be employed. Considering the above, it was decided that in-situ shelling trials should be conducted using Inconel 718.

2.7.4 In-situ Shelling

In-situ shelling studies following the work of Das et al.[11] focus on Ti-6Al-4V. Several process variables not previously studied by Das et al. have been investigated. Qiu et al.[12] chose to leave powders in the canister core un-sintered, resulting in significant mismatch between LPBF canister and HIPped core microstructure. Cai et al.[14] investigated the influence of HIPping temperature on microstructure, finding higher temperatures to improve levels of homogeneity between canister and core. Finally, Leicht et al.[15] and Frisk et al.[16] decided to implement EPBF at the shelling stage as opposed to LPBF, and investigated the

influence of canister wall thickness. Thinner walls were found to result in increased radial shrinkage.

While Das et al.[11] also proposed Ni-base superalloy IN625 for the in-situ shelling process, no further studies have been performed on Ni-base superalloys. This is thought to be the result of the propensity of Ni-base superalloys to produce stable oxide films. Stable oxides formed on the surfaces of powders and PBF canister would prevent sufficient bonding between canister and core. A review of the literature revealed oxide stability to be most significantly influenced by oxidation environment. Lower partial pressures of oxygen and higher temperatures tend to result in the formation of a more stable oxide in a significant number of Ni-base superalloys.

Also not investigated in the literature, is the influence of surface roughness on bonding between canister and powders. This is most like because all Ti-6Al-4V studies showed excellent bond strength between canister and core.

Regarding the advantages of in-situ shelling over PM HIPping and PBF, the geometric dependence of productivity was highlighted, illustrating in-situ shelling to only be superior when considering relatively large and complex components. Further advantages of the in-situ shelling process may be found in the processing of crack susceptible alloys. Residual stresses generated in PBF provide the mechanical force necessary for crack formation to occur. Larger components tend to result in an increase in residual stresses resulting from an increase in the magnitude of thermal gradients. However, if only the shell of the component is scanned, thermal gradients are lower in magnitude and easier to control through manipulation of process parameters, and consequently the propensity for cracking can be reduced.

CHAPTER 3

RESEARCH AIM AND OBJECTIVES

3.1 Research aim

The overall aim of this project is to, increase PBF and/or HIP productivity by utilisation of the in-situ shelling process for Inconel 718 superalloy components. In order for the in-situ shelling process to be considered as a viable candidate for industrial implementation, tensile properties of the Inconel 718 material should be equivalent to or better than those of wrought Inconel 718.

3.2 Research objectives

As in-situ shelling involves the hybridisation of multiple material processing routes, it is sensible to address the project aim by first gaining an understanding of the process-microstructure-property relationship for each processing technique. With this in mind the research objective are as follows:

1. To assess the suitability of Inconel 718 powders for processing by PM HIPping, LPBF and EPBF (Chapter 5).

2. To investigate the material-microstructure-property relationships in PM HIPping of Inconel 718 (Chapter 6).

3. To optimise LPBF and EPBF process parameters to meet the property requirements of a HIPping canister (Chapter 7).

4. To investigate the mechanisms of bonding between PBF canister and PM HIPped powder in the in-situ shelling process (Chapter 8).

5. To optimise in-situ shelling parameters for stronger bonding across the PBF-PM HIPped interface (Chapter 8).

6. To compare the efficiency and cost of the in-situ shelling method, state-of-the-art HIPping and LPBF for processing of a complex component geometry (Chapter 8).

Chapter 4

Experimental Methodology

4.1 Introduction

This chapter starts with an overview of the progression of research, outlining each of the experiments performed and the reasoning behind why they were conducted. Following this the experimental methods employed for sample preparation and evaluation of Inconel 718 in powder and bulk forms is explained.

4.2 Research Progression

As outlined in chapter 3, the experimental work was broken down into five objectives, examining the process-microstructure-property relationships for each processing technique involved in the in-situ shelling process. LPBF and HIPping experiments were all performed at the Advanced Materials Processing Lab (AMPLab) at the University of Birmingham, whereas EPBF experiments were performed at IHI R&D Headquarters in Yokohama Japan; figures 4-1 and 4-2 outline the chronological order of experiments performed at each site respectively, providing a brief explanation as to why the experiment was conducted. Experiments aligned side by side in each figure were performed in parallel. Samples produced for LPBF experiments performed in parallel were produced during the same LPBF machine run. Section 4.3 onwards discusses the methodology of each experiment in greater detail, including specimen geometries and analyses performed.

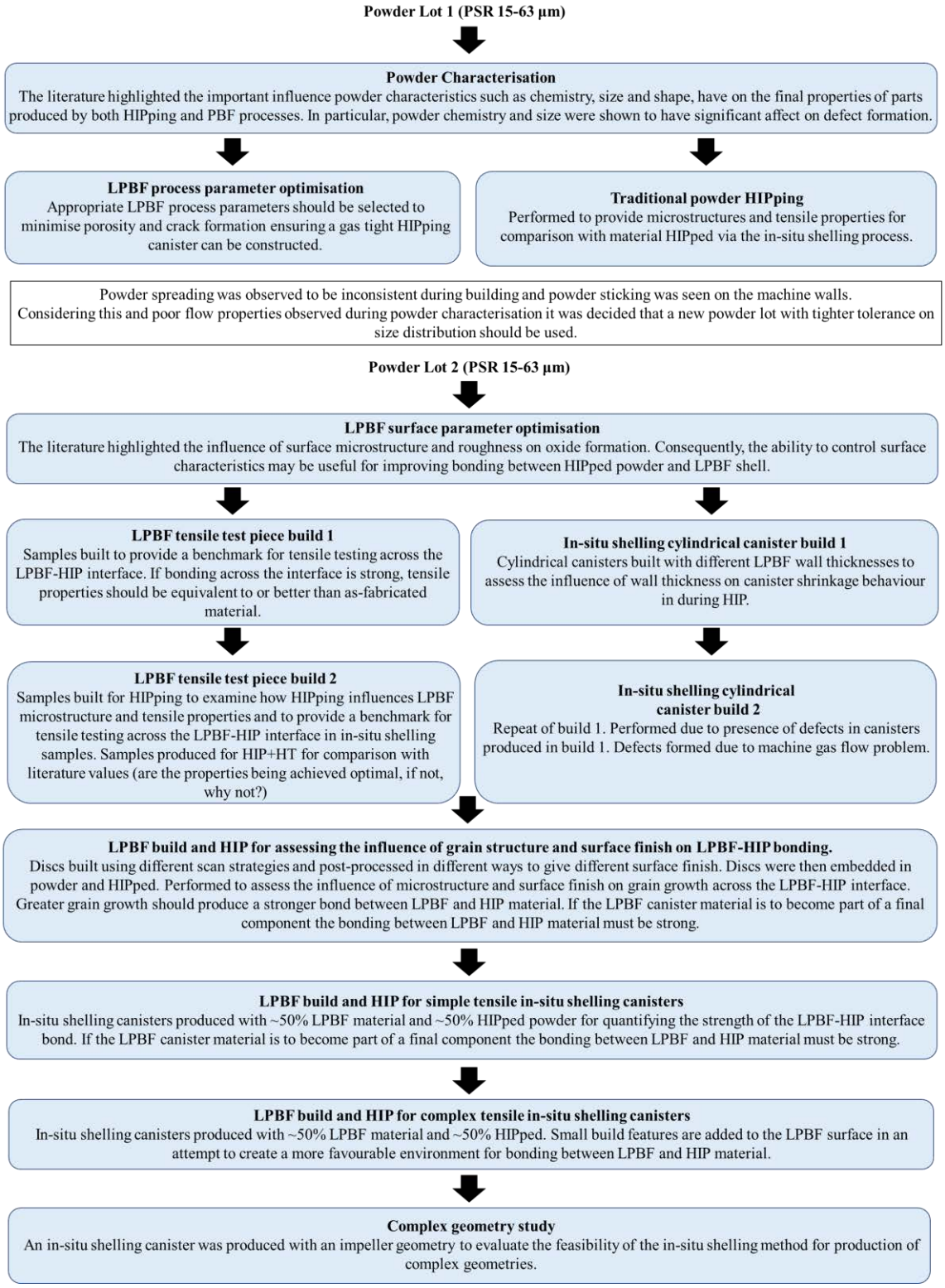

Figure 4-1: Chronological order of LPBF, HIPping and in-situ shelling experiments performed at AMPLab. Experiments placed side by side in the flow chart were performed in parallel.

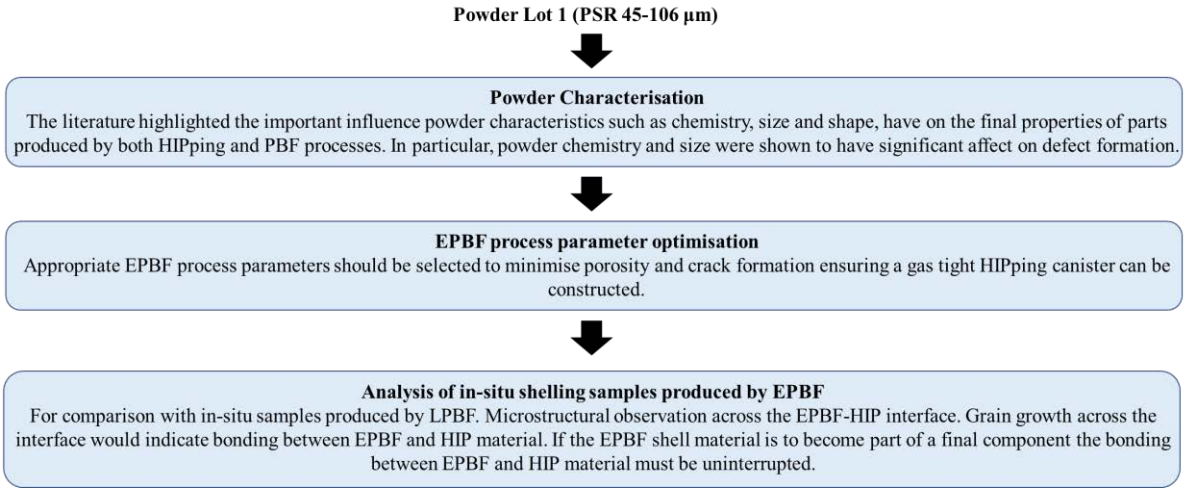

Figure 4-2: Chronological order of EPBF experiments conducted at IHI R&D headquarters in Yokohama, Japan.

4.3 Powder characterisation

4.3.1 Powder size distribution and morphology

Powder size distribution was analysed by two methods. While the first method of laser particle size distribution is advantageous due to its high level of accuracy and its ability to quantify large sample sizes, for powders with higher density however, keeping the powders in suspension for measurement can be difficult and consequently results may be skewed towards the finer particle size range. Consequently, LPSD measurements were verified by scanning electron microscopy (SEM).

i. SEM

To image the powder, small samples of powder from two separate bottles were poured onto a sheet of white paper, which was gently shaken until the powder had dispersed across the page. An SEM stub with carbon tape stuck to it was then pressed on top of the powder,

sticking the particles to the tape. The powder particles could then be observed by SEM. Several low magnification images of the powder particles were taken, which were then thresholded in ImageJ[153] (see figure 4-3) and the particle diameters measured using the ImageJ particle analyser. Dual contrast backscatter electron (BSE) and secondary electron (SE) imaging was found to be most appropriate for thresholding.

a) **b)**

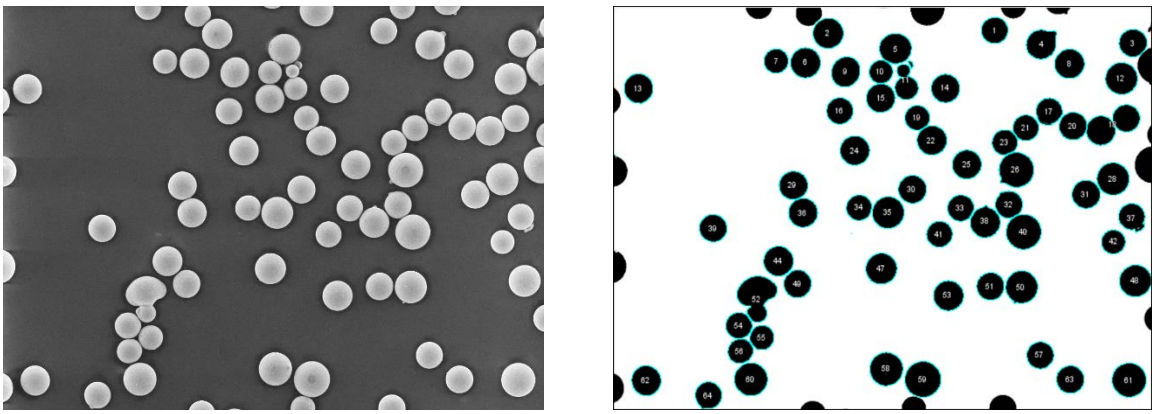

Figure 4-3: Dual contrast SEM image of powder before thresholding (a) and after thresholding with powder particles for measurement identified (b). Incomplete powder particles, i.e. particles at the edge of the image are excluded from measurement.

ii. LPSD

LPSD powder measurements were performed on a SYMPATEC HELOS LPSD [154] fitted with a SUCELL automated wet dispersing unit [155]. Powders were suspended in a solution of distilled water and Na4P207 before being added to the dispersing unit. Upon beginning the measurement, liquid in the dispersing unit undergoes sonication to agitate and break apart agglomerated particles. The liquid powder solution is then pumped from the dispersing unit to pass between two glass panels, through which Laser light is shone. Figure 4-4 depicts the optical set-up of the system. Powder particle size is quantified using the

principle of Fraunhoffer diffraction, which states intensity of diffracted light is a direct function of particle size, with larger particles yielding a higher intensity of scattered light.

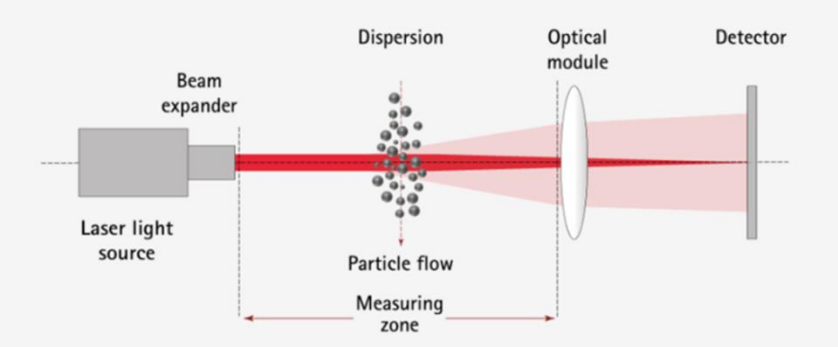

Figure 4-4: Optical set-up of SYMPATEC HELOS LPSD system. Taken from [156].

4.3.2 Powder flowability

There are multiple methods by which powder flowability can be assessed and much debate as to the applicability of each method for various types of PM process. In the present study four types of flow measurement were performed to characterise the flowability of the powders; Hall flow, apparent and tap density for calculating the Hausner ratio, Schulze ring shear and flow energy by FT4 rheometer. Hall flow is the current industry standard, and the most common value reported on metal powder certificates. Apparent and tap density measurements are often reported when characterising powders for HIPping, while shear tests are becoming increasingly popular in the characterisation of powders for AM. Flow energy measurements by FT4 are becoming an increasingly popular alternative to more traditional measurements. They were performed for EPBF powders as an alternative to Schulze ring shear testing as Schulze ring shear equipment was not available at the IHI R&D site.

i. Hall flow

Hall flow measurements are performed by measuring the time it takes for 50g of metal powder to flow through the orifice of a calibrated Hall flowmeter funnel [157]. To do this, a finger is placed over the orifice on the underside of the funnel, which is then filled with 50g of powder. Simultaneously a stopwatch is started, and the finger removed to allow powder to flow from the orifice; this action should be performed by the same person. The longer it takes for all the powder to flow through the orifice the lower the flowability of the powder. There is no specific flow rate at which powder is considered to be free flowing, consequently hall flow is a relative measure and only useful when comparing one powder to another.

ii. Apparent and tap density (Hausner ratio)

For LPBF powder lots apparent and tap density measurements were performed using a calibrated density cup with a known volume of 25 cm^3. The cup was weighed on a laboratory scale and the weight recorded. For apparent density measurements, the cup was filled with powders until overflowing and then carefully levelled off using a flat edge. The weight of the cup containing the powder was then measured. The tap density measurement starts in the same way as the apparent density measurement, however once the powders are levelled for the first time, the cup is then placed on a vibrating plate until the level of the powder in the cup drops. The cup is then topped up with more powder and vibrated again; this is repeated until the powder level no longer drops, at which point the weight of the cup and powders is measured. Each measurement is performed three times. Apparent and tap density are calculated by dividing the weight of the powder in the cup by the cup volume.

For EPBF powders, apparent and tap density measurement were conducted in a calibrated graduating cylinder, which was provided with a tap density tester. For apparent density

measurements the cylinder was placed on a scale, and the scale was zeroed. Powder was filled to the 50ml mark, and the weight of the powder was recorded. The cylinder was then placed on the tap density tester and the number of taps set to 1000. The powder level was monitored, and the test stopped once the level of powder was no longer changing. The new powder volume was recorded, and the tap density calculated based on the initial weight and new volume. Apparent and tap density can be used to quantify the flow behaviour by calculating the Hausner ratio, the ratio of tap density to apparent density. A Hausner ratio of less than 1.25 indicates the powder has good flowability.

iii. Schulze ring shear

The Schulze ring shear test assesses the flowability of a powder based on the force required to shear powder over powder, under a normal applied force and zero applied force. The force required to shear one layer of powder over another under loaded conditions, is the referred to as the consolidated yield stress. The force required to shear one layer of powder over another with zero applied force is the unconfined yield stress. By taking a ratio of these two values, known as the free flow coefficient (FFC), the flow behaviour of the powder can be inferred. A powder with a FFC greater than 10 is considered to be free flowing.

Figure 4-5 shows an illustration of the test equipment. Powder is poured into the bottom ring and carefully levelled, ensuring the powder is not compressed. The lid is then placed onto the powder, followed by the tie rods and another rod normal to the centre of the lid. To shear the powder, the bottom cell is rotated relative to the lid, with the tie rods and cross beam maintaining the lid position. The surfaces of the lid and bottom cell in contact with the powder have small teeth on them preventing shearing of the powder against their surfaces [158]. In the first measurement step a defined force is applied normal to the powder, and the cell

rotates to shear the powder; following this the force is decreased and the cell is rotated in the opposite direction. The normal force is reduced several times until no external force is being exerted anymore.

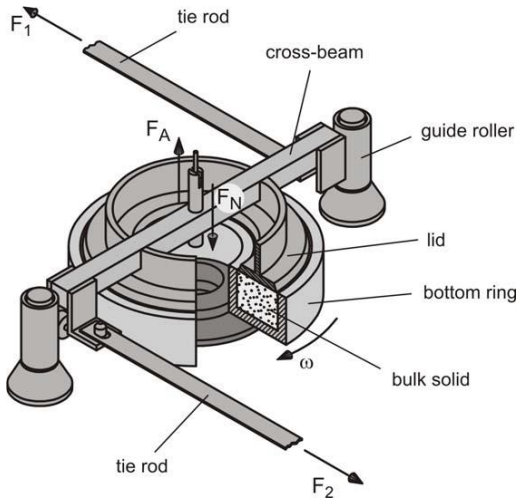

Figure 4-5: Shear cell of a Schulze ring shear tester. Taken from [158].

Figure 4-6 shows an example of the measurement results generated by shear testing. The semi-circular plots are Mohr's stress circles and describe all stresses experienced at a single point within the bulk solid. The largest circle represents the stress experienced during the first measurement stage (confined yield stress) and the smallest the last measurement stage (unconfined yield stress). The FFC value is calculated by dividing the vertical stress from the first measurement (σ_1) by the vertical stress from the last measurement (σ_c).

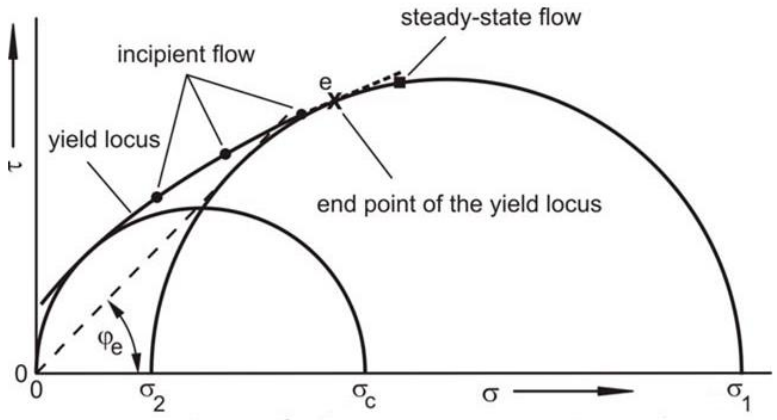

Figure 4-6: Example of Mohr's stress circles and the corresponding yield limit generated for a powder subjected to shear stress. Adapted from [158].

iv. FT4 rheometer- flow energy

Schulze ring shear test facilities were not available for characterisation of EPBF powders. Literature does however exist for reasonable comparison of shear test measurement values to the results of flow energy tests performed using an FT4 rheometer [159], which was available at the IHI R&D site. To perform the energy flow tests, powders are placed into a glass graduating cylinder into which a propeller is turned, as the propeller moves down through the powder, powders are consolidated, and the force required for rotation of the propeller is increased. The propeller is then rotated back up through the powders to define the unconsolidated stress. For further details of measurements refer to [160]. Following acquisition of flow energy values, literature was used to produce a comparative shear value for Inconel 718 to compare with Schulze shear ring values produced for LPBF powders.

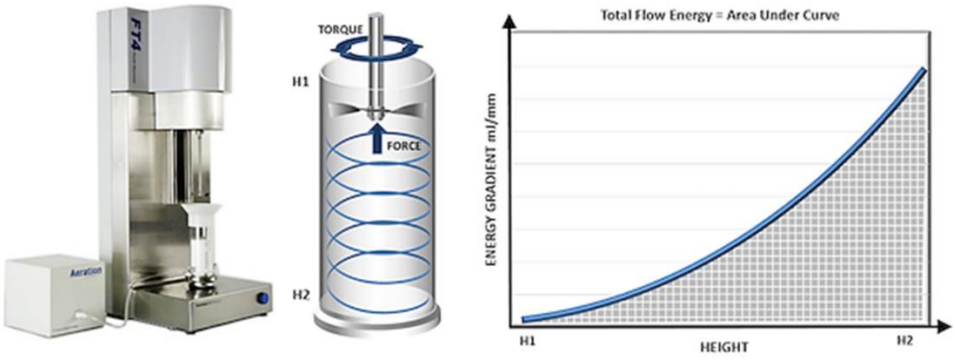

Figure 4-7: Schematic of aeration testing and resulting energy graph. Taken from [161].

4.3.3 Powder Chemistry

i. Inductively coupled plasma-optical emission spectroscopy (ICP-OES)

ICP-OES was performed to assess the bulk chemical composition of the powder. For this procedure, a powder sample is dissolved in acid; this solution is then burned in argon plasma. Atoms become excited in the heat of the plasma and emit radiation. An optical spectrometer is then used to measure the intensity of radiation and match this to existing data from calibration samples for multiple different elements.

ii. Fusion analysis

Concentrations of oxygen and nitrogen are analysed using fusion analysis. The powder sample is heated in a graphite crucible under an inert atmosphere. Carbon from the crucible reacts with oxygen in the sample to create CO_2, which is then measured by infrared detection. Nitrogen is measured during the same process; when heated, molecular nitrogen is given off which can then be quantified using a thermal conductivity cell.

iii. Combustion analysis

Carbon and sulphur are quantified by combustion analysis. Powder samples are heated in an atmosphere of oxygen, to encourage the formation of CO_2 and SO_2. Levels of CO_2 and SO_2 are quantified by an infrared detector and the carbon and sulphur content determined by the concentration of their compounds.

4.4 PM HIPping

A mild steel canister with internal diameter 40 mm, height 60 mm and wall thickness 3 mm with outgassing tube attached (figure 4-8) was filled with Inconel 718 powders from powder lot 1 PSR 15-63 μm. Powder filling was performed in a glovebox with argon atmosphere, with less than 200 ppm of oxygen. Following powder filling, the top of the outgassing tube was sealed before removing the canister from the glovebox and shaking the HIP canister for 20 minutes to compact the powders. Figure 4-9 shows the HIP canister shaker. The canister was then returned to the glovebox and the powder level topped up. Powder filling and shaking was performed until the powder level no longer changed after shaking.

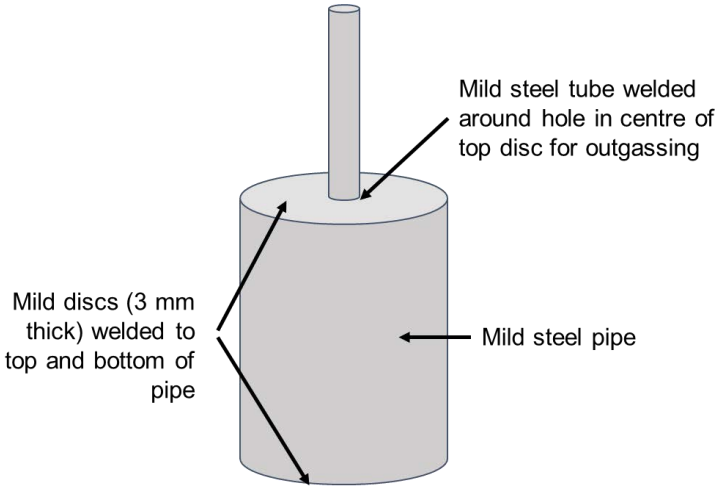

Figure 4-8: Design of mild steel canister used for traditional HIPping of Inconel 718 powders.

Figure 4-9: HIP canister shaker.

After filling the HIP canister, it is necessary to remove any trapped argon gas from the powders, as this can prevent full densification of the powders during HIPping. To outgas the canister, the outgassing tube was attached to the outgassing rig (figure 4-10) using a gas tight seal. Two things were done to prevent removal of powder from the canister during outgassing;

firstly, a fine mesh filter was placed just above the top of where the outgassing tube was secured (indicated in figure 4-10). Secondly, the vacuum was introduced in two stages; the first vacuum valve (indicated in figure 4-10) was opened in increments allowing a slow pull of gas from the canister until a pressure of approximately 10^{-2} mbar was achieved. Following this a secondary valve (indicated in figure 4-10) was slowly opened until the pressure reached approximately 10^{-4} mbar. The canister was then left at this pressure to outgas for 24 hours. After 24 hours the vacuum valves are closed, and the outgassing tube is heated with an oxyacetylene torch and crimped to seal the canister.

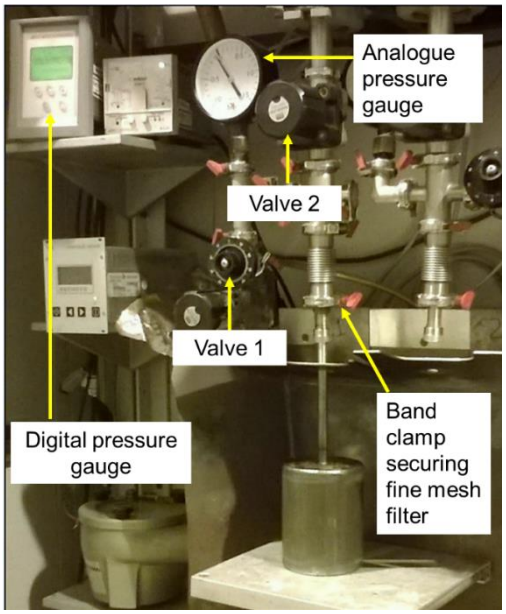

Figure 4-10: Outgassing rig with HIPping canister attached. Modified from [162].

HIPping was conducted using the EPSI HIP system (figure 4-11) located in AMPLab at The University of Birmingham. Maximum operating temperatures and pressures are 1450 °C and 200 MPa respectively.

Figure 4-11: EPSI HIP system. Taken from [162].

HIPping temperature, pressure and dwell time for the Inconel 718 powder were, 1180°C, 120 MPa and 3 hours respectively. Heating rates were 5 °C/min and cooling rates 10 °C/min. Temperature and pressure were raised simultaneously. The HIP parameters implemented were optimised in previous work performed at the University of Birmingham and are similar to those previously reported in the literature [1-3]. Post HIP, the top and bottom of the mild steel canister were removed by electro-discharge machining (EDM) and several bars cut from the remaining material, from which specimens for tensile testing and microscopy were prepared. Figure 4-12 shows the locations of samples cut from the canister and indicates the cross-sections of samples 1 and 2, examined for microstructural analysis. Samples 3 and 4 were machined for tensile testing according to procedures outlined in section 4.5.3.

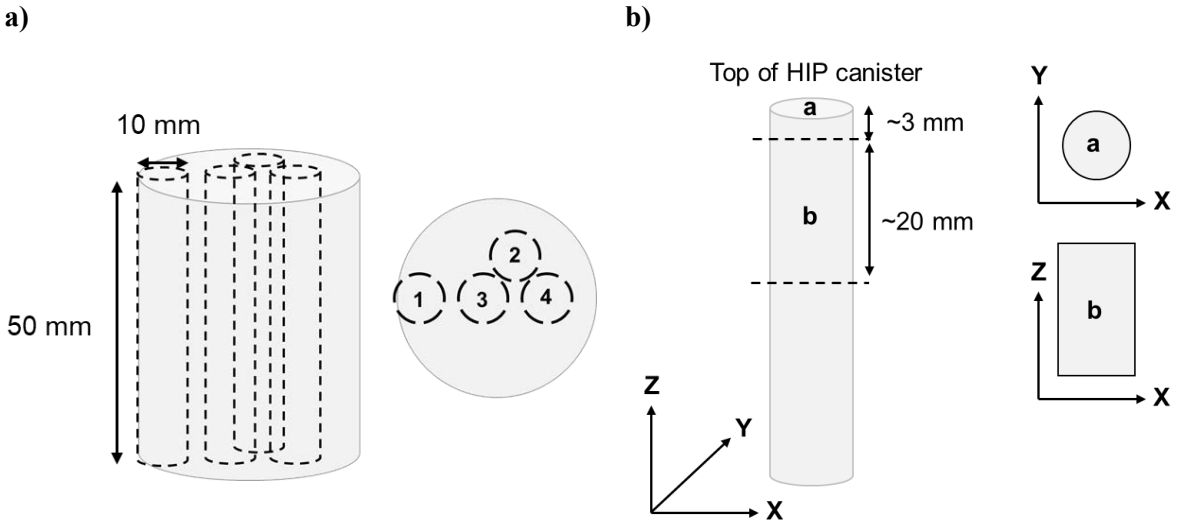

Figure 4-12: Schematic highlighting a) the position of samples cut from the Inconel 718 HIPped powder and b) the position of cross-sections observed in samples 1 and 2 microstructural analysis.

4.5 LPBF

LPBF specimens were produced on a Concept M2 laser powder bed system (figure 4-13) located in AMPLab at The University of Birmingham. Specifications of the system can be seen in table 4-1. Available scan strategies and adjustable parameters are summarised in table 4-2 and figure 4-14.

a) b)

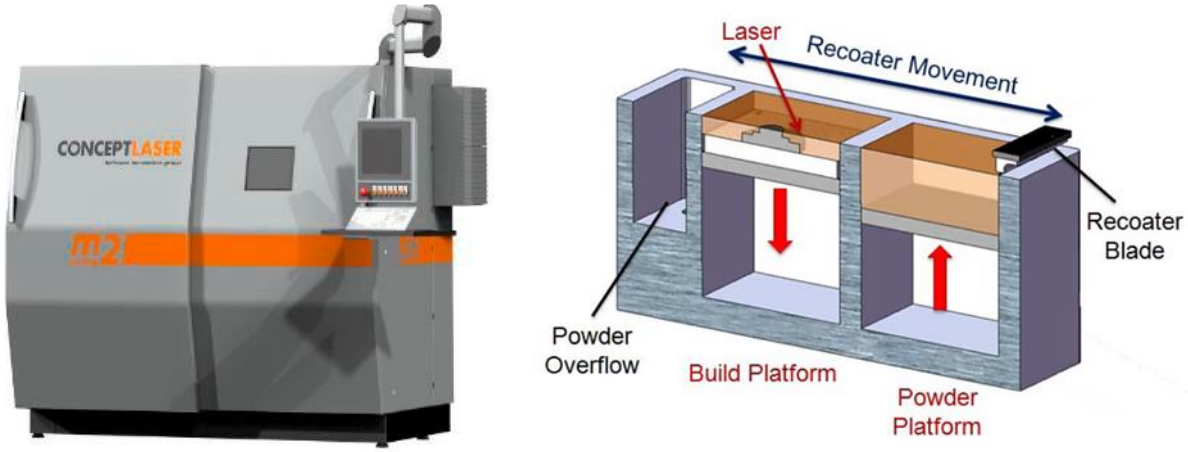

Figure 4-13: a) Concept M2 laser Cusing system. Taken from [163]. b) Schematic of inside of Concept M2. Taken from [96].

Table 4-1: Specifications of the Concept M2 system located at The University of Birmingham.

Laser	Rofin Nd:YAG fibre laser (λ 1064 nm)
Maximum laser power (W)	400
Maximum scan speed (mm s^{-1})	7000
Minimum layer thickness (µm)	20
Maximum build height (mm)	280
Operating atmosphere	Argon
Recoater type	Flexible rubber

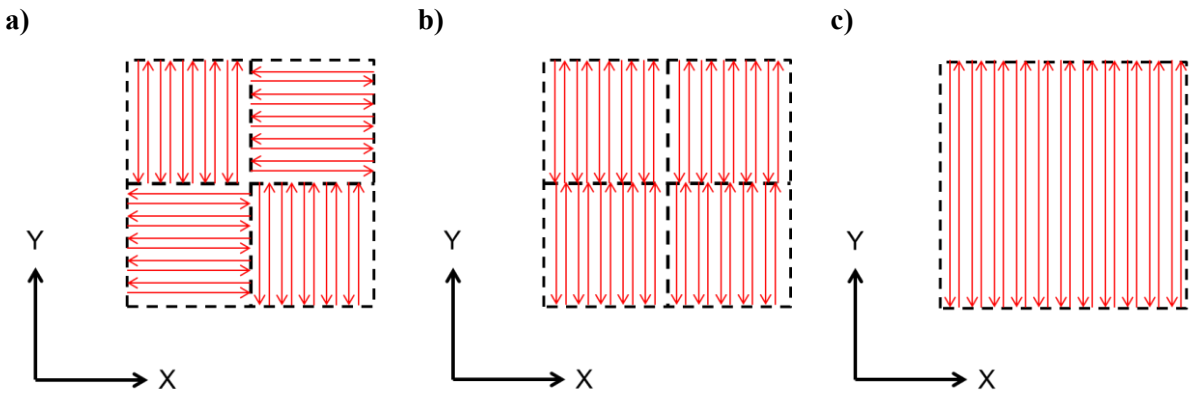

Figure 4-14: Illustrations of available scan strategies on the Concept M2. a) chess scan strategy; b) Island scan strategy; c) simple (hatch) scan strategy.

Table 4-2: Parameters relating to scan strategies on the Concept M2. Default laser spot size is 150 µm.

Parameter	Description
a1	The hatch spacing divided by the laser spot size
a2	The island/chess offset divided by the laser spot size. This determines the distance by which a square in the island or chess pattern is shifted in the X and Y axis with each subsequent layer.
a3	The contour offset divided by the laser spot size.

4.5.1 Process parameter optimisation

i. Influence of process parameters on porosity and cracking

In order to assess the influence of LPBF processing parameters on defect formation and microstructure, a fractional factorial study, based on a central composite design (CCD), was implemented. LPBF process variables investigated included laser power, scan speed, scan spacing and layer thickness.

Initial LPBF studies were performed using powder lot 1 PSR 15-63 μm. LPBF variables were investigated for curved thin wall structures (figure 4-15), with three different thicknesses of 1, 1.5 and 2 mm. The curved wall geometry allowed for multiple parameter combination to be tested while closely reflecting the canister geometry implemented in the in-situ shelling work in chapter 8; if perfect semi-circular walls were built matching a half canister geometry exactly, many more LPBF builds would have had to have been performed to test the same number of parameter combinations. The interaction of process parameters with wall thickness was investigated as the influence of canister wall thickness on shrinkage is also examined in in-situ shelling studies; literature showed wall thickness to influence the isotropy of densification of HIPping canisters. The scan strategy implemented can be seen in figure 4-15 (b). Walls were scanned at 45° to the X and Y axis and the scan direction was rotated by 90° every other layer. This scan strategy results in a combination of long and short scan tracks, providing a compromise on large thermal gradients produced by long tracks and overbuilding at the part edges produced by short scan tracks. Table 4-3 summarises the LPBF parameters implemented. Three builds were conducted with three different build layer thicknesses of 20, 40 and 60 μm. A range of laser powers and scan speeds have been reported in the literature [150, 164-167] encompassing combinations of low laser power (below 200 W) and slow scan speed (less than 1000 mm s^{-1}) and high laser power and fast scan speed. Given the large range of parameters utilised previously, the field of laser power and scan speed range investigated was narrowed based on the results of previous studies conducted at the University of Birmingham on LPBF of Inconel 718 GA powders, in which high laser powers and fast scan speeds were found to yield acceptable microstructures. A single slow scan speed parameter was however also investigated. The range of hatch distance investigated encompasses 50 %

to -25 % overlap of scan tracks, assuming a minimum and maximum laser spot size of 60 and 90 µm respectively. The negative term describes separation of scan tracks, i.e., no overlap.

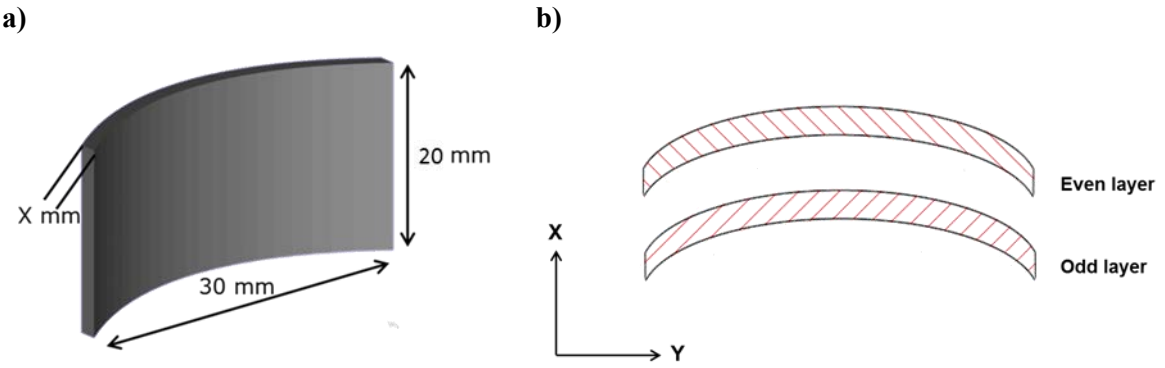

Figure 4-15: a) Geometry and b) scan strategy of LPBF walls for investigation of LPBF process structure relationships. Three different wall thicknesses were built: 1, 1.5 and 2 mm.

Table 4-3: LPBF processing parameter combinations investigated for fabrication of Inconel 718.

Parameter Set	Laser Power (W)	Scan Speed (mm s^{-1})	Hatch distance (mm)
1	300	1425	0.06
2	225	1425	0.045
3	225	600	0.06
4	225	1425	0.075
5	210	1590	0.057
6	225	1425	0.06
7	240	1260	0.057
8	210	1260	0.057
9	240	1590	0.063
10	225	1425	0.06
11	240	1260	0.063
12	210	1260	0.063
13	240	1590	0.057
14	300	2250	0.057
15	225	2500	0.045

Following sample production, walls were cold mounted by layer thickness and wall thickness as shown in figure 4-16, and ground and polished according to the procedure laid out in section 4.8. The XY cross-sections of walls were imaged by optical analysis, and then the entire resin block was cut down the centre line (indicated in figure 4-16-b) to reveal the XZ cross-section for imaging. Samples were imaged in this way so as to reveal any defects caused by powder spreading issues; such defects would be present in the same location of each wall.

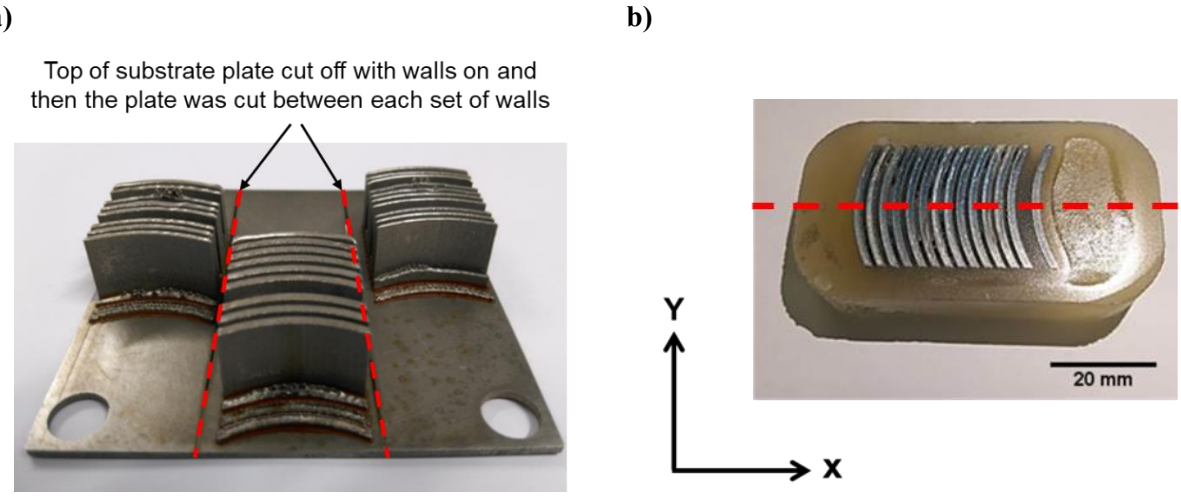

Figure 4-16: a) sectioning of plate for mounting of LPBF wall samples and b) photograph of cold mounted XY cross-sections of walls for layer thickness 40 µm and wall thickness 1.5 mm.

ii. Influence of surface process parameters on surface roughness

Curved walls (figure 4-15) were produced in 1, 1.5 and 2mm thicknesses with 40 and 60 µm layers. Hatch melting parameters used were those optimised for minimal porosity and no cracking in the LPBF process parameter optimisation study (table 4-4), with different parameter sets chosen for different wall thicknesses. Immediately following hatch melting, a contour scan was performed around the edge of the wall. Contour scan parameters varied were laser power, scan speed and number of scans. Parameters were chosen based on previous studies conducted in another Ni-base superalloy [168]. Contours were positioned such that the track centre was aligned with the edge of the wall surface, as seen in figure 4-17. A summary of contour parameters can be seen in table 4-5. Average surface roughness (Ra) values were recorded for each of the curved walls on both concave and convex surfaces using the Kosaka Laboratory-SE1700 Surface roughness meter located in Surface Engineering in Metallurgy

and Materials at the University of Birmingham. Measurement parameters used are summarised in table 4-6.

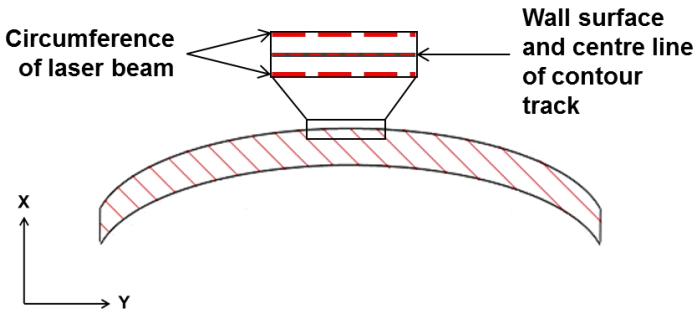

Figure 4-17: Schematic showing contour position for LPBF walls.

Table 4-4: LPBF hatch parameters used for melting of walls in contour study.

Wall thickness (mm)	Laser Power (W)	Scan Speed (mm s^{-1})	Hatch distance (mm)
1	210	1260	0.057
1.5	240	1260	0.057
2	300	1425	0.06

Table 4-5: LPBF contour parameters tested for each wall thickness and build layer thickness.

Parameter Set	Laser Power (W)	Scan Speed (mm s^{-1})	Number of contours
1	125	2500	1
2	125	2500	2
3	150	1000	1
4	150	1000	2
5	200	800	1
6	200	800	2

Table 4-6: SE1700 measurement settings for surface roughness measurements of LPBF samples.

Parameter	Setting
V.mag	1000
H.mag	20
Measurement length	2.5 mm
Drive speed	0.1 mm s^{-1}
Cutoff Lc	0.25 mm
Filter	2CR
Stylus Radius	2 μm

4.5.2 LPBF tensile testing

Tensile testing was performed for as fabricated, +HIPped and HIPped + HT LPBF specimens. As fabricated and HIPped LPBF samples were tested to provide a benchmark for tensile testing across the LPBF-HIP interface in in-situ shelling samples, as well as providing values for comparison with the literature, ensuring state-of-the-art conditions are being matched. HT was done at the request of IHI for comparison with traditional production methods and existing literature. All LPBF tensile specimens were produced by building cylinders of 10 mm diameter and 50 mm height. Four as fabricated, two HIPped and four HIPped + HT specimens were produced; the latter samples were HIPped and HT prior to being machined, according to the specifications in figure 4-18. HIP conditions were the same as those used for traditional power HIPping and can be seen along with HT conditions in table 4-7. As with the powder HIPping temperature and pressure were raised and dropped in parallel. Heat treatments were carried out in a TAV vacuum furnace, equipped with gas fan quench capability. Sample temperatures were monitored using in-situ thermocouples with error limits of +/- 1°C.

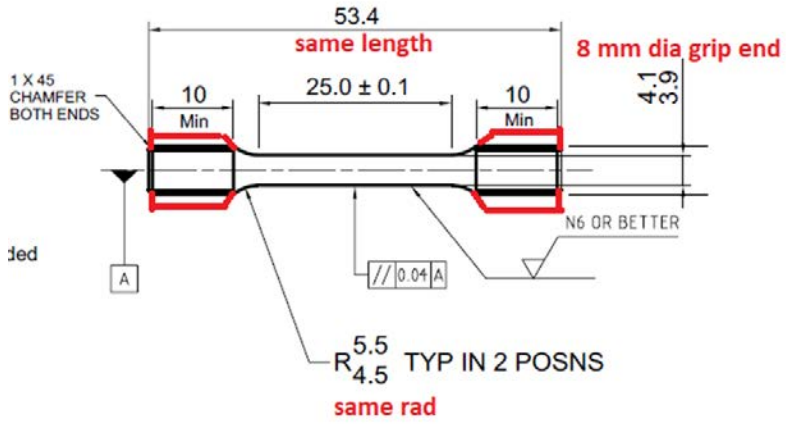

Figure 4-18: Round bar tensile specimen drawing. Dimensions adhere to the ASTM E8M standard.

Table 4-7: HIP and HT conditions used in production of LPBF+HIP and LPBF+HIP+HT tensile specimens.

Treatment	Stage	Temperature (°C)	Time (Hrs)	Pressure (MPa)	Heating/cooling rate or method (°C/min)
HIP	n/a	1180	3	120	+5 / -10
HT	1	980	1	vacuum	Gas quench
	2	720	8	vacuum	+10 / -0.8 to 620°C
	3	620	8	vacuum	-10

As fabricated and HIPped samples were tensile tested at room temperature (RT) only and HIPped + HT samples were tested at RT and elevated temperature (ET), 650°C. RT tensile testing was performed according to ASTM standard E8M and ET testing to ASTM standard E21.

4.6 In-situ shelling

4.6.1 Influence of wall thickness on shrinkage

Figure 4-19 shows the geometry of the cylindrical LPBF in-situ shelling canisters. The cylinder at the top of the canister is there to allow attachment of a piece of mild steel tubing for outgassing and sealing of the canister. An outgassing tube cannot be built directly onto the canister as the dimensional tolerance and surface roughness resulting from the LPBF process would not produce an outgassing tube that would ensure a gas tight seal during the outgassing process. In addition, directly heating the LPBF component for crimping of an LPBF outgassing tube may result in the formation of liquation cracks in the heat affected zone (HAZ), diminishing the mechanical integrity of the in-situ canister. The main canister is joined to the top LPBF cylinder by a cone with a wall angled at 40°; this was deemed to be a sufficient angle for the wall to be self-supporting, important as the building of internal support structures inside the canister would influence powder packing and deformation behaviour. Canisters were produced in four different wall thicknesses, 0.75, 1, 1.5 and 2 mm. Originally it was planned to build canisters in just three thicknesses (1, 1.5 and 2 mm), however as the 1 mm thick walls produced some of the densest parts during LPBF process optimisation it was decided that a thinner wall should also be trialled during the in-situ shelling stage. The internal dimensions for each canister were the same for all four wall thicknesses, ensuring as close to equivalent powder volumes as possible. By maintaining the same quantity of powder in each canister, any differences in shrinkage and/or deformation observed during HIPping of the canisters would result from the difference in wall thickness and not the powder volume.

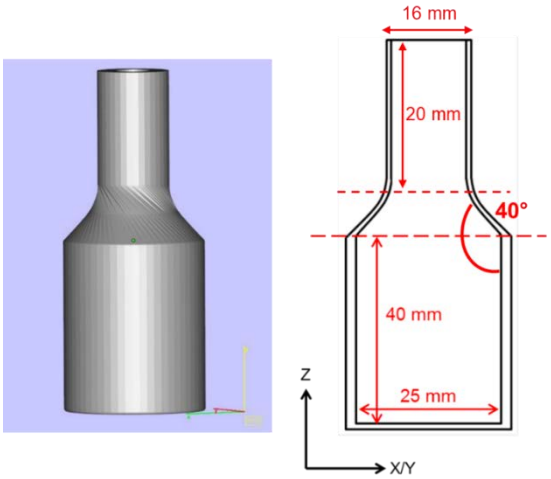

Figure 4-19: CAD image of in-situ shelling canister and schematic of cross-section with added dimensioning.

Table 4-8 summarises the LPBF parameters used for each wall thickness of canister. Results of the LPBF process parameter optimisation showed porosity defects to be strongly linked to wall thickness but grain structure and precipitation not to vary significantly, consequently LPBF parameters were chosen based on minimising defects in the canister walls. As an optimisation study had not been completed for 0.75 mm walls, parameters implemented for 1 mm thick canisters were also used for the 0.75 mm canisters. The base of each canister was scanned using the chess scan strategy (figure 4-14-a) as it was believed using a simple scan strategy to scan the large area of the canister base would result in an increase in residual stresses and peeling of the canister base from the substrate plate during building. The width and length of the chess scan pattern was set to 7.5 mm.

Table 4-8: LPBF hatch and contour parameters used for production of in-situ shelling canisters.

Hatch Parameters			
Wall thickness (mm)	**Laser Power (W)**	**Scan Speed (mm s^{-1})**	**Hatch distance (mm)**
0.75 & 1	210	1260	0.057
1.5	240	1260	0.057
2	300	1425	0.06
Contour Parameters			
Wall thickness (mm)	**Laser Power (W)**	**Scan Speed (mm s^{-1})**	**Number of contours**
0.75, 1, 1.5 & 2	125	2500	2

Two canisters were produced in each wall thickness. All canisters were built on support structures so they could be easily removed from the plate without losing powders from inside the canister. Support structure design and parameters can be seen in figure 4-20 and table 4-9 respectively.

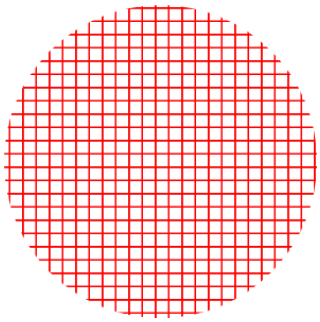

Figure 4-20: Support structure design for in-situ shelling canisters.

Table 4-9: LPBF support structure parameters.

Laser Power (W)	Scan Speed (mm s^{-1})	Distance between support structure lines (mm)
175	1250	1

Following production of the in-situ shelling canisters, the canisters were shaken to reduce the powder height below the top of the canister allowing welding of the mild steel outgassing tube to the LPBF canister without melting any powders inside the top of the canister. Once the outgassing tube was attached, powders were topped up and shaken according to procedures outlined in section 4.4. Following filling, the canisters were outgassed for 24 hours and sealed according to procedures outlined in section 4.4.

HIPping was performed at 1230°C with pressure and dwell time of 120 MPa and 3 hours respectively. Temperature and pressure were raised and lowered simultaneously. Heating and cooling rates were 5°C /min and 10°C per minute respectively. The HIPping temperature used for the in-situ shelling canisters was 50°C higher than that used for HIPping of powder in a mild steel canister. It was decided to go to a higher temperature as it was thought that this may reduce PPBs observed in the microstructure of traditionally HIPped powders. The 1230°C was 10°C below the solidus temperature of the LPBF material, measured by DSC (figure 4-21). HIPping at or above the solidus risks liquating the eutectic phases observed in the interdendritic segregation in LPBF shell. This may lead to liquation cracking compromising the gas tight nature of the thinner walled shells.

Following HIPping, in-situ shelling canisters were sectioned from top to bottom and the whole cross-section was cold mounted in resin as shown in figure 4-22.

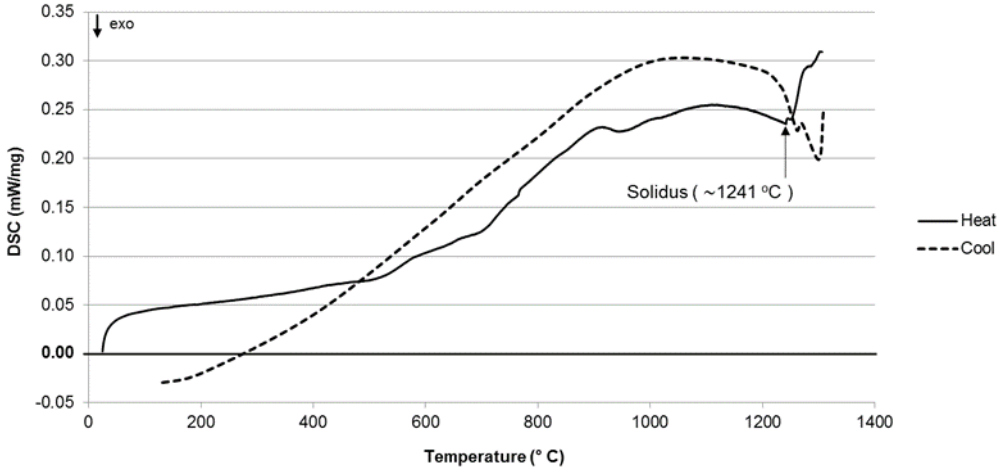

Figure 4-21: DSC heating and cooling curves for LPBF Inconel 718 material.

Figure 4-22: Photograph of LPBF in-situ shelling canister cross-section mounted in resin.

4.6.2 Influence of LPBF grain structure and surface finish on bonding across the LPBF-PM HIPped interface

As discussed in chapter 2 section 2.1 analogies can be drawn between the SSDB process and the mechanism of bonding across the LPBF-PM HIPped interface. Similar surface preparation procedures to those observed in SSDB work were carried out on LPBF Inconel 718 discs which were then HIPped in Inconel 718 powder. It was believed that by removing any existing stable oxide films through grinding, polishing and cleaning bonding between the LPBF material and PM HIPped powder would be improved. In addition, by removing surface oxides formed in LPBF processing, a better understanding of the oxide development at the LPBF-PM HIPped interface can be achieved. Parallel to this, a study into the influence of grain morphology was also conducted. Results observed in the earlier in-situ shelling studies reported in chapter 8 showed most of the grain growth across the LPBF-HIP interface to include twin grain morphologies. Therefore, it was thought that if the percentage of twin boundaries that form at the interface can be increased, bonding across the interface will be stronger. One proposed mechanism for twin boundary formation is the grain boundary dissociation model. The model proposes twin formation by the following mechanism: a high angle grain boundary dissociates into a coherent twin boundary (Σ3), incoherent twin boundary and a low energy boundary in order to reduce overall interfacial energy [169]. The higher the grain boundary angle, the higher the propensity for dissociation is, and the more Σ3 boundaries that are formed. Previous studies in the LPBF of Ni-base superalloys have shown the chess scanning strategy available on the Concept M2 to result in an increase in the number of high angle grain boundaries relative to the simple hatch scan strategy [138]. Discs for surface preparation were produced with both chess and simple scanning strategies. Beam parameters were equivalent for both scan strategies (table 4-9). Discs were placed in a mild steel canister

surrounded by Inconel 718 powder and separated by tantalum foils (figure 4-23). Tantalum forms very stable oxides and consequently does not bond with the powder, making the foils easily visible; this meant they could be used to identify the locations of discs within the powder. Foils were placed at sufficient distance from the discs so as not to influence the oxidation behaviour across the LPBF-HIP interface.

Table 4-9: LPBF parameters used for producing discs for examining the influence of scan strategy and surface finish on bonding across the LPBF-HIP interface.

Laser Power (W)	Scan Speed (mm s^{-1})	Hatch distance (mm)
240	1260	0.057

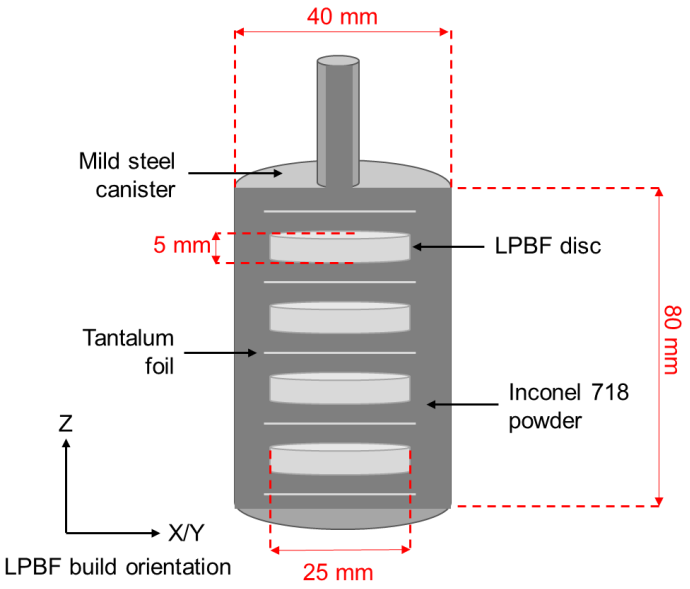

Figure 4-23: Schematic of disc LPBF disc placement in mild steel HIPping canister.

Prior to placing the discs in the HIPping canister surface roughness measurements were performed across the top and bottom surfaces of each disc. Table 4-10 summarises the setting for measurements performed on the Kosaka Laboratory-SE1700 Surface roughness meter.

Table 4-10: SE1700 measurement settings for surface roughness measurements of LPBF samples.

Parameter	Setting
V.mag	1000
H.mag	20
Measurement length	8 mm
Drive speed	0.1 mm s^{-1}
Cutoff Lc	0.25 mm
Filter	None applied
Stylus Radius	2 μm

Following HIPping of the discs in the Inconel 718 powder the canister was cut down it's centre by EDM, to reveal the cross-section of all four discs as illustrated in figure 4-23 line. The half canister was then sectioned in the XY plane at the locations of the tantalum foils. The Z cross-section of each sample was then ground, polished, and etched according to procedures outlined in section 4.8. Examination of the interface between LPBF disc and HIPped powder was performed using both optical BSE SEM.

4.6.3 Tensile testing of the LPBF-PM HIPped interface of in-situ shelling canisters

Two HIPping canister geometries were devised for LPBF to test the tensile strength of the LPBF-PM HIPped interface. The first geometry (figure 4-24-a) was designed to test the tensile strength between the top surface of the LPBF canister base and PM HIPped material. Thee second (figure 4-20-b) was designed to examine the impact of interlocking mechanisms on the strength of bonding between the LPBF canister wall and PM HIPped material (figure 4-25-a). In the initial planning of this work, it was considered that to increase the strength of the bond between the LPBF canister and HIPped powder some form of mechanical interlock could be utilised. This would have involved building in-situ shelling canisters with interlocks such as those seen in figure 4-25-b. During this work however, it became apparent that the continuous oxide formed at the LPBF surface would likely still be the inhiation point for failure; the tensile design in figure 4-24-b is a simple way to test if mechanical interlocking features can overcome the impact of the oxide film and improve the strength at the interface.

Samples constructed for testing of the base bond were built using a simple scan strategy and a combination of simple and chess scan strategies. The base of the combination samples was produced using a chess scan strategy while the walls were formed by a hatch scan strategy; this was done as implementation of the chess scan strategy for small components, i.e., thin walls, tends to create problems with geometrical accuracy such as overbuilding. Canister wall thickness was 0.75 mm with outer diameter of 20 mm and height of 65 mm. Canister size was calculated assuming up to 30% shrinkage of the canister during HIPping based on the likely packing density of the powders. Tensile bars with the same geometry as used for LPBF tensile

tests (figure 4-18) were machined and tensile testing conducted at RT according to ASTM standard E8M.

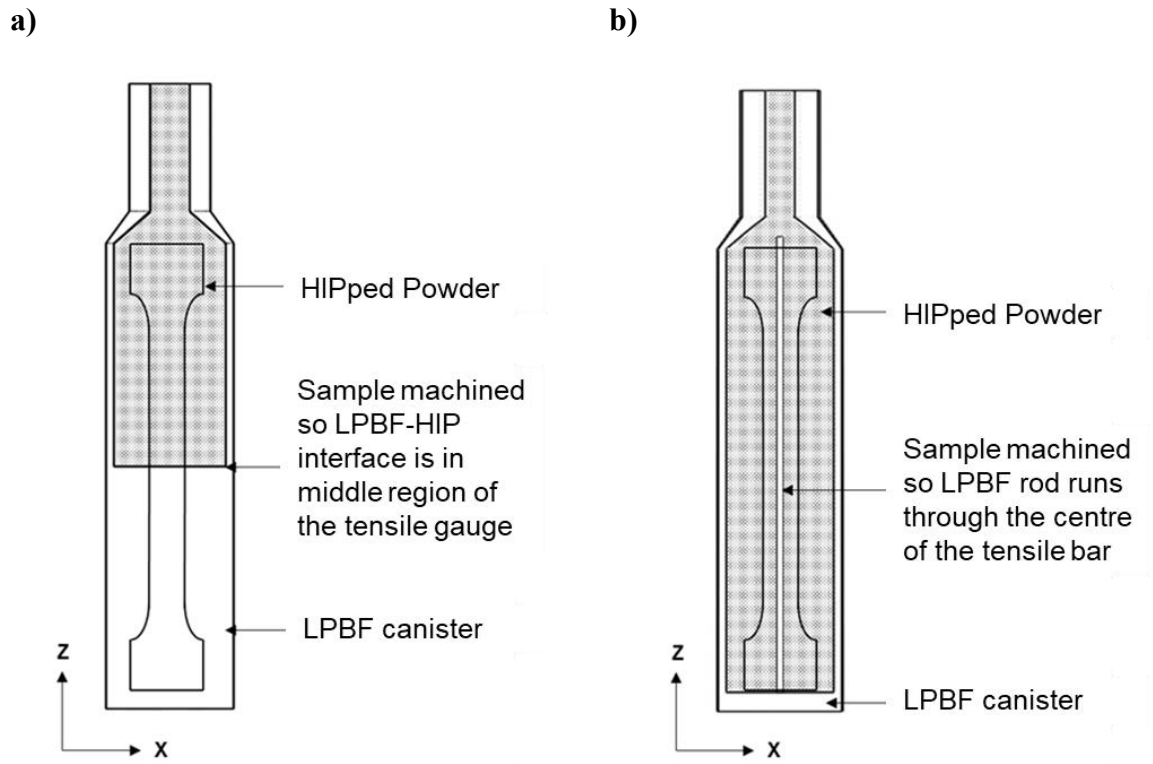

Figure 4-24: Illustrations depicting the XZ cross-sections of HIPping canisters manufactured via the in-situ shelling method: a) canister designed for testing strength of the base interface b) canister designed for testing strength of the side wall interface.

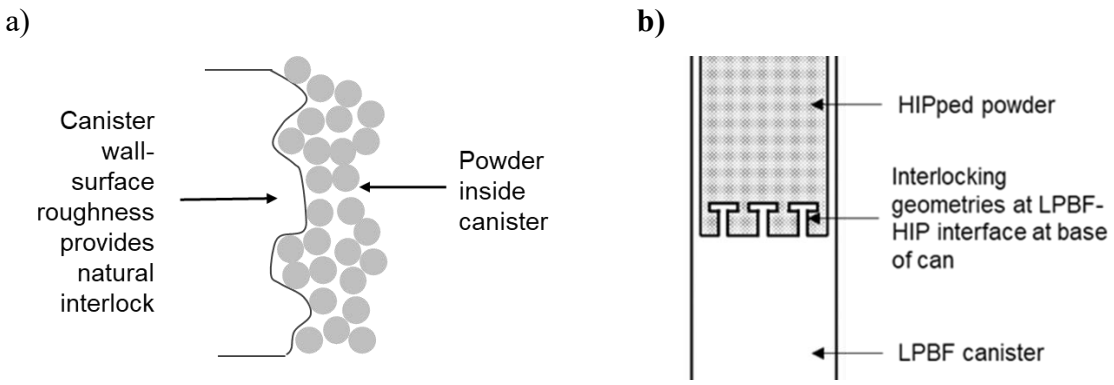

Figure 4-25: Illustrations of interlocking features at the LPBF-PM HIPped interface in in-situ shelling canisters: a) naturally occurring interlock at the canister wall; b) example of interlock that can be produced by LPBF.

i. Influence of surface features on bonding across the LPBF-PM HIPped interface

Tensile testing with the second in-situ shelling canister design showed mechanical interlocking to be unsuccessful in overcoming the impact of the oxide film on failure. Consequently, it was decided that any modification to the LPBF surface should focus on, one, breaking the continuity of oxide film, and two, encouraging recrystallisation of grains, allowing grain growth across the LPBF-HIP interface. During the melting of a single layer in LPBF, oxides may form on the surface of the melt pool during solidification, creating an oxide film across the whole top surface of the part being built. These oxides will be remelted and incorporated into the melt during deposition of consecutive layers. However, the final layer of the build will still exhibit oxide films. Adding surface features whose top surface area are minimal, reduces the maximum theoretical size of continuous oxide films that can be formed. Figure 4-26 shows illustrations of three different geometric features that were chosen for building onto the surfaces of LPBF canisters. Two features, whose surface area graduate

from large to small were chosen in addition to a lattice unit structure. The hemisphere and cone features, having large surface area at the base can cover a significant area of the canister top surface. By graduating from a large to small surface area oxide films present in previous layers can be completely remelted, being replaced by the smaller area of oxide film with each subsequent layer. While the hemisphere and cone structure are similar regarding top surface area, powder packing around each structure will differ resulting in a variation in the quantity of point contacts and different levels of recrystallisation. The lattice structure was chosen as in addition to having small top surface area, it also provides some level of mechanical interlock as powder will be trapped on the underside of the lattice structure.

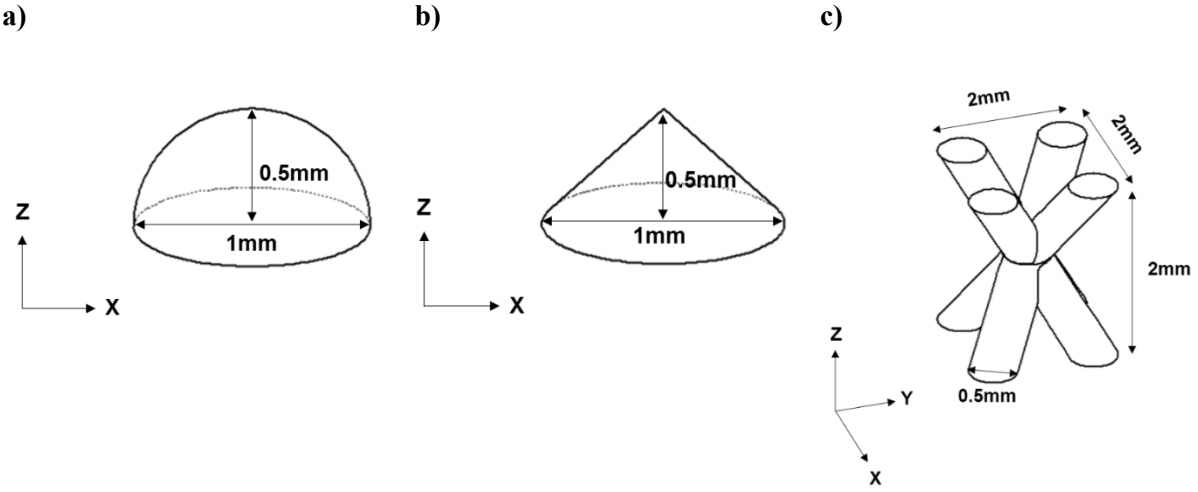

Figure 4-26: Drawings of different geometries added to the internal surfaces of in-situ shelling canisters: a) hemisphere; b) cone; c) lattice unit.

Three in-situ shelling canisters of each tensile design (figure 4-24-a and -b) were produced with each different surface feature geometry shown in figure 4-26. Following HIPping two

out of three canisters were machined for tensile testing according to parameters outlined in section 4.5.2. The remaining in-situ shelling canister was sectioned down the centre line and the region containing the LPBF-HIP interface was cut from the sample (figure 4-27) and ground, polished and etched according to procedures in section 4.8.

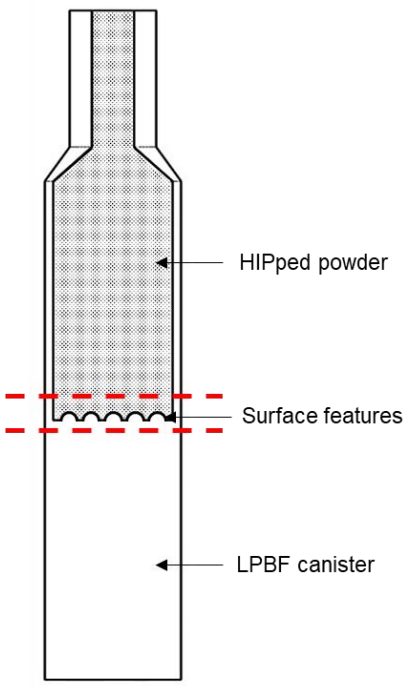

Figure 4-27: Schematic illustrating cuts for cross-sectional observation of the LPBF-HIP interface in complex geometry in-situ shelling canisters produced for tensile testing.

4.7 EPBF

EPBF specimens were produced on an Arcam Q20+ system (figure 4-28) located at the IHI R&D site in Yokohama, Japan. The system was originally designed for production of Ti-6Al-4V components but adapted for Ni-base superalloys. Machine specifications can be

seen in table 4-11. Scanning strategies available are hatch scan (figure 4-14-c) and contour scan (figure 4-29).

a) **b)**

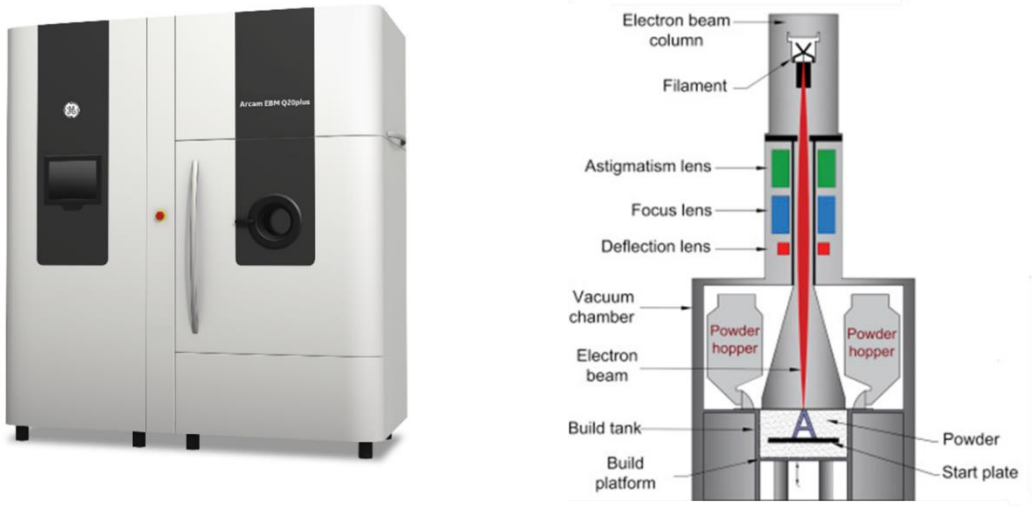

Figure 4-28: a) ARCAM Q20+ system. Taken from [170]. b) Schematic of inside of Arcam Q20+ system. Taken from [99].

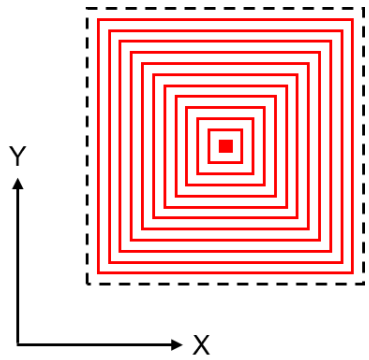

Figure 4-29: Schematic of contour scan strategy. Contours are scanned from the outer surface to the centre of the wall.

Table 4-11: Specifications of the Arcam Q20+ system located in IHI Corporation, Yokohama, Japan.

Beam acceleration voltage (keV)	60
Maximum beam current (mA)	50
Maximum deflection speed (m s^{-1})	8000
Minimum layer thickness (µm)	40
Maximum build height (mm)	380
Build atmosphere (mbar)	4 x 10^{-3} (partial pressure of He)
Recoater type	Flexible stainless-steel rake

4.7.1 Influence of processing parameters on porosity and microstructure

Investigations of process-microstructure relationships in EPBF were performed using similar curved wall structures to those built in LPBF (figure 4-15-a). Due to having limited time for access to the Arcam Q20+ EPBF system, wall height was reduced from 20 mm to 15 mm and samples were only produced in two layer thicknesses, reducing overall build time. Layer thicknesses were 50 µm and 75 µm. The size range of powders utilised for EPBF, necessitates thicker powder layers relative to those used in LPBF. For the build constructed with 50 µm layers, two thicknesses of walls were produced, 1 mm and 2 mm. Only 1 mm walls were produced for the build with 75 µm layers. It was originally intended that a hatch scan strategy similar to that used for LPBF studies should be implemented for EPBF builds, however due to a problem with machine software following an update from Q20 to Q20+, the contour strategy was the only strategy that could be implemented. Table 4-12 summarises the EPBF melt parameters investigated. Parameters were chosen based on an existing set of process conditions developed prior to the machine update from Q20 to Q20+. The contour offset value is equivalent of the hatch distance, with the offset being the distance between the

centre lines of two adjacent contours. The target build temperature was 1000 °C. Preheat and post-heat parameters were undisclosed.

Table 4-12: EPBF processing parameter combinations investigated for fabrication of Inconel 718.

Parameter Set	Beam Current (mA)	Focus Offset (mA)	Scan Speed (mm s^{-1})	Contour Offset (mm)
1	4	24	1260	0.1
2	4	24	600	0.1
3	5	25	1425	0.1
4	7	28	1800	0.2
5	7	28	1800	0.2
6	10	30	3000	0.1
7	10	30	3000	0.3
8	7	27	600	0.3
9	4	24	3000	0.1
10	8	28	500	0.3

Following production, the EPBF walls were sectioned down the centre line to reveal the XZ cross-section followed by cutting half of the sample down the middle line to revel the XY cross-section, as shown in figure 4-30. Specimens were hot mounted in Bakelite and ground and polished according to procedures outlined in section 4.8. Optical images were obtained for the entire XZ cross-section and half of the XY cross-section. BSE SEM imaging was also conducted at the top middle and bottom of XZ cross-sections and at serval points across the top surface of the XY cross-section as indicated in figure 4-30.

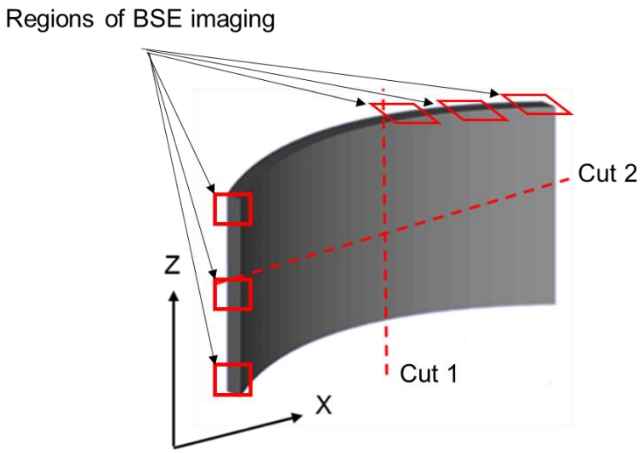

Figure 4-30: Cut up of EPBF for optical and SEM analysis. Regions of BSE SEM imaging are indicated.

4.7.2 In-situ shelling

It was the original intention that in-situ shelling samples of a similar geometry to those produce in LPBF be produced in EPBF. However due to machine instabilities following the machine update as discussed in chapter 7, it was not possible to build gas tight specimens. In light of this, EPBF specimens produced prior to this study were supplied by IHI Corporation for analysis. Parameters used for production of the samples and for HIPping cannot be disclosed. EPBF in-situ shelling samples were provided in three difference wall thicknesses -2, 3 and 5 mm -for microstructural analysis. A 4 mm wall thickness sample was also supplied, however upon inspecting the microstructure of this sample it became obvious that this sample was not Inconel 718 and there had been a mix up in the specimens. Figure 4-31 shows a schematic of the sample and sectioning and locations of microstructural observation by optical and SEM.

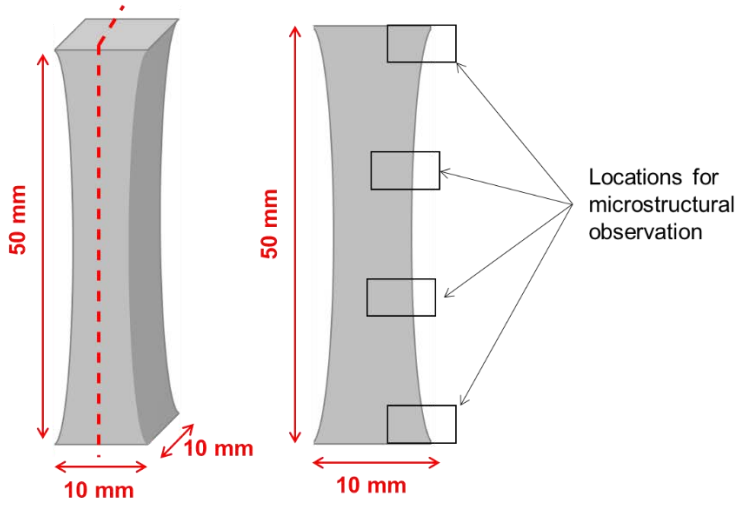

Figure 4-31: Schematic of EPBF in-situ shelling samples provided by IHI Corporation. Optical microscopy and SEM were performed across the EPBF-PM HIPped interface at the top middle and bottom of the sample.

4.8 Metallurgical preparation for microstructural observations

Samples for optical and SEM analysis were cut by wire electro-discharge machining (EDM) and/ or a precision cutting machine fitted with SiC cutting disc. Following cutting samples were either cold mounted in VersoCit-2 Acrylic resin or hot mounted in Bakelite depending on the sample size and method by which the sample was to be observed.

Sample grinding and polishing was performed using the following steps:

1. Piano 120 disc with water as lubricant (5 to 10 minutes).
2. Largo disc with DiaDuo Allegro/Largo 9µm diamond solution (Aprox.5 minutes).
3. Dac disc with DiaDuo 3µm diamond solution (3 to 5 minutes).
4. Nap disc with DiaDuo 1µm diamond solution (3 minutes).
5. Chem disc with a diluted 0.1µm Alumina suspension (5 minutes).
6. Ultrasonic cleaning in soap solution (30 minutes)

Three different etchants were used depending on the microstructural features to be observed. To reveal grain structures samples were submerged in Kalling's reagent 2 (5g $CuCl_2$ + 100 ml HCl + 100 ml ethanol) for up to 30 seconds, checking the sample condition every 5 seconds. If grain structures could not be revealed by Kalling's etch, samples were re-polished and electrolytically etched in a 10 % dilution of Oxalic acid. The mounted samples were submerged in etchant solution alongside a copper plate connected to the negative probe of a benchtop power supply (figure 4-32). The sample was then contacted with a conducting pin connected to the positive probe of the power supply. Etching was performed using 4 volts for 5-10 seconds. For observations of γ' and γ'' samples were electrolytically etched in a 10% dilution of phosphoric acid, using the same parameters that were implemented for Oxalic acid etching.

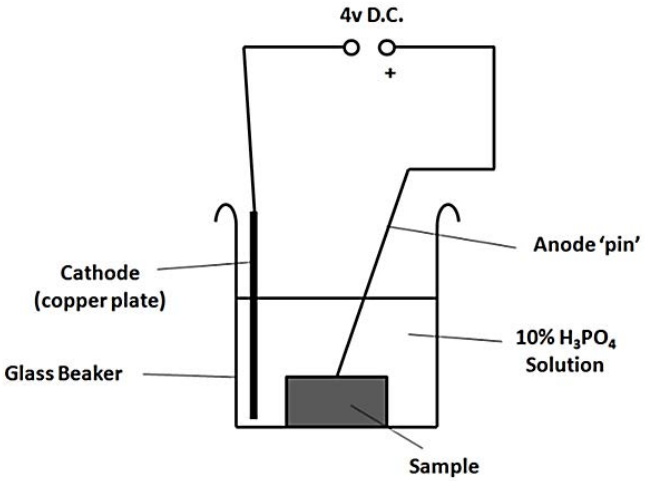

Figure 4-32: Schematic of electrolytic etching process. Taken from [171].

4.9 Microscopy

4.9.1 Optical

Optical microscopy of LPBF specimens was performed on a Zeiss Axioskop 2 optical microscope equipped with monochrome CCD camera and motorised stage. Optical microscopy of EPBF specimens was conducted on a Leica DM 2500 with motorised stage.

4.9.2 SEM

SEM was performed by several microscopes according to the requirements for sample analysis and location of experiments. Table 4-13 summarises microscopes used and for what purpose. Generally, acceleration voltages of between 20 and 25 kV were implemented, with the exception of the Hitachi TM series, which have a maximum acceleration voltage of 15 kV.

Table 4-13: Summary of SEMs used and for what purpose.

SEM	Beam source	Purpose of use
Hitachi TM3000	Tungsten filament	BSE & EDS of large sample mounts
Hitachi TM3030 Plus	Tungsten filament	Fractography
Phillips XL30	LaB_6	SE, EBSD
Jeol 6060	Tungsten filament	BSE, EDS
Jeol 7000	FEG	High magnification imaging, EDS and WDS
Tescan Mira-3	FEG	EBSD
Hitachi SU-70	FEG	Sample analysis performed while at IHI corporation.

4.10 In-situ shelling for complex geometries

Table 4-14 summarises the laser processing parameters implemented for producing impellers by in-situ shelling. As the CAD design of the impeller has been adjusted throughout the study, further methodology relating to this work can be found alongside the results in chapter 9.

Table 4-14: LPBF hatch and contour parameters used for production of in-situ shelling impellers.

Hatch Parameters		
Laser Power (W)	**Scan Speed (mm s^{-1})**	**Hatch distance (mm)**
210	1260	0.057
Contour Parameters		
Laser Power (W)	**Scan Speed (mm s^{-1})**	**Number of contours**
125	2500	2

Chapter 5

Powder Characterisation

5.1 Introduction

For all PM processes, powder can be assessed on the basis of three categories of characteristic; morphology, chemistry and microstructure [172]. The optimum conditions for chemistry and microstructure tend to be independent of process, for example, minimising internal porosity, inclusions and other sources of contamination. Optimal morphology on the other hand can vary significantly from process to process. Chapter 2 highlighted the powder requirements for each PM process studied in this work. PBF processes require powders with good flowability to ensure homogeneous and consistent powder layers. Such powders tend to be spherical in morphology and large in size. While EPBF is capable of melting larger powders and thicker powder layers, LPBF is not as efficient and therefore requires thinner layers and consequently smaller powder particles. It is preferable to use larger powders in PM HIPping as this will minimise PPB formation.

This chapter will examine the suitability of powder chemistries, morphologies and bulk properties for each of the processing routes outlined above. Several characterisation methods have been employed and their advantages and disadvantages will be discussed in the context of the PM process for which powders are being characterised.

Two lots of Inconel 718 powders were produced by plasma atomisation by AP&C Materials and divided into two size ranges, 15-63 μm and 45-106 μm, suitable for processing by LPBF and EPBF respectively. Initially only one lot of powder was supplied, however following this characterisation and initial experiments, it was decided that powder lot 1 may cause some

problems for processability. Initial LPBF and HIPping trials were performed using LPBF powder lot 1, while later LPBF and LPBF in-situ investigations were performed using lot 2. All EPBF experiments used powder lot 1.

5.2 Powder chemistry

Table 5-1 shows the chemistry of Inconel 718 powder lots 1 and 2 as measured by ICP-OES, combustion and fusion analysis. There is little difference in the concentration of major alloying elements between lots 1 and 2 and all are within the acceptable limits of nominal values. Concentrations of some of the minor alloying elements differ between the lots; in particular there are significant differences in Si and B content with lot 1 having over three times as much Si as lot 2, and lot 2 having over four times the B content of lot 1. Carbon concentrations are a little on the high side and could cause problems in regards to PPB formation during HIPping. Trace amounts of V and W can also be observed and are likely present as the result of contamination from the ingot melting process, prior to atomisation.

Table 5-1: Inconel 718 powder chemistry for each powder lot and nominal chemistry for comparison.

	Lot 1	Lot 2	Nominal
Ni	51.41	52.43	52.5
Fe	18.9	19.07	18
Cr	19.57	18.8	19
Nb	5.02	5.09	5
Mo	3.07	2.93	3
Ti	0.93	0.84	0.8
Al	0.53	0.49	0.6
C	0.051	0.043	0.04
Co	0.1	<0.02	<1
Si	0.22	0.06	0.2
Mn	0.05	0.14	0.2
Cu	<0.02	<0.02	0.1
V	0.03	0.04	-
W	0.07	<0.02	-
Ta	<0.02	0.02	<0.5
Mg	0.0001	< 0.0001	-
B	0.0004	0.0017	<0.006
P	0.006	<0.005	<0.015
S	0.004	0.001	<0.015
O	0.022	0.025	-
N	0.02	0.013	-

BSE imaging of the surfaces of powder particles (figure 5-1) showed a number of contrasting phases to be present. Closer examination revealed two precipitate morphologies, one cubic (figure 5-2 (a)) and one spherical (figure 5-2 (b)).

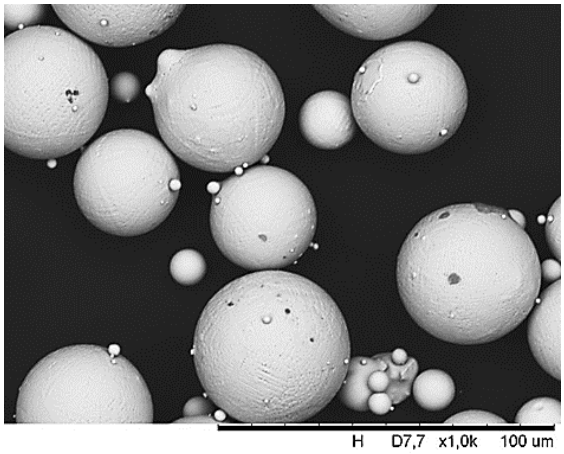

Figure 5-1: BSE micrograph of powder lot 1.

a) **b)**

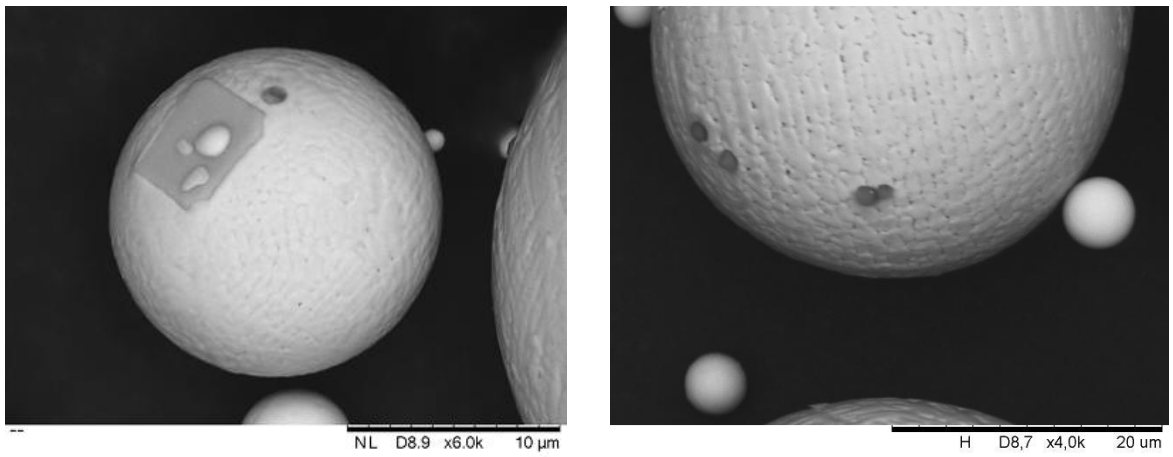

Figure 5-2: BSE micrograph of powder lot 1. a) cubic phase; b) spherical phase

EDS was performed on a number of each of the cubic and spherical phases. Figure 5-3 shows the typical EDS spectrum produced for the cubic phase. The phase was found to be particularly high in Ti; this combined with the morphology of the phase would suggest it is a Ti carbide or carbonitride precipitate. The EDS spectrum for the spherical phase is presented in figure 5-4. The phase is mostly composed of Al and Mg and is likely an oxide precipitate. Other studies have also identified Ti carbides and Al-Mg oxides on the surfaces of plasma atomised Inconel 718 powders [114]. Considering the rapid cooling rates powders undergo

during plasma atomisation it is likely that these oxides had already formed in the wire feedstock material. Mg oxides would likely be inherited by the material during VIM or ESR, in which it is used in refractory lining and slag respectively [173].

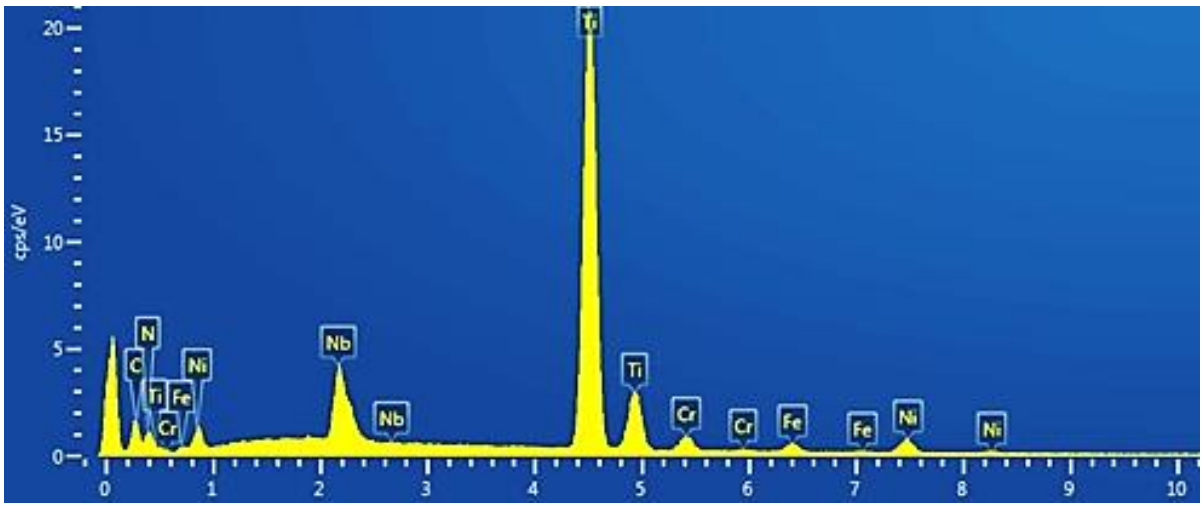

Figure 5-3: EDS spectrum for dark cubic phase observed in figure 5-2 (a).

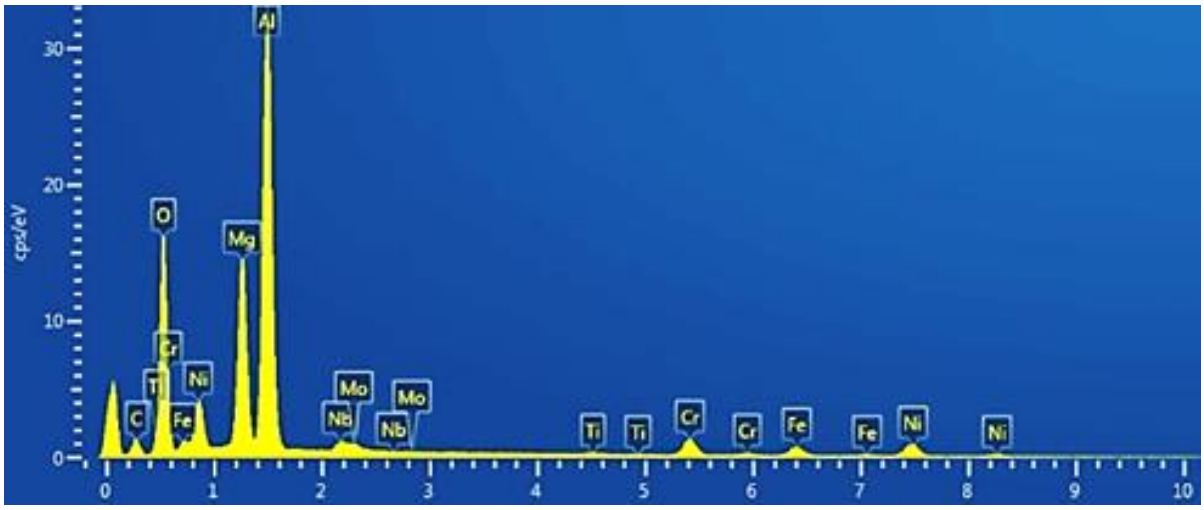

Figure 5-4: EDS spectrum for dark spherical phase observed in figure 5-2 (b).

Following external examination, powders were cross-sectioned and observed internally. BSE imaging (figure 5-5) showed high levels of interdendritic segregation. EDS was performed in

regions of higher and lower segregation, spectrum 1 and 2 respectively. Table 5-2 summarises the results of the EDS, showing the interdendritic segregation to be primarily composed of Nb.

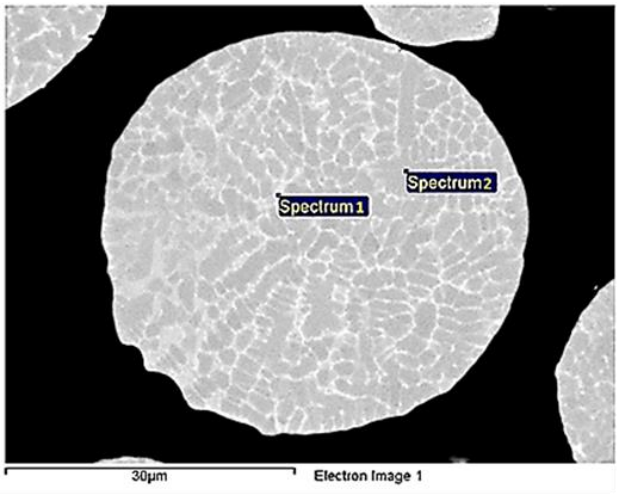

Figure 5-5: BSE image of powder lot 1 cross-section. The locations of two EDS spectrums (table 5-2) are indicated.

Table 5-2: Quantification of elemental segregation as measured by EDS.

Element	Spectrum 1 (wt. %)	Spectrum 2 (wt. %)
Al (K)	0.30	0.32
Ti (K)	1.32	0.67
Cr (K)	17.64	19.12
Fe (K)	16.14	19.44
Ni (K)	46.90	49.76
Nb (L)	8.22	2.73
Mo (L)	3.13	2.57

XRD was performed for powder lot 1, the results of which can be seen in figure 5-6. The peak positions and intensities observed correlate strongly with the γ matrix phase. Peaks for TiC,

Al and Mg oxides observed by EDS were not observed, indicating the quantities of existing precipitation within the powder to be very low.

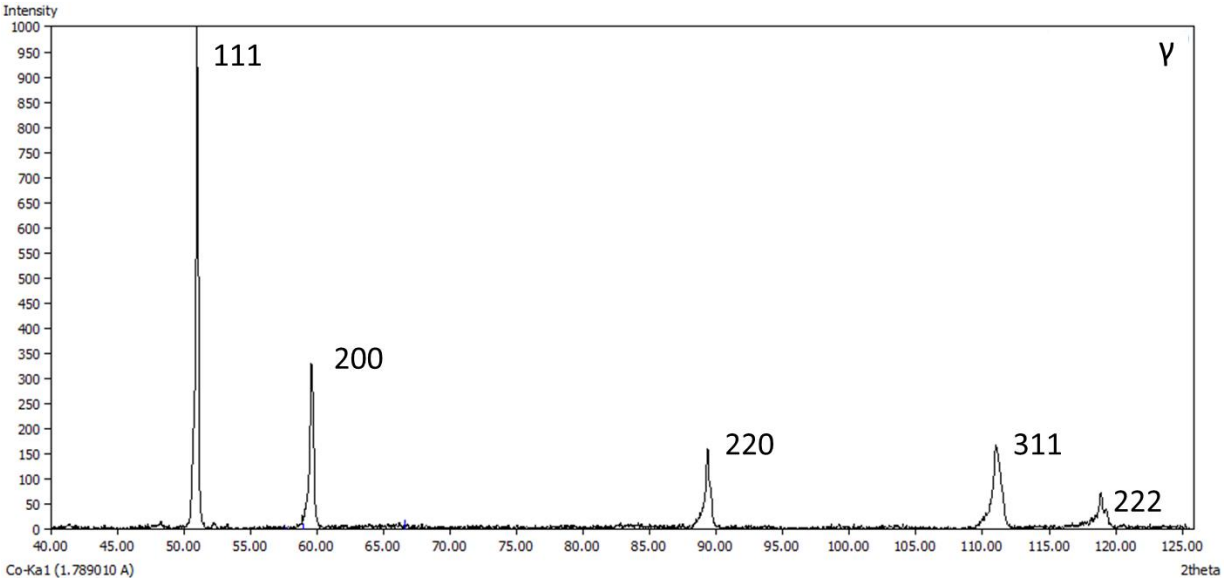

Figure 5-6: XRD spectra for powder lot 1.

5.3 Powder morphology

SE imaging was performed at low and high magnifications to evaluate the size and morphology of powders. Typical images of LPBF powder lots 1 and 2 can be seen in figure 5-7 (a) and (b) respectively. Fine particles were more prominent in powder lot 1 relative to powder lot 2. Both powder lots appear to be spherical, however the occasional irregular powder particle can be observed. Satellites also appear to be a common occurrence throughout both powder lots. Closer inspection of the powder surface revealed dendritic structures in both LPBF powder lots; surface porosity formed by solidification shrinkage can also be observed. Regarding the EPBF powder (figure 5-7 (c)), initial observations suggest powders are close to the specified size range. The particles have the same spheroidicity as LPBF powders and possess a similar quantity of satellites. High magnification imaging

(figure 5-7 (f)) reveals dendritic structures, coarser than those in the LPBF powders. This is to be expected as larger powders should cool more slowly allowing time for coarsening of solidification structures. Surface porosity appears to be less than in the LPBF powder range, which again can be linked to the difference in cooling rate; slower cooling rates should minimise liquid trapping between dendrites, reducing solidification shrinkage.

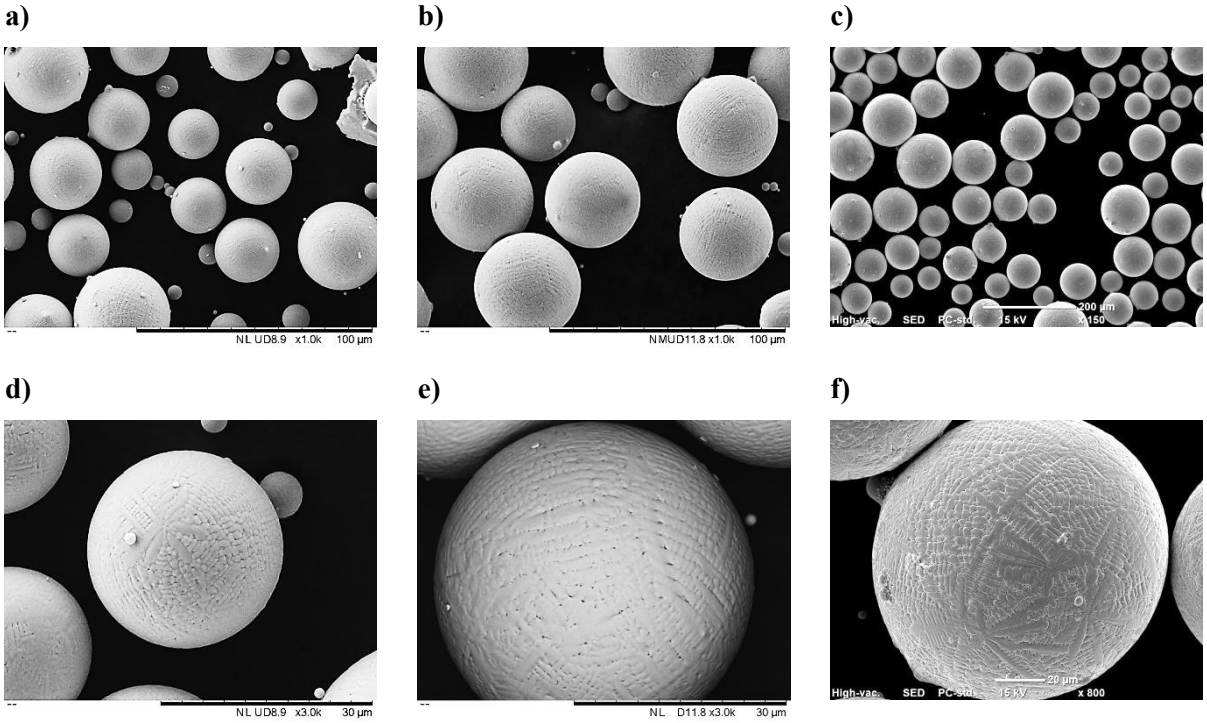

Figure 5-7: SE images of three different IN718 powders. a) & d) LPBF Lot 1; b) & e) LPBF lot 2; c) & f) EPBF.

Several low magnification SEM images were used to quantify the diameters of LPBF and EPBF powders. Details of image processing and measurement can be found in chapter 3. Table 5-3 shows the distribution of particle diameter size, as well as D10, D50 and D90 values, for each powder lot/specification. Specified size ranges for LPBF and EPBF processes are indicated by the shaded cells. As can be seen form the table, for both LPBF and EPBF specifications, there are powders that fall outside of specification; typically due to being

smaller. Particles with diameters smaller than 15 μm for the EPBF powders make up less than 5 % of total measured powders, thus it is likely that these small powders are in fact satellites that have broken off from larger particles. For both LPBF powder lots however, the percentage of particles less than 15 μm is very high, and cannot be wholly attributed to satellites. While both lots still possess large quantities of fine powder, there is some improvement from lot 1 to lot 2, with lot 2 possessing a lower percentage of particles with less than 15 μm diameter, as well as having a higher D50 value.

Table 5-3: Number standard size distribution obtained from SEM images of different powders lots and size ranges. The size ranges recommended by machine manufacturers for LPBF and EPBF are highlighted in grey.

	Number standard distribution (%)		
Size Range (µm)	**LPBF Lot 1**	**LPBF Lot 2**	**EPBF Lot 1**
X ≤ 15	55.05	39.38	2.35
15 < X ≤ 30	33.94	27.49	0
30 < X ≤ 45	11.01	32.19	2.35
45 < X ≤ 60	-	0.94	35.29
60< X ≤ 75	-	-	21.18
75< X ≤ 90	-	-	21.18
90< X ≤ 106	-	-	10.59
106 < X ≤ 120	-	-	7.06
D10 (µm)	3.64	1.37	47.17
D50 (µm)	13.27	22.16	65.96
D90 (µm)	30.19	38.86	98.85

Figure 5-8 (a) and (b) summarise the results of three LPSD measurements for LPBF powder lots 1 and 2. LPSD was not performed for EPBF powders as LPSD equipment was not available at the site of the EBPF machine. LPSD data for LPBF powder lot 1 (figure5-8 (a)) shows two peaks, one around 34 µm particle diameter and one at 87.5 µm (it should be noted

that this is the maximum diameter that can be measured with the implemented lens). The presence of a secondary peak in LPSD is a common indicator of powder agglomeration, which suggests the powder contains high quantities of fine powder; this would be concurrent with the powders observed by SEM. LPBF power lot 2 (figure 5-8 (b)) on the other hand does not exhibit any secondary peak, indicating a reduction in the number of fine powders from lot 1 to lot 2. Again this is in line with what is observed in SEM.

a)

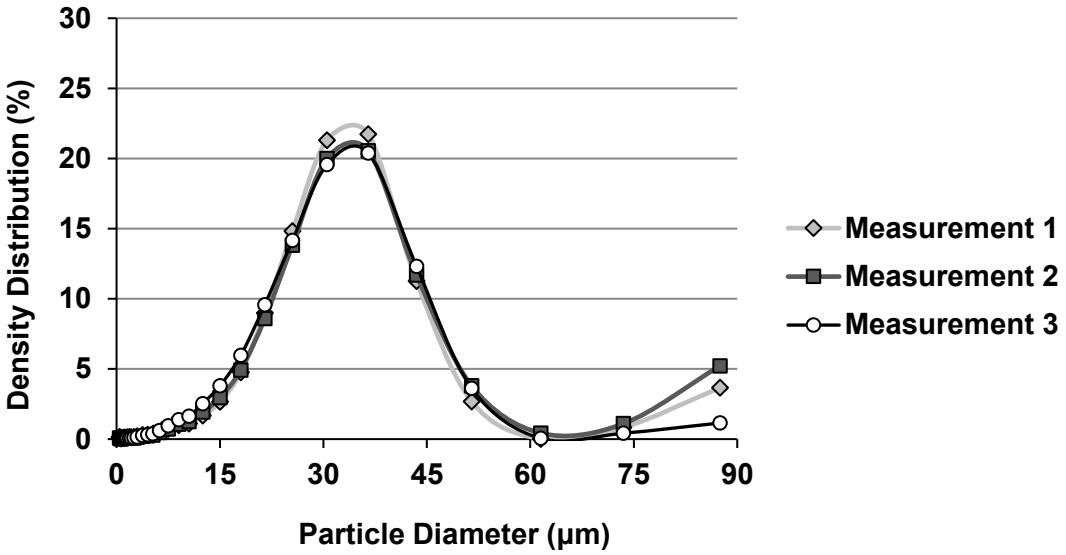

D10 = 14.42; D50 = 28.11; D90 = 42.40

b)

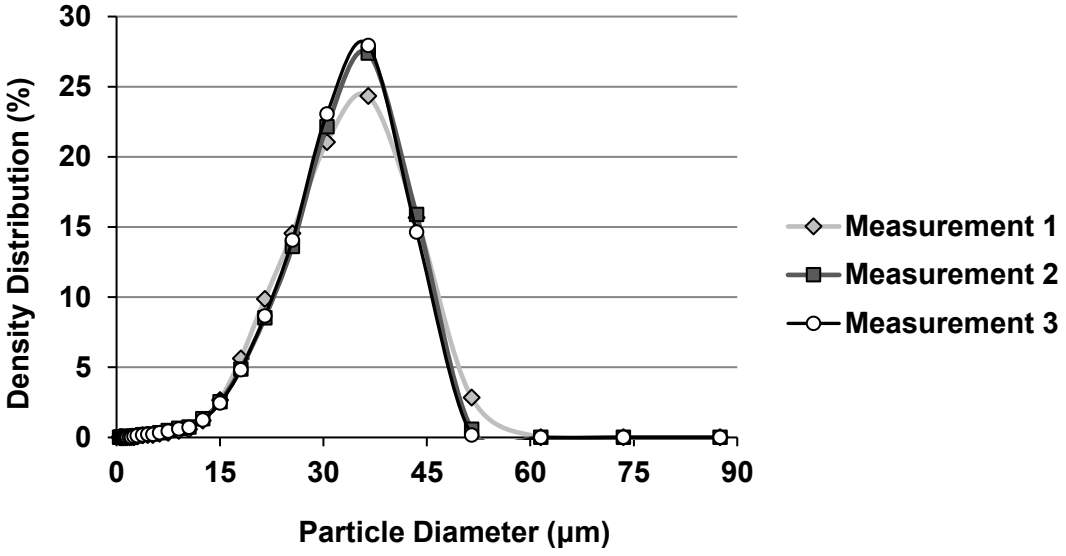

D10 = 17.01; D50 = 28.95; D90 = 39.48

Figure 5-8: Distribution of powder particle size as measured by LPSD. a) LPBF Lot 1; b) LPBF Lot 2. The average D values (in µm) for all three measurements are presented at the bottom of each graph.

Table 5-4 summarises the powder size distributions measured by LPSD in volume and number standard percent, as well as the number standard distribution measured by SEM. Volume standard distribution gives the percentage of powder particles of a specified size based on their volume; for example, for two particles, one of diameter 10 μm and one of diameter 1 μm, the percentage of powder particles with 1 μm diameter is 0.1% and those with 10 μm diameter 99.9%. In the case of number standard distribution however, each particle would account for 50% of the total particles. Hence by using volume standard distributions, it is not always possible to have a true idea of the number of fine particles, and thus the behaviour of the powder may be different from expected.

For the number standard distributions measured by LPSD and SEM, a reduction in fine powders from lot 1 to lot 2 can be observed for both measurement methods; however the actual numbers differ significantly. Discrepancies in the numbers could be accounted for by the difference in sample size between each method; for the LPSD the number of powder particles measured is most likely in the thousands, however for the SEM measurements, the total number of particles measured is in the low hundreds.

Table 5-4: Particle size distribution measured by LPSD presented as volume standard distribution and number standard distribution. Number standard distribution measured by SEM is included for comparison.

	Volume standard distribution LPSD (%)		Number standard distribution LPSD (%)		Number standard distribution SEM (%)	
Size Range (μm)	**LPBF Lot 1**	**LPBF Lot 2**	**LPBF Lot 1**	**LPBF Lot 2**	**LPBF Lot 1**	**LPBF Lot 2**
X ≤ 15	10.89	6.58	44.46	24.33	55.05	39.38
15 < X ≤ 30	48.81	50.28	41.75	62.52	33.94	27.49
30 < X ≤ 45	32.65	41.95	13.39	13.15	11.01	32.19
45 < X ≤ 60	3.53	1.19	0.4	-	-	0.94
60< X ≤ 75	0.79	-	-	-	-	-
75< X ≤ 90	3.73	-	-	-	-	-

5.4 Powder flowability

5.4.1 Schulze ring shear test

Figures 5-9 (a) and (b) show the Mohr's stress circle and yield loci results of the Schulze ring shear test for powders lots 1 and 2 in the LPBF size range. The differences in flow behaviour of each powder are clear when comparing the Mohr's stress circles for the unconfined yield stress. The stress circle for powder lot 2 is approximately half the size of the powder lot 1, resulting in an FFC value more than two times the value of powder lot 1. While the FFC value of powder lot 1 is less than 10 (the threshold value for free flowing powder), it is not significantly less and therefore this powder would still be expected to flow under the right processing conditions. The differences observed in FFC value are concurrent with the quantity of fine powder particles, as with a higher ratio of fine particles, powder flowability should be reduced.

a)

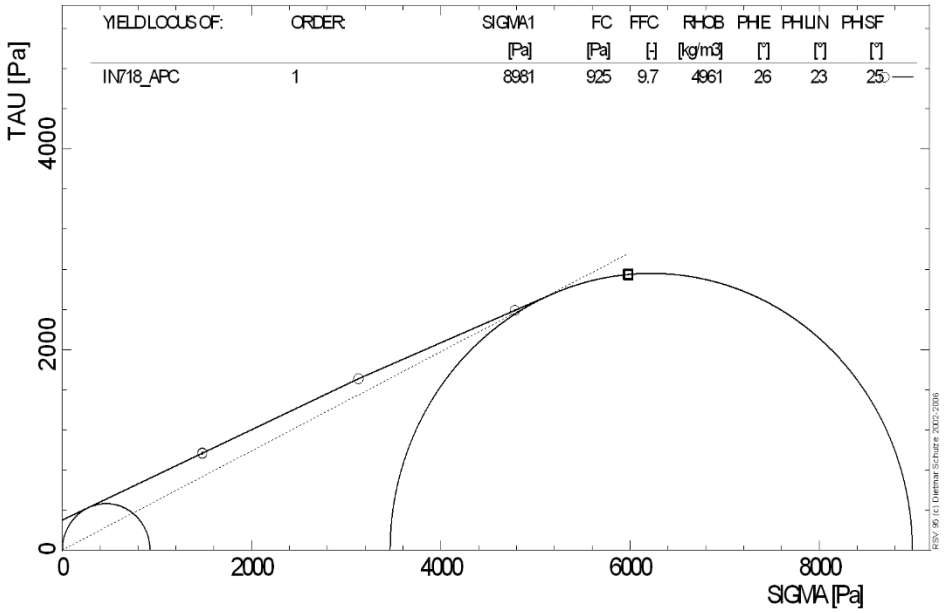

b)

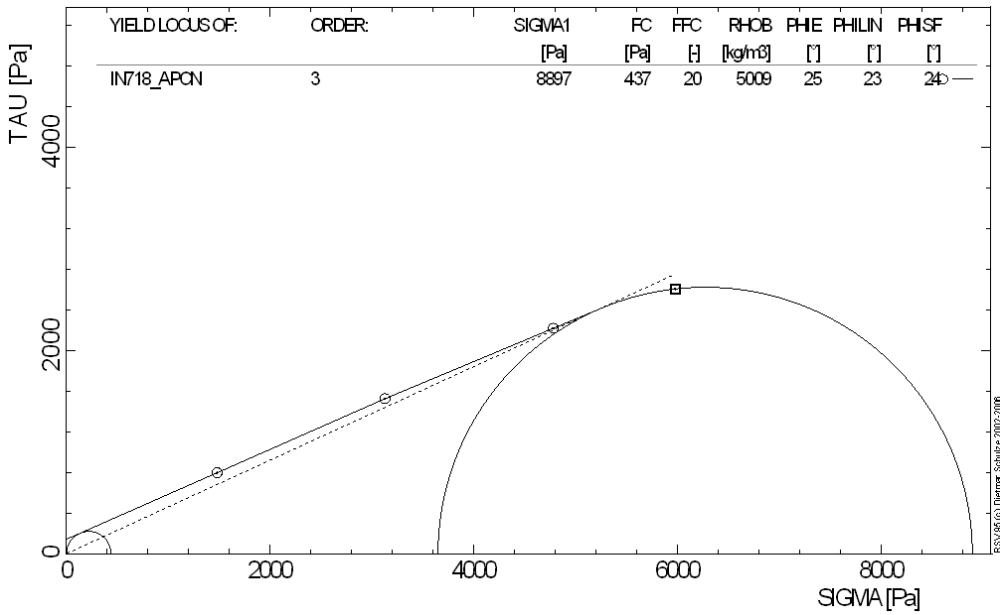

Figure 5-9: Yield locus and Schulze ring shear data for, a) LPBF powder lot 1 and b) LPBF powder lot 2.

5.4.2 Flow energy measurements

Results of flow energy measurements performed for EPBF powder can be seen in figure 5-10. As with Hall flow, measurements are relative and without a second sample to compare the powders to, little information can be interpreted. Nguyen et al. [174] performed flow energy and shear tests for Inconel 718 powders using an FT4 rheometer. The powder size range and corresponding test results can be observed in table 5-5. Flow energy measurements are primarily concerned with the energy required to achieve repeatable patterns of flow under different loading conditions; generally the lower the energy the better the flowability of the powder. Comparing the results of this study with those of Nguyen et al. it appears as though for the majority of measurements, energy values are lower for the EPBF powders measured here compared to those reported by Nguyen et al. for their LPBF powders. Assuming the FFC value follows a similar trend, it would be expected that if shear measurements were to be performed for EPBF powders, the FFC would exceed a value of 15.

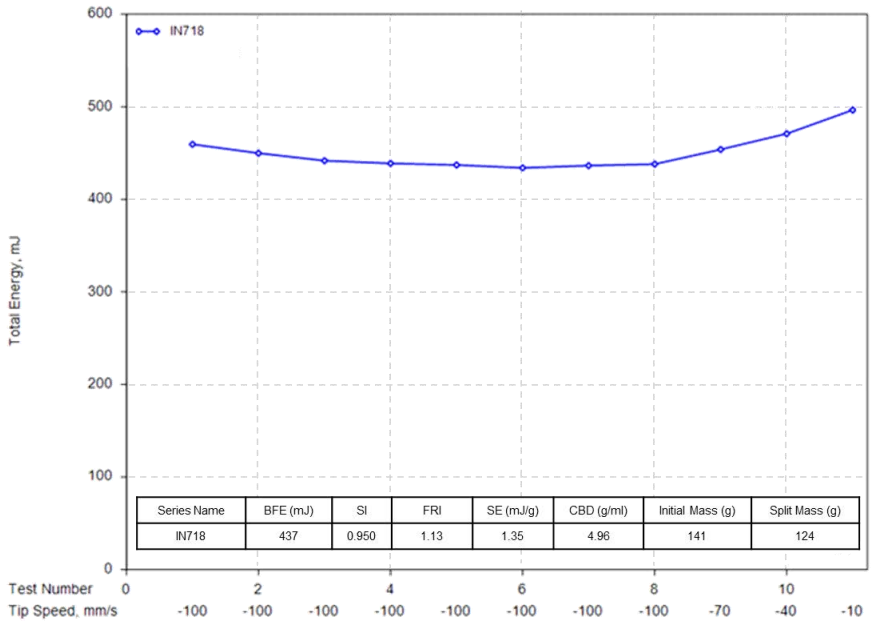

Figure 5-10: Results of flow energy measurements performed using FT4 powder rheometer for EPBF powders.

Table 5-5: Particle size values and corresponding flow energy and shear test measurements for Inconel 718, performed by Nguyen et al. [174].

D10 (µm)	D50 (µm)	D90 (µm)	BFE (mJ)	SI	FRI	SE (mJ/mg)	CBD (g/ml)	FFC
21.37	31.24	49.52	1032	1.03	1.09	3.32	4.63	15.1

5.4.3 Hall flow, apparent and tap density

Results of Hall flow measurement and apparent and tap density measurements are summarised in table 5-6. There are no reported results for Hall flow of the LPBF powder lots, as this powder kept sticking in the orifice of the Hall flowmeter. Typically, when this happens, a Carney flowmeter, with a larger orifice should be used to perform the test, but this equipment was not available. The sticking of powder to the orifice, while an indication of

poor flowability, does not discount the powder as suitable for PBF, as the mechanisms of flow differ significantly between the measurement technique and processing technique. The EPBF powder lot flowed freely through the Hall flowmeter orifice, indicating improved flowability relative to the LPBF powder lot.

Hausner ratios calculated from apparent and tap density measurements were basically equivalent for all three powders, and less than 1.25 indicating good flowability. Given that EPBF and LPBF powder lots have significantly different size distributions, it might be expected that the tap density would differ more between the two. Discrepancies in the measurements may be the result of differences in measurement method. LPBF measurements were calculated using a constant volume and measuring changes in powder weight, whereas EPBF measurements were performed with a constant powder weight and measurement of variation in powder volume. The powder size distribution, Schulze ring shear tests and differences in powder behaviour during Hall flow appear to be in better agreement relative to apparent and tap density measurements and may prove to be a better indication of flowability during processing.

Table 5.6: Results of Hall flow test and apparent and tap density measurements for LPBF and EPBF powder lots.

	Apparent Density		Tap Density		Hausner Ratio	Hall Flow (s/50g)
	g/cm^3	Relative to solid (%)	g/cm^3	Relative to solid (%)		
LPBF Lot 1	4.59	55.82	5.00	60.88	1.09	n/a
LPBF Lot 2	4.31	52.49	4.75	57.76	1.10	n/a
EBPF Lot 1	4.77	58.03	5.23	63.63	1.10	12.58

5.5 Implications of powder characteristics for HIPping and PBF processes

5.5.1 Chemistry

Carbon and oxygen concentrations and the presence of existing carbide and oxide precipitates at the powder surfaces create favourable conditions for PPB formation, which could cause problems not only for bonding between powder particles in HIPping but also for bonding between powder and the HIPping canister wall during the in-situ shelling process.

Niobium segregation within the powder should not be a cause of concern during HIPping, as the high temperature and applied stress create favourable conditions for the diffusion of Nb, which occurs by vacancy exchange [175, 176]. Conditions during PBF however are less favourable with large thermal gradients likely to lead to increased levels of segregation and formation of eutectic γ-laves [177].

5.5.2 Flowability

In PBF processes powder flow properties play an important role in the ability to spread a consistent layer of powder across the build plate. The spherical morphology of powder particles seen here is very beneficial for the flow properties, however the quantity of fine powders observed in both LPBF and EBPF powders is concerning. Significant differences were observed in the flowability of LPBF lots 1 and 2 when measured by Schulze ring shear testing; this can be attributed to LPBF powder lot 1 having both a smaller average particle size and a wider ranging particle size distribution [158, 178]. Powder shear test data has been shown to correlate reasonably well with powder flowability in AM processing [178, 179]. Comparisons of flow measurement techniques and observed flow behaviour during binder-jet processing of 316L powders, showed specific energy values generated by flow energy

measurements, and FFC values produced by shear measurements, to correlate best with flow behaviour during processing [179]. This holds well for the EPBF powder measurements, for which an FFC value of greater than 15 is predicted based on a comparison with flow energy measurements performed for Inconel 718 LPBF powders[174].

Further flow measurements were not as conclusive in their results as the Schulze ring shear test. Hall flowmeter measurements could not be successfully completed for LPBF powder size ranges, though this is not unusual. In a review of powder characterisation, Vock et al. [178] suggest most LPBF powders would not reach the flowability limits necessary for successful completion of the Hall flowmeter test; yet they also state that this does not limit the powders use for AM processes. It was concluded that Hall flow measurements may still be suitable for ranking of powders for the EPBF process, though without another powder to compare the data to the measurement is somewhat irrelevant.

5.5.3 Packing density

Shrinkage is more uniform in PM HIPping when powder packing density is higher, as with increasing packing densities the distribution of voids become more homogeneous [52]. The particle geometry most suited to packing in differing geometries and capable of achieving the highest packing densities is a sphere [180]. Packing densities are also improved by having a wide powder particle size distribution. Comparison of the two LPSD plots produced for LPBF powders lots 1 and 2 (figure 5.8 (a) & (b)) shows minor differences in powder size distribution with powder lot 2 having a slightly wider range. According to the powder size measurements performed by SEM the EPBF powders have a much wider distribution than the LPBF making them more suited for higher packing densities. This is also represented by the tap density data, with tap densities for EPBF powders being several percent higher than those

for LPBF powders. Consequently, it would be expected that shrinkage is more uniform in in-situ shelling samples produced with EPBF relative to those made with LPBF.

High packing densities are also beneficial to the PBF processes as with higher packing densities heat distribution within the powder bed is more homogeneous [105]. Lower packing densities have been shown to encourage the formation of unstable keyhole welding conditions resulting in the formation of keyhole porosity [115, 181]. It would therefore be expected that for the same energy input conditions, parts produced with EPBF powders would have fewer instances of keyhole porosity relative to those produced with LPBF powders.

5.6 Summary

No significant differences in chemistry could be observed between powder lots and size distributions. High oxygen and carbon contents make PPB formation favourable, and it is expected to be prominent in both LPBF and EPBF powders; yet, it should be somewhat reduced for EPBF due to their larger average particle size.

Resulting from differences in available characterisation facilities for LPBF and EPBF powders, few direct comparisons could be made regarding the flowability of each powder size range. Nevertheless, given the well-established relations between particle morphology and size and flowability, it is expected that EPBF powders will have superior flow relative to LPBF powders.

Powder packing density was shown to be higher in EPBF powders. Consequently, shrinkage of canisters produced by in-situ shelling with EPBF is expected to be less, and more homogeneous, compared to parts produced with LPBF. In addition, EPBF process stability is

expected to be superior to LPBF, resulting in the formation of fewer defects for a given energy input.

Chapter 6

Powder Metallurgy Hot Isostatic Pressing

6.1 Introduction

The primary focus of this study is to provide proof of concept for the in-situ shelling processes by successfully bonding Inconel 718 powder to PBF Inconel 718 shells by utilising the HIPping process. There are many variables effecting the bond strength, however most important is the fraction of grain growth across the PBF-PM HIPped interface. There are two routes by which grain growth across the boundary may be impeded: firstly by the formation of oxides at the surface of Inconel 718 PBF shells and secondly by the formation of PPBs in the PM HIPped Inconel 718.

This chapter starts by examining the chemistry and microstructure of Inconel 718 powders HIPped in a mild steel canister. The powders used in this study were Lot 1 PSR 15-63 μm. Results of the powder characterisation indicated PPB formation was likely to be prominent in these powders, due to relatively high oxygen and carbon content as well as the precipitation of existing Al/ Mg oxides and TiC. In addition, these powders had significantly higher quantities of fine particles reducing the length of the diffusion path for the formation of surface precipitates. Proceeding microstructural examination, room temperature tensile testing was carried out. This was performed primarily to provide a comparison for later tensile testing of the PBF-PM HIPping bond.

6.2 Oxygen content of PM HIPped material

Oxygen concentration in the PM HIPped sample was measured using fusion analysis. Prior to HIPping the powder contained 220 ppm of oxygen, however after HIPping oxygen concentrations had increased to 339 ppm. A small increase in oxygen is to be expected as oxygen and/ or moisture can be picked up during filling of the powders into the canister, even in the strictly controlled environment of an inert gas glovebox. While the increase in oxygen concentration appears small, even little changes can make a difference to the PPB formation. MacDonald et al.[74] found a difference of just 45 ppm to increase the quantity of PPBs observed in CM247LC. Consequently, an increase of 119 ppm would be expected to significantly effect PPB formation.

6.3 Influence of the diffusion zone on microstructure

Figure 6-1 shows a low magnification BSE micrograph of the HIPped Inconel 718 powder and the mild steel canister. The diffusion zone is approximately 250 μm in depth. Figure 6-2-a and -b show slightly higher magnification BSE micrographs of the PM HIPped powder in the diffusion zone and centre of the canister. The diffusion of carbon from the canister appears to be significant, given the quantity of carbides precipitated in this region. EDS mapping was performed in the diffusion zone (figure 6-3) and showed the majority of precipitates to be high in Nb indicating them to be NbC carbides. The formation of NbC carbides is favourable due to the interdendritic segregation of Nb observed in the powders and the temperatures at which HIPping was conducted; above the γ', γ'' and δ solvus but below the temperature for onset of dissolution of MC type carbides.

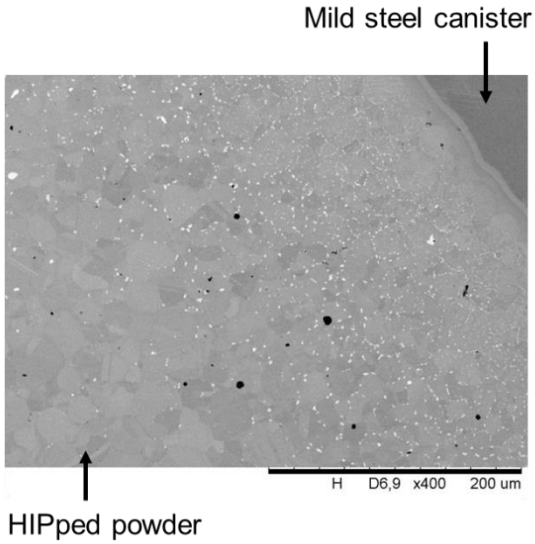

Figure 6-1: BSE micrograph showing the diffusion zone in the HIPped Inconel 718 powder. Mild steel canister is pictured in the top right corner.

a) **b)**

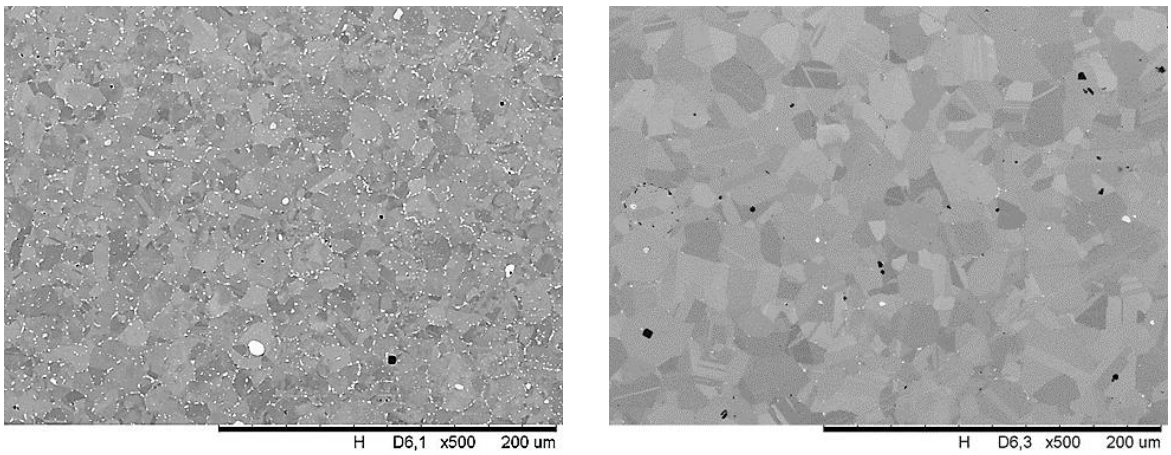

Figure 6-2: BSE micrographs of PM HIPped Inconel 718 in two locations. a) near the canister wall in the diffusion zone; b) in the canister centre.

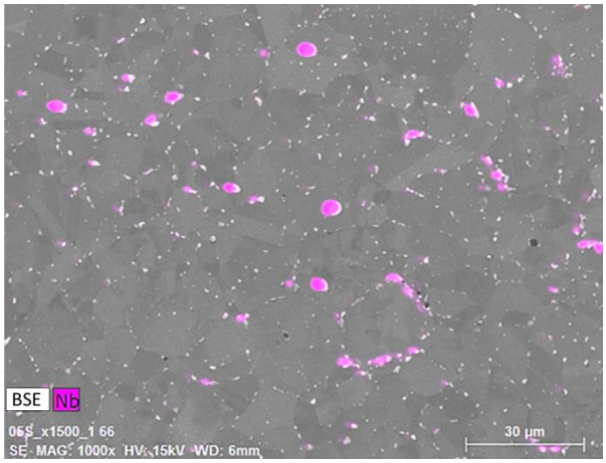

Figure 6-3: BSE micrograph showing carbide precipitation in PM HIPped Inconel 718 and overlaying EDS map for Nb.

The influence of the diffusion zone is not often discussed in the literature as it is generally accepted that it is removed along with the canister, to prevent heterogeneity in the material and consequently mechanical properties. However, present research suggests the diffusion zone may have a significant effect on the remaining material. NbC precipitates don't only appear to be in excess in the diffusion zone, but quantities appear to be less than expected in the remainder of the HIPped material. This is likely the result of the precipitation of NbC in the diffusion zone creating a concentration gradient for Nb, drawing Nb from the material at the center of the canister. A reduction in Nb at the centre of the canister may be detrimental to mechanical properties, as without adequate concentrations of Nb, sufficient volume fractions of strengthening phases such as γ'' cannot be precipitated.

6.4 PPBs

While PPBs are more prevalent in the diffusion zone, due to the increase in carbide precipitation, they can still be observed in the microstructure at the canister centre, where carbide precipitation is substantially less. Figure 6-4 shows a higher magnification

micrograph of the powder microstructure at the centre of the HIPping canister. A small quantity of finer NbC carbides can be seen along the PPBs though a higher fraction is seen intragranularly. Some NbC precipitates have maintained their positions after grain growth has occurred beyond their associated PPBs. PPBs at the centre of the canister are primarily marked by the fine precipitation of a darker contrasting phase suspected to be Al_2O_3. The precipitation of Al_2O_3 at PPBs is commonly reported for Inconel 718 as powders are generally HIPped at temperatures above the γ', γ'' and δ solvus and consequently above temperatures at which Cr_2O_3 is no longer stable. WDS and EDS line mapping were used to analyse the chemistry across several PPBs that did not show significant precipitation of NbC carbides. Many PPBs were too small to resolve any chemical differences however some PPBs composed of larger precipitates could be resolved. Figure 6-5 shows the typical outcome of these measurements. Strong peaks were produced both for oxygen and Al, providing further evidence of the precipitation of Al_2O_3.

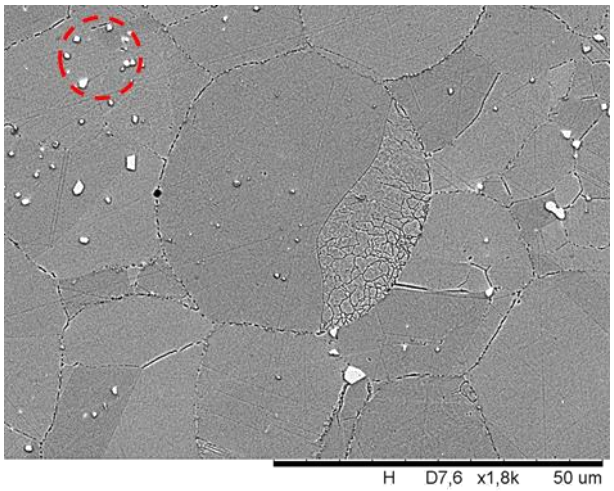

Figure 6-4: High magnification BSE micrograph showing precipitation at PPBs outside of the diffusion zone. The red dashed circle indicates a region where PPB precipitates have remained following grain growth outside of their PPB. Sample was electrolytically etched in 10% Oxalic acid solution.

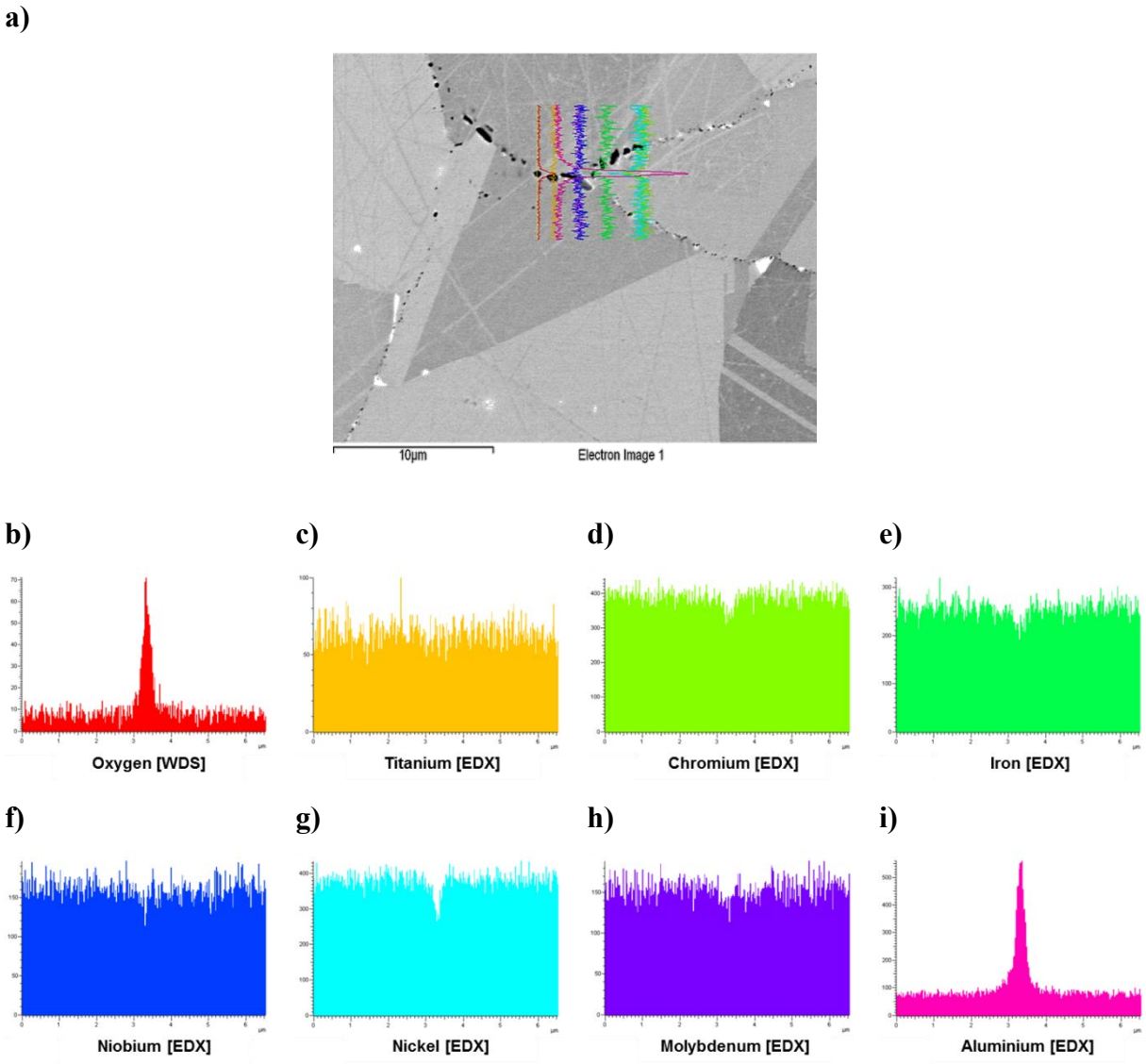

Figure 6-5: WDS and EDS line maps across a PPB in the centre of the HIPped powder: a) BSE SEM image with line maps overlaying; b) to i) corresponding WDS and EDS spectra.

Compared to other studies PM HIPping Inconel 718 under similar HIPping conditions[92, 93] PPBs were more prevalent in the current study. Both Chang et al.[92] and Yao et al.[93] show almost no PPBs to be present in Inconel 718 HIPped in the temperature range of 1180°C to 1200°C. Neither study however reports the oxygen content of the powder. Studies by

Rao et al.[90] on the other hand show similar quantities of PPBs as is observed here; the average size and oxygen content of Inconel 718 powder being 50 μm and 275 ppm respectively. Most of the literature suggested smaller powder particle sizes, irrespective of oxygen content, to lead to increased levels of recrystallisation and consequently reduce PPB formation; therefore, it would be expected that LPBF powders, in the size range of 15-63 μm, would result in a reduction in PPBs, however that is not the case seen here. Studies by MacDonald et al.[74] showed oxygen content to have the greater impact on PPB formation in CM247LC, with smaller powder particle size only enhancing the properties of HIPped powders with already low oxygen content.

Considering the relationship between powder particle size and PPB formation in other materials -Al, Ti, Steel -it may be concluded that whether oxygen or powder particle size has the dominant effect on PPB formation is dependent on the type of oxide formed at the powder surface. Studies of PM HIPped Al showed PPBs for all powder size ranges[75] however studies in 316L steel[76] showed a dependence of PPBs on particle size range and studies of Ti-6Al-4V[77] showed no PPBs to be present for any of the tested powder size ranges. 316L steel is a Cr oxide former and Ti-6Al-4V favours the formation of Ti oxides. In HIP studies of Ni-base superalloys in which Al oxide was the favoured oxide composition, PPBs were always observed, irrespective of powder particle size[54, 70, 74]; however in studies Ni-base superalloys favouring Cr oxides, PPBs were less effected by oxygen content and more dependent on powder particle size[72]. Considering the stability of each of these oxides, it may be concluded that the influence of powder particle size on PPB formation is dependent on the stability of the composition of the oxide that is favoured. For the most stable oxide, Al, PPBs will be more closely linked to the oxygen content of the powders, however for less stable oxides, Cr and Ti, PPBs will be more dependent on characteristics such as particle size.

6.5 Additional phases and precipitation

6.5.1 Carbides and oxides

In addition to the precipitation of NbC carbides and Al_2O_3, Ti-Nb carbides/ carbonitrides can also be observed. Figure 6-6 shows a typical BSE micrograph of the multi-metal carbide/ carbonitride and the accompanying EDS spectra. The precipitates are similar in size to those observed on the powder surfaces in chapter 5, suggesting they may have been inherited from the powder. This is plausible as the temperature for onset of dissolution of MC type carbides and carbonitrides in Inconel 718 is approximately 1220°C [182]; 40°C higher than the HIPping temperature used in the present study. Several smaller Ti rich precipitates, suspected to have formed during HIPping can also be observed (figure 6-7). They are oxy-carbonitrides with Al-Mg oxide rich cores surrounded by Ti-Nb carbonitrides. The oxide core acts as a nucleation site for the nitride which in turn acts as a nucleation site for the carbide [173]. Precipitation of Ti nitrides occurs in the liquid state in Inconel 718 [183]; as HIPping is a solid state diffusion process, the oxy-carbonitride precipitates must result as the consequence of nucleation of an MC type carbide from a oxy-nitride inherited from the powder.

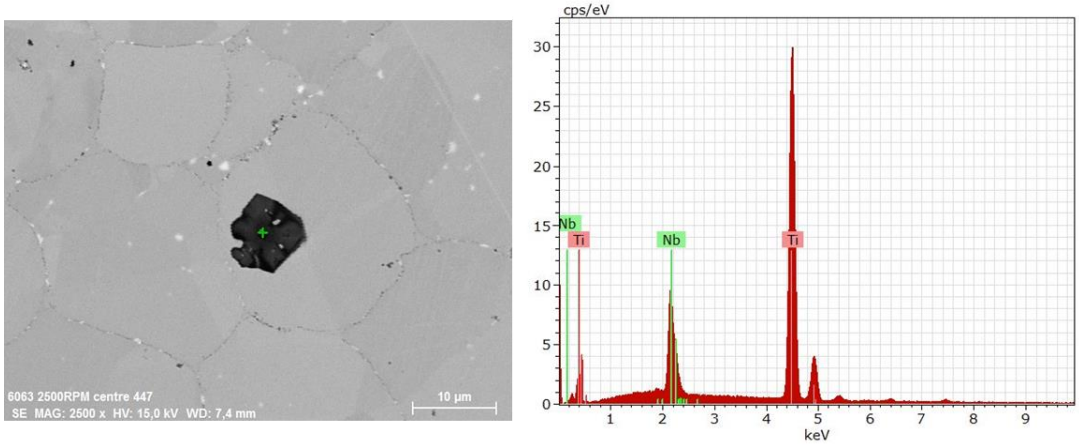

Figure 6-6: BSE micrograph of multi-metal carbide and accompanying EDS spectra.

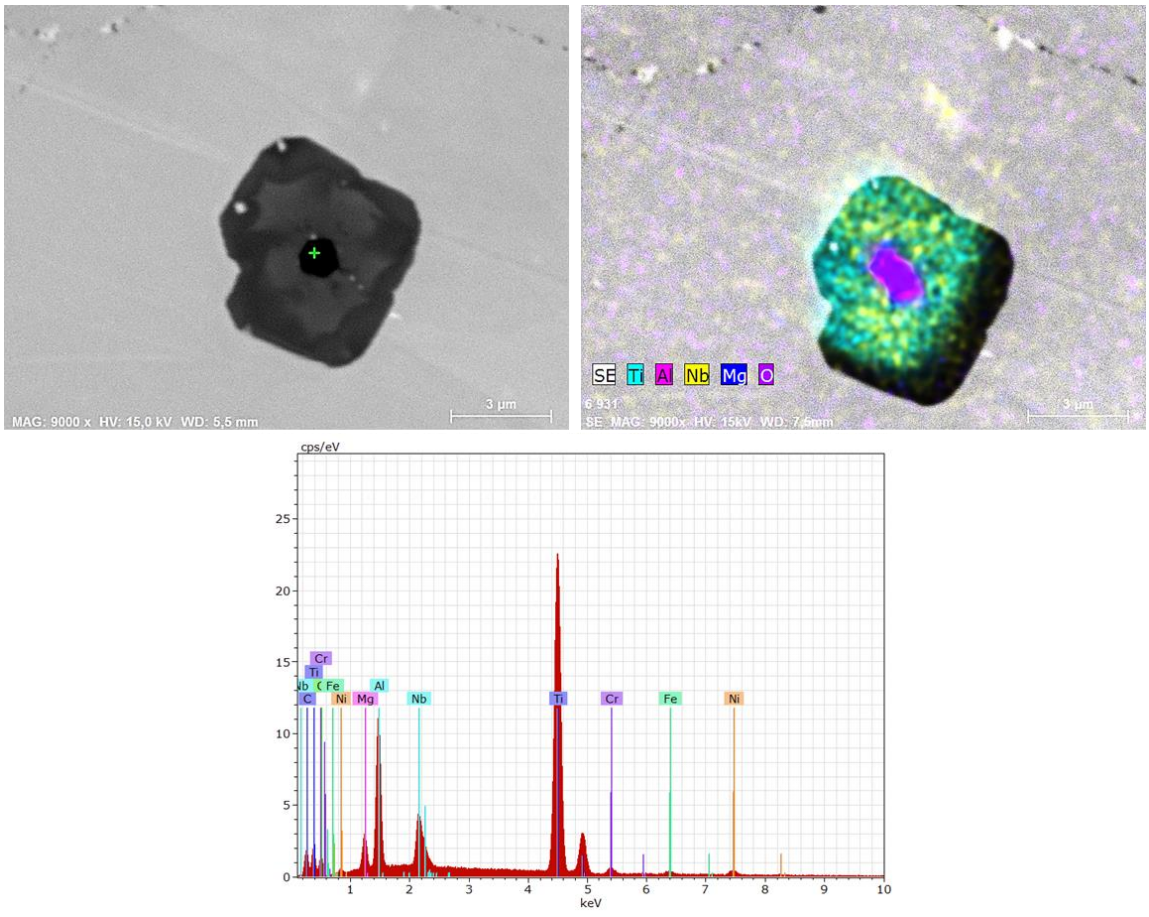

Figure 6-7: BSE micrograph of multi-metal oxy-carbide and accompanying EDS spectra.

6.5.2 GCP phases -γ', γ'' & δ

The precipitation of γ', γ'' and δ is commonly reported in the PM HIPping of Inconel 718. For powders HIPped under similar conditions to this study, both γ' and γ'' have been reported as having diameters in the tens of nanometres and consequently can only be observed by TEM. The expected size of δ precipitates is expected to be small and hence may be difficult to discern from fine discrete NbC carbides by SEM, particularly when distributed along the grain boundary. As it was not within the scope of this work to perform TEM studies, phase analysis was performed using XRD (figure 6-8). Comparing the powder XRD with XRD performed on the HIPped powder, an increase in peak width and intensity can be seen at the peaks corresponding to the γ {200}, {220} and {311} planes. These peak positions closely neighbour those of peaks corresponding to the same set of planes in the γ'. An increase in intensity of the second XRD peak may also result from precipitation of γ'' and δ. A second peak corresponding to the δ {232} plane can also be seen emerging from the peak corresponding to the γ/γ' {311} plane. Finally, an additional peak appears to be emerging between two theta values of 70° and 75°, this would correspond to {220} plane of the MC carbide.

a)

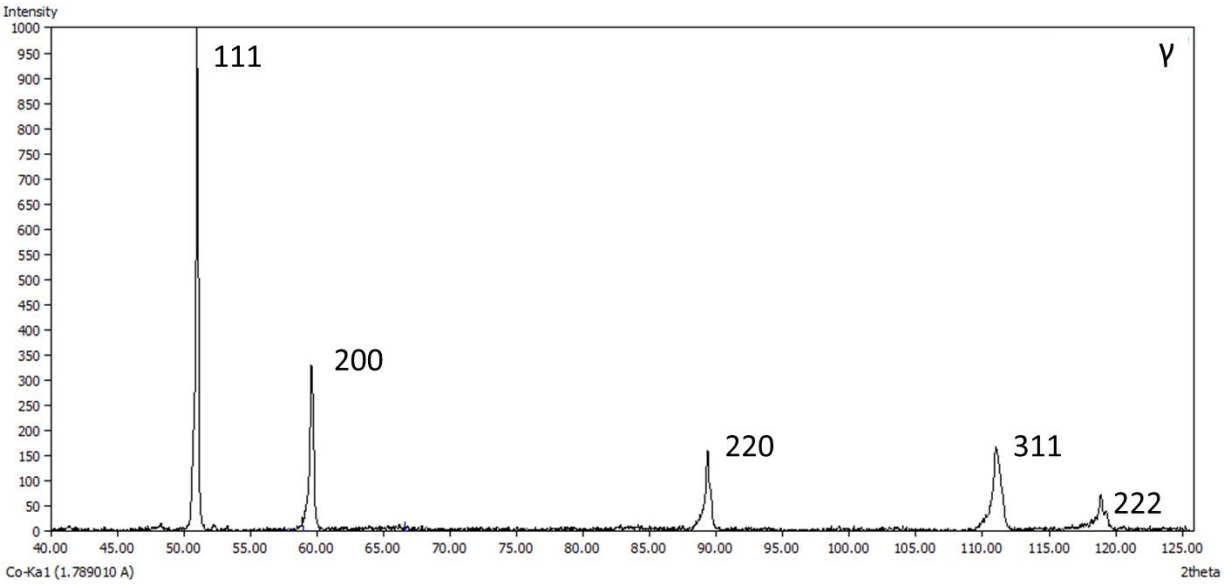

b)

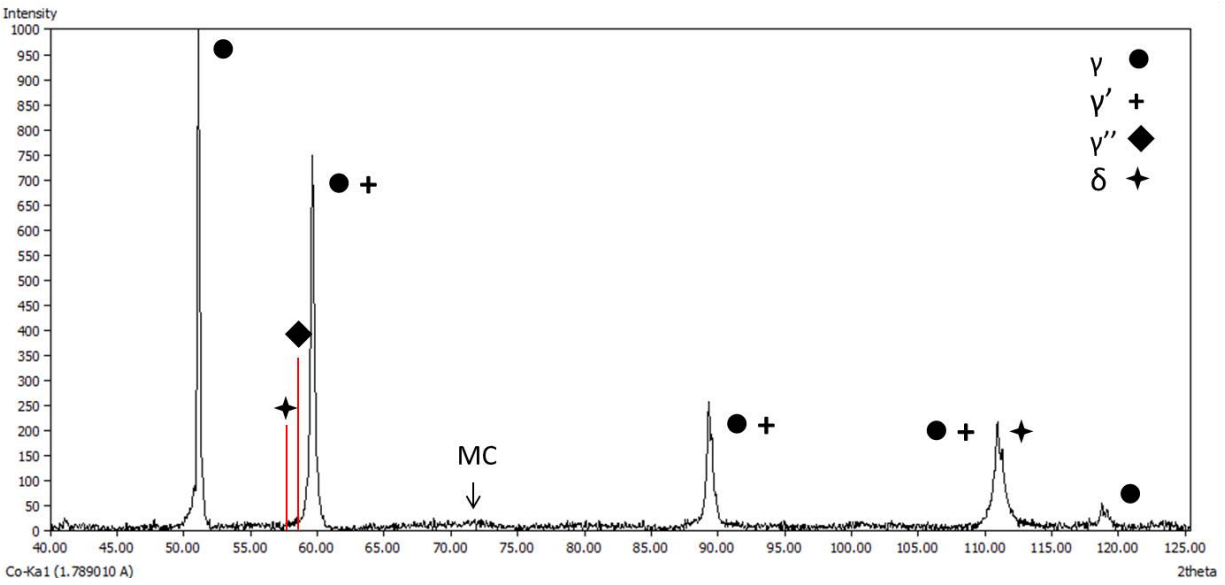

Figure 6-8: XRD spectra for a) Inconel 718 powder and b) PM HIPped Inconel 718.

6.6 Grain Morphology

Grain size and morphology were examined by EBSD in two locations within the canister- the top and middle. Figure 6-9-a shows the EBSD map for the top of the sample and figure 6-9-b the map for the middle of the sample. A significant difference in grain size and

morphology can be observed for the two locations, with a higher quantity of large grains observed in the middle of the sample relative to the top. Grains are mostly irregular in shape; however multiple straight grains can also be observed in the middle sample. This straight grain morphology is indicative of the formation of Σ3 CSL boundaries, so called twin boundaries. As discussed in chapter 2, due to the deformation and high temperatures experienced by powders, twin boundaries are a common occurrence in PM HIPped Ni-base superalloys. Table 6-1 summarises grain measurement data for each sample location. The higher quantity of twin boundaries in the powder HIPped in the middle of the sample would suggest they underwent somewhat higher degrees of deformation.

a) **b)**

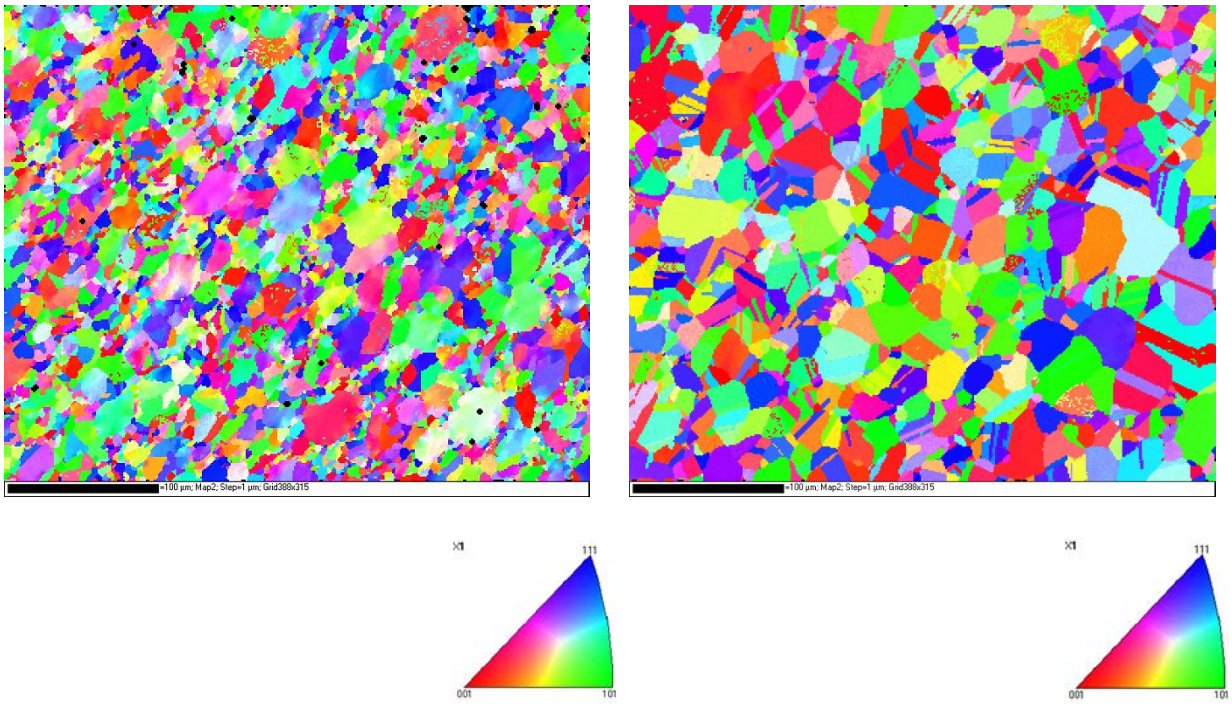

Figure 6-9: EBSD maps with IPF colouring for HIPped powder: a) top of the HIP can; b) middle of the HIP can.

Table 6-1: Grain data taken from EBSD analysis of two HIPped powder samples.

	Top (figure 6-8-a)	Middle (figure 6-8-b)
Number of grains	3139	931
Min grain dia. (µm)	1.13	1.51
Max grain dia. (µm)	36.58	79.43
Ave. grain dia. (µm)	7.04	12.93
Σ3 CSL grain boundaries (%)	5.7	23.3

EBSD was also performed for the powder cross-sections (figure 6-10) in an effort to quantify grain size for comparison with the two HIPped powder samples. The average grain size of the powder particles was found to be 6.61 µm, similar to that of the HIPped powder sample taken from the top of the HIPping canister. This would suggest that recrystallisation and grain growth was limited in the top of the canister relative to the middle.

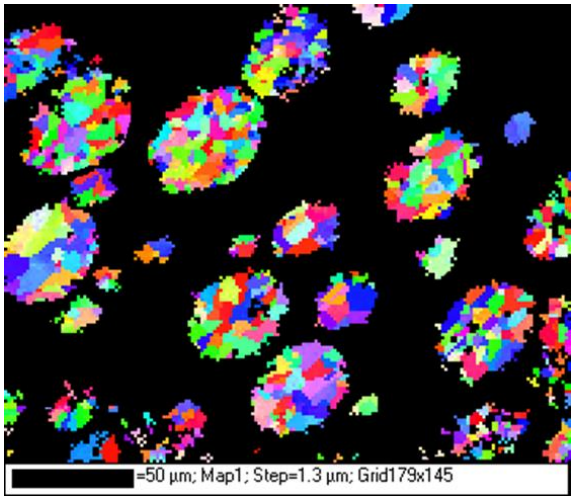

Figure 6-10: EBSD of powder lot 1. Average grain dia. 6.61 µm

Given the size of HIPping canister and dwell time it can be assumed that differences in recrystallisation do not result from temperature differences across the canister. Consequently the variation must stem from a localised difference in chemistry or stress state. Several studies have examined the influence of powder particle size on the microstructure of PM HIPped Ni-base superalloys [74, 82, 92]. Chang et al.[184] and Bartos et al. [82] found recrystallisation to be greater in smaller powder particles. This was attributed to the increased contact area of fine particles relative to coarse particles. The overall stress applied to each powder particle is the sum of the stresses at each contact point on the particle; as finer particles have a greater number of contacts, the overall stress is higher resulting in an increased degree of deformation, relative to the larger powder particles. It would be logical to assume a difference in powder particle size between the top and middle of the canister, as separation of particles according to size can occur during vibration of the HIPping canister at the filing stage. Subjecting the canister to vibration or tapping for a prolonged amount of time can cause larger powder particles to come to the top of the canister, in a phenomenon known as the Brazil nut effect [185]. In order to discern any differences in powder particles size, the diameters of a number of PPBs were measured in each of the samples. The average diameter of PPBs in the HIPped powder from the top of the canister was 33.79 μm and the diameter of those from the middle of the canister 38.15 μm. Such a small discrepancy is unlikely to be the cause of the differences in grain morphology observed, and consequently it is more likely to be attributed to a variation in chemistry. In the PM HIPping of CM247LC, MacDonald et al. [74] observed a reduction in the levels of recrystallisation in fine powders relative to coarse, which was ascribed to the increased Oxygen content of the finer particles. They suggested deformation of smaller powders was limited due to an increase in PPB networks resulting from the higher oxygen content. Similar work in Inconel 718 came to the same conclusion [70]. In the present

study however, the oxygen content of the powders is equivalent and the number of PPBs does not seem to differ significantly between samples. Furthermore, twin boundaries can be observed inside PPBs suggesting PPBs do not impede the migration of grain boundaries and resulting recrystallisation inside the powder. A number of fine precipitates can be observed in the EBSD map of the sample taken from the top of the canister; likely fine NbC carbides or Al oxides. Chang et al. [92] found recrystallisation to be limited in larger Inconel 718 powder particles HIPped at lower temperatures. This was thought to be the result of an increased number of precipitates within the sample, inherited from the powders. It was suggested that Inconel 718 behaves in a similar way to micro alloyed steels, in which intragranular NbC precipitates have been shown to impede static recrystallisation during isothermal holding. Given the increased presence of precipitates in the top sample, it is feasible to conclude differences in grain morphology and recrystallisation result from a random difference in precipitation. However, it should be noted that powder particle size may still have some influence on recrystallisation, as estimating powder diameter by PPB diameter measurement may not be the most appropriate method, and powder size differences may be more significant than reported.

6.7 Tensile testing

RT tensile testing of as-HIPped samples was performed to quantify the influence of PPBs and provide a set of tensile data to compare with tests later carried across the PBF-PM HIPped interface of in-situ shelling samples. Tensile specimen geometries and testing parameters can be found in chapter 4.

Figure 6-11 shows the yield strength, UTS and elongation values measured for the as-HIPped samples. Also shown are values reported in the literature for Inconel 718 powders HIPped under similar conditions. HIPping conditions of both studies are summarised in table 6-2.

Table 6-2: HIPping conditions reported for production of PM Inconel 718 samples for tensile testing from the two studies whose results are shown in figure 6-10.

Study	Temperature (°C)	Pressure (MPa)	Dwell time (Hrs)
Rao et al. [90]	1200	120	3
Yao et al. [93]	1200	Undisclosed	3

a)

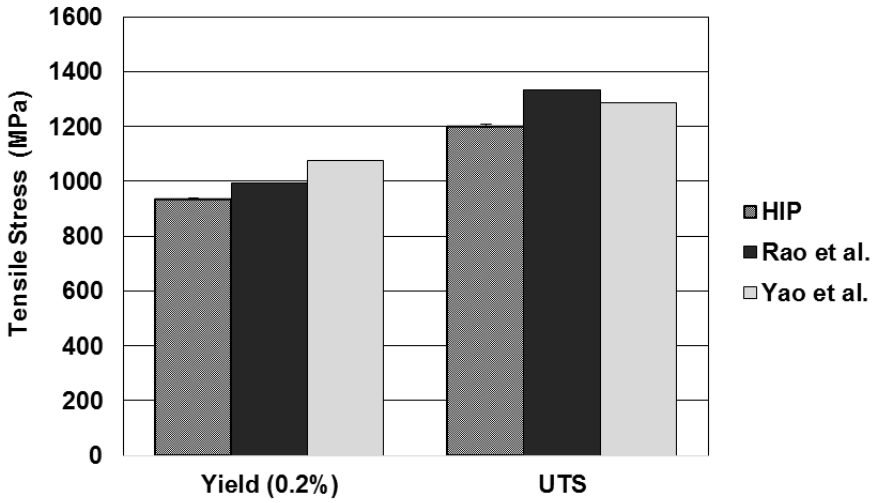

b)

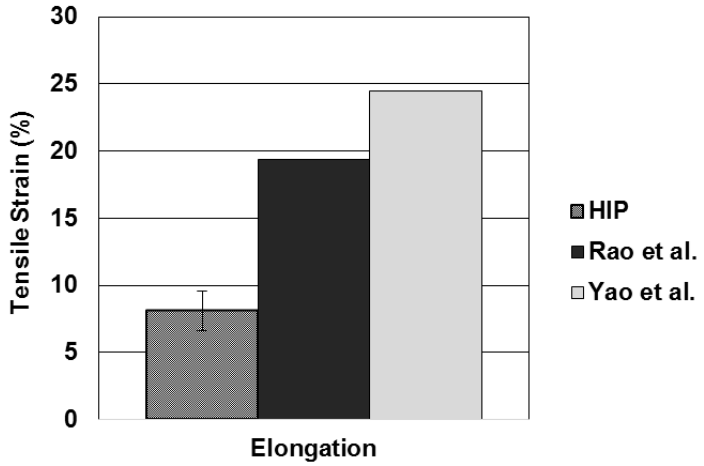

Figure 6-11: Comparison of RT tensile test results for as-HIPped samples with values from literature. a) yield and UTS; b) elongation.

Yield and UTS were consistent for both HIP samples with maximum values of 940 MPa and 1209 MPa respectively. Increased variation however was observed in regard to elongation, with minimum and maximum values of 6.6 and 9.6 % respectively. Discrepancies in elongation may result from a variation in the quantity of PPBs in each tensile specimen. One tensile specimen was produced from material cut from the centre of the HIPped powder and

the other between the centre and diffusion zone. Observations of microstructures in section 6.3 suggested a concentration gradient of Nb formed between the PM HIPped material at the centre of the canister and that at the edge, owing to the large quantities of NbC carbide precipitation in the diffusion zone. Consequently, graduating quantities of NbC carbides precipitating at PPBs may have also occurred, creating local differences in ductility.

Tensile values are significantly less than those reported in the literature. This is likely to be the result of several things: a difference in, HIP canister material, HIPping temperature, powder characteristics and tensile test conditions. Firstly, it should be noted that the strain rate implemented by Yao et al. for tensile testing was half that used by the present study and Rao et al. and consequently would result in a significant increase in elongation. Secondly, samples in the current study were HIPped at 1180°C whereas those HIPped in the two comparative studies were HIPped at 1200 °C. Even small differences in HIPping temperature, such as that seen here, have been shown to significantly influence the yield strength and elongation of as-HIPped Inconel 718 samples. In elevated temperature tensile testing, changing the HIPping temperature from 1180°C to 1210°C increased the yield strength by approximately 180 MPa and elongation by 5% [92]. This appeared to be the result of a significant increase in grain recrystallisation at the higher temperatures. Several differences can also be observed in the powder characteristics between studies. Table 6-3 summarises the differences in the carbon and oxygen content of the powders. Oxygen content was not disclosed in the study of Yao et al. however PREP powders were used for HIPping and it is therefore likely that oxygen content was equivalent or less than that measured for the present study.

Table 6-3: Carbon and oxygen content of powders used in this study and those of the studies of Rao et al. [90]and Yao et al. [93].

	Carbon (Wt. %)	Oxygen (Wt. %)
The present study	0.051	0.022
Rao et al.	0.03	0.027
Yao et al.	0.02	Undisclosed

The trend in carbon content observed between the present study and two comparative studies follows the trend of the elongation measurements: with increasing carbon content resulting in a reduction in yield strength and elongation. In addition to the carbon content of the virgin powders the carbon concentrations in HIPping canister should also be considered. This study used mild steel canisters for HIPping, while Rao et al. used stainless steel canisters. Yao et al. did not disclose canister material. Stainless steel canisters have been shown to prevent the formation of a diffusion zone owing to both their low carbon content and higher quantities of alloying elements[54]. As discussed throughout this chapter the formation of diffusion zone may significantly influence PPB formation and availability of Nb for precipitation of strengthening phases. Specimens produced by Rao et al. showed significant quantities of γ" precipitates and specimens produced by Yao et al. contained greater quantities of discrete δ at grain boundaries; an increase in the precipitation of these strengthening elements likely results from an increase in availability of Nb, due to Nb not being tied to carbon in NbC.

In a material unaffected by precipitate strengthening, a smaller ratio of yield strength to UTS (Y/T) implies a greater degree of plastic deformation and consequently should be accompanied by an increase in elongation. In the present study, however, elongation is extremely poor relative to samples produced by Rao et al. whose Y/T values were approximately equivalent to those observed in the present study. Samples from the two

comparative studies are likely to have a higher quantity of strengthening precipitates, including γ', γ'' and δ, relative to those observed here, however the quantity and size of precipitates produced by HIPping alone is unlikely to have a significant effect on tensile strength. Given the observed microstructures and tensile data of each study, it could be concluded that the improved properties observed in comparative studies result from a reduction in PPBs and an increase in recrystallisation of grains.

6.7.1 Fractography

Low magnification SE imaging of the fracture surface (figure 6-12-a) shows a surface composed of individual powder particles, suggesting the dominant failure mechanism to be crack propagation along PPBs, confirming reasoning behind the reduction in elongation. Closer inspection of the fracture surface (figure 6-12-b) revealed a dual mode of failure, with both features indicative of ductile and brittle failure. Dimpling is visible on the surfaces of individual powder particles and around smaller precipitates within the particles suggesting a degree of failure by micro-void coalescence. Material pull-out is also visible around larger precipitates at the PPBs. Furthermore, observation of precipitates within the PPBs reveals on multiple occasions fractured precipitates concurrent with the tensile data observed (figure 6-13).

a) b)

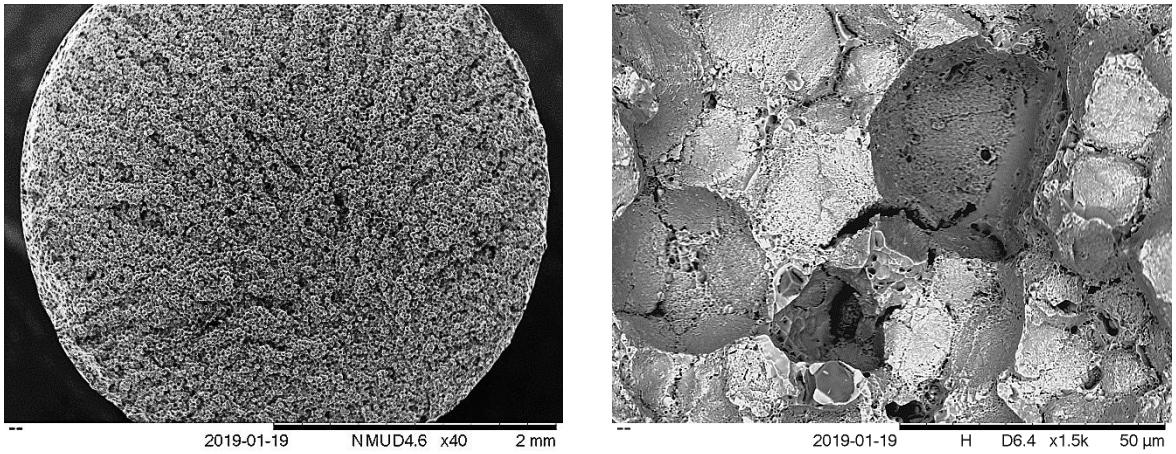

Figure 6-12: SEM micrographs of HIP fracture surface: a) low magnification SE image of entire fracture surface and b) high magnification BSE image.

a) b)

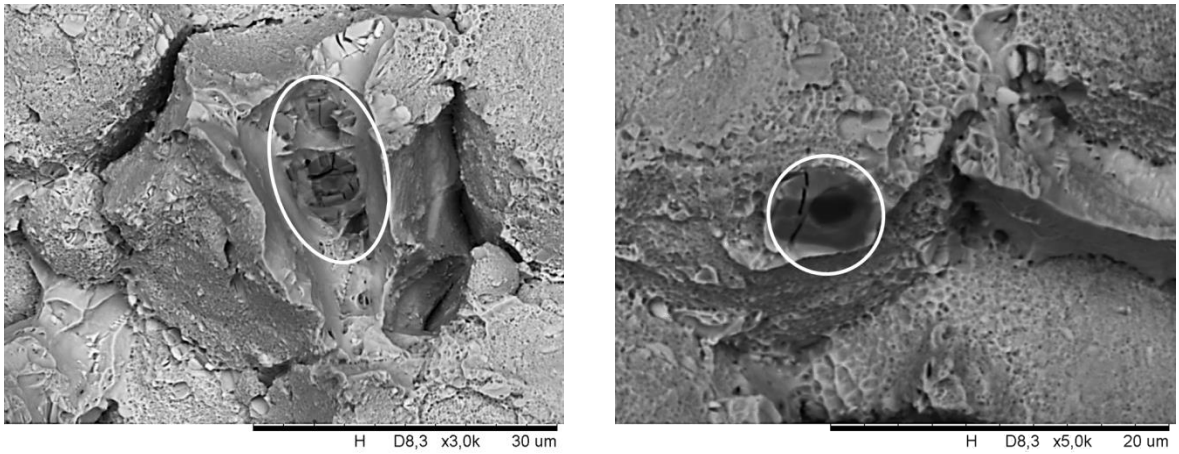

Figure 6-13: BSE SEM micrographs highlighting broken precipitates embedded in the fracture surface of HIPped specimens after tensile testing: a) fractured TiC carbides; b) fractured oxy-carbide embedded in fracture surface. Fractured precipitates are circled.

6.8 Summary

Powder characteristics were found to have a substantial influence on the microstructure and tensile properties of the PM HIPped material. Carbon and oxygen concentrations were thought to encourage the formation of PPBs, with PPBs composed predominantly of NbC carbide and discrete Al_2O_3 precipitates. The smaller particle size of LPBF powders was not found to be beneficial in reducing PPBs through recrystallisation mechanisms as was suggested in the literature. It was proposed that, for Ni-base superalloys favouring stable Al oxide precipitation, oxygen content would have more influence on PPB formation than powder particle size.

NbC carbides were found to be the most prevalent precipitate, resulting from the existing segregation of Nb in the powder and a HIPping temperature below the dissolution temperature of MC carbide. In addition to NbC carbides, Ti carbides/ carbonitrides, and oxy-carbonitrides were also observed by SEM. Gamma prime, γ'' and δ were not observed by SEM, however XRD data indicated some of their precipitates to be present.

Localised differences in grain morphology were observed, with some areas showing increased recrystallisation and grain growth relative to others. This was mainly attributed to a difference in precipitation observed in each region, however, may also have resulted from differences in powder size.

RT tensile test results reflected the observed microstructure of the HIPped material. A significant reduction in elongation resulted from the widespread precipitation of brittle NbC carbides, as well as the presence of Ti carbides/ carbonitrides and oxy-carbonitrides; which could all be observed at the fracture surfaces of samples. Reduced yield strength and UTS

values relative to other studies, were attributed to the greater presence of PPBs and a reduction in recrystallisation of grains.

The influence of the diffusion zone was a recurring theme throughout these PM HIPping studies. The diffusion zone was shown to influence NbC carbide distribution, which in turn influenced the distribution of PPBs and levels of recrystallisation within the PM HIPped material; this ultimately effecting the tensile properties of the material. Consequently, going into the in-situ shelling work it is predicted that the microstructures of the PM-HIPped material will be more homogenous, due to their being no concentration gradient between the canister and the powder.

Chapter 7

Powder Bed Fusion

7.1 Introduction

For the in-situ shelling process to be a success the requirements for an effective HIPping canister must first be fulfilled:

- The canister must be strong and malleable; the HIPping canister needs to be ductile enough to deform and exert force on internal powders to densify them and be strong to ensure the shell does not fail under pressure.
- The canister must not contain surface connected cracking or porosity; surface connected cracks and pores allow gas to permeate the HIP shell preventing deformation and densification of the shell and internal powders.

Each of these requirements should be optimised for in the PBF stages of production. Strength and ductility are affected by grain size and phase precipitation, which in turn can be affected by PBF processing parameters such as, beam power, scan speed, scan strategy and layer thickness. The presence of surface connected porosity and cracking is affected by both core PBF parameters and contour/surface parameters.

This chapter initially examines the influence of process parameters on defect formation and microstructure of LPBF Inconel 718 walls. This is followed by a surface optimisation study intended to understand how LPBF parameters might be used to manipulate surface finish to benefit the in-situ shelling process. Process parameter optimisation is conducted for EPBF, and comparisons are drawn between LPBF and EPBF in regard to defect formation and

microstructure. Finally heat treatment investigations are performed for LPBF specimens examining their influence on microstructure and tensile properties.

7.2 LPBF

Figure 7-1 shows the completed LPBF builds for each layer thickness. It is notable from the photographs that a significant number of walls built using a 20 µm layer thickness did not complete building. These walls were stopped as the result of over-building and crowning (see figure 7-2), which was putting other walls at risk of not completing due to a lack of powder spreading.

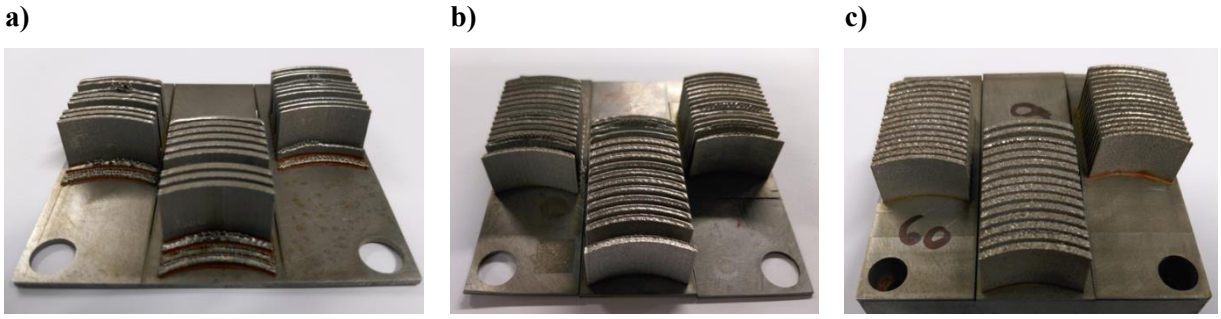

Figure 7-1: Completed LPBF Inconel 718 builds for different build layer thicknesses: a) 20 µm; b) 40 µm; c) 60 µm.

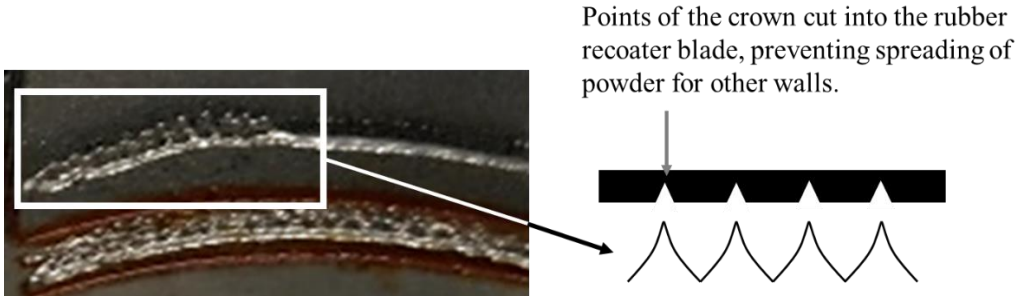

Figure 7-2: Zoomed in image of crowning on a wall built using 20 µm layer thickness and explanation of effect of crowning on the recoater blade.

The overbuilding and so-called crowning observed in the samples built with 20 μm is most likely to result from an inconsistency in powder layers. By number standard distribution at least 11 % of powders in lot 1 exceed 30 μm in diameter and by volume standard 50 % are in excess of 30 μm. Building with a layer thickness less than the average powder particle size can lead to a reduction in the packing density of powder particles, as larger particles are removed from the powder bed as they continue to be pushed by the recoater blade which is set at the level of the layer thickness. Studies in both LPBF and EPBF have shown inconsistencies in melt pool geometry resulting from reduced packing densities. Figure 7-3 shows simulated melt pool geometries as a function of powder packing density. It can be seen that melt pools have a more pronounced concave structure when packing densities are lower. Examination of the crown structure in figure 7-2 shows similarities with the concave structure of the melt pool. Furthermore, the orientation of the structure follows the orientation of the scan tracks. While the melt pool sides do not initial exceed the powder bed, it is believed that with each new additional layer the edges of the melt pool extend further.

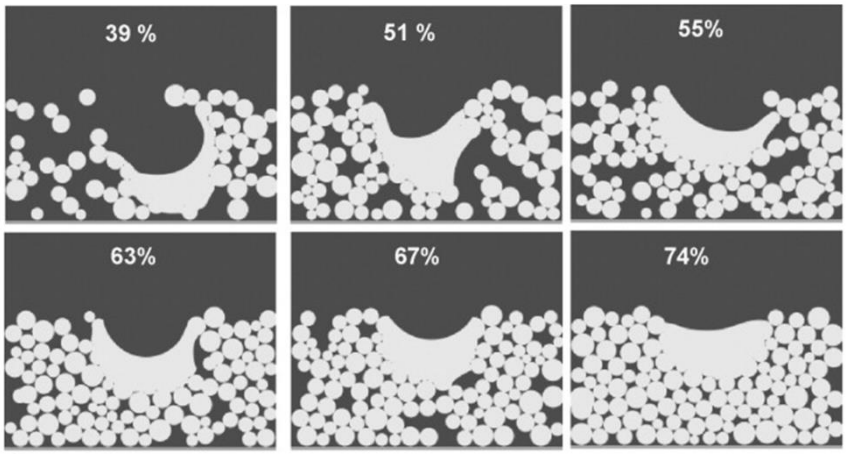

Figure 7-3: Simulated melt pool geometry as a function of powder packing density. Taken from [115].

Comparing the process parameters of parts in which crowning occurred and didn't occur within the 20 µm build, the majority of crowning walls were melted using fast scan speeds. Faster scan speeds have also been shown to lead to higher levels of melt pool distortion relative to slow scan speeds, resulting in similar geometries to those observed for melt pools formed in powder beds with low packing densities [186].

7.2.1 Defect formation n LPBF walls

i. Porosity

Figure 7-4 shows typical optical images of the XY and XZ cross-sections obtained for each set of walls. Three morphologies of porosity were observed in the LPBF walls -lack of fusion (LoF) voids, gas porosity and keyhole porosity. Figure 7-5 shows optical micrographs of porosity observed in the XZ cross-sections of 2 mm thick walls built with 40 µm layer thickness (figure 7-5-a) and 60 µm layer thickness (figure 7-5-b).

a) b)

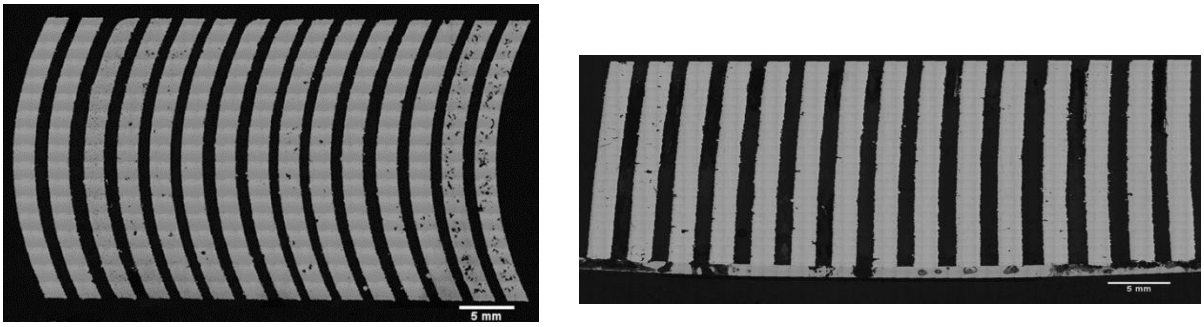

Figure 7-4: Optical micrographs of cross-sections of walls with 60 µm layer thickness and 2 mm wall thickness. a) XY cross-section; b) XZ cross-section.

a) b)

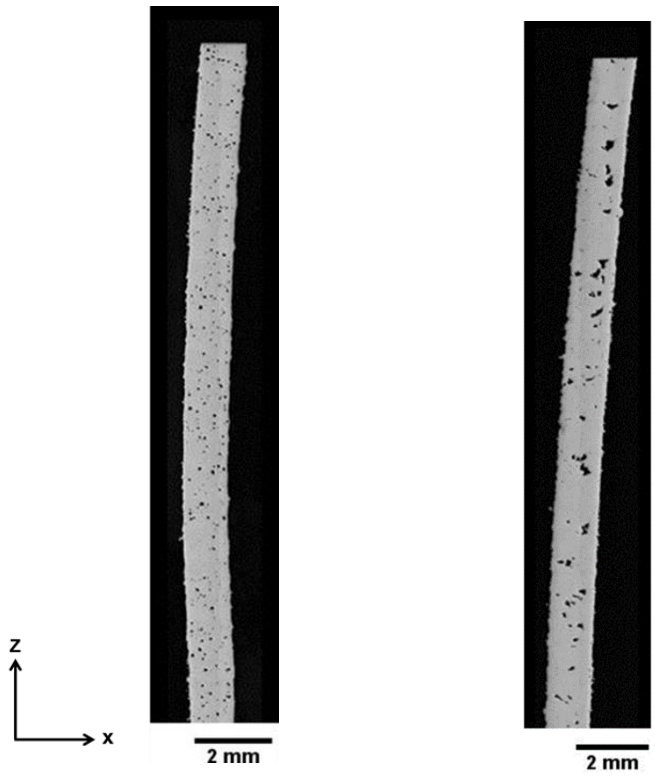

Figure 7-5: micrographs of XZ cross-section of walls with high area fractions of porosity. a) keyhole porosity in wall built with 40 µm layer thickness; b) LoF porosity in wall built with 60 µm layer thickness.

Keyhole porosity was observed in several of the walls but was substantial in the walls built using the highest energy densities. Gas porosity was observed in all walls and was classified by its size and its location towards the top of the melt pool. No porosity was observed in the cross-sections of the powder samples examined and consequently it is believed gas porosity observed here was formed during processing. Figure 7-6 shows an SEM micrograph of gas porosity in the cross-section of a melt pool; a keyhole pore can also be observed at the bottom of the melt pool. LoF voids (figure 7-6-b) were most prominent in the walls built using 60 µm thick layers, suggesting energy densities were insufficient for the quantity of powder that required melting.

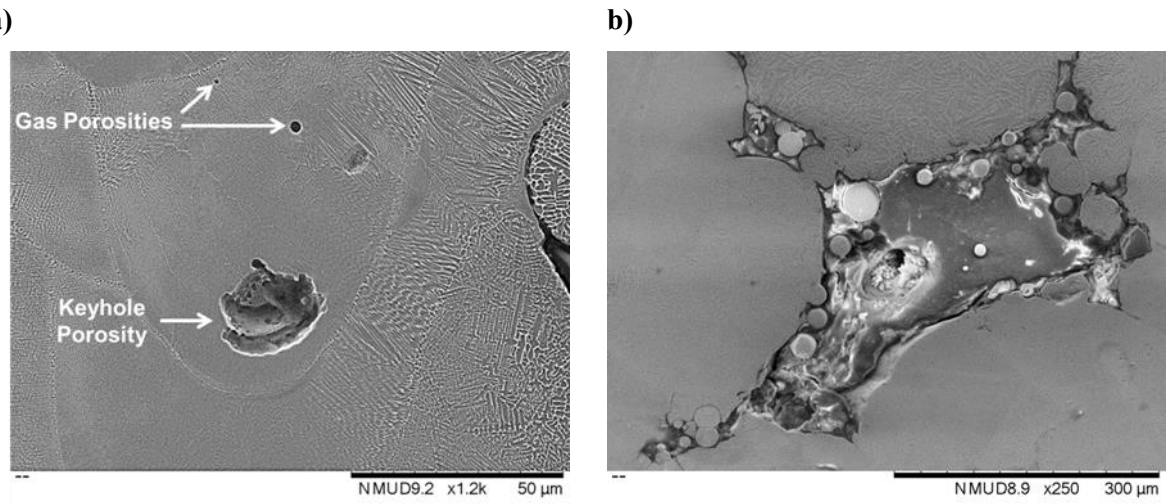

Figure 7-6: Dual contrast SE/BSE micrographs of porosity in LPBF walls. a) a keyhole pore and gas pores in a melt pool and b) LoF void.

As each morphology of porosity has a different formation mechanism it is logical to assume that different LPBF parameters will affect different types of porosity in different ways. To that end, when examining the influence of LPBF build parameters on porosity, in addition to examining porosity as a whole, each of the morphologies of porosity has also been analysed separately. Table 7-1 shows the results of an ANOVA analysis examining the relationship between LPBF parameters and all three modes of porosity. Porosity was separated by the plane in which it was observed- XZ or XY. This was done, as LoF voids can occur in the XY plane, resulting from large spacing between scan tracks, without clearly presenting in the XZ plane. The results suggest laser power has a significant effect on porosity formation in the XZ plane and a near significant effect on porosity formation in the XY plane. Scan speed also shows more significant influence over porosity in the XZ plane as opposed to the XY plane. As is to be expected scan spacing has a more significant effect on porosity in the XY plane compared to the XZ plane. Layer thickness and wall thickness appear to have the most significant influence over porosity formation in the XZ plane.

Table 7-1: Results of ANOVA for LPBF build parameters and area fraction of porosity observed in XY and XZ planes.

	F-Value		**P-Value**	
	XZ Porosity	**XY Porosity**	**XZ Porosity**	**XY Porosity**
Laser Power (W)	4.6	3.22	0.034	0.075
Scan Speed (mm s^{-1})	4.7	2.29	0.032	0.133
Scan Spacing (mm)	1.39	3.14	0.242	0.079
Layer Thickness (mm)	11.99	0.87	0.001	0.353
Wall Thickness (mm)	9.69	0.22	0.002	0.638

The mechanism by which wall thickness influences porosity, is likely related to the heat accumulated across several adjacent scan tracks as opposed to the instantaneous heat imparted by the laser in a single scan track. Figure 7-7 shows the simulated evolution of melt pool temperature and shape during the scanning of two adjacent scan tracks in IN718[187]. Comparing the melt pool in figure 7-7-a (the first scan track) with that in 7-7-b (the second scan track) the melt pool width and length are larger. This occurs as residual heat from the scanning of the first track increases melting in the second track; the melt pool will continue to grow until a thermal equilibrium is reached in which the first scan tracks have solidified and are conducting heat away from the melt pool. The length of scan track will influence the residual heat accumulated as shorter scan tracks will have less time for heat to dissipate before the laser returns on itself. Consequently, melt pools are expected to be larger in the thinner walls resulting in an increase in part density.

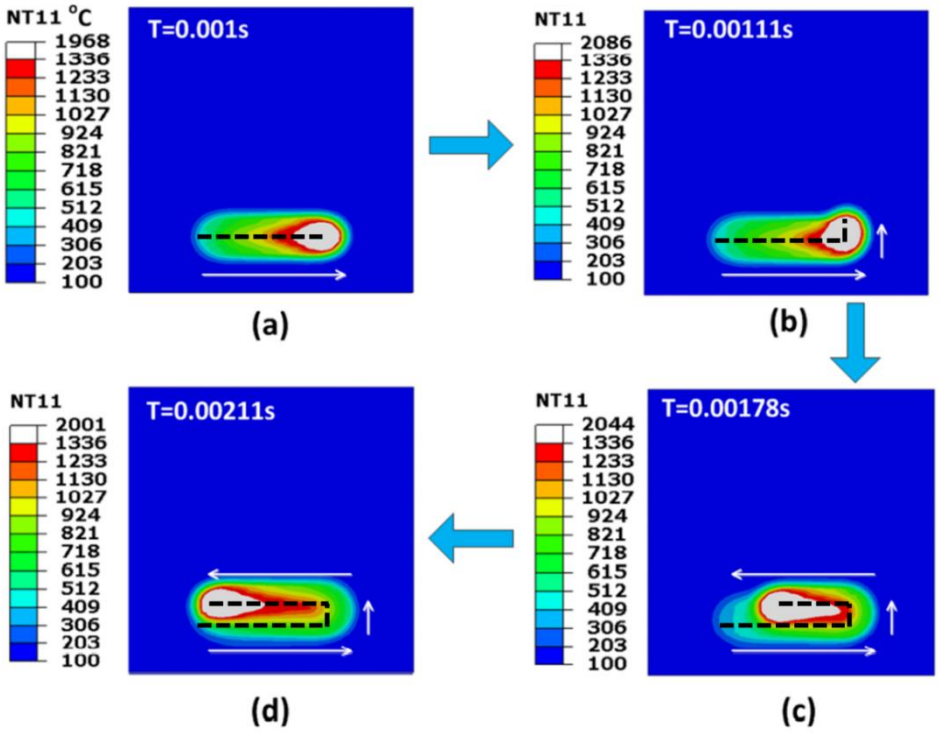

Figure 7-7: Simulated melt pool and temperature evolution in raster scan of two adjacent scan tracks in IN718: a) first track; b) turning point; c) second track part 1 & d) second track part 2. Adapted from [187].

Layer thickness like scan spacing, is more specific to a single build direction; the XZ plane. For a constant laser power and scan speed, a thinner powder layer results in increased re-melting of the previous layers, allowing for pore closure. Figures 7-8 through 7-10 show the area fraction of porosity as a function of linear energy density (LED) for the three different layer thicknesses investigated. In walls built using 20 µm thick layers no LoF voids were observed, and the lowest energy densities result in less than 1% area porosity. As energy density increases, percentage of area porosity does also, resulting from the formation of keyhole pores. Some LoF voids were observed in the walls processed using 40 µm layer thicknesses, however their reoccurrence was low; the lowest linear energy densities correspond to these walls. As with the 20 µm layer builds, as energy density is increased

towards 0.15 J mm^{-1} area fraction of porosity decreases. Beyond energies of 0.35 J mm^{-1} keyhole pores form, though the area fraction of porosity is somewhat lower than that observed in the 20 µm builds. As discussed earlier, LoF voids were most prominent in 60 µm builds and can be observed in walls up until a LED of greater than 0.15 J mm^{-1} is implemented. Keyhole porosity was also observed in the 60 µm build, however the quantity of pores was significantly less compared to the two thinner build thicknesses.

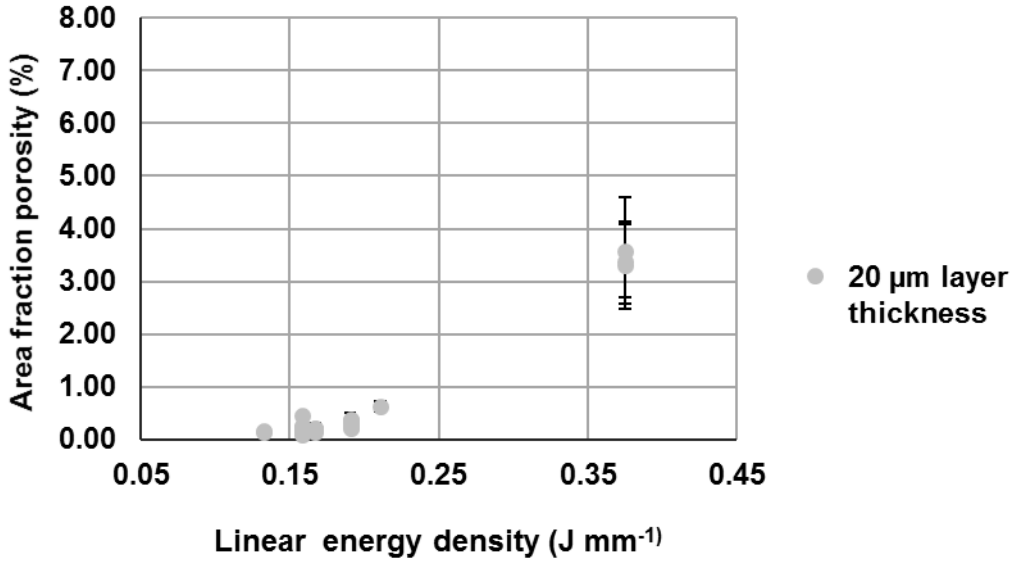

Figure 7-8: Scatter graph showing the influence of LED on area fraction of porosity for LPBF walls with 20 µm thick layers.

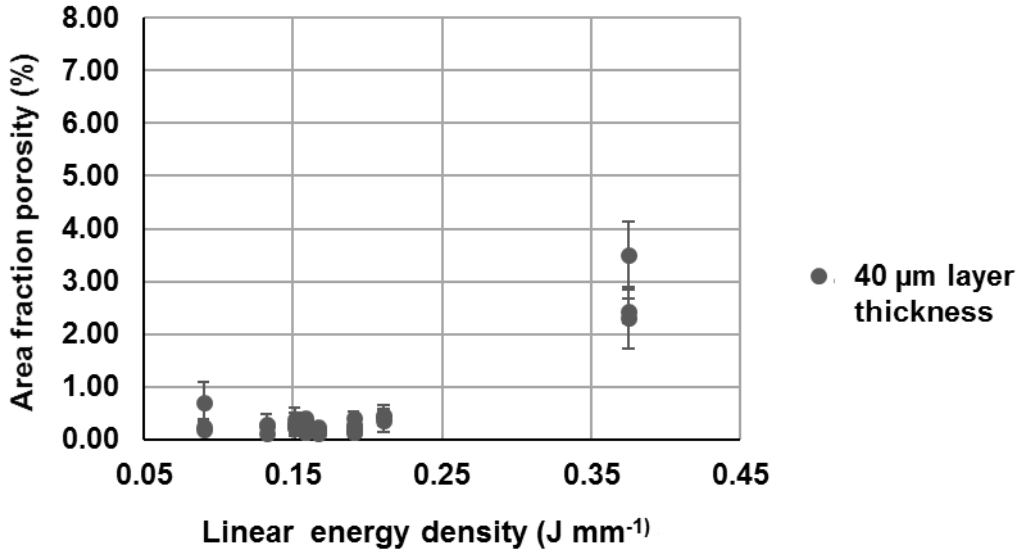

Figure 7-9: Scatter graph showing the influence of LED on area fraction of porosity for LPBF walls with 40 µm thick layers.

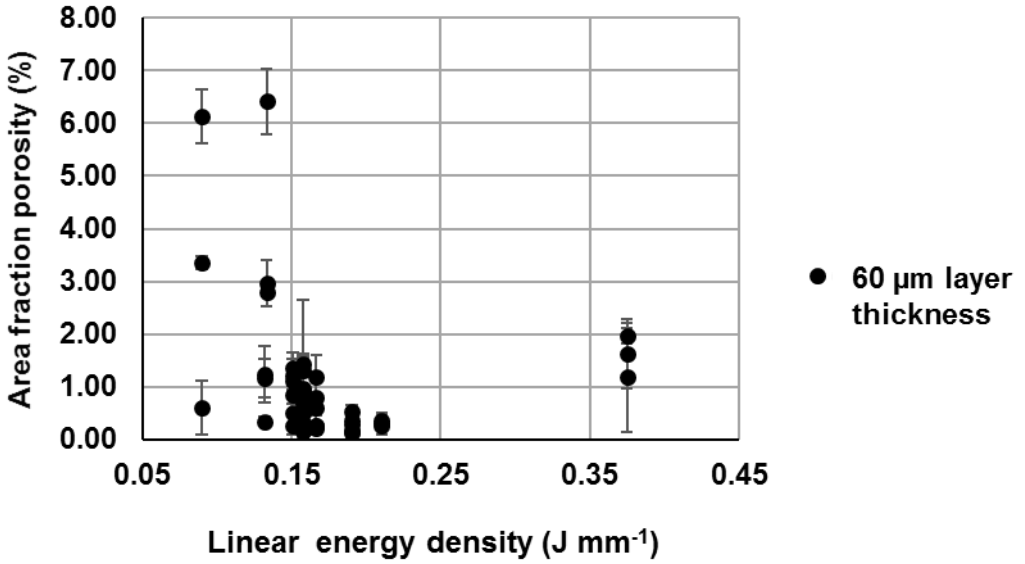

Figure 7-10: Scatter graph showing the influence of LED on area fraction of porosity for LPBF walls with 60 µm thick layers.

From figure 7-10 it can be observed that samples containing either LoF voids or keyhole pores can possess similar area fractions of porosity. While higher area fractions of porosity can hinder mechanical properties, the morphology of porosity also has a significant effect. A keyhole pore is typically round while the LoF void is jagged; for the same size pore the LoF void is more likely to result in failure due to an increase in stress concentrations at the edge of the pore leading to crack formation. With this in mind, a second ANOVA was performed to see if the dominant porosity mode within a sample was significantly influenced by one or a combination of LPBF parameters. Table 7-4 shows the results of the ANOVA. It was found that mode of porosity was significantly influenced by three variables- scan speed, layer thickness and wall thickness.

Table 7-2: Results of ANOVA for LPBF build parameters and the dominant mode of porosity observed.

	F-Value	**P-Value**
Laser Power (W)	0.54	0.464
Scan Speed (mm s^{-1})	108.63	< 0.0001
Scan Spacing (mm)	2.97	0.088
Layer Thickness (mm)	16.04	< 0.0001
Wall Thickness (mm)	5.78	0.018

Figures 7-11 and 7-12 illustrate the influence of these parameters on the dominant mode of porosity. Wall thickness was found to have very little influence on the morphology of porosity in the 20 µm builds, however as build thickness was increased the influence of wall thickness became more significant, with thicker walls containing a higher area fraction of LoF voids. Layer thickness significantly influenced keyhole porosity formation, increasing the area fraction of pores with decreasing layer thickness. As discussed in section 7.2.1 powder packing density in the 20 µm build was likely to be lower than in the 40 and 60 µm. Lower

packing densities tend to lead to inhomogeneity in the powder bed. Considering the mechanisms of keyhole pore formation, it would be logical to conclude that inhomogeneity in the powder bed could lead to morphological changes in keyhole melt pools resulting in collapse of the pool and the formation of keyhole pores. Keyhole porosity was also found to be more pronounced in walls produced with slow scan speeds, this is concurrent with the work of Berger et al. [118] who found slower welding speeds to lead to less stable melt pool conditions. The majority of walls with keyhole porosity however also belonged to the group of parameters with the highest energy density and consequently scan speed may not be the only contributing factor. Keyhole porosity formation is more likely in high energy density conditions due to the increased quantity of metal vapour generated by higher melt pool temperatures. Generally, LoF was found to increase with increasing scan speed, except for a beam speed of 2250 mm s^{-1}; all the walls produced with this scan speed had laser beam powers of 300 W and an AED of 2.34 J mm^2. Studies by Carter et al. [113] found area energy densities greater than 1.5 J mm^2 to eliminate LoF voids in Inconel 718 and other Ni-base superalloys.

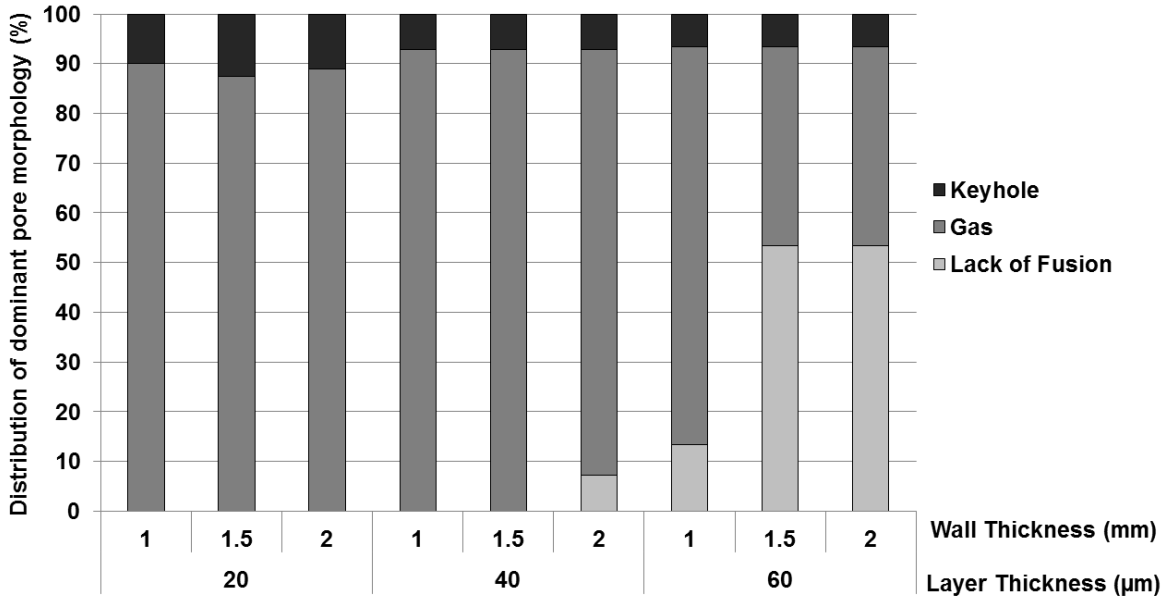

Figure 7-11: Chart illustrating the distribution of different pore morphologies observed in LPBF walls as a function of wall and layer thickness.

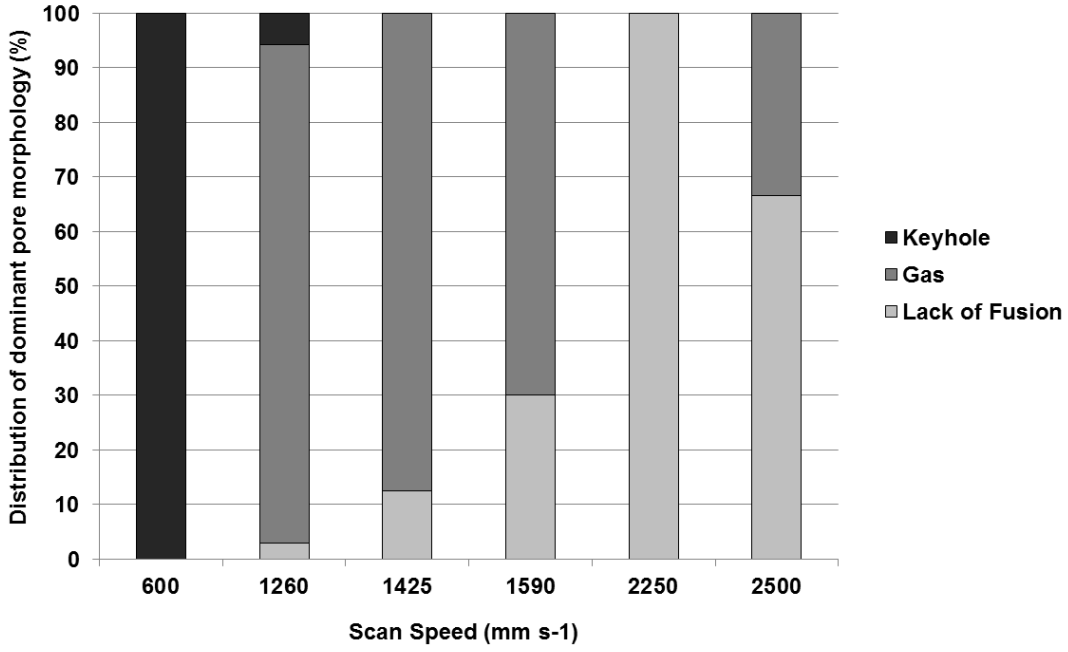

Figure 7-12: Chart illustrating the distribution of different pore morphologies observed in LPBF walls as a function of scan speed.

ii. Cracking

Cracking was observed in numerous samples in both XZ and XY cross-sections. Cracking in the XZ cross-section was parallel to the build direction and propagated along a single line for several millimetres. Figure 7-13 shows an optical image of typical cracking behaviour in samples built with 20 µm layers. Cracking was particularly dominant in these samples with 50% of the walls built with 20 µm layers containing cracks. Conversely only 28% of walls built with 40 µm layers and 6% of walls built with 60 µm layers contained cracks.

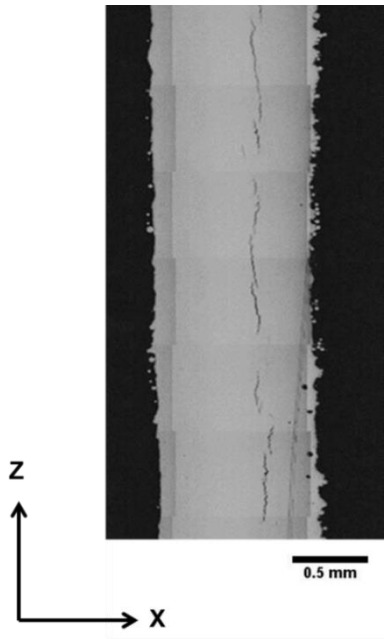

Figure 7-13: Optical image of cracking in 1 mm thick wall built with 20 µm layer thickness.

Etching and SE imaging of the samples (figure 7-14) revealed cracks to initiate and propagate along the grain boundaries where there is a large quantity of segregation. Substantial segregation of Nb was observed in the cross-sections of powders and, due to large thermal gradients and rapid solidification in LPBF, it was expected that similar segregation would be

observed in the LPBF samples. As discussed in chapter 2, materials are more susceptible to liquation cracking when low melting point phases are present at the grain boundaries. The levels of Nb segregation observed here make it highly likely that eutectic γ-laves would form within the segregation. Figure 7-15 shows a high magnification BSE image of segregation observed in the LPBF walls, in which precipitates can be observed. The morphology of precipitation would indicate the precipitates to be a combination of discrete NbC carbides and laves; both of which are commonly reported in the literature [166, 188-190].

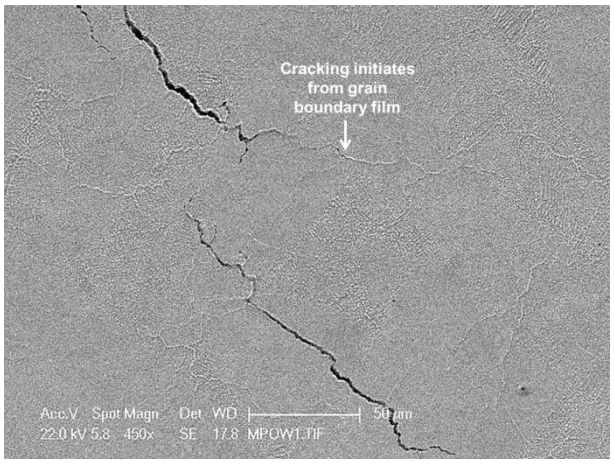

Figure 7-14: SE micrograph showing liquation cracking observed in XY cross-section of 1 mm wall built with 20 µm layer thickness.

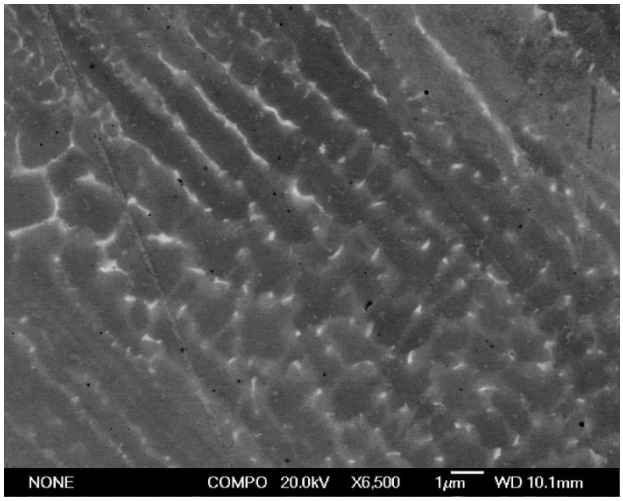

Figure 7-15: High magnification BSE micrograph showing precipitation within the Nb segregation. The morphology of emerging precipitates would suggest they are a combination of laves phase and MC type carbides.

The mode of cracking observed, may explain the dominance of cracking in samples built with 20 µm layers. Reducing layer thickness increases the number of reheats of previous layers, leading to more instances of precipitation dissolution at the grain boundaries, increasing the likelihood of liquation cracking. This however may not be the only explanation for the increase in crack occurrence with thinner build layers. Cracking observed in the 20 µm builds tended to be isolated to a similar location in each sample. This would imply that the residual stresses within each 20 µm build were distributed in a comparable way, also suggesting a difference in residual stress between builds of different layer thicknesses. To the best of the author's knowledge, no literature exists on the influence of layer thickness on residual stress in SLMed Ni-base superalloys; however, studies have been performed for Ti64 and 316L stainless steel [191, 192]. Both Ali et al.[191] and Kruth et al.[192] show for an equivalent density part built in two different layer thicknesses, the part built with thicker layers has lower residual stress relative to the part built with thin layers. Thicker powder layers have been

shown to lead to an increase in melt pool size and a decrease in cooling rate, owing to the insulating effects of the powder which reduce conductive heat loss to previously deposited layers and the build substrate [191, 193, 194]. Ali et al.[191] also showed that the thermal gradient from the top to the bottom of the melt pool was dependent on layer thickness, with thicker layers resulting in reduced thermal gradients. Both the slower cooling rates and reduced thermal gradients will contribute to a reduction in residual stress.

7.2.2 LPBF microstructure

i. Grain structure

Figures 7-16-a and -b show BSE micrographs of typical grain structures as seen in the XY and XZ cross-sections of the LPBF walls. BSE imaging was used to show grain contrast as it was not possible to resolve grain structures by etching and optical imaging, due to heavy etching of cellular, dendritic, grain and melt pool boundaries resulting from substantial Nb segregation. As is common with LPBF materials, grains in the XZ cross-section are columnar in morphology, extending over more than one build layer. The majority of grains are between 250 and 500 μm in length and between 5 and 20 μm in diameter. Grain morphology and size were not found to differ significantly between walls.

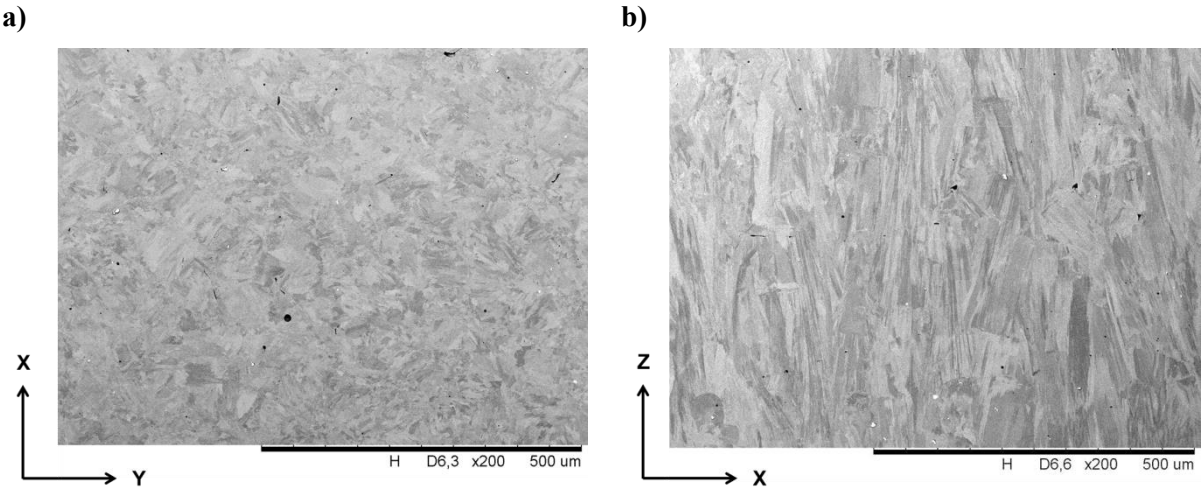

Figure 7-16: BSE micrographs highlighting the grain structures in a 2 mm wall with 40 µm build layers: a) XY cross-section and b) XZ cross-section.

Figure 7-17 shows optical images of melt pools revealed by etching in 1 mm (figure 7-17-a and -b) and 2 mm walls (figure 7-17-c and -d) for 40 (figure 7-17-a and -c) and 60 µm (figure 7-17-b and -d) build layer thicknesses. Overall melt pools in the 60 µm build appear be slightly less consistent in geometry relative to those in the 40 µm build, though consistency does improve with increasing wall thickness from 1 to 2 mm. As shown in figure 7-7-c, the size of the melt pool at the turning point of the scan path increases significantly due to residual heat effect, as the laser progresses along the next scan path the melt pool size decreases relative to the turning point, eventually reaching a stable condition. However, if the scan path length and laser scan speed do not allow enough time for the melt pool to stabilise before reaching the next turning point, the melt pool will continue to grow, until enough material has solidified to effectively conduct heat away from the newly deposited tracks, reducing the residual heat effect. Due to the cutting angle of the walls relative to the scan track direction, figure 7-24 shows cross-sections of the melt pools at different times during the melt pool evolution.

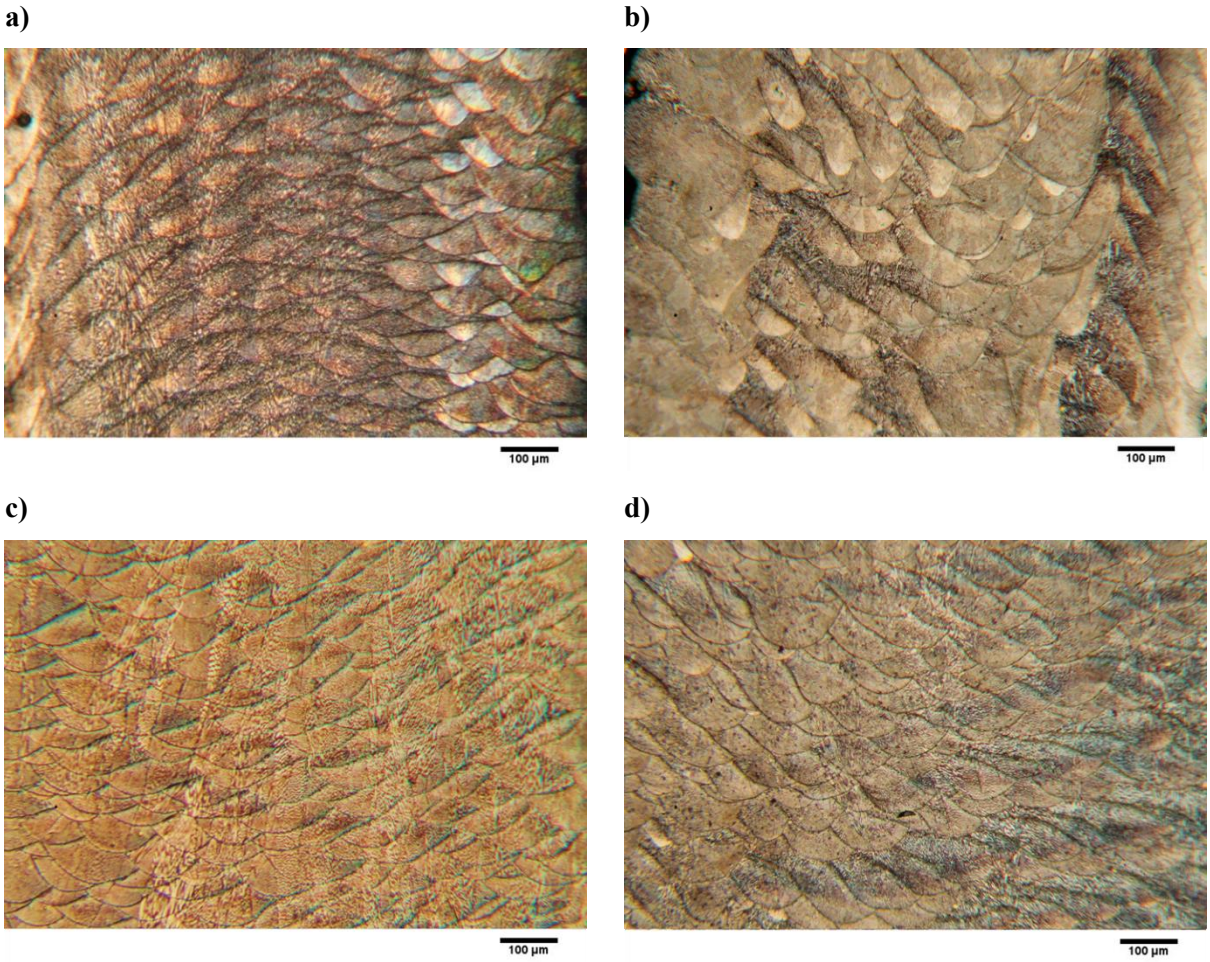

Figure 7-17: Optical images of melt pools revealed by etching of LPBF walls. a) 1 mm thick wall built with 40 µm layers; b) 1 mm thick wall built with 60 µm layers; c) 2 mm wall built with 40 µm layers and d) 2 mm wall built with 60 µm layers.

ii. Precipitation

Section 7.2.1-ii showed SEM micrographs of the Nb segregation associated with liquation cracking in 20 µm layer thicknesses, small NbC carbide and laves could be seen to be precipitating out of the segregation. In addition to the fine precipitation observed, larger MC type carbides could also be found (figure 7-18). Such precipitates are still relatively small and consequently are thought to have formed during processing; likely coarsening during the thermal cycling of earlier deposited layers. EDS spectra show precipitates to be composed of

both Nb and Ti (figure 7-18-c) indicating a similar formation mechanism to the multi-metal precipitates observed in HIPping. Precipitation was found to be similar for all processing conditions.

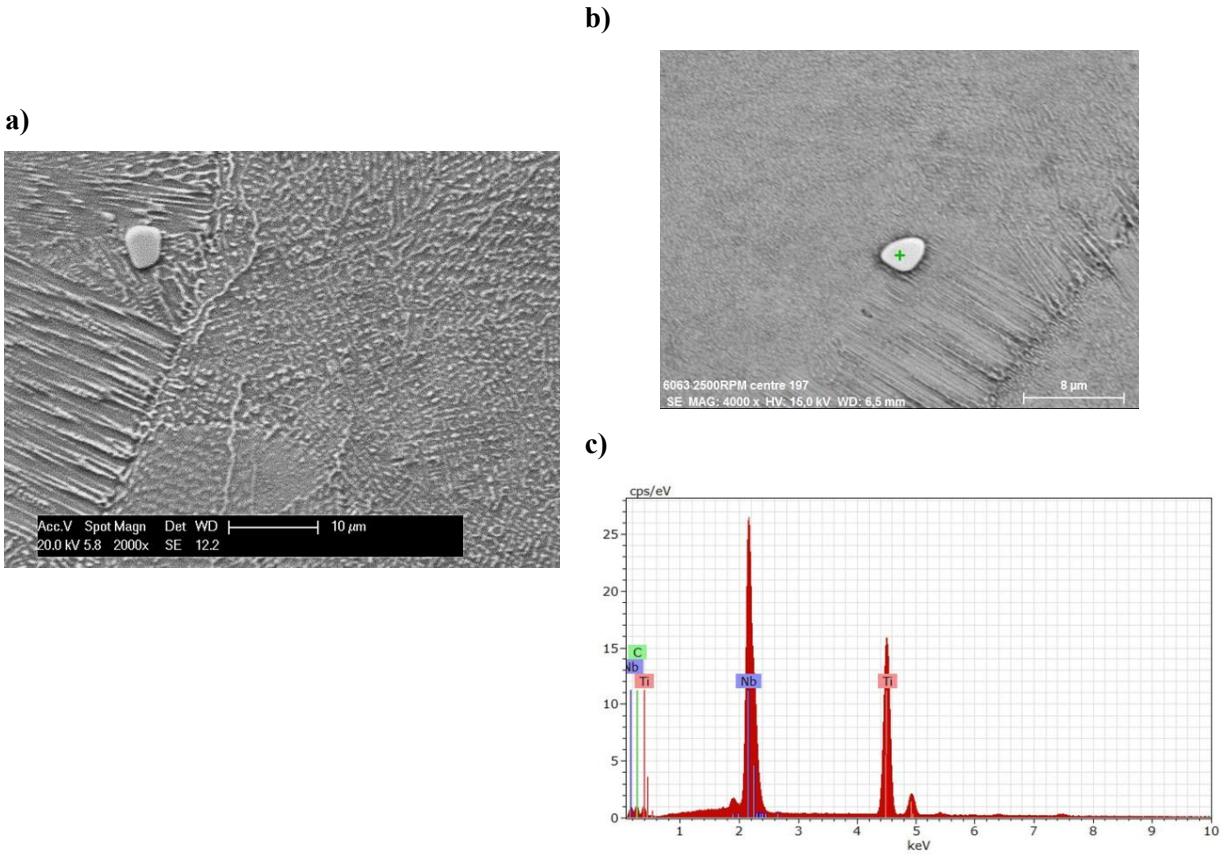

Figure 7-18: MC carbide precipitation in LPBF walls. a) SE micrograph of etched wall showing MC carbide; b) BSE micrograph of multi-metal carbide and c) EDS spectra associated with multi-metal carbide observed in (b).

7.3 LPBF surface optimisation

Following the identification of suitable LPBF parameters for minimising porosity and cracking, a small study was performed to understand the influence of LPBF hatch and contour parameters on surface roughness. Hatch parameters investigated included layer thickness, wall thickness, laser power and scan speed. Contour parameters investigated included laser

power, scan speed and number of contour scans. Figure 7-19 shows photographs of LPBF walls with the lowest (figure 7-19-a) and highest (figure 7-19-b) surface roughness. Minimum average surface roughness achieved was 4.5 μm and maximum 11.48 μm.

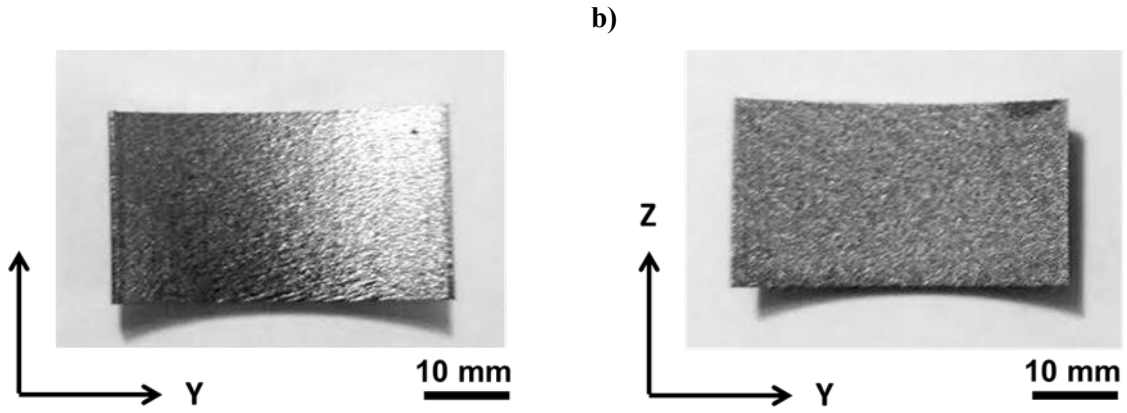

Figure 7-19: LPBF Inconel 718 walls exhibiting a) minimum average surface roughness and b) maximum average surface roughness.

ANOVA was performed to examine the relationship between LPBF parameters and Ra (table 7-3). Both hatch laser power and contour laser power were found to have a significant effect on Ra, with increasing power increasing Ra. Layer thickness was also found to have a significant influence with the 60 μm builds having higher Ra relative to the 40 μm builds. Number of contours is not quantified as having a significant effect on surface roughness in the ANOVA; however, when the data for each layer thickness of build is analysed separately, it can be seen that number of contour scans does have a significant effect on surface roughness in the 40 μm layer samples (figure 7-20) with two contour scans resulting in reduced surface roughness relative to one. When only a single contour is performed, laser power does not influence Ra, however when two contours are scanned, increasing laser power increases Ra.

Table 7-3: ANOVA for LPBF processing parameters (hatch and contour) and Ra.

SLM Parameter	F-Value	P-Value
Layer thickness (µm)	6.4	0.0223
Wall thickness (mm)	Aliased	
Hatch laser power (W)	3.73	0.0713
Hatch scan speed (mm s^{-1})	2.29	0.1493
Hatch spacing (mm)	Aliased	
Contour laser power (W)	12.87	0.0025
Contour scan speed (mm s^{-1})	0.2009	0.66
Number of contour scans	0.0764	0.7858

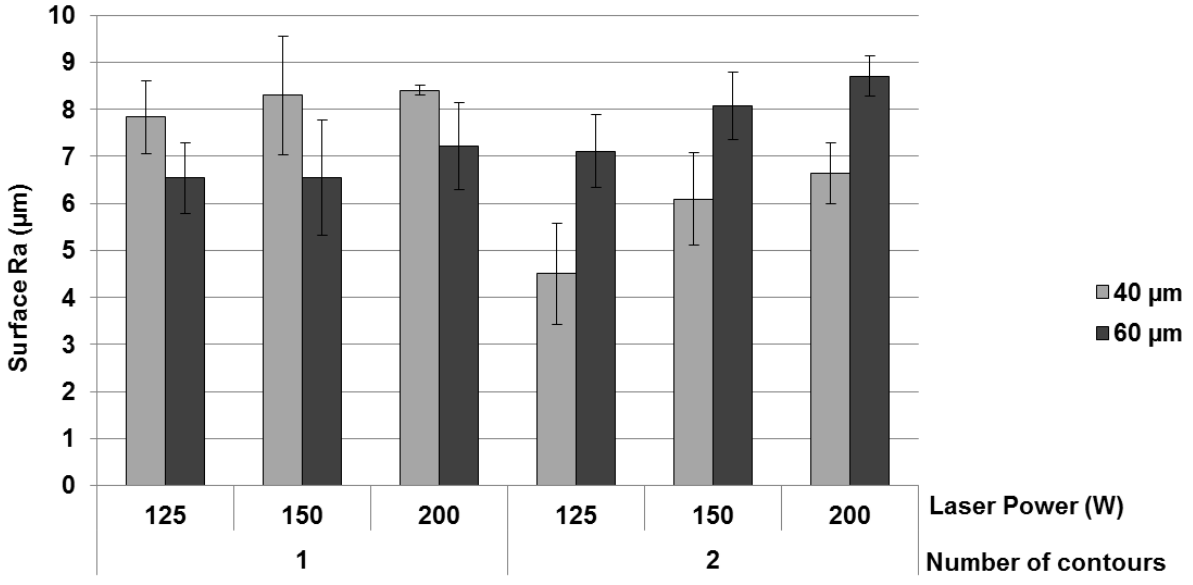

Figure 7-20: Influence of layer thickness, laser power and number of contour scans on surface roughness.

The influence of layer thickness on surface roughness most likely results from an increase in the number of larger powder particles present in the powder bed. LPSD of powder lot 2 showed at least 15 % of powders to have diameters greater than 45 µm. In the 40 µm layer builds a number of these particles will be removed by the recoater blade as they protrude from the powder bed; however, in the 60 µm layer build the majority of particle will lie below the level of the recoater blade as it reaches the end of the build plate. This is conducive with the surface roughness observed in EPBF in which larger powder particles are implanted.

As discussed in chapter two the LPBF process can be somewhat chaotic, especially in systems such as the Concept M2 used here. Gas flow in the system can interact with metal vapours produced during melting causing localised movement of powders. Bidare et al. [195] studied the laser interaction with powders during LPBF by high framerate imaging and schlieren imaging. They observed the removal of powder surrounding the melt area in both single track scans and raster scans (figure 7-21). Powder was both drawn into and blown away from the melt pool by the force of the melt pool vapour plume. For higher laser powers and scan speeds, disruption to the powder bed was found to be greater. In consideration of the work of Bidare et al. two mechanisms explaining the influence of contour parameters on surface roughness can be hypothesised. The primary reason for surface roughness in PBF is the attachment of partially sintered and unmelted powder particles to the surface of the high density parts. If surface roughness is to be reduced, the number of powder particles attaching to the part surface must be also. Denuded regions around parts in the studies from Bidare et al. vary in size but tend to be in the range of hundreds of micrometres (figure 7-21). If powders are to attach to the surface of the part during contouring, either the part surface must cross the denuded zones to reach the powders, or the powders have to cross the zone to reach the surface. If the part surface is to have sufficient flow to cross the denuded zone, temperatures

greater than liquidus must be achieved and sustained during contouring. While temperatures above the liquidus can certainly be achieved by the contour parameters used here, the time for which the surface is at temperature is highly unlikely to be long enough to allow sufficient flow, even for the smallest denuded zones observed. Furthermore, such flow would result in significant geometric discrepancies which have not been observed here. The pull of powders towards the parts during scanning is a more plausible explanation. Single contour scans resulted in higher levels of surface roughness for the 40 μm build layers, whereas double contour scan reduced surface roughness significantly; given this behaviour, it could be believed that during the first contour scan powders remaining in and at the edge of the denuded zone are pulled towards the part, much in the same way they are during hatch melting. The second contour scan then acts to melt the newly attached powder particles incorporated them into the part surface. As laser power is increased however, additional powder particles may be pulled towards the part during the second contour scan, though available powders are expected to be few.

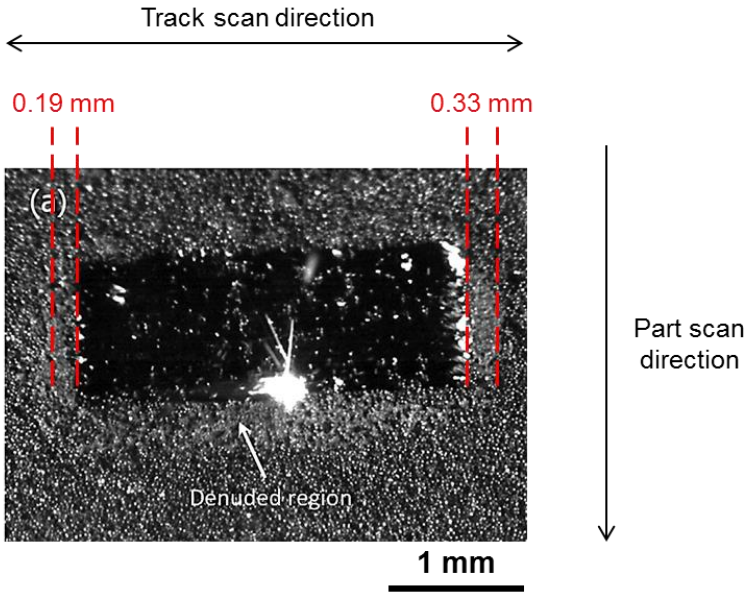

Figure 7-21: Snapshot image of powder distribution during laser scanning in LPBF. Modified from [195].

7.4 EPBF

Figure 7-22 shows photographs of the completed builds. In both figure 7-22-a and -b some walls can be seen to be missing; these walls were of so little density that when subjected to compressed air, to remove the powder cake from around the walls, the walls crumbled along with the powder cake. One of the walls in fig 7-22-a has also become detached from the plate, which can be attributed to poor bonding between the part and plate. The extremely low density observed of some of the parts was unexpected as parameters did not differ too significantly from those that had been optimised for the Q20 system. The alterations to the EPBF system from Q20 to Q20+ should not have resulted in significant differences in machine behaviour; however, previously optimised preheat conditions were found to be relatively unstable and as a consequence a significant amount of spatter was observed during part melting. It was later discovered that the minimum beam spot size had increased

significantly following the machine upgrade. Increasing the spot size, reduced the peak intensity of the beam and consequently the level of sintering that could be achieved during preheat was reduced. This resulted in a soft powder cake that collapsed at the melting stage. In addition, larger beam spot sizes can lead to an increase in charge accumulation of the powders, resulting in smoke events during preheating. Smoke events can vary in magnitude and smaller localised events may not always be visible to the machine operator. Such small events would result in localised denudation of the powder within the powder bed.

a) **b)**

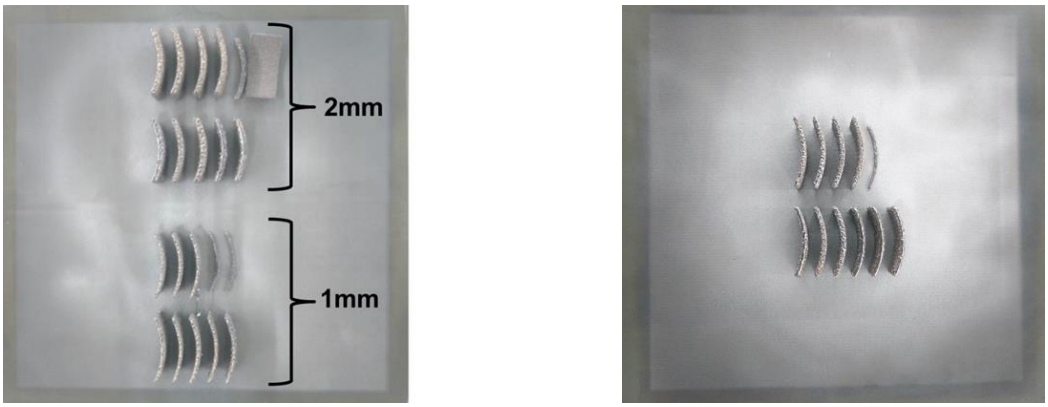

Figure 7-22: Completed EBM builds in different layer thicknesses and wall thicknesses: a) 1 mm and 2 mm walls built with 75 µm layer thickness; b) 1 mm thick walls built with 50 µm layer thickness.

7.4.1 Defect formation in EPBF walls

i. Porosity

Only a single mode of porosity was observed in the EPBF samples, LoF. This was to be expected as no gas porosity was observed in the powder cross-section and as EPBF is carried out in vacuum gas entrainment cannot occur during processing. Keyhole porosity

formation is also less likely to occur in EPBF due to the absence of atmospheric gases that can be pulled into the melt pool on collapse. Figure 7-23 shows the cross-sections of walls built with the lowest and highest area energy densities. LoF voids in the XZ cross-section of the highest density wall (figure 7-23-d) are mostly confined to a single location at the top of the wall. Given the high density observed in the remainder of the sample this LoF likely formed from an inconsistency in powder spreading and/ or localised denudation of the powder bed by a smoke incident.

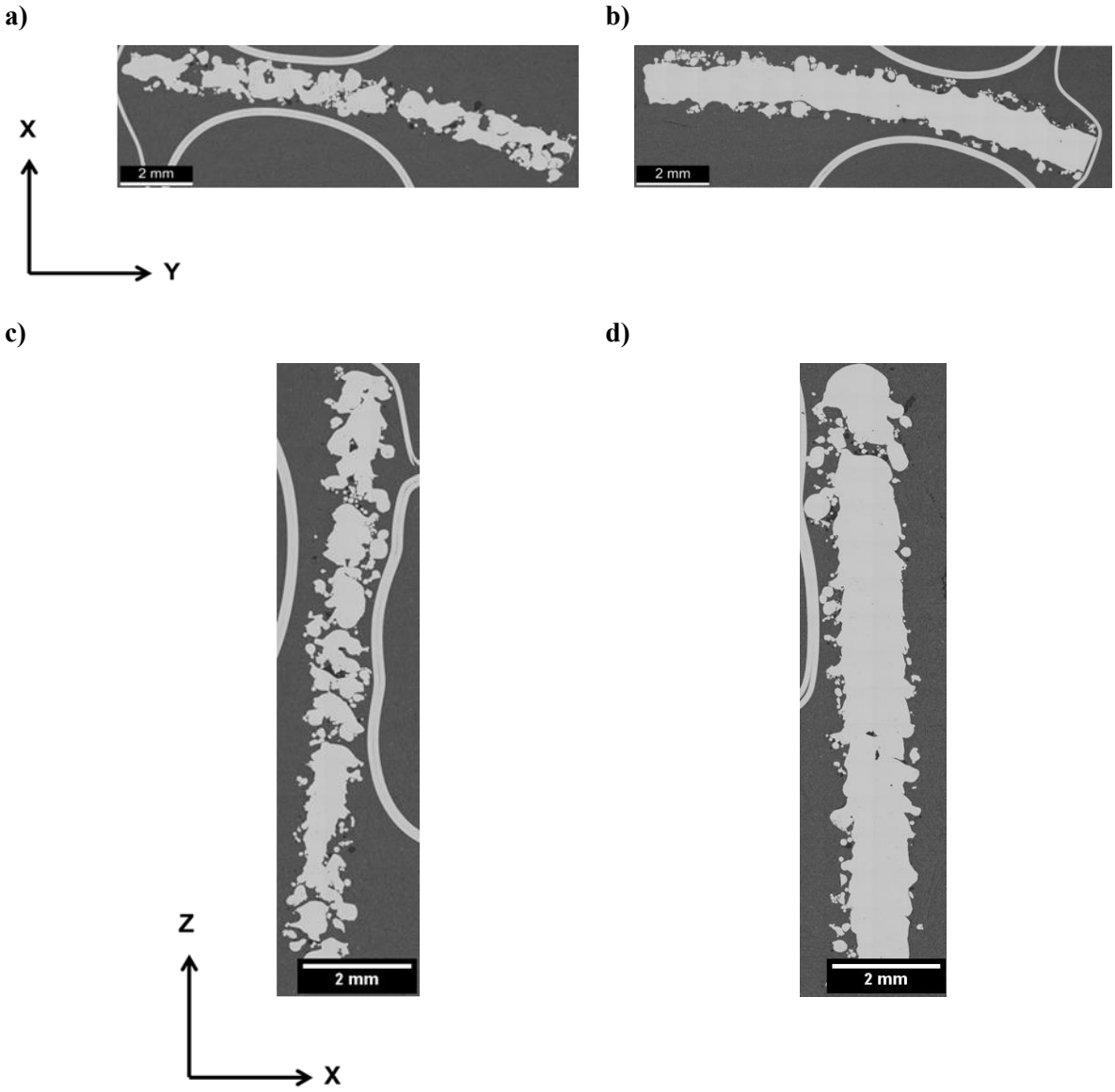

Figure 7-23: Optical micrographs of EPBF walls built in 75 µm layers with: a) & c) low energy density conditions; b) & d) high energy density conditions.

Table 7-4 shows results of ANOVA analysis for EPBF samples. Beam current, focus offset, scan speed and scan spacing played a significant role in the formation of porosity. Scan speed followed by beam current have the most significant effect on area fraction of porosity, with an increase in scan speed and decrease in beam current leading to an increase in area fraction of porosity. Focus offset control the beam spot size, with increasing offset current defocusing the

beam. Wall thickness does not have the same influence on porosity in EPBF as it does in LPBF. For LPBF samples it is believed that decreasing LoF in the thinner walls resulted from an increase in heat accumulation owing to the shorter scan tracks reducing heat dissipation time between laser scan passes. As EPBF is performed at elevated temperature cooling rates of parts are somewhat slower compared to LPBF and consequently small differences in geometry may not carry the same affect that they do in LPBF. In addition, the sintering of powders prior to melting in EPBF may also affect the heat accumulation; the necking of powder particles allows for conduction of heat between particles and consequently the potential for heat accumulation is reduced.

Table 7-4: Results of ANOVA for EPBF build parameters and area fraction of porosity.

	F-Value	**P-Value**
Beam Current (mA)	24.4	6.91E-05
Focus Offset (mA)	4.04	0.057382
Scan Speed (mm s^{-1})	65.64	6.7E-08
Scan Spacing (mm)	12.4	0.002026
Wall Thickness (mm)	0.01	0.928549
Build Layer Thickness (mm)	0.08	0.776115

Figures 7-24 and 7-25 show scatter plots of the area fraction of LoF voids as a function of LED. EPBF samples follow similar trends to the LPBF; with increasing energy density, area fraction of porosity is reduced. Significant deviation can be seen in the measurements taken from the XZ and XY cross-sections for walls built with energy densities less than 0.4 J mm^{-1}. This would suggest the size of LoF voids below this energy density threshold were dictated by the packing density of the powder bed. Comparing the layer thicknesses for the 1 mm thick walls, walls built with linear energy densities ranging from 0.4 to 0.96 J mm^{-1} had an overall smaller area fraction of porosity when built with 50 μm as opposed to 75 μm.

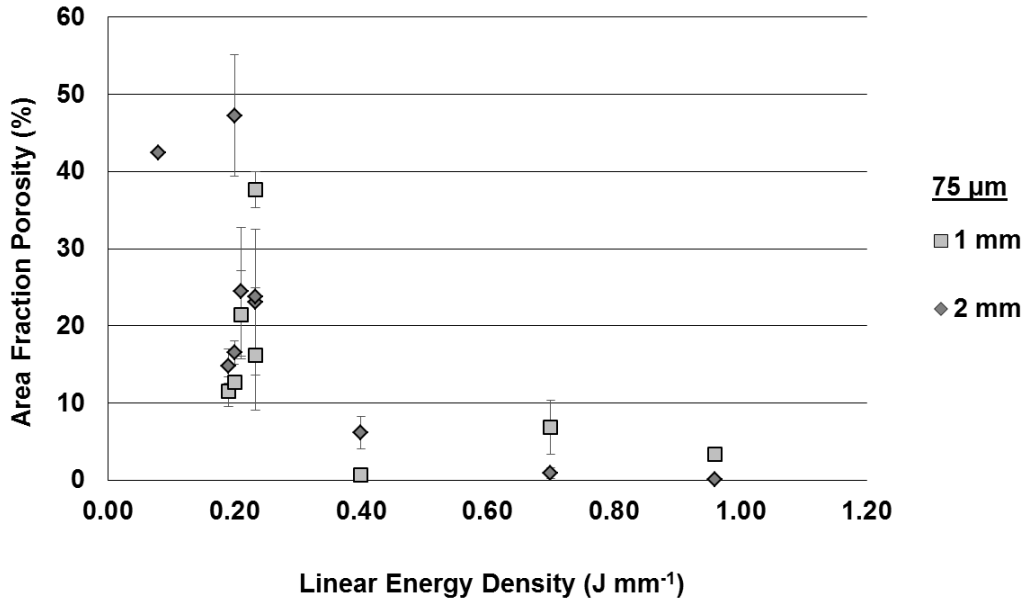

Figure 7-24: Scatter graph showing the influence of LED on area fraction of porosity for EPBF walls with 75 µm thick layers.

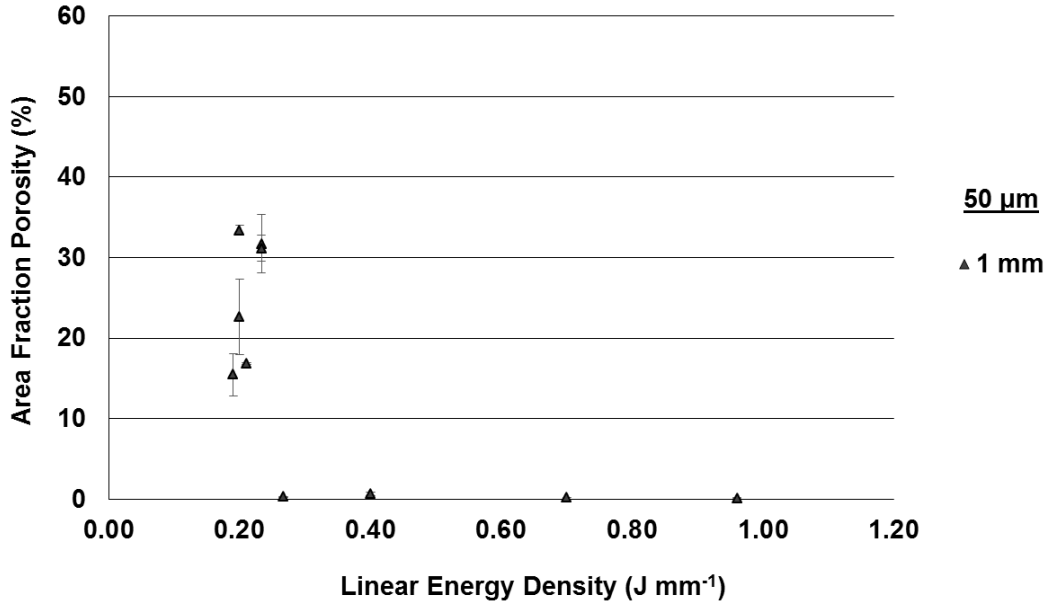

Figure 7-25: Scatter graph showing the influence of LED on area fraction of porosity for EPBF walls with 50 µm thick layers.

7.4.2 EPBF Microstructure

i. Grain morphology

As with LPBF specimens the EPBF specimens exhibited columnar grain structure from the top to bottom of the walls. Figure 7-26 shows optical images of etched XZ cross-sections in the top 3 mm of EPBF walls built with equivalent beam current, scan speed, focus offset and contour offset, for different wall thickness and layer thickness. Two types of dendritic structure can be observed, cored dendritic structures (CDS) and diffuse dendritic structures (DDS). Variation in dendritic structure at the top of Inconel 718 EPBF walls has been previously reported in the literature[151]. However not previously observed, is the influence of layer and wall thickness on the transition from one structure to another. Comparing walls built with different layer thicknesses, CDS develops earlier in the build for thinner layers (figure 7-26-a) relative to thicker (figure 7-26-c). Comparing 2 mm and 1 mm walls in 75 μm thick layers it can also be seen that CDS develops earlier in the build, though not as early as for 50 μm layers. CDS in welding of Ni-base superalloys is commonly accompanied by a change in the primary growth direction of dendrites[151], this is thought to occur as a consequence of dendritic fragmentation and the nucleation of new grains ahead of the solidification front[196], resulting from fast cooling rates within the melt pool. In LPBF it has been shown the thicker powder layers result in larger melt pools and slower cooling rates within the melt pool[193, 194, 197]; the results observed here suggest similar phenomena occur in EPBF, as walls built with 50 μm layers exhibit an increase in CDS implying faster melt pool cooling rates. Increase in CDS in 2 mm wall thicknesses can be attributed to the additional material available to conduct heat away from the melt pool increase cooling rates.

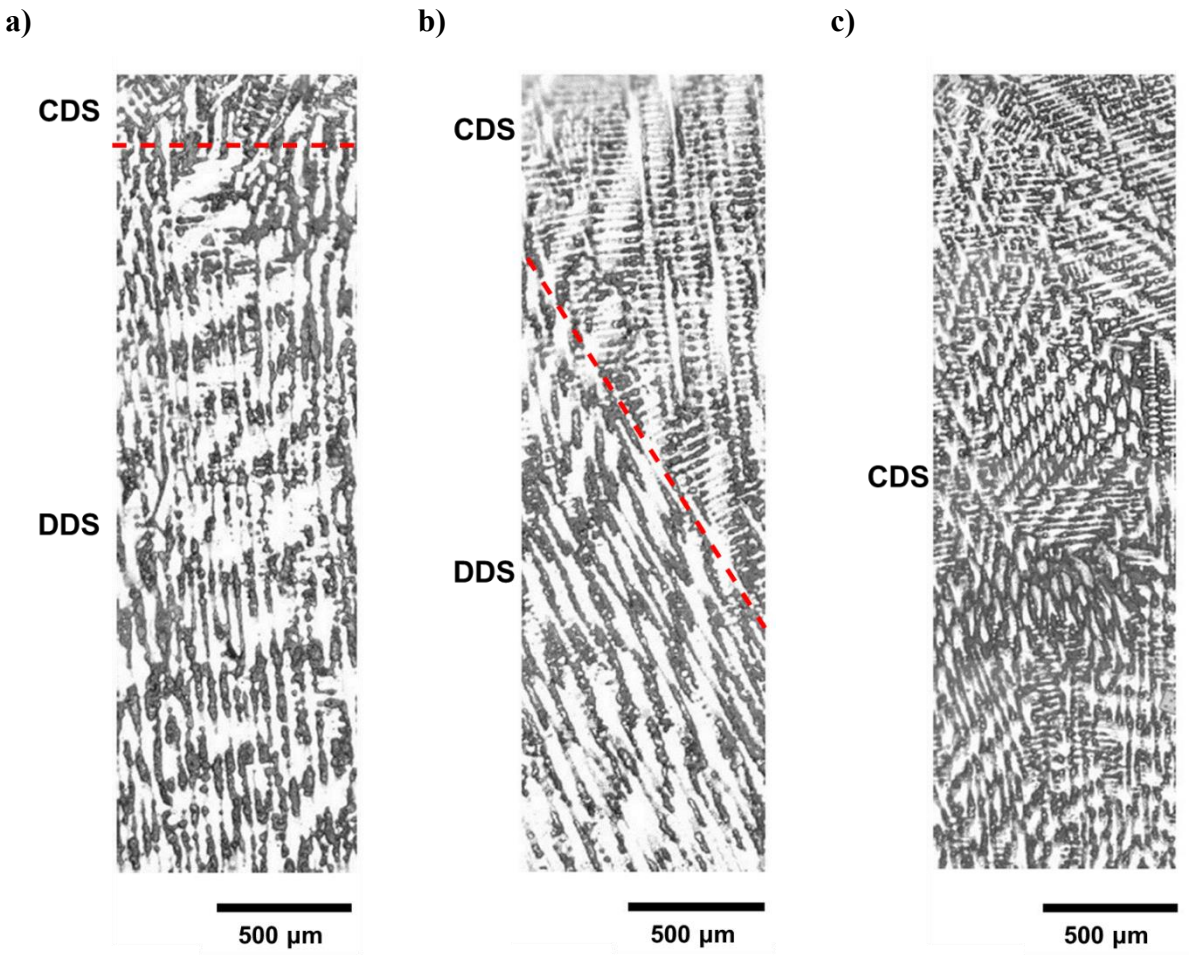

Figure 7-26: Optical images of the etched XZ cross-section at the top of three EPBF walls showing cored dendritic structure (CDS) and diffuse dendritic structure (DDS): a) 1 mm thick wall built with 0.075 mm layer thickness; b) 2 mm wall built with 0.075 mm layer thickness and c) 1 mm wall built with 0.05 mm layer thickness. All walls were processed with the same beam current, scan speed, focus offset and contour offset.

ii. Precipitation

Figure 7-27 shows optical and BSE micrographs of the XY cross-section of the highest density EPBF wall. The cross-section of dendrites can be seen and are surrounded by solute rich regions from which discrete carbides have precipitated. Dendrite cross-sections and carbides appear to vary in size across the XY cross-section, increasing in size from the

centre of the wall (figure 7-27-d) to the outer edge (figure 7-27-b). This implies faster cooling at the wall centre, which agrees with the scan strategy. As the outer contour is scanned first, it acts as a heat sink for its adjacent contour, and that contour acts as a heat sink for the next and so on. In addition, heat from contours toward the wall centre will act to coarsen the dendrite and precipitates in the outer contours.

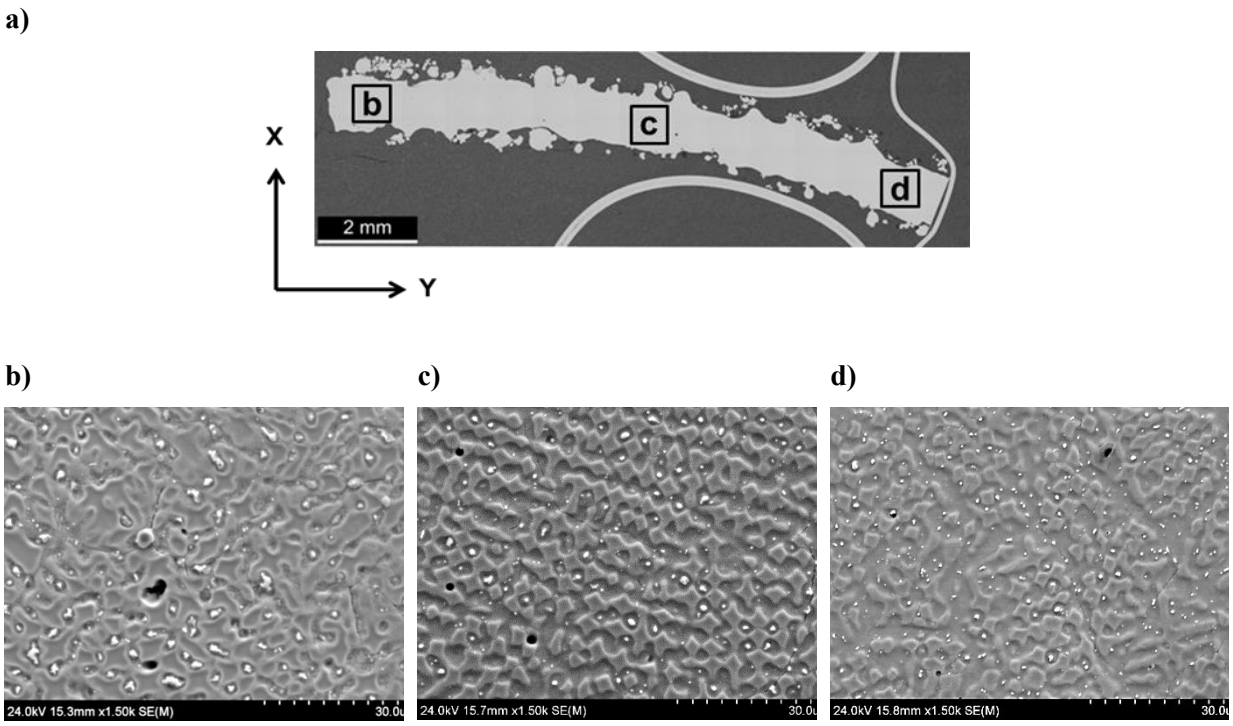

Figure 7-27: XY cross-section of high density EBM wall: a) optical micrograph with regions of microstructural analysis indicated; b) – d) BSE SEM micrographs from regions indicated in (a).

Figure 2-28 shows BSE micrographs for the highest density wall taken at the top, middle and bottom of the sample. Precipitation varies significantly over the height of the build. Toward the top of the wall precipitation if extremely fine as seen in figure 7-27. Moving down the wall, precipitates increase in size and quantity.

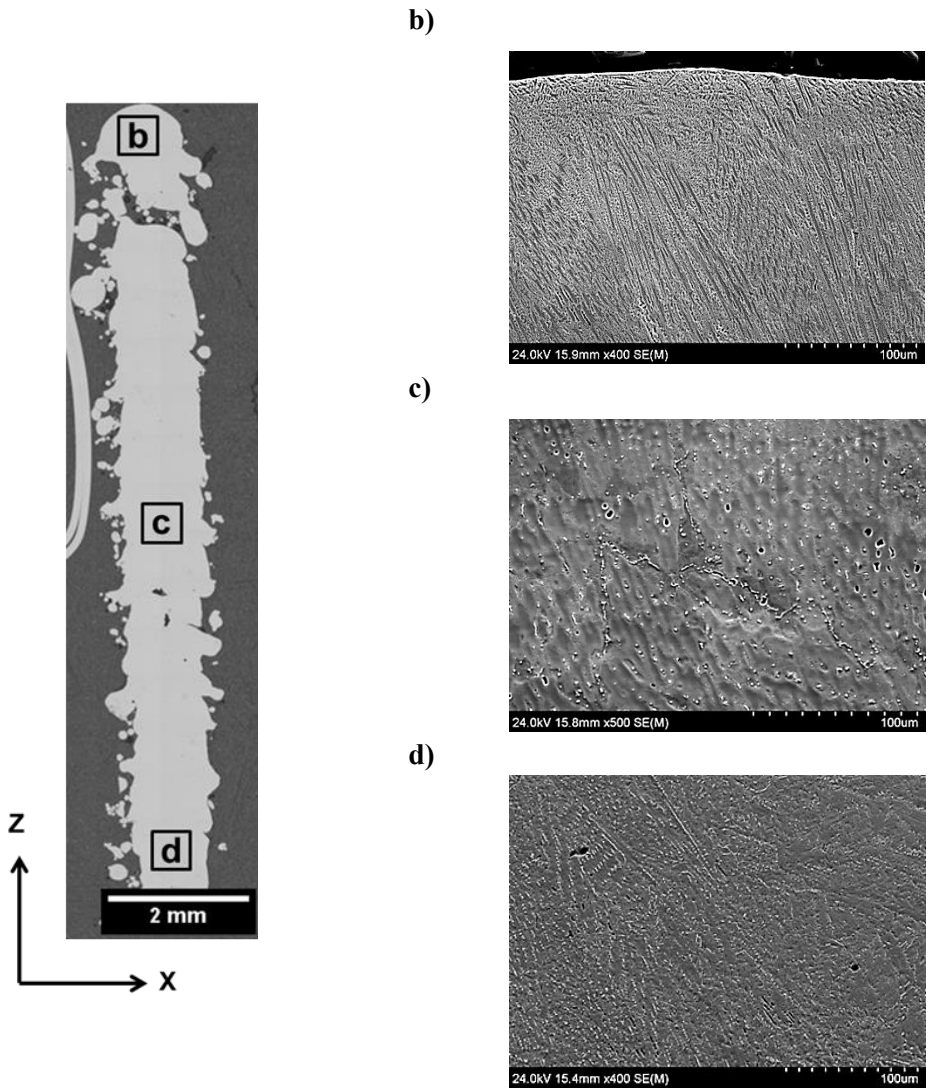

Figure 7-28: XZ cross-section of high density EBM wall: a) optical micrograph with regions of microstructural analysis indicated; b) – d) BSE SEM micrographs from regions indicated in (a).

Precipitation was primarily composed of MC type carbides and δ (figure 7-29). The δ is easily identifiable by its platelet morphology and orientation of approximately 45° to the build direction which typically follows the <001> direction.

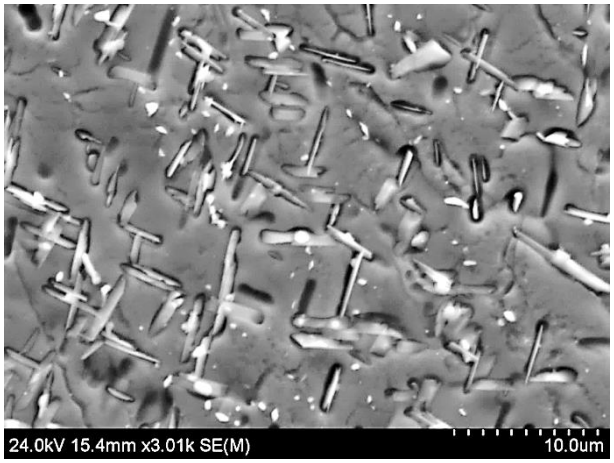

Figure 7-29: BSE micrograph showing delta and MC carbide precipitation in the bottom of an EPBF wall.

Figure 7-30 shows a TTT diagram for Inconel 718, with a red spot indicating the temperature read by the thermocouple at the bottom of the substrate plate (approximately 980 °C) and the approximate time at temperature. Conditions toward the bottom of the samples were clearly favourable for the precipitation of the δ phase. The quantity and location of δ phase can be used to estimate the difference in temperature from the bottom to the top of the walls. Studies by Azadian et al. [198] showed δ precipitation to transition from intragranular to intergranular at temperatures of approximately 1000 °C. As the location of δ precipitation in the middle of the wall is predominantly intergranular, this would suggest a temperature difference of roughly 20 °C between the bottom and middle of the wall. Moving to the top of the wall, δ precipitation can barely be seen and instead the majority of discrete precipitates are MC carbides, this would suggest temperatures at the top of the wall are in the region of the δ solvus, approximately 1020 °C.

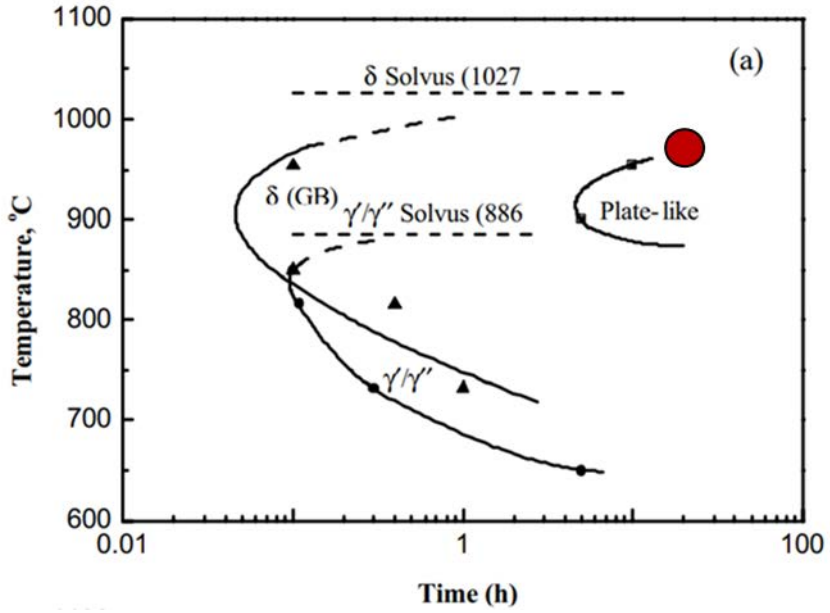

Figure 7-30: TTT diagram for IN718, highlighting the temperature at which the bottom layers of the EBM build were maintained and for how long they were held at temperature. Adapted from [199].

In addition to delta and MC carbide precipitation, multi-metal oxy-carbides such as those observed in PM HIPping can also be seen in the EPBF material (figure 7-31). Oxy-carbides precipitating in the EPBF material are significantly smaller than those in PM HIPped and have a more pronounced octagonal structure, typical of an oxy-carbide possessing an $MgO + Al_2O_3$ core.

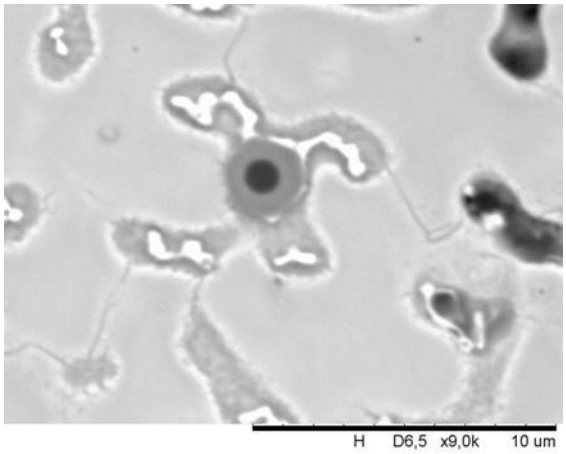

Figure 7-31: BSE micrograph showing multi-metal oxy-carbide in XY cross-section of EPBF wall.

7.5 LPBF versus EPBF

7.5.1 Energy density comparison for LoF formation in LPBF and EPBF

LPBF and EPBF parameters were chosen such that they would have similar beam powers and an overlapping range of LEDs. Comparing the LED plots in sections 7.2.1-i and 7.4.1-i for LPBF and EPBF respectively, it appears as though the threshold LED for elimination of LoF is less for LPBF (0.15 J mm^{-1}) compared to EPBF (0.2 J mm^{-1}). Given the difference in efficiency of heat transfer between each process however, it would be expected that threshold energies would be less for EPBF. This would imply that for comparison of EPBF and LPBF the LED model is not suitable. With this in mind, porosity data for LPBF 40 µm builds and EPBF 50 µm builds were replotted as a function of AED, according to equation 7-1 (figure 7-32). Incorporating the spot size into the energy density calculation, allows the influence of beam peak intensity with varying focus offset in EPBF to be accounted for. Laser spot size was interpolated using previous measurements performed for different beam powers using an Ophir laser profilometer. Laser power and corresponding spot

sizes can be seen in table 7-5. Electron beam spot sizes were interpolated from previous measurements of beam dimeter obtained using a knife-edge positioned over a Faraday cup. Electron beam measurements were not performed as part of this work and consequently cannot be disclosed.

$$\mathrm{AED} = \frac{\mathrm{P}}{2\mathrm{r} \cdot \mathrm{V}} \qquad \text{Eq. 7-1}$$

Where, P is beam power in watts, r is the beam radius in mm and V is beam velocity in mm s^{-1}.

Table 7-5: Laser beam diameter as a function of laser power.

Laser power (W)	Beam diameter (mm)
50	0.053
100	0.063
200	0.066
300	0.085
400	0.086

From figure 7-29 it can be seen that the threshold energy density for onset of LoF is approximately 0.6 J mm^{-2} for EPBF and 1.4 J mm^{-2} for LPBF, indicating EPBF to be significantly more efficient for melting than LPBF.

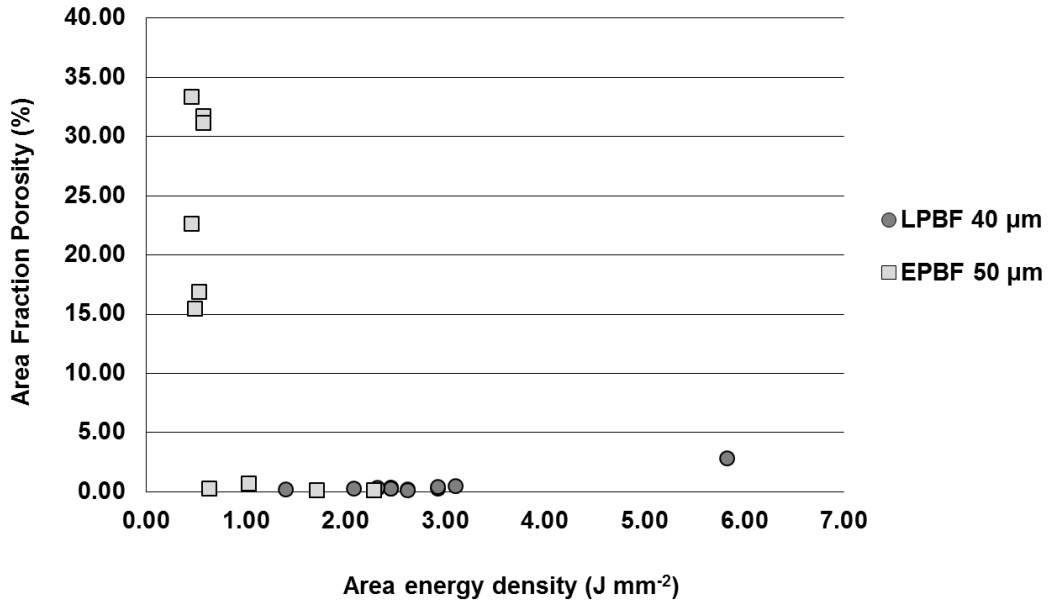

Figure 7-32: Comparison of the area energy density porosity relationship for LPBF and EPBF. Wall thickness were 1 mm.

In order to obtain a better approximation of differences in heat transfer at the melt stage of each process, the process operating temperature must be accounted for. To do this, the energy required to heat the powder from the process temperature to the solidus temperature should be compared for each process. The energy required to heat the powder to solidus can be calculated by multiplying the integration of the specific heat capacity over the process temperature range by the temperature range (Eq. 7-2).

$$\mathrm{H} = \int_{T_0}^{T_m} C_p \, dT \, \Delta T \qquad \text{Eq. 7-2}$$

Where, C_p is specific heat capacity in J $K^{-1}g^{-1}$. The resulting integrals of C_p as a function of temperature range are given by equations 7-3 and 7-4, obtained from the work of

Agazhanov et al. [200]. Equation 7-4 was assumed for the calculation of C_p in the range of 1361 to 1533 °K.

$$\int_{298}^{800} c_p dT = 0.362 + 2.118 \times 10^{-4} T \qquad \text{Eq. 7-3}$$

$$\int_{1070}^{1361} c_p dT = 0.639 - 3.355 \times 10^{-6} T \qquad \text{Eq. 7-4}$$

Calculated C_p values were substituted into equation 7-2 to give the energies required for the melting stage of each PBF process. The energy required to raise the powder temperature from room temperature to solidus, as in the case of LPBF, was calculated to be 846.97 J g^{-1}; whereas to raise the temperature from 1000 °C to solidus, as in the case of EPBF, requires just 163.69 J g^{-1}. This would suggest the elevated temperature used in the EPBF process contributes significantly to melting of powders, and as such the efficiencies of heat transfer during the melt stage do not differ as substantially as they appear to in figure 7-32. Consequently, it may be concluded that beam parameters used in LPBF such as laser power, scan speed and beam diameter, may be translated to EPBF with equivalent results in regard to defect formation. Translation of such parameters in the opposite direction however, (EPBF to LPBF) are less likely to yield equivalent results.

7.5.2 Microstructure and precipitation

The most significant difference between LPBF and EPBF microstructures is the homogeneity of microstructure. LPBF walls exhibit similar grain size, morphology, and

precipitation throughout, however EPBF specimens show a graduating microstructure from the bottom to the top of the build. Columnar grains in LPBF are 250-500 μm in length and 5-20 μm in diameter. While it would be expected that EPBF, being carried out at elevated temperature, would exhibit coarser grains relative to LPBF, this is not the case; grain diameters in the bottom of EPBF specimens are in the range of 5 to 10 μm. This likely results from the precipitation of vast quantities of δ, which restrict growth of the grains.

The vast majority of precipitates observed in LPBF specimens is in the nanometre range and consists of MC type carbides, δ and laves. Precipitation observed at the top of EPBF walls is similar in size to the largest NbC carbides observed in the LPBF specimens; suggesting that as build height increases the cooling rates achieved in LPBF are approached in EPBF.

7.6 Influence of post process HIP and HT on LPBF tensile properties

7.6.1 Tensile properties of as-fabricated Inconel 718

Tensile testing was performed for as-fabricated LPBF samples to provide comparisons for HIP and HIP + HT tensile data. Figures 7-33 and 7-34 show the results of RT tensile testing for the as-fabricated LPBF samples. The average yield, UTS and elongation are all substantially lower compared to values seen in the literature. In addition, significant variation exists between samples. The sample with the lowest elongation had a tensile strain of just 0.37 %; suggesting the presence of defects within the sample.

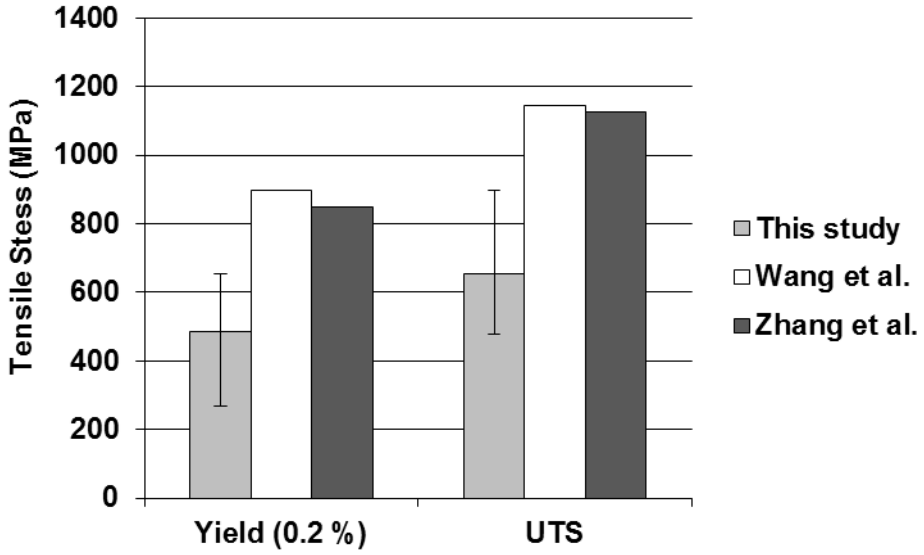

Figure 7-33: RT tensile yield and UTS results for as-fabricated LPBF Inconel 718. Data for two studies in the literature are also presented. Tensile test direction was parallel to the build direction for all specimens.

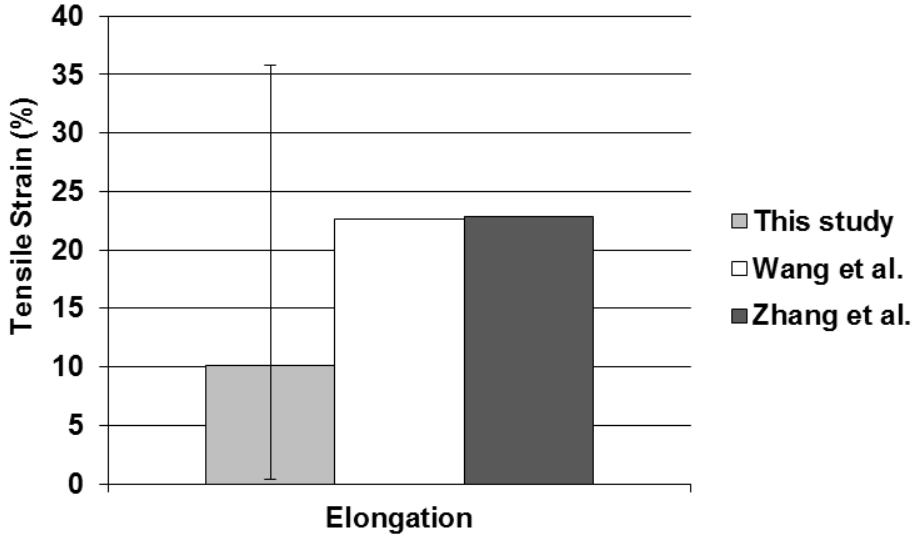

Figure 7-34: RT tensile elongation results for as-fabricated LPBF Inconel 718. Data for two studies in the literature are also presented. Tensile test direction was parallel to the build direction for all specimens.

i. Fractography

Fractography was performed to understand the reason for the diminishment in tensile properties. Figure 7-35 shows the fracture surfaces of the two tensile specimens exhibiting the worst performance. Large, unmelted powder particles can be clearly seen in the fracture surface. These particles will have acted as crack initiators leading to early failure of the specimens. Figure 7-36 shows the fracture surface of the tensile specimen with the best performance. The fracture surface is clear of unmelted powder.

a) **b)**

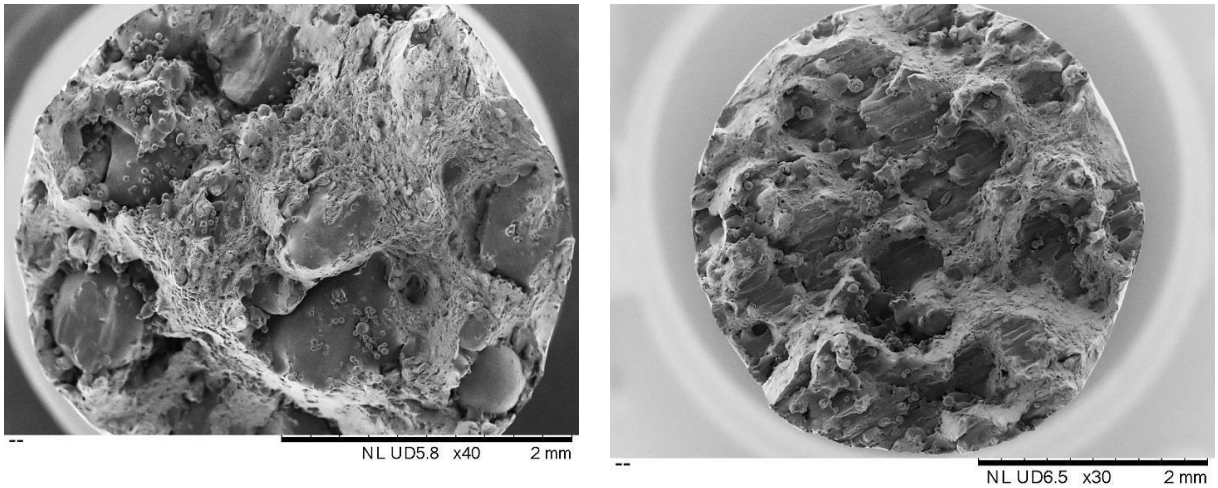

Figure 7-35: SE micrographs of the fracture surface of LPBF samples exhibiting the lowest yield, UTS and elongation.

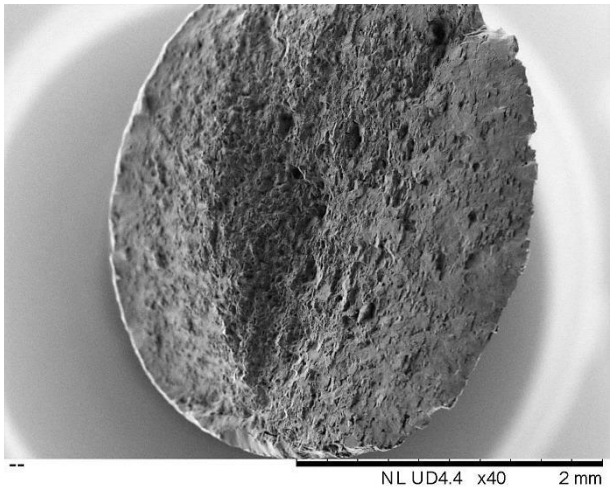

Figure 7-36: SE SEM micrograph showing fracture surface of sample with 35.8 % elongation.

The size of the unmelted powder particles in the tensile bars range from 400 to 600 µm. In addition, some of these larger particles have smaller spherical particles on their surfaces; both the size and morphology of the unmelted regions suggest they are spatter particles formed during processing. Spatter particles are created when molten metal is ejected from the melt pool during processing or powder particles are entrained in metal vapour. The larger spatter particles observed in the tensile bar are indictive of melt ejection[201]. Khairallah et al.[202] simulated the melt flow and mechanism of spatter formation by melt ejection. Figure 7-37 shows graphics of the simulated melt behaviour. A build-up of liquid occurs ahead of the melt pool depression -incident location of the laser- spilling over the front of the melt pool as the laser progresses forward. When the melt pool depression is disrupted, either through switching off of the laser or a change in direction, the melt pool collapses and the liquid ahead of the melt pool breaks away. The keyhole vapour plume then exerts force on this liquid ejecting it from the melt pool. Due to the surface tension the ejected melt will break up into a series of smaller melt droplets.

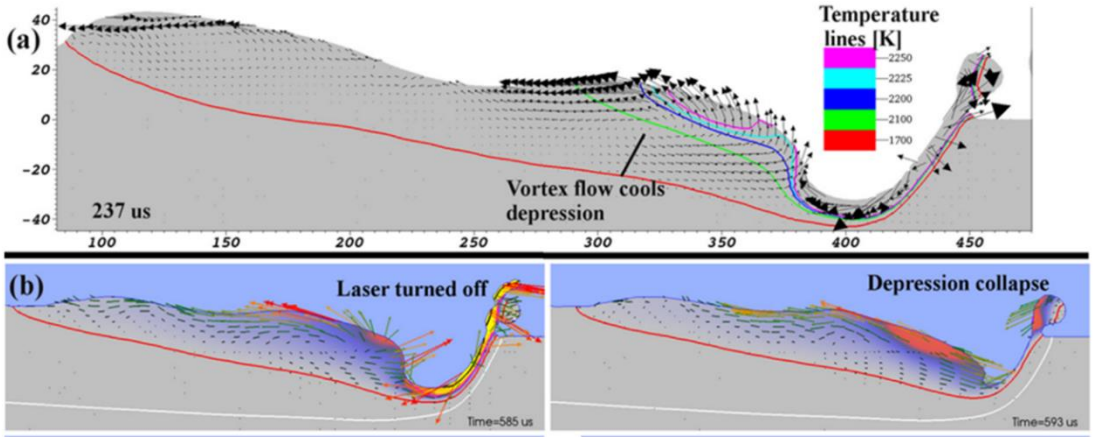

Figure 7-37: Graphical illustration of simulated melt behaviour leading to the formation of spatter particles. Modified from [202].

The gas flow in LPBF systems is responsible for removing spatter particles in addition to maintaining low oxygen environments. If gas flow velocity is not sufficient, spatter particles will fall back into the powder bed. Smaller particles will be remelted and incorporated into the build part, yet larger particles, such as those seen in the tensile bars, will require significantly more energy to remelt them. The discrepancies in tensile properties of as-fabricated specimens likely results from the location of specimens on the build plate relative to the gas flow extraction. Figure 7-38 illustrates the location of gas inlet and outlet in the model of Concept M2 LPBF system used in these studies. The gas inlet and outlet are position on the backside of the machine system. An array of pipes span the entire depth of the machine system to channel the inlet gas; while this appears as though it would create a linear flow of gas, a pressure difference will occur according to the location of each pipe, with the pipe closest to the main inlet line having higher flow pressure. Furthermore, the extraction pressure will be increased closer to the outlet pipe. This ultimately results in an increase in gas flow

rate toward the back of the machine system and a slower flow rate at the front of the system. Consequently, spatter removal will not be as efficient on the front side of the build plate.

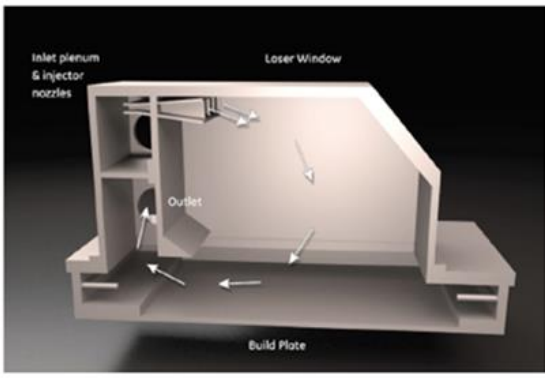

Figure 7-38: Graphic showing gas flow inlet and outlet positions in the model of Concept M2 LPBF system used in this study.

7.6.2 Tensile properties of LPBF + HIP Inconel 718

HIPping was performed on the LPBF specimens for tensile testing in order to provide a comparison for strength testing of the in-situ shelling LPBF-PM HIPped interface.

i. Microstructure of LPBF + HIP Inconel 718

Figure 7-39 shows an optical image of the LPBF material post HIPping. The grains have grown in diameter, previously ranging from 5 to 20 μm and now averaging approximately 60 μm. Etching is no longer revealing segregation around dendrites indicating diffusion of Nb films.

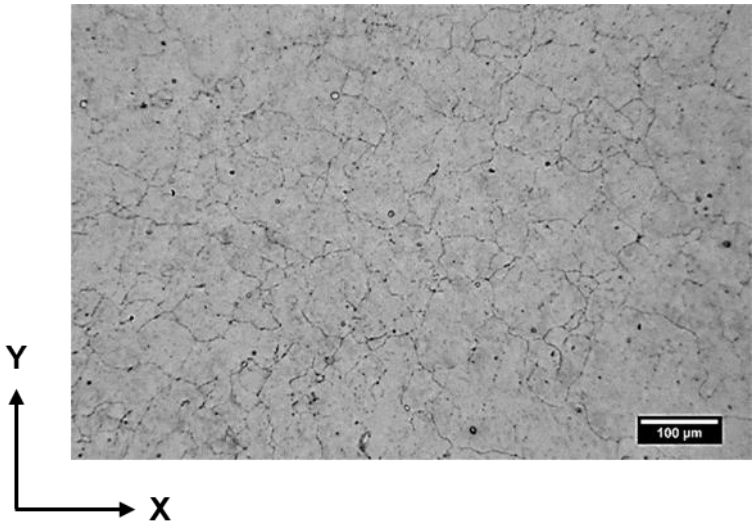

Figure 7-39: Optical micrograph of etched LPBF + HIP Inconel 718

Dual contrast SEM imaging of the SLM+HIP samples (figure 7-40) revealed three morphologies of precipitate. Most precipitates are NbC carbides. A limited number of bright particles have a needle/ platelet type morphology and are likely δ precipitates. These precipitates tend to present closer to the grain boundaries whereas NbC carbides are distributed within the grains as well as along grain boundaries. In addition to carbides and delta, multi-metal oxy-carbides, such as those seen in PM HIPping and EPBF samples have appeared.

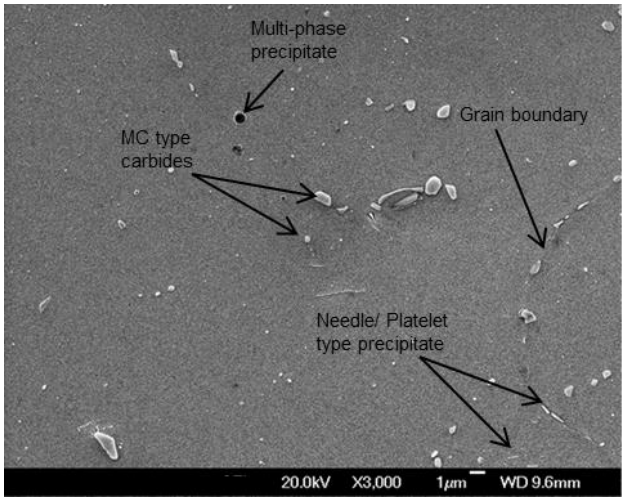

Figure 7-40: Dual contrast (BSE+SE) micrograph of precipitates in LPBF + HIP microstructure.

Surprisingly very little literature could be found comparing the microstructure of as-fabricated and LPBF + HIP Inconel 718[203] with previous studies opting to apply both HIP and HT together, often applying homogenisation or stress relief treatments prior to HIPping[47, 149, 167, 204]. Furthermore, studies examining the influence of just HIP[203] on LPBF samples do not examine the precipitation in the LPBF + HIPped samples, disclosing only optical images of the grain structure (figure 7-41); some platelet like features do however appear in the optical images suggesting the presence of delta precipitation as is seen in this study. Comparing optical images from this work with those in figure 7-41, grain size in the present study is significantly smaller; this may result from an increased level of recrystallisation in this work owing to the higher temperatures and pressures implemented (1180°C and 120 MPa respectively).

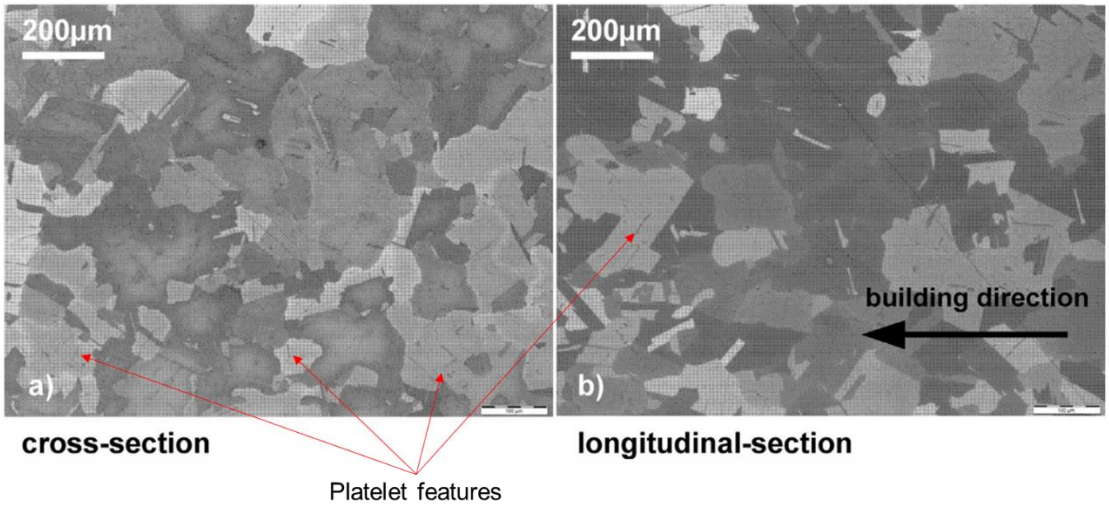

Figure 7-41: Light microscope images of etched (Kalling 2) LPBF samples post HIPping (1150 ◦C/100 MPa/4 h) from the work of Tillmann et al.[203]. Platelet like features suspected to be δ precipitates are indicated by the arrows.

ii. Tensile properties

Figures 7-42 and 7-43 show the results of tensile testing performed on LPBF + HIP samples. Yield and UTS are significantly higher in the LPBF + HIP specimens compared to the as fabricated specimen. Improvement in mechanical properties following HIPping result from two things, firstly the absence of segregation and laves phase, and secondly the precipitation of MC type carbides and small quantities of delta at the grain boundaries. While yield and UTS have improved significantly they do not reach the minimum requirement of AMS standard 5662 for wrought + HT Inconel 718, resulting from a lack of γ'', which would not have had time to precipitate during the HIPping cycle. As expected, elongation has declined relative to the as-fabricated sample, resulting from recrystallisation of grains such that fewer grains are oriented in the direction of applied tensile stress.

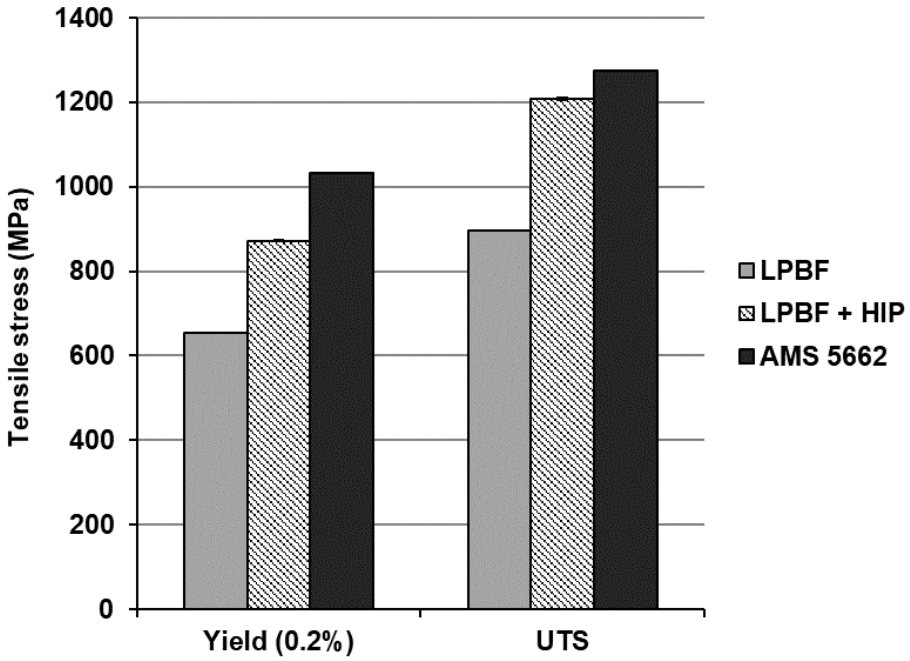

Figure 7-42: RT tensile yield and UTS results for LPBF+HIP Inconel 718. Data for the best performing tensile specimen in as-fabricated state, and the minimum required standard wrought + HT properties are included for comparison.

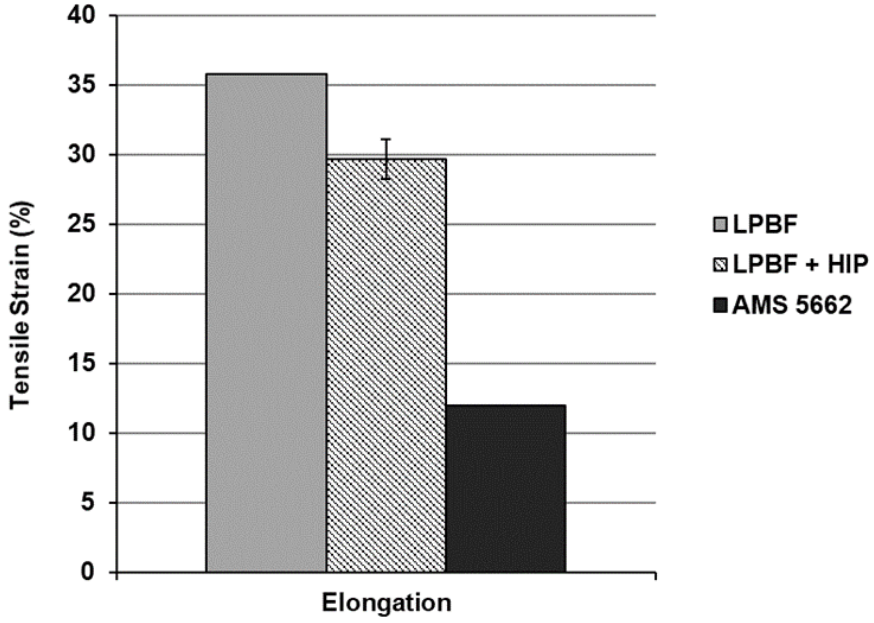

Figure 7-43: RT tensile elongation results for LPBF+HIP Inconel 718. Data for the best performing tensile specimen in as-fabricated state, and the minimum required standard wrought + HT properties are included for comparison.

iii. Fractography

Examination of the fracture surface of LPBF + HIP tensile specimens (figure 7-44-a and -b) shows a mixed mode of failure at the centre of the specimen with a more ductile mode of failure observed at the outer edge. This is concurrent with the tensile data, that shows a decline in elongation relative to the best as-fabricated specimens (figure 7-43). Figure 7-44-b shows a typical image of fracture surface within the centre region of the specimen. Multiple MC type carbides and multi-metal oxy carbides can be observed on the surface. The γ matrix exhibits micro-void coalescence suggesting a ductile mode of failure, while the precipitates remain undeformed or possess clean fractures due to their brittle nature. Grain boundary cracking is also observed, which may result from the precipitation of grain boundary δ seen in figure 7-39.

a) **b)**

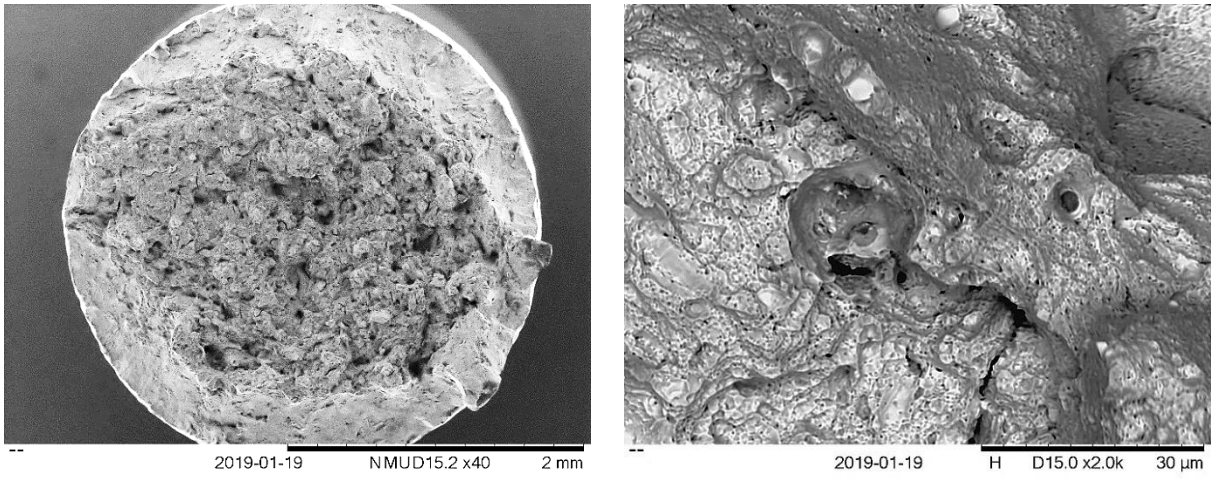

Figure 7-44: SEM micrographs of LPBF + HIP fracture surfaces: a) low magnification SE image of entire fracture surface; b) high magnification BSE image of carbides and oxy-carbides on fracture surface.

7.6.3 Tensile properties of LPBF + HIP + HT Inconel 718

A standard HT consisting of solutionising and double ageing was applied to LPBF + HIP specimens to see if precipitates observed in LPBF + HIP specimens could be replaced with more favourable strengthening precipitates such as γ' and γ''.

i. Microstructure

Figure 7-45 shows an optical micrograph of the grain structure of LPBF + HIP + HT material as revealed by etching. Very little has changed in the morphology or size of grains between the LPBF + HIP and LPBF + HIP + HT material. In regard to precipitation, all three phases previously observed are still observed following HT. Carbides however seem to be more evenly distributed and of a smaller size on average (figure 7-46), suggesting some dissolution of the phase. Higher magnification imaging of the etched microstructure reveals a network of precipitates in a size range less than 100 nm (figure 7-47-a). While there are some precipitates of elongated morphology in the microstructure, they are not of the typical disc/ acicular morphology of the γ'' and resemble more of the spherical morphology of γ' that presents prior to ageing. Figure 7-47-b shows a comparable microstructure produced by SLM of IN718 followed by a homogenisation heat treatment (1150 ° C for 2 hrs), air cooling and ageing (700 ° C for 12 hrs). While the HT stages differ significantly between samples, the initial homogenization stage of the HT developed by Li et al. [6] is similar in temperature and time to the HIP treatment implemented here. Li et al. [6] observed both γ' and γ'' to have a circular morphology following implementation of their novel HT. Li et al. performed TEM to verify the presence of γ' and γ''.

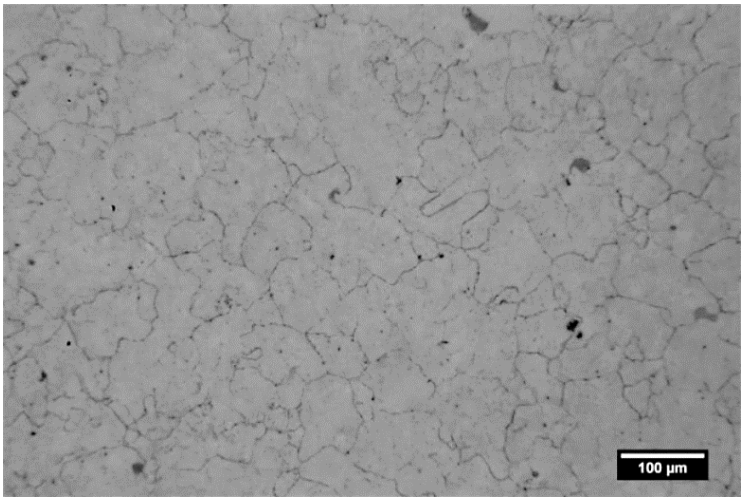

Figure 7-45: Optical micrograph of etched LPBF + HIP + HT specimen.

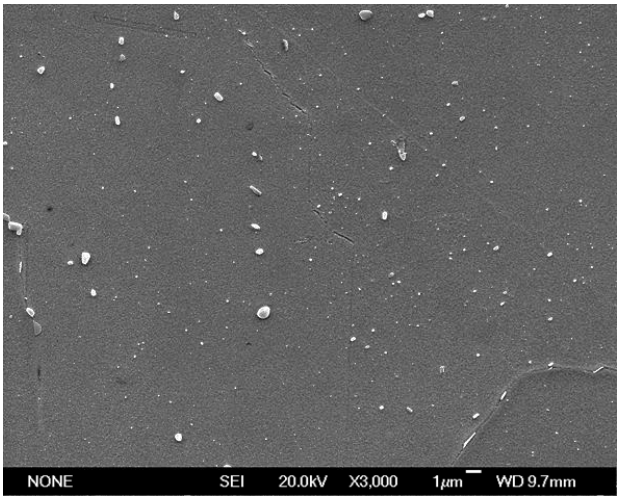

Figure 7-46: Precipitates in LPBF + HIP + HT microstructure.

a) b)

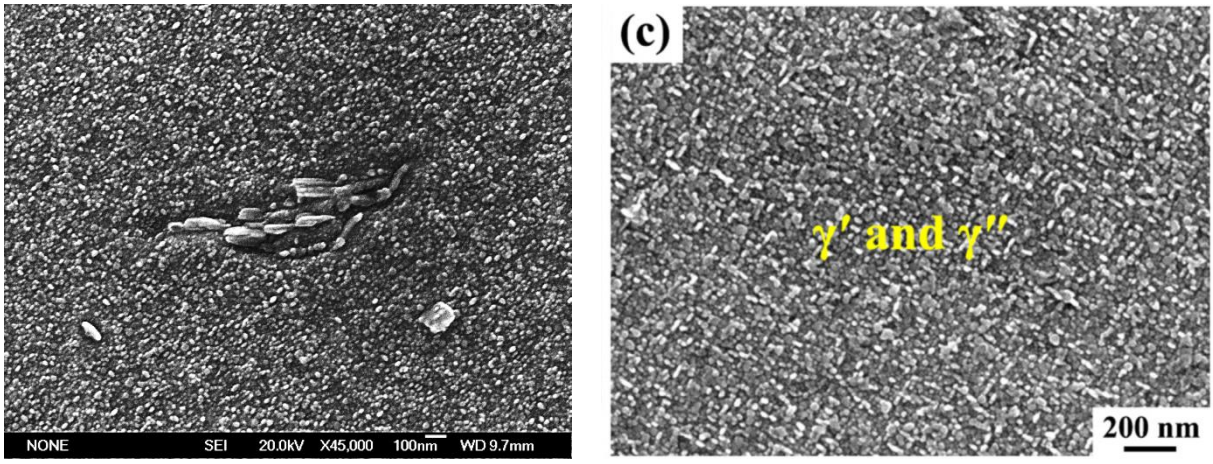

Figure 7-47: High magnification SE SEM micrographs of precipitates in HT Inconel 718 fabricated by LPBF: a) microstructure of LPBF + HIP + HT sample produced in this study and b) microstructure of LPBF + HT sample produced in studies by Li et al. [6].

ii. Tensile properties

Figure 7-48 shows the tensile yield and UTS properties for LPBF + HIP + HT samples. Properties exceed those of both LPBF + HIP and the minimum required standard, indicating the precipitation observed in figure 7-46-a is in fact γ' and γ''. Elongation properties can be seen in figure 7-49; while significantly higher than the minimum required standard for both RT and ET testing, there has been a reduction in elongation from the LPBF + HIP sample. This is concurrent with the increase in strength owing to precipitation of γ' and γ'', following the strength plasticity trade-off model. Results of LPBF + HIP + HT tensile testing from the literature have been provided for comparison[149]. To the best of the authors knowledge, these are the best tensile results achieved for Inconel 718 processed by LPBF with HT. Yield and UTS values obtained from this study are significantly lower than those achieved by Kuo et al.[149]. This is thought to result from the difference in HT conditions. Kuo et al. compared two HT conditions, one standard HT and one direct ageing treatment. They found

direct ageing to lead to improved properties as this restricted coarsening of δ precipitates observed prior to HT. Solutionising was found to result in an increase in intragranular coarse δ precipitation. Given that these studies applied solutionising prior to aging, it may be suggested that increased quantities of δ precipitation have occurred here and as such precipitation of γ' and γ" have been restricted.

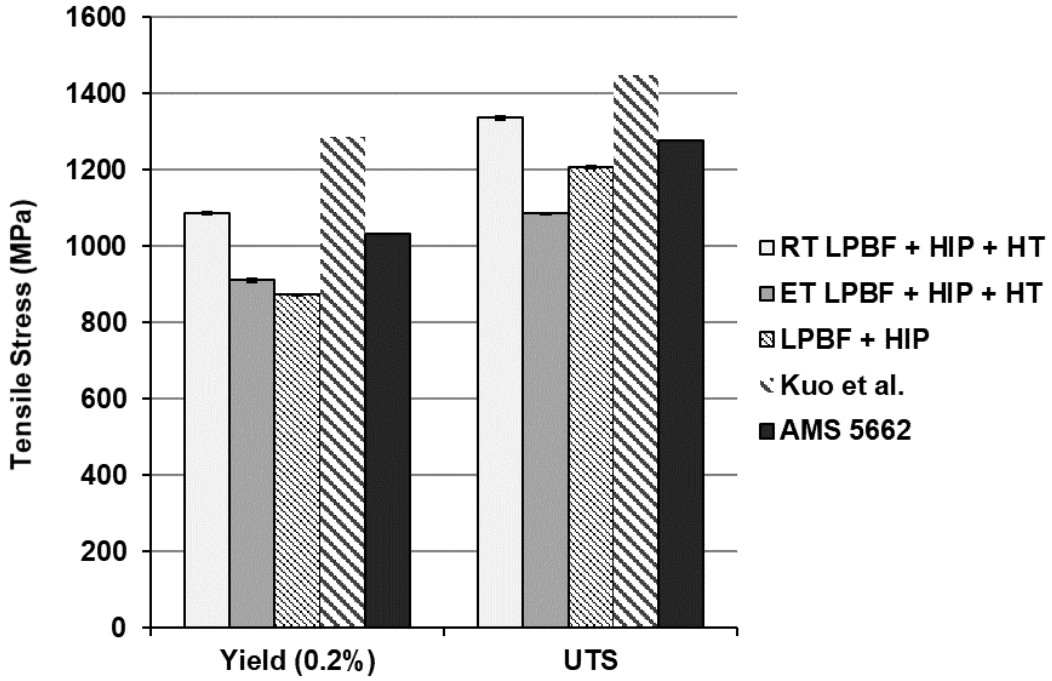

Figure 7-48: RT and ET tensile yield and UTS results for LPBF+HIP+HT Inconel 718. Data for LPBF+HIP, and the minimum required standard wrought + HT properties are included for comparison.

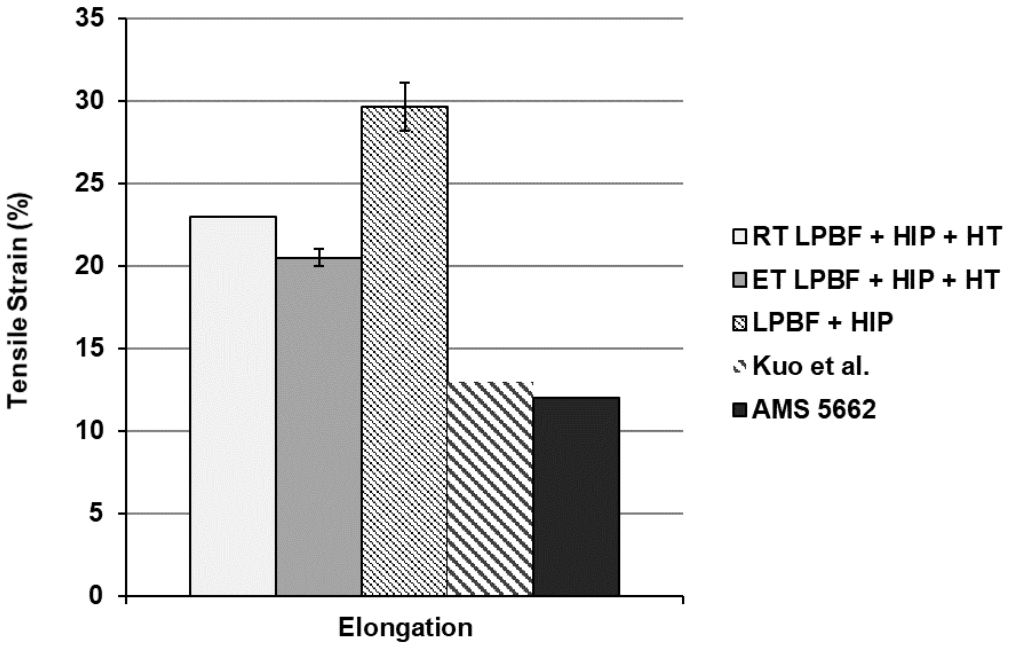

Figure 7-49: RT and ET tensile elongation results for LPBF+HIP+HT Inconel 718. Data for LPBF+HIP, and the minimum required standard wrought + HT properties are included for comparison.

7.7 Summary

The importance of matching powder size to layer thickness was highlighted. It was hypothesised that significant variation in the porosity values results in localised removal of powder from the build plate and consequently an increase in the formation of LoF voids and keyhole pores. Considering the propensity of defect formation in 20 and 60 µm layer LPBF builds, 40 µm layer thicknesses should be used for production of HIPping canister in the in-situ shelling work. In both LPBF and EPBF LoF was found to follow the energy density trends previously observed in the literature for PBF of Ni-base superalloys. A comparison of energy required to melt powders resulting in high density parts was presented, showing that the elevated build temperature in EPBF has a significant influence on the energy required to melt.

Grain size and precipitation in the LPBF and EPBF walls did not differ significantly as a function of processing parameters. Microstructures of the LPBF walls were relatively homogenous in both XZ and XY cross-section. Conversely in EPBF walls, microstructural variation was observed from the top to the bottom of walls and across the XY cross-section. Consequently, HIPping canister constructed in EPBF may require homogenisation HT prior to HIPping, as microstructural variation could result in anisotropic shrinkage.

Studies investigating the influence of LPBF process parameters on surface finish, showed surface roughness to be controllable. Average surface roughness was influenced by layer thickness, hatch and contour laser power, contour scan speed and the number of contour scans performed. It has been suggested that increasing surface roughness may increase the number of point contacts between LPBF canister walls and powder in in-situ shelling canisters, resulting in increased recrystallisation at the LPBF-PM HIPped interface and leading to an improvement in bonding. Consequently, the contour parameters exhibiting the highest surface roughness across all hatch parameters will be implemented at the in-situ shelling stage.

Tensile properties of as-fabricated LPBF specimens were seen to vary significantly. This was observed to be due to a reduction in melting of some of the tensile specimens. It was concluded that significant spatter formation occurred during building of the as-fabricated specimens, which was then reincorporated into the powder bed. It was suggested that this was the result of poor gas flow in the Concept M2 LPBF system. HIPping and HT of LPBF samples resulted in an improvement of tensile properties, owing to recrystallisation of grains, grain boundary delta precipitation during HIPping and the precipitation of γ’ and γ’’ in HT.

Chapter 8

In-situ Shelling

8.1 Introduction

The work thus far, has provided an understanding of the behaviour of Inconel 718 powder in PM HIPping, LPBF and EPBF. The objective of this work being, to optimise conditions in each process such that when the processes are combined in the in-situ shelling method, optimal microstructures can be achieved. PM HIPping studies showed PPB formation to be substantial in Inconel 718 powders, resulting in poor tensile properties. Favourable microstructures and tensile properties were achievable in LPBF, however inconsistencies in data presented concerns for repeatability of process. Significant levels of porosity were observed in EPBF due to poor processing conditions and samples showed inhomogeneity in the microstructure, which if HIPping parameters were not adapted, could lead to variation in deformation behaviour during densification of component cores in HIPping.

This chapter will initially examine the influence of wall thickness on the densification of LPBF in-situ shelling samples, followed by examination of the PM HIPped and LPBF+HIP microstructure. Proceeding this the influence of LPBF surface finish and scan strategy and build orientation on grain growth across the LPBF-PM HIPped interface are assessed. A variety of surface features are then built onto the base and wall of LPBF cans to ascertain if bond strength can be improved by altering surface geometry. In-situ shelling samples are produced utilising EPBF, and their microstructures compared with those produced by LPBF. Finally, a proof-of-concept study is presented for the LPBF in-situ shelling of an impeller

component, examining the economics of the LPBF in-situ shelling process relative to state-of-the-art HIPping for a complex geometry component.

8.2 Influence of LPBF canister wall thickness

The European Powder Metallurgy Association (EPMA) produced a design guide[8] for HIPping canisters in which it is stated that wall thickness is important for controlling anisotropy of shrinkage, however when reviewing the literature very few papers could be found to comment on this. The absence of research into this area is likely to stem from the fact that the most efficient way to construct a cylindrical HIPping canister is to use pipe, consequently the user is restricted to dimensions specified by the production standards. A benefit of using LPBF to build HIPping canisters is that wall thickness can be easily tailored, and as a result the influence of wall thickness on anisotropy of shrinkage can be examined more freely. Eight canisters were built with four different wall thicknesses of 0.75, 1, 1.5 and 2 mm.

8.2.1 As-fabricated canisters

During removal of canisters from the plate, it was observed that one of the canisters with 1.5 mm wall thickness had a large hole in its side (figure 8-1). Such a large defect is likely to result from a repeated lack of powder spreading to the build area.

Figure 8-1: Hole in the side of LPBF canister with wall thickness 1.5 mm.

Following removal of the canisters from the plate outgassing tubes were welded to the top of each canister and a gas leak test was performed using the outgassing rig described in chapter 4. If the canister did not reach the target pressure (10^{-2} mbar) within 20 minutes, then it was suspected to have had surface connected porosity and deemed not to be unsuitable for HIPping. Only three out of the remaining seven canisters passed leak testing. Canisters that passed leak testing were prepared for HIPping as outlined in chapter 4. Two of the canisters that failed leak testing- 0.75 mm and 2 mm wall thickness- were emptied of powder and sectioned to see if surface connected porosity could be observed. While no obvious porosity could be observed in the side walls of the canister, large lack of fusion voids could be seen in the base of each canister (figure 8-2).

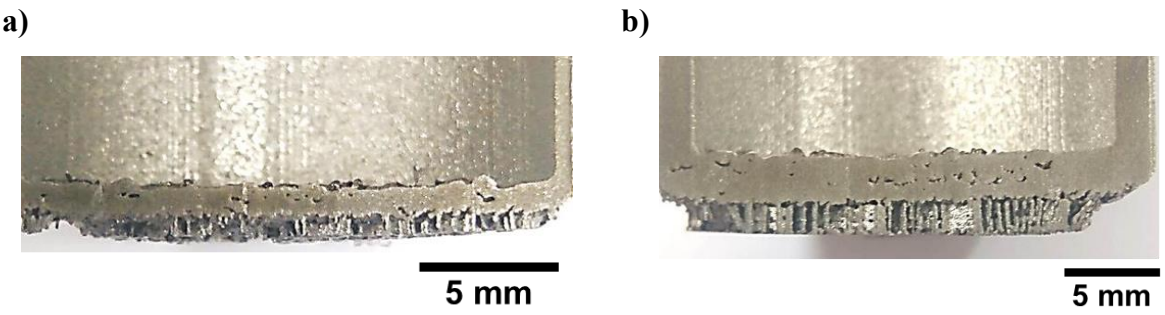

Figure 8-2: Photographs of the base cross-section of two LPBF in-situ shelling canisters. a) canister with 0.75 mm wall thickness & b) canister with 2 mm wall thickness.

LoF voids commonly result from two things, poor powder spreading and/or a lack of energy for melting. For a canister with 2 mm wall thickness, approximate average scan length in the base of the canister is 6.5 mm whereas in the walls of the canister it is 2.9 mm. As discussed in chapter 7 scan line length can have a significant effect on the temperature and consequently the geometry of the melt pool, with shorter scan tracks leading to an increased accumulation of heat and larger melt pools. Having optimised the parameters for the canisters using thin wall structures, it is highly likely that the formation of LoF voids in the base of the canisters is the result of having smaller melt pools arising from less heat accumulation between the longer scan tracks in the scanning of the base.

8.2.2 Canister shrinkage

Figure 8-3 shows an image of the three canisters with wall thicknesses, 0.75, 1 and 2 mm, after being removed from the HIP. Canisters have turned black during HIPping resulting from the precipitation of a continuous oxide scale. Measurements of the minimum and maximum diameters and height of the canisters were taken using callipers, as described in figure 8-4.

Figure 8-3: In-situ shelling canisters after being removed from the HIP.

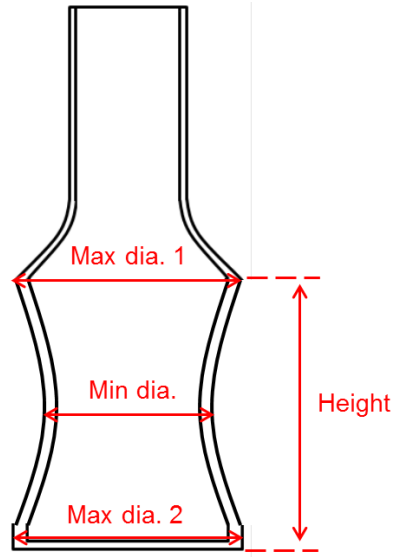

Figure 8-4: Locations of canister measurement positions.

Figure 8-5 shows the radial and longitudinal shrinkage of in-situ shelling canisters as a function of wall thickness. Shrinkage appears to be significantly higher in the 0.75 mm canisters

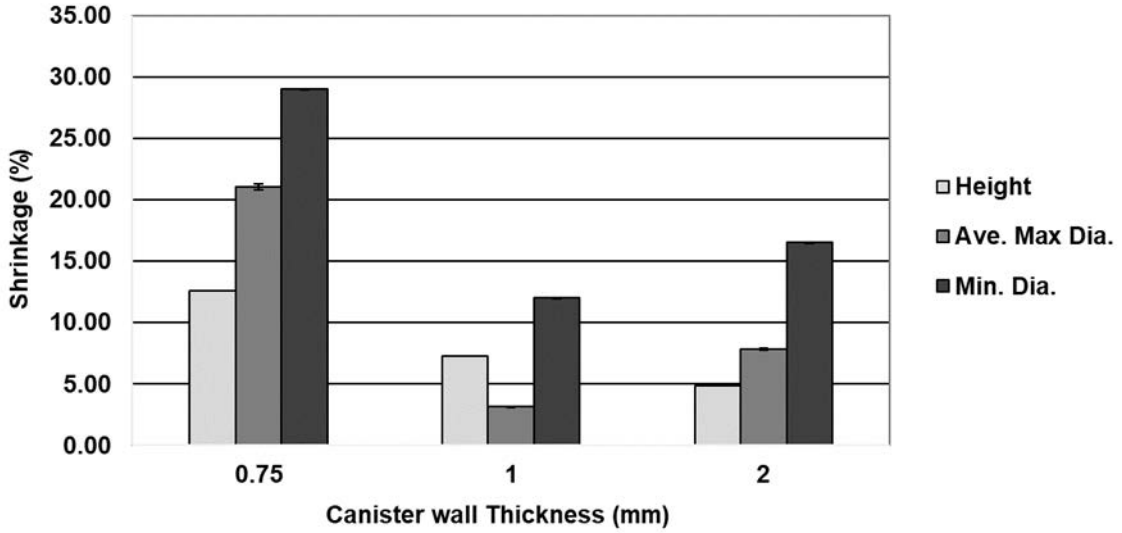

Figure 8-5: Shrinkage in in-situ shelling canisters as a function of canister wall thickness.

Substantial differences in shrinkage, such as is seen here, are likely due to inconsistencies in powder packing between canisters. While the canisters all went through the same process about powder filling post LPBF, during LPBF the position of canisters on the substrate plate may have affected the size of powder particles encapsulated in each canister, and therefore influence the potential packing densities that can be achieved. However, in later HIP runs for other research projects, it was discovered that the pressure regulation of the HIP had not been properly functioning. The time at which the HIP had started to malfunction was unknown and consequently it was decided that a repeat experiment should be conducted.

Four more canisters were produced for the repat experiment, one for each wall thickness. All four canisters evacuated successfully after powder filling and were put into the HIP. Figure 8-6 shows the shrinkage as a function of wall thickness for all four canisters. The canisters with wall thicknesses of 1- and 1.5- mm had significantly reduced shrinkage compared to those with 0.75- and 2-mm wall thicknesses. The canisters were cross sectioned from top to bottom down their centre line. In both canisters cracking was observed at the

location where the outgassing tube was welded to the LPBF canister (figure8-7). It is very possible that liquation cracking occurred in the LPBF canister during welding, and under the pressure of the HIP cracks opened and propagated toward the surface along the weld seam. As discussed earlier, surface connected cracking would allow an influx of gas into the HIP canister preventing full consolidation of the powders.

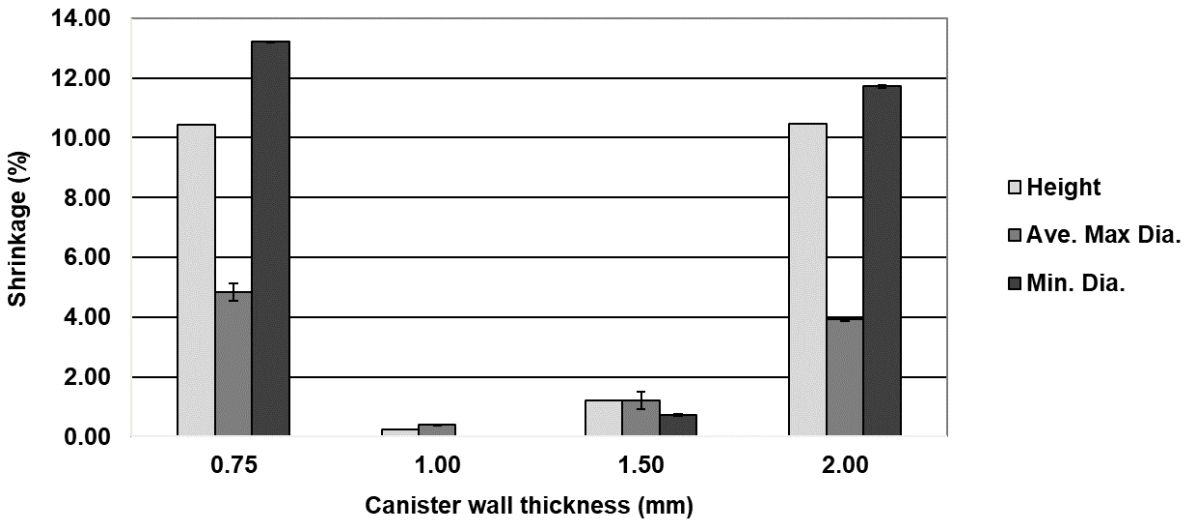

Figure 8-6: Shrinkage in in-situ shelling canisters as a function of canister wall thickness for the second in-situ shelling trial.

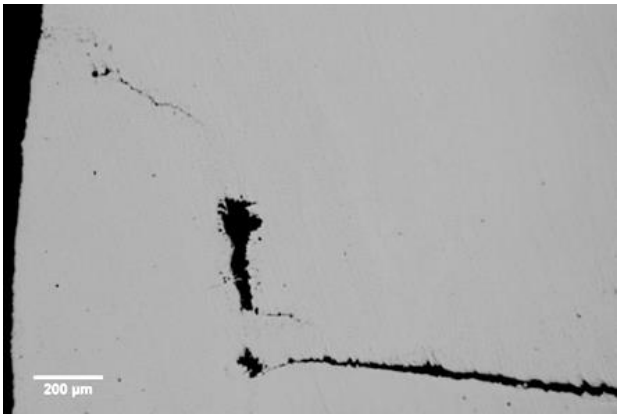

Figure 8-7: Optical micrograph of cracking and surface connected void at the weld between the LPBF canister and mild steel filling/outgassing tube.

Longitudinal shrinkage (height) of the 0.75- and 2-mm wall thickness canisters did not differ significantly; however radial shrinkage did, with increased shrinkage in the canister with 0.75 mm wall thickness. This was to be expected as increasing the wall thickness to diameter ratio increases the resistance to deformation[205]. Given the equivalent shrinkage in the longitudinal axis for both canisters, these results conflict with the existing literature. Previous studies have shown that decreasing wall thickness for a constant canister diameter, results in the ratio of longitudinal and radial shrinkage to tend towards one[50-52], however in these studies canisters with walls as thin as 0.75 mm were not considered.

8.3 HIPped powder microstructure

Following HIPping, canisters from both the first and second in-situ shelling trials were sectioned longitudinally down their centre lines. Upon sectioning of the samples from the first study, multiple LoF voids could be observed in the HIPped powder of canisters with 1- and 2-mm wall thicknesses (fig, 8-8-a). This was consistent with the results of the shrinkage measurements presented in section 8.2.2. A variation in contrast of the LoF voids in BSE

imaging suggested some of the voids possessed different chemistries. EDS mapping (figure 8-8-b) revealed Al to be present in several of the voids. While Alumina suspension was used for final polish of the samples and could have been left deposited in the voids, it was highly unlikely as each sample was ultrasonically cleaned in soap solution for 30 minutes following polishing, followed by several repetitions of washing samples in ethanol and drying. To confirm the presence of Al oxides in the powder, samples of the powder reclaimed from the build were examined. Figure 8-9 and 8-10 show BSE and EDS analysis of the reclaimed powder particles. In addition to the discrete Al oxides and Ti carbides that were observed during initial powder characterisation, dark splatters of undefined morphology can also be observed on the powder surface. Furthermore, some powder particles appear to be slightly darker than others. EDS line scans between lighter and darker powder particles (figure 8-10) showed an increase in Al contents in the slightly darker powder particle. The darker contrast observed in BSE is therefore likely to result from a coating of Al on the powder particle. As discussed in chapter 2, it is common for light elements such as Al to vaporise during melting as the beam powers required for melting heavier elements produce temperatures significantly higher than the melting temperature of the lighter elements. Metal vapours should be pulled away from the powderbed by a constant stream of inert gas flowing above the powderbed, however if the gas velocity is too slow, metal vapours will cool and condense over the powder bed falling back onto the powders[201]. The concept M2 system used in these studies uses a constant flow of argon gas to remove metal vapours and spatter from the build area; accordingly, oxygen content is in the range of 100 to 200 ppm. Such low concentrations of oxygen increase the affinity of Al for oxygen[31] and consequently Al vapour tends to combine with oxygen in the atmosphere during condensation resulting in the formation, and deposit into the powderbed, of Al oxide.

a) b)

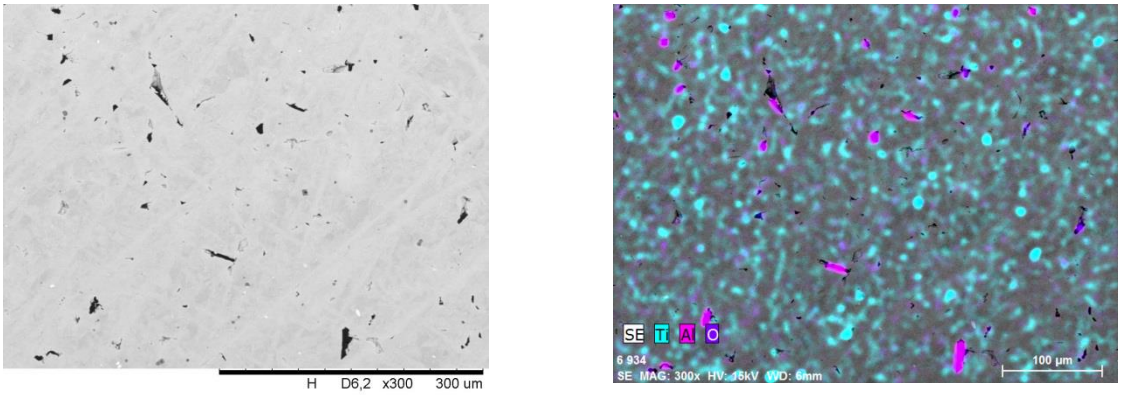

Figure 8-8: SEM micrographs of cross-sections of HIPped powder in the 2 mm thick in-situ shelling canister. Microstructures are typical of those observed in the 1 mm canister also. a) BSE image and b) BSE image with overlying EDS map.

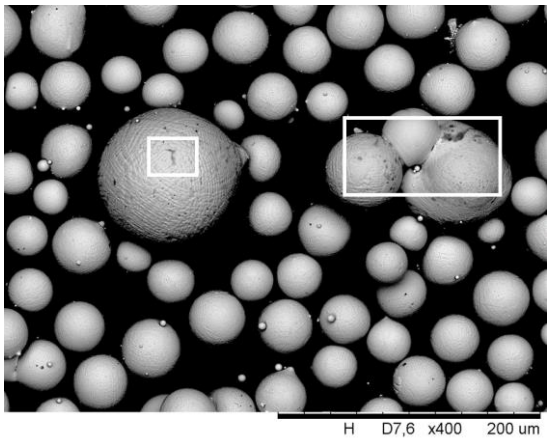

Figure 8-9: BSE image of powder particles reclaimed from the LPBF stage of the first in-situ shelling trial. Regions of deposits on powder are indicated by the white box.

a) **b)**

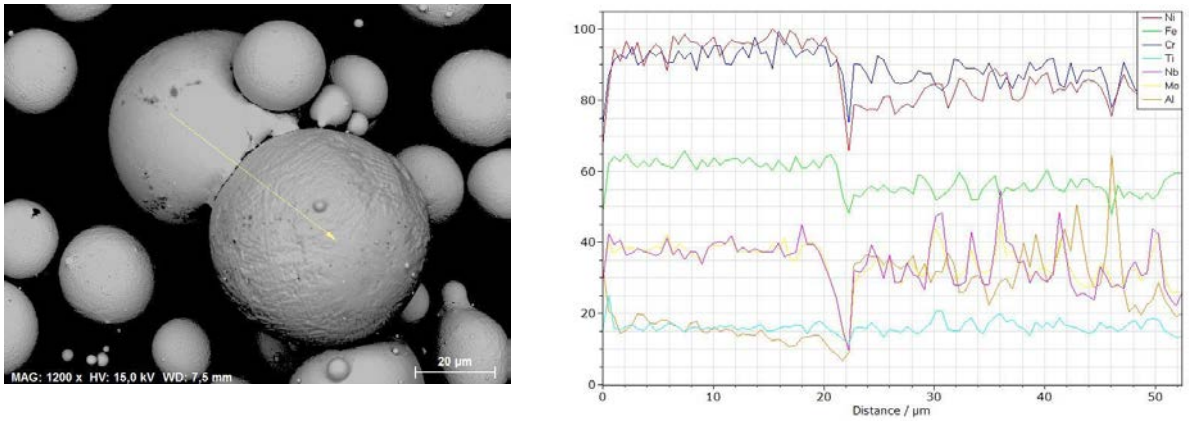

Figure 8-10: Two adjoined powder particles overserved in powder reclaimed from the LPBF stage of the first in-situ shelling trial: a) BSE image with indication of direction of EDS line scan and b) spectra for the EDS line scan.

The presence of Al and Al oxide deposits in the reclaimed Inconel 718 powder may also explain the LoF voids observed in the base of the canisters that failed leak testing (figure 8-2). While it was originally speculated that LoF voids occurred due to insufficient energy for melting of the larger base area, relative to the thin walls for which parameters were optimised; it could well be that insufficient removal of Al vapor from above the build area resulted in attenuation of the laser beam power as it passed through the metal vapour and onto the powderbed[107]. As the first set of canisters were produced with the LPBF tensile bar build it may also be deduced that large spatter particles could have been incorporated into the powderbed in the area of the canister builds.

8.3.1 PPBs

HIPped powders inside the 0.75- and 2-mm in-situ shelling canisters produced in the second build study, were examined for PPBs. BSE images were taken at several locations within the HIPped powder, at the top, middle and bottom, and centre and edge of the canisters. Figure 8-11 shows the typical microstructures for powders HIPped in 0.75 mm and 2 mm in-situ shelling canisters. Both powders contain multiple PPBs independent of location within the canister. This is in contrast to the traditionally HIPped powders in which PPBs showed location dependance. The improvement in homogeneity of PPBs in the in-situ shelling canisters is likely to result from two things; firstly, as the canister and powder material are the same, there is no increase in carbon content at the canister wall promoting the formation of a diffusion zone. Secondly, during preparation of the in-situ canisters for HIPping, less time was required on the HIP can shaker to reach tap density, and consequently powder particle size separation, due to Brazil nut effect, was less likely to occur. As discussed in chapter 6, smaller power particle sizes tend to lead to an increase in PPBs, owing to the larger surface area to volume ratio. The increased efficiency of powder filling may have resulted from the smaller canister size used for in-situ shelling canisters relative to the traditional HIPping canister; and/or filling the majority of powders during the LPBF build improved initial powder packing.

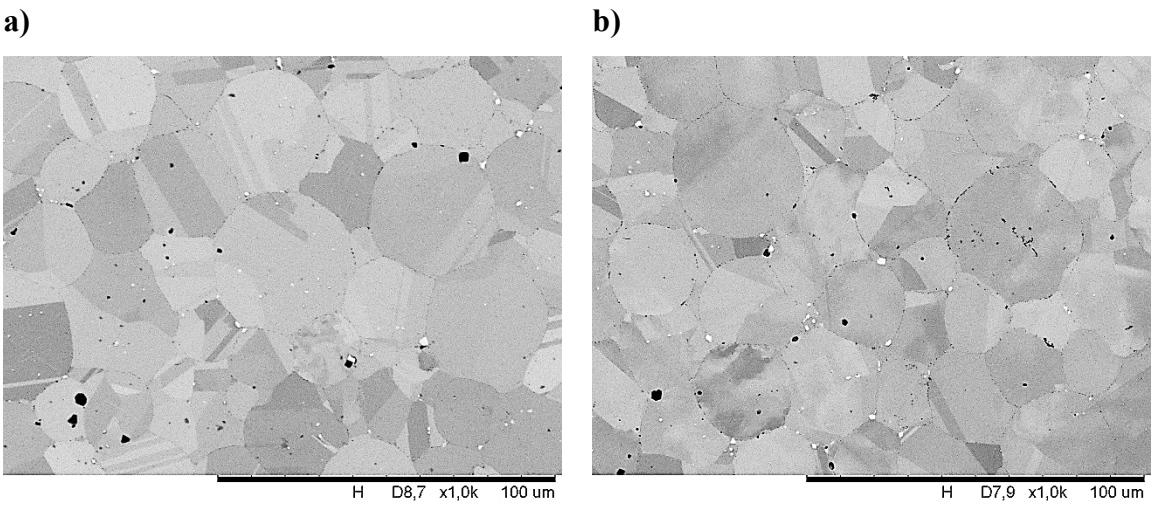

Figure 8-11: BSE micrographs showing HIPped powder microstructure in in-situ shelling canisters with two different wall thicknesses: a) 0.75 mm and b) 2mm. Dark contrasting regions were confirmed to be holes created by carbide dropout during sample preparation.

PPBs seem to be more defined compared to those observed outside of the diffusion zone in the traditionally HIPped material. Relative to the traditionally HIPped powders, there appears to be an increase in discreet oxides along PPBs. As with PPBs in the traditionally HIPped material WDS and EDS line scans were performed to assess chemistries at the PPBs. Figure 8-12 shows a significant increase in Ti at the PPB as well as a small increase in Al. Oxygen concentrations differ very slightly across the PPB, though not to the same extent as the Ti or Al. Figure 8-13 on the other hand highlights considerable increases in several elements including oxygen, across the PPB, suggesting an array of carbides and oxides are precipitating along PPBs. While it is possible for titanium peaks to result from the presence of titanium oxides, it is highly unlikely that this is the case, as it would be expected that such precipitates would also be accompanied by chromium oxides, and no increase in chromium is observed.

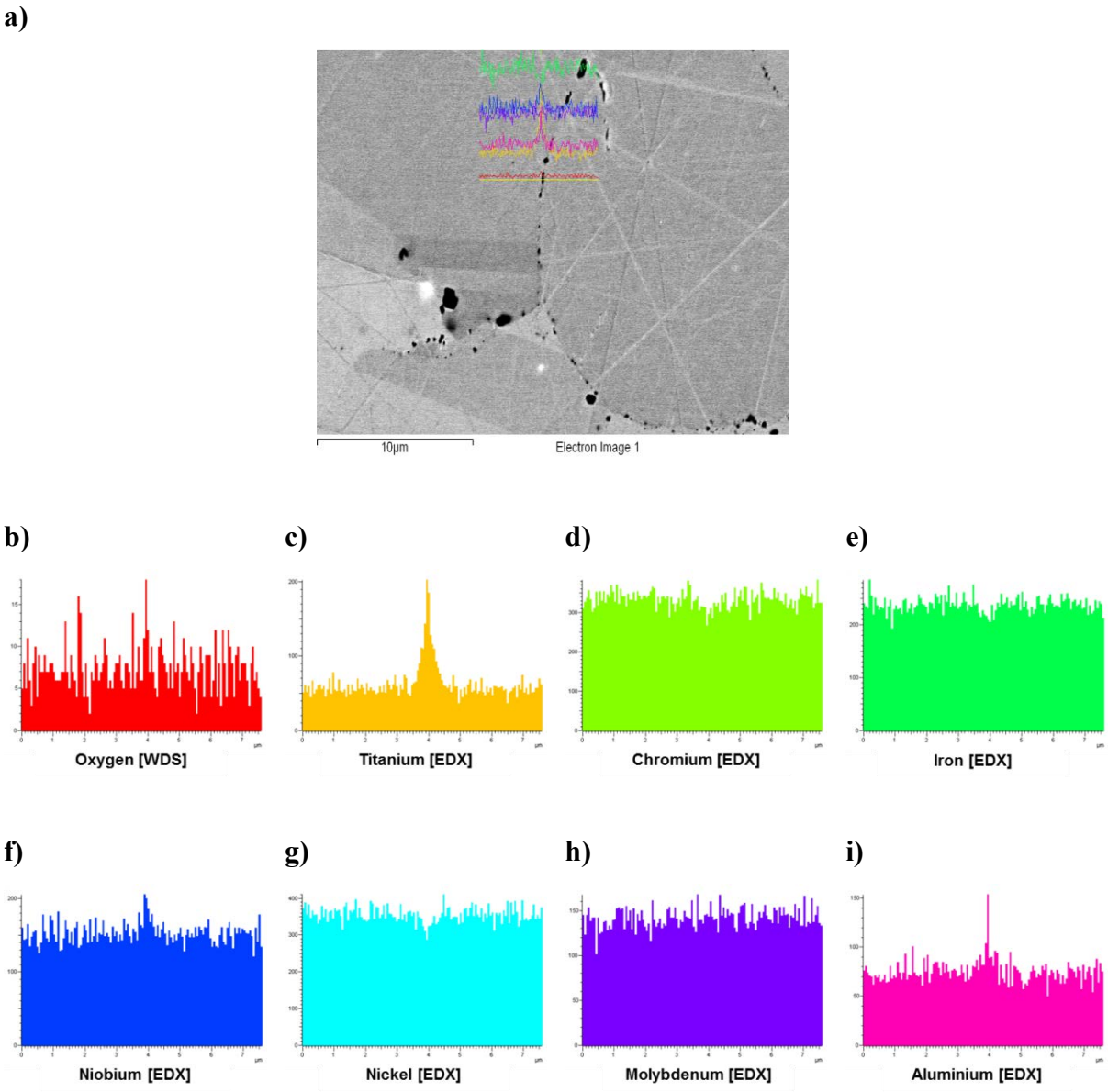

Figure 8-12: WDS and EDS line maps across a PPB in powder HIPped in an in-situ shelling canister: a) BSE micrograph with line maps overlaying; b) WDS line map for oxygen; c)-i) EDS line maps for remaining elemental constituents of Inconel 718.

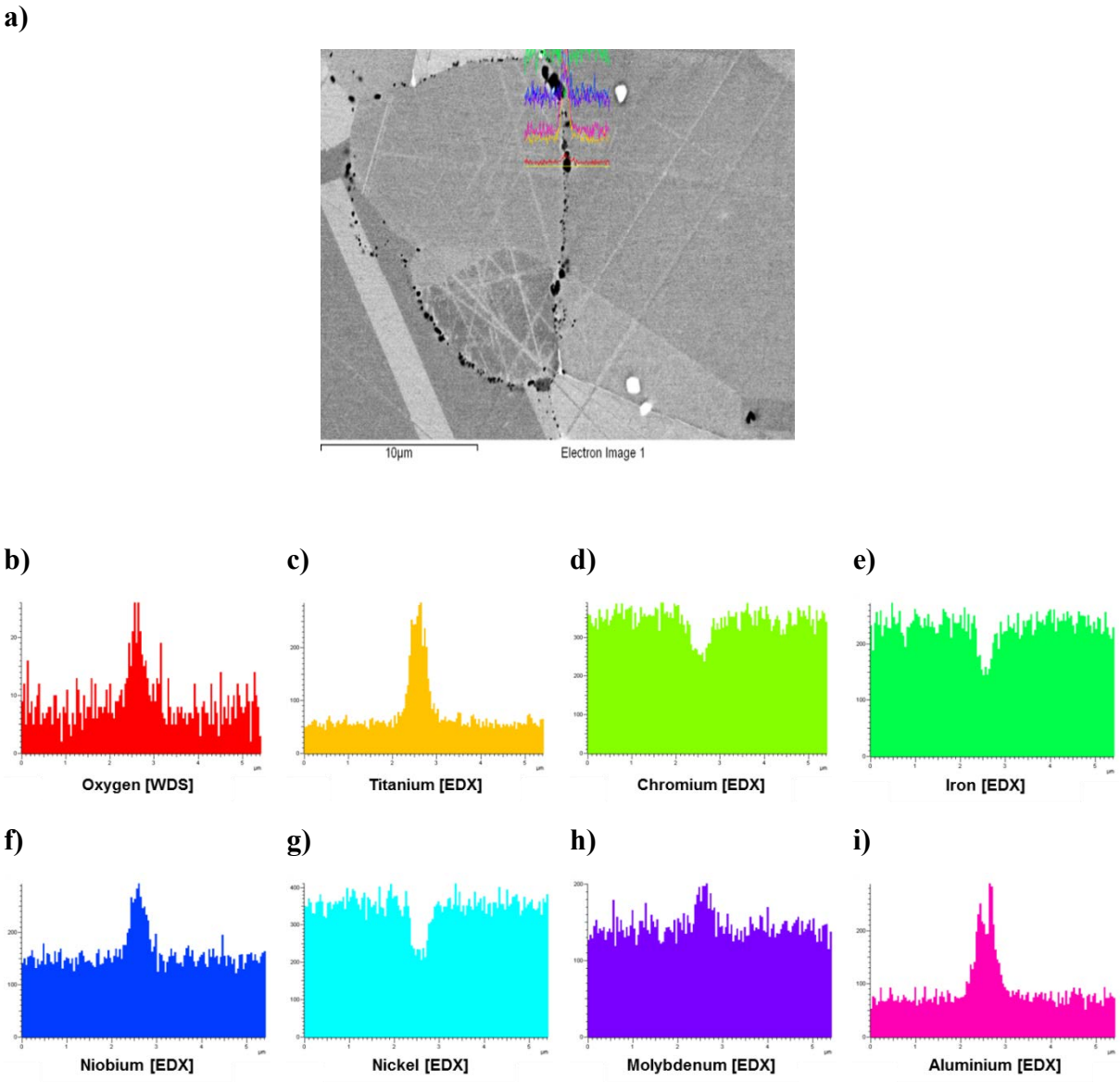

Figure 8-13: WDS and EDS line maps across a PPB in powder HIPped in an in-situ shelling canister: a) BSE micrograph with line maps overlaying; b) WDS line map for oxygen; c)-i) EDS line maps for remaining elemental constituents of Inconel 718.

The increase in discrete oxide precipitation observed in the powder of in-situ shelling canisters relative to the traditionally HIPped powder, is likely related to the condition of the powders used in each experiment. In PM HIPping experiments the powders used were fresh powders, however in in-situ shelling experiments the powders used were a mix of reused and fresh powder; furthermore, the powders inside the in-situ shelling canister have been processed during LPBF. The formation of spatter particles was discussed in the previous chapter. Any spatter particles falling into the build area could end up inside the in-situ shelling canister. Gasper et al.[201] classified Inconel 718 spatter particles into seven types by particle size range, morphology and chemistry. The two types of spatter particle identified with chemical differences were powder particles with discrete spots of Al oxide on the surface and powder particles with continuous coating of Al oxide, such as that seen in figure 8-10. Given the morphology of oxides decorating PPBs, it may be suggested that spatter particles with oxide spots were incorporated into the powder inside the in-situ shelling canisters.

8.3.2 Grain morphology

Figure 8-14 shows EBSD maps for the HIPped powders. Very little difference can be observed in the grain size or morphology of the powders HIPped in each thickness of canister. Both lots of HIPped powder exhibit multiple grain morphologies with random orientation. Quantitative analysis, shown in table 8-1, indicates similar grain sizes for each powder, with powders HIPped in the 0.75 mm canister exhibiting slightly bigger grains. A slightly higher percentage of Σ3 grain boundaries are observed in the powder HIPped in the 2 mm canister compared to the 0.75 mm canister. The difference however cannot be considered significant, and the percentage of Σ3 boundaries in either case, is not so high that it would affect the mechanical properties of the material. Relative to the traditionally HIPped powders,

percentage of Σ3 boundaries for both powders are similar to that measured in the middle of the canister.

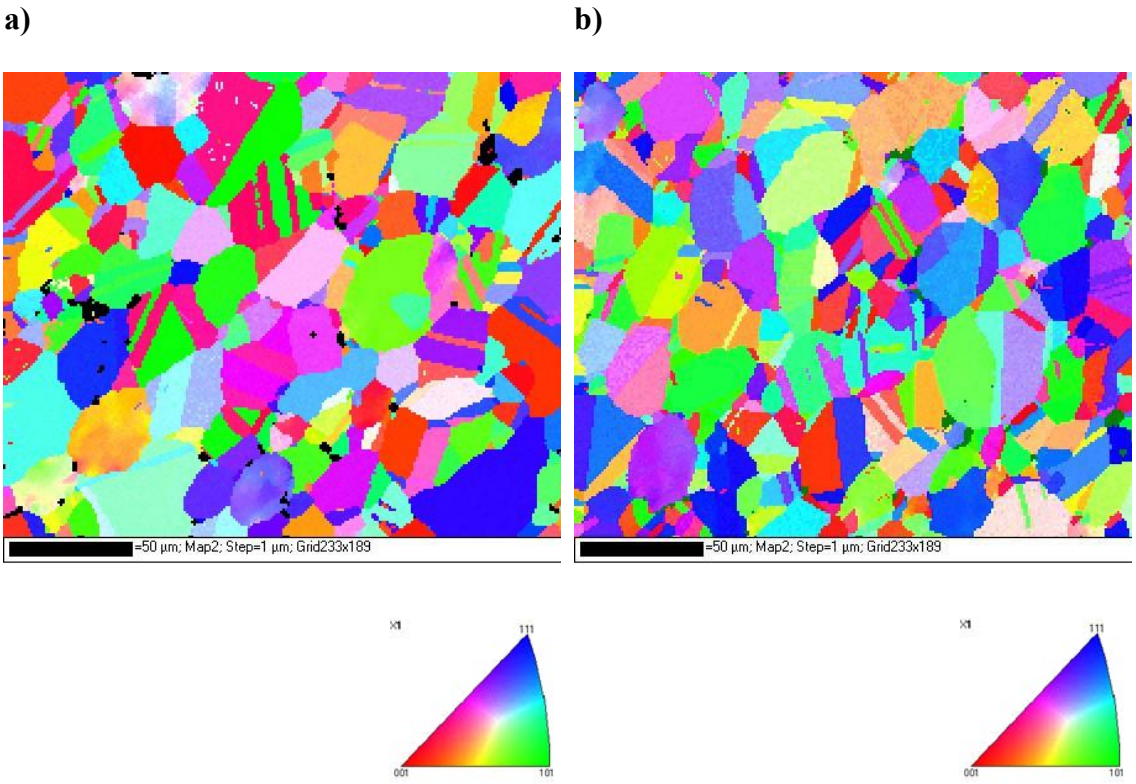

Figure 8-14: EBSD maps with IPF colouring for HIPped powder: a) in the 0.75 mm canister; b) in the 2 mm canister.

Table 8-1: Grain data taken from EBSD analysis of two HIPped powder samples.

	0.75 mm canister	**2 mm canister**
Number of grains	259	339
Min grain dia. (µm)	1.58	1.41
Max grain dia. (µm)	61.98	74.58
Ave. grain dia. (µm)	14.59	12.79
Σ3 boundaries (%)	20.2	23.9

8.4 Microstructure of the LPBF canister

In addition to analysing the HIPped power, the microstructure of the LPBF wall of the canister was examined. This is important as with the in-situ shelling process the canister is not removed, and consequently its microstructure contributes to the mechanical properties of the final component. During HIPping, dendritic and grain boundary segregation visible in the LPBF material disappeared and the NbC carbides, previously observed within the segregation, coarsened. While some carbides follow the existing grain boundaries, a significant number are aligned in a linear pattern like that exhibited by the segregation in the LPBF material. Figure 8-15 shows an image of segregation in the XZ plane of an LPBF sample and the transformed microstructure in in-situ shelling canister after HIPping. A quantitative analysis of carbides showed no significant difference between the two shell thicknesses (table 8-2).

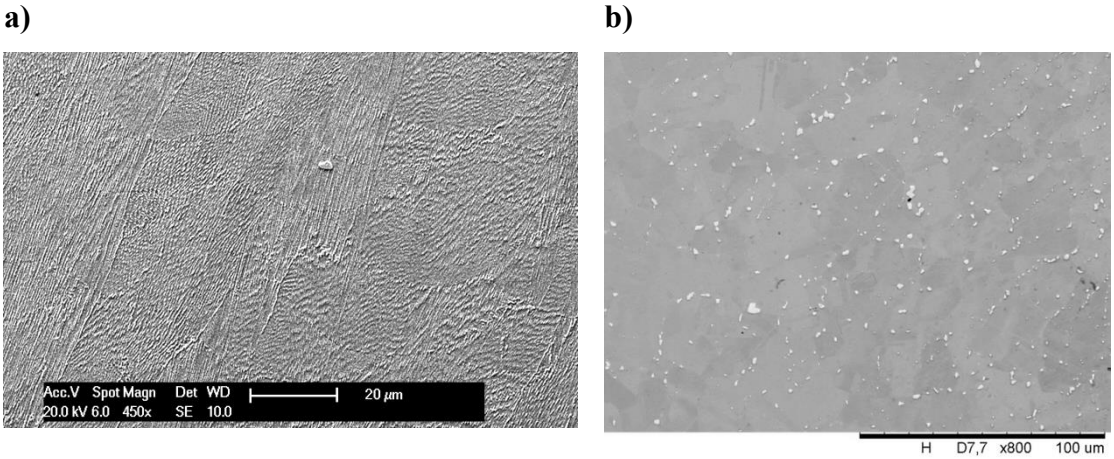

Figure 8-15: NbC carbide distribution in a) XZ plane of LPBF wall and b) XZ plane of the in-situ shelling canister.

Table 8-2: Quantification of precipitation after in the in-situ shelling canister.

Shell Thickness (mm)	Ave. number of carbides	Ave. carbide Dia. (µm)	SD carbide Dia. (µm)
0.75	536	2.84	0.17
2	531	2.76	0.28

EBSD mapping was performed (figure 8-16) to quantify grain size and characterise grain morphology in the LPBF shell. Maps were performed in the region where the canister diameter was smallest. Following HIPping, grains in the LPBF walls have transitioned from a columnar morphology to a more equiaxed morphology. Additionally, a loss of texture is observed, suggesting recrystallisation of the LPBF shell during HIPping. Table 8-3 summarises grain data taken from the EBSD maps. When comparing the two thicknesses of in-situ shelling canister, grain size in the 0.75 mm canister is slightly larger than that in the 2 mm. In addition, the percentage of Σ3 boundaries is higher in the 2 mm canister. This would suggest increased recrystallisation in the canister with 2 mm wall thickness. Results of the shrinkage measurements suggested a greater degree of deformation in the 0.75 mm canister and consequently it would be assumed that this canister would exhibit more recrystallisation. Given the size of EBSD map (0.04 mm^2) discrepancies are likely to result from slight differences in the location of observations. Recrystallisation and twin boundary formation are likely to be more prominent where the highest degree of deformation has taken place. This would be at the centre of the canister where the diameter is the smallest; the closer EBSD is performed to this region the more likely it is that twin boundaries will be observed.

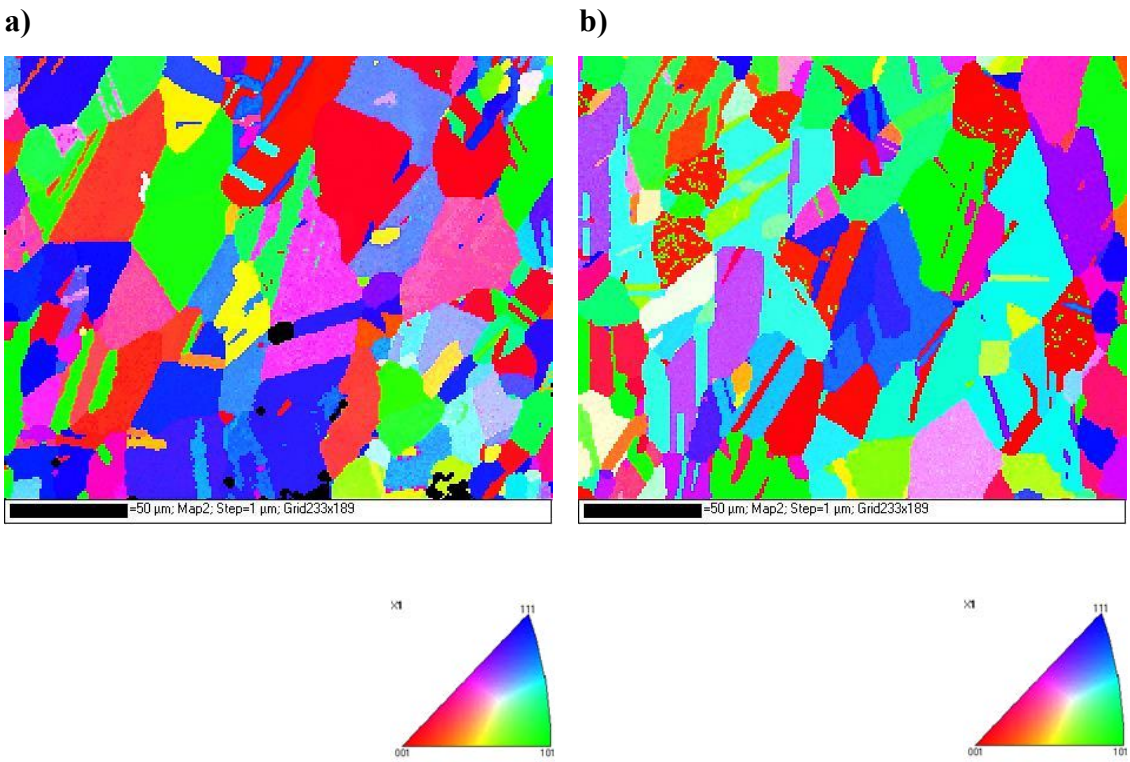

Figure 8-16: EBSD maps with IPF colouring for the in-situ shelling canister: a) 0.75 mm thick canister and b) 2 mm thick canister.

Table 8-3: Grain data taken from EBSD analysis of two HIPped powder samples.

	0.75 mm canister	2 mm canister
Number of grains	243	267
Min grain dia. (µm)	1.12	1.08
Max grain dia. (µm)	84.34	88.28
Ave. grain dia. (µm)	15.15	14.45
Σ3 boundaries (%)	24.2	38.3

8.5 Bonding across the LPBF-PM HIPped interface

Optical images across the LPBF- PM HIPped interface (figure 8-17) in both in-situ shelling canisters shows a clear division between the LPBF shell and PM HIPped material; made evident by a significant difference in grain size and morphology. The boundary between the LPBF shell base and PM HIPped material appears to be more clearly defined than that between the LPBF wall and PM HIPped material, likely to result from the presence of a thicker oxide layer at the base compared to the side wall. The higher surface roughness exhibited by the side walls relative to the top surface, make conditions for stable oxide formation less favourable, as surface stress concentrations lead to the formation of cracks within the oxide scale.

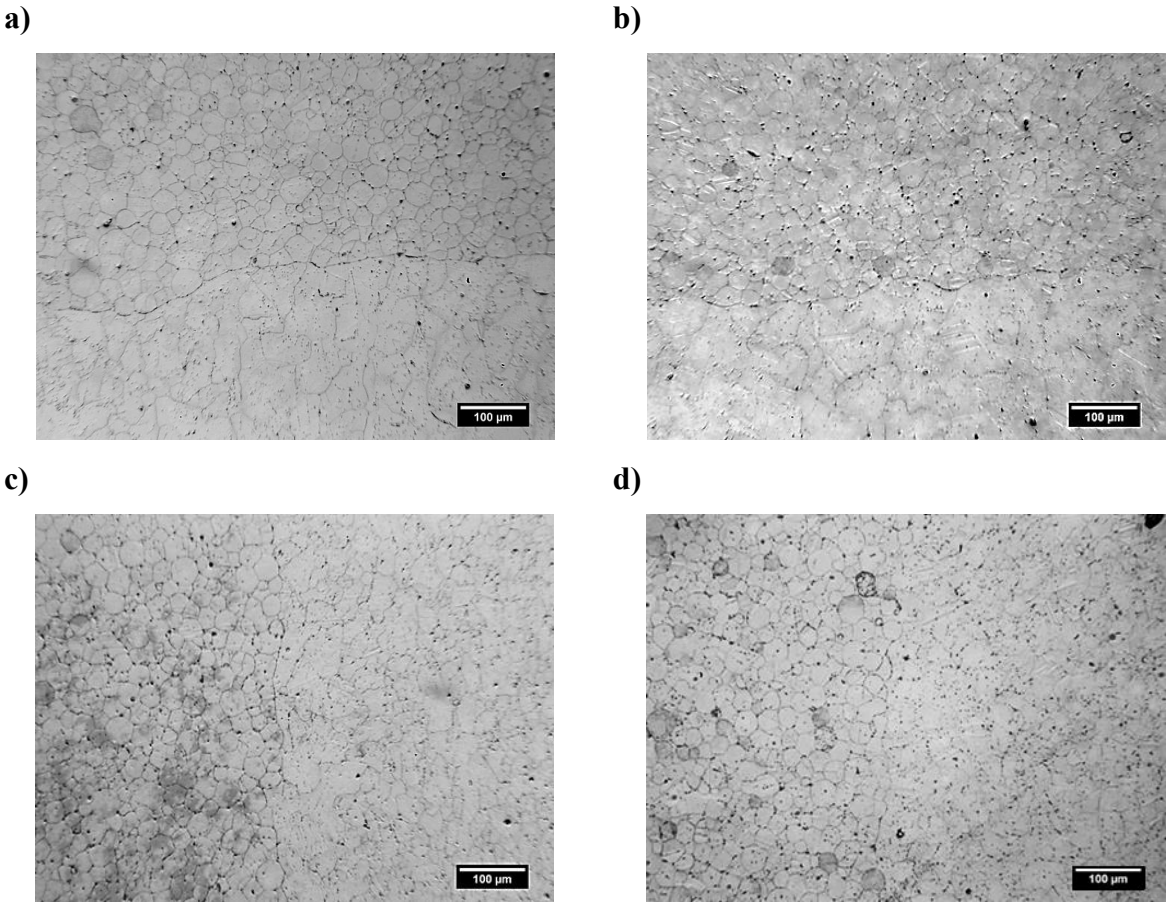

Figure 8-17: Optical micrographs of the LPBF-PM HIPped interfaces in: a) 0.75 mm canister base; b) 2 mm canister base; c) 0.75 mm canister side wall; d) 2 mm canister side wall.

Higher magnification BSE imaging (figure 8-18) highlights the presence of small carbides and δ at the LPBF-PM HIPped interface (figure 8-18-a) as well as what appear to be oxides (figure 8-18-b). Several instances of twin boundary formation across the interface can also be observed (figure 8-18-b). It is commonly reported that the formation of twin boundaries can prevent the growth and propagation of oxides [206] and consequently their formation is favourable for increasing bonding across the LPBF-PM HIPped interface.

a) b)

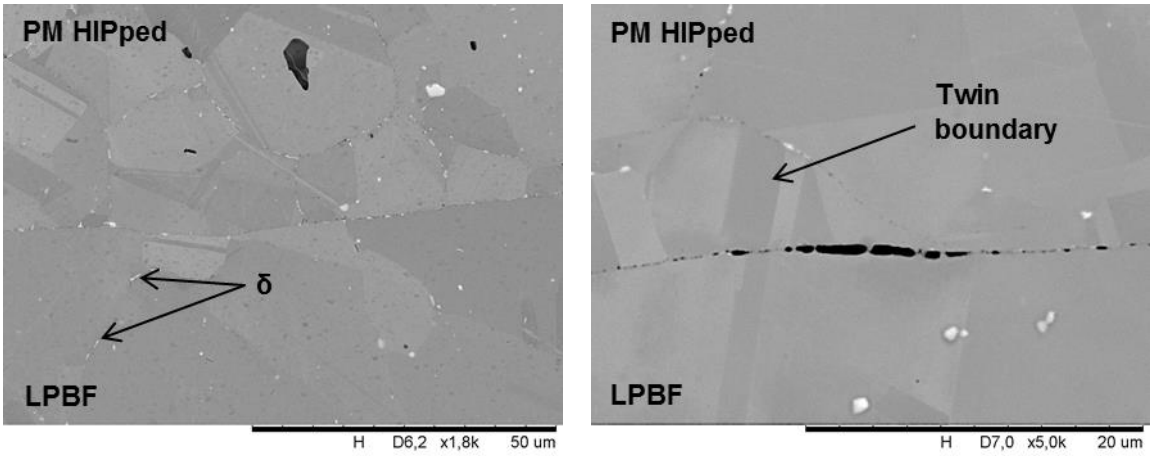

Figure 8-18: BSE micrographs at the base LPBF-PM HIPped interface of in-situ shelling canisters: a) X 1800 and b) X5000.

8.6 Influence of LPBF grain structure and surface finish on bonding across the LPBF-PM HIPped interface

8.6.1 As-fabricated discs

To effectively assess the influence of surface finish and grain structure (twinning) on bonding across the LPBF-PM HIPped interface, it was decided that samples should be produced for bonding with virgin powder. This way increased PPB formation due to powder contamination should not influence bonding and consequently any results observed could be attributed to the LPBF material alone. As discussed in chapter 4, LPBF discs were produced in simple and chess scan strategies, and one of each disc ground and cleaned. Table 8-4 shows the surface roughness measurements of as fabricated and ground LPBF discs prior to them being buried in powder for HIPping. In the as fabricated state, discs built with the chess scan

strategy had a significantly lower surface roughness relative to those built with a simple scan strategy; however, this may result from the surface roughness measurement process. The chess scan pattern did not appear to be visible on the surface of as fabricated discs and consequently, surface roughness measurements may have been conducted both perpendicular and parallel to the direction of the top surface scan track. Measurements for the simple scanning strategy on the other hand were always conducted perpendicular to the direction of the top surface scan lines as the direction of the top surface scan could be calculated based on the starting scan direction and number of layers. Surface roughness measurements conducted perpendicular to the scan direction result in higher surface roughness as several scan tracks are crossed during the measurement, with each track being roughly parabolic in nature. Following grinding of the discs surface roughness was similar for both simple and chess scan strategies.

Table 8-4: Average surface roughness (R_a) of as fabricated LPBF discs and discs with surface finishing and cleaning. R_a reported for as fabricated condition was measured across the tracks, i.e. perpendicular to scan track length.

Scan Strategy	**Simple**		**Chess**	
Surface finish	**As fabricated**	**Ground**	**As fabricated**	**Ground**
R_a (µm)	42.58	0.23	15.52	0.77

In addition to measuring surface roughness prior to HIPping, grain structure was also examined in the as fabricated discs. Figure 8-19 shows EBSD maps of LPBF discs for a simple (figure 8-19-a) and chess (figure 8-19-b) scan strategy. The size of the map is such that the top two layers of each disc are observed, ensuring that both grains in tracks scanned perpendicular and parallel to the cross-section are seen. The average grain size in the chess

scan strategy appears to be smaller than that observed in the simple scan strategy. Carter et al.[138] observed each square within the chess scan strategy to consist of coarse grains at the centre region and finer grains at the edges. This was attributed to a so-called "band heating" effect, in which the entire square was instantaneously heated, cooling faster at the edges and slower at the centre. The position of the chess scan pattern then being shifted every new layer resulted in a reduction of epitaxial grain growth, and the formation of a finer grain structure.

a)

b)

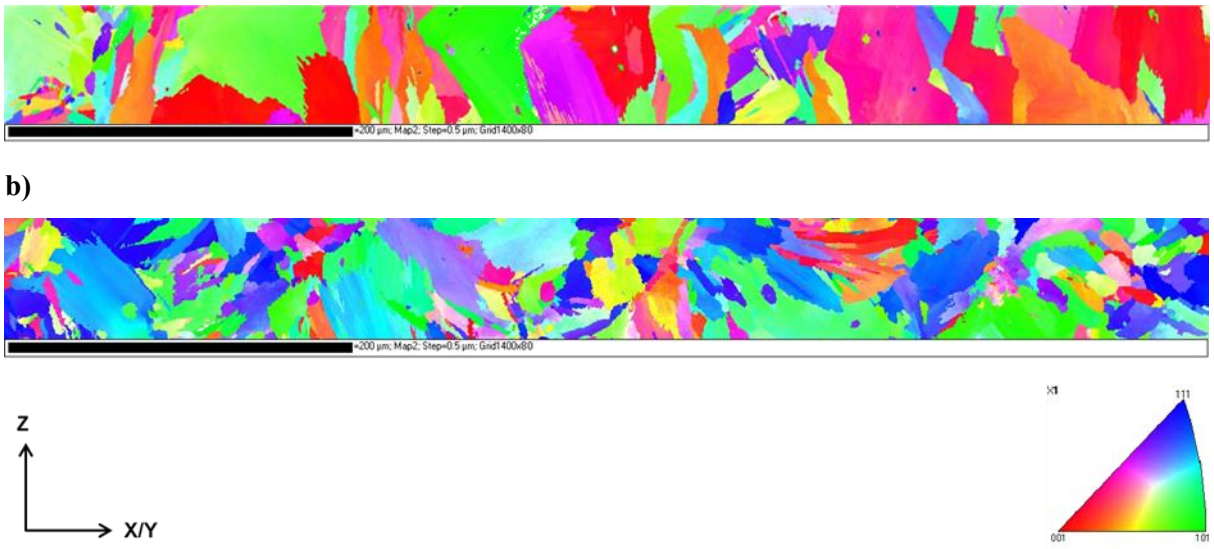

Figure 8-19: EBSD maps with IPF colouring for LPBF discs. a) hatch scan strategy; b) chess scan strategy.

8.6.2 Microstructure at the LPBF-PM HIPped interface

Post HIPping the microstructures of the LPBF discs HIPped in powders were observed along the longitudinal LPBF- PM HIPped interface. No distinguishable differences could be observed between discs produced by chess and hatch scanning strategies; however, surface finishing did appear to have some effect. Figure 8-20 shows optical images of the interface

microstructure for discs processed with the chess scan strategy. The interface at the disc that underwent surface preparation (figure 8-20-a) is much more defined than the disc that had no post-processing treatment given (figure 8-20-b). Instances of twinning across the interface can also be observed in the as-fabricated sample, suggesting a greater degree of recrystallisation at the interface.

a) **b)**

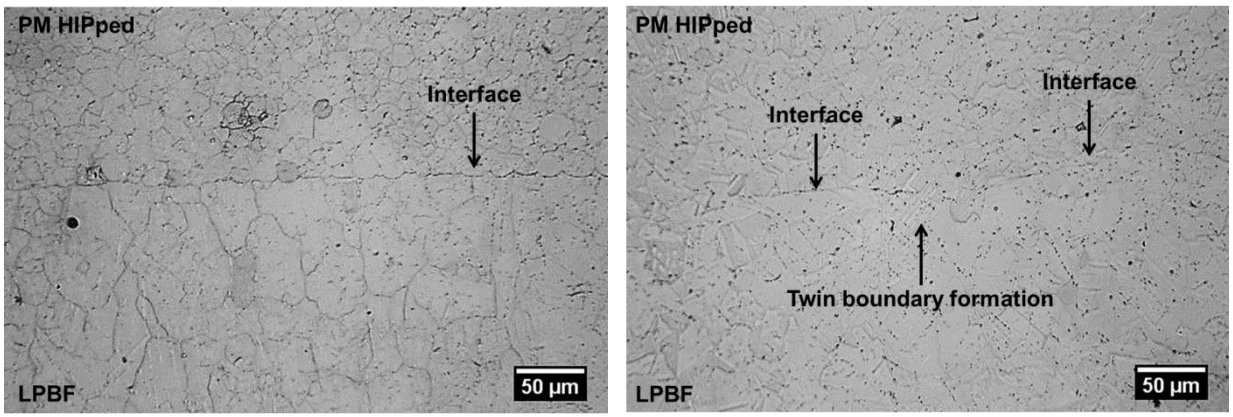

Figure 8-20: Optical micrographs of LPBF-PM HIPped interface for chess scan strategy discs with different surface roughness: a) polished; b) as-fabricated.

It was originally hypothesised that increasing the number of point contacts at the interface would result in increased recrystallisation and grain growth across the interface. The discs were all HIPped in the same canister of powder and consequently it is logical to assume powder size distribution at the interface with each disc is similar. Considering this, the surface roughness profiles for each disc (figure 8-21 and 8-22) were examined to determine the distance between surface peaks. Table 8-5 summarises the average distance between surface peaks for each disc. The average distance between peaks for the ground samples is significantly less than the smallest diameter of powder particle, suggesting point contact at the interface would be dictated by the powder packing. The average peak distance for as-

fabricated samples however is just slightly smaller than the average powder particle size. Consequently, there may be instances along the interface where powder particles sit between the surface peaks, increasing the number of point contacts between LPBF canister and powder; that is assuming the troughs do not mirror the curvature of powder particles, which is highly unlikely.

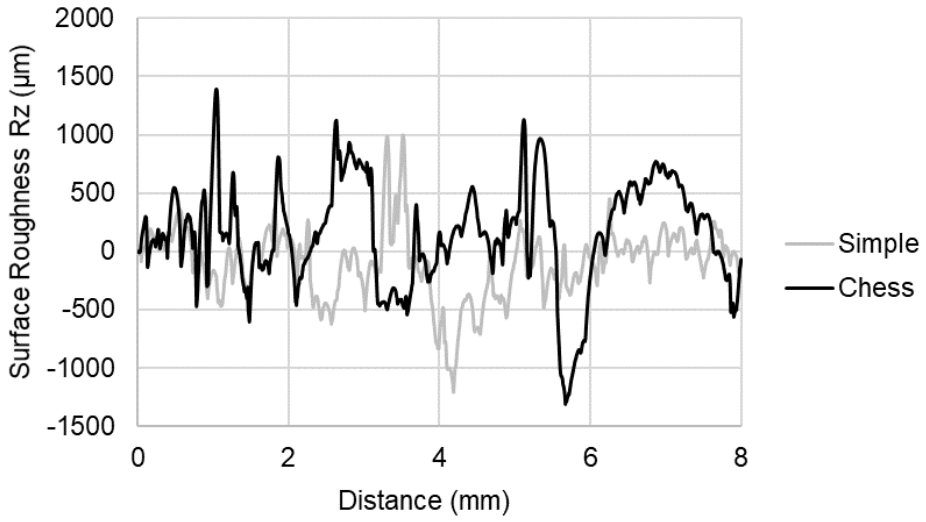

Figure 8-21: Surface roughness profiles for as-fabricated LPBF discs.

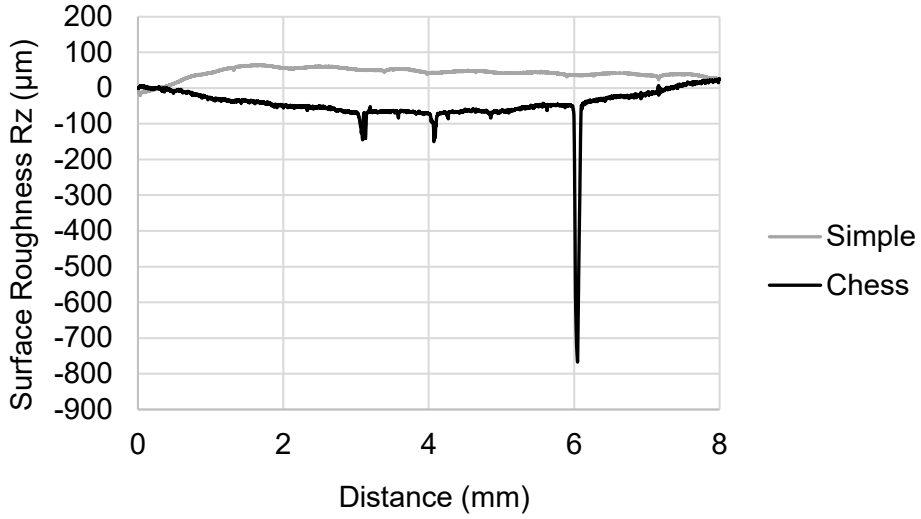

Figure 8-22: Surface roughness profiles for ground discs.

Table 8-5: Average distance between surface peaks for as-fabricated and ground discs.				
Scan Strategy	**Simple**		**Chess**	
Surface finish	**As fabricated**	**Ground**	**As fabricated**	**Ground**
Peak distance (mm)	0.032	0.0055	0.026	0.0062

8.7 Tensile testing of the LPBF-PM HIPped interface

Tensile tests were performed across the LPBF-PM HIPped interface as a way to more wholly quantify the strength of bonding across the interface. Tensile specimens were produced to test bond strength at the interface at the base of the canister and wall of the canister, as described in chapter 4.

8.7.1 The base interface

Figure 8-23 shows yield and UTS values illustrating the strength of the LPBF-PM HIPped interface. Compared to LPBF+HIP and PM HIPped material, yield and

UTS are significantly reduced indicating failure of the tensile specimen to result from the interface. Samples built using a chess scan strategy had slightly better elongation than those produced by a hatch scan strategy (figure 8-24) but not significantly so.

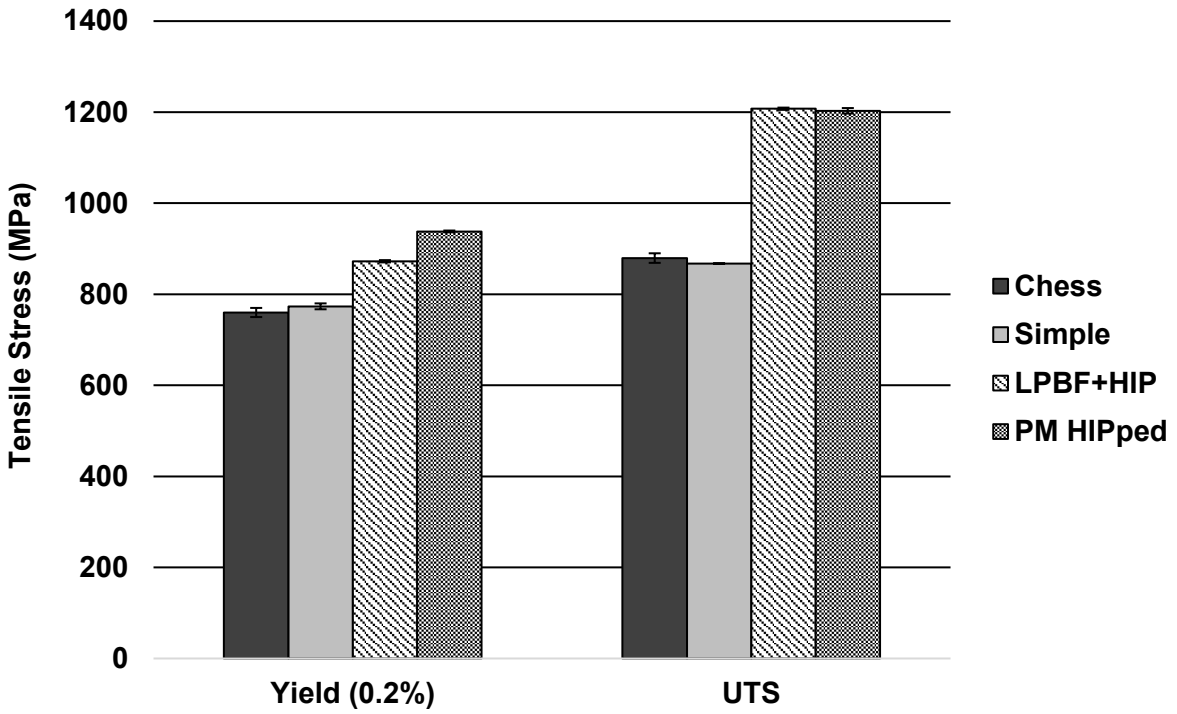

Figure 8-23: RT tensile yield and UTS across the base interface as a function of scanning strategy. Values for PM HIPped material and LPBF+HIP material are provided for comparison.

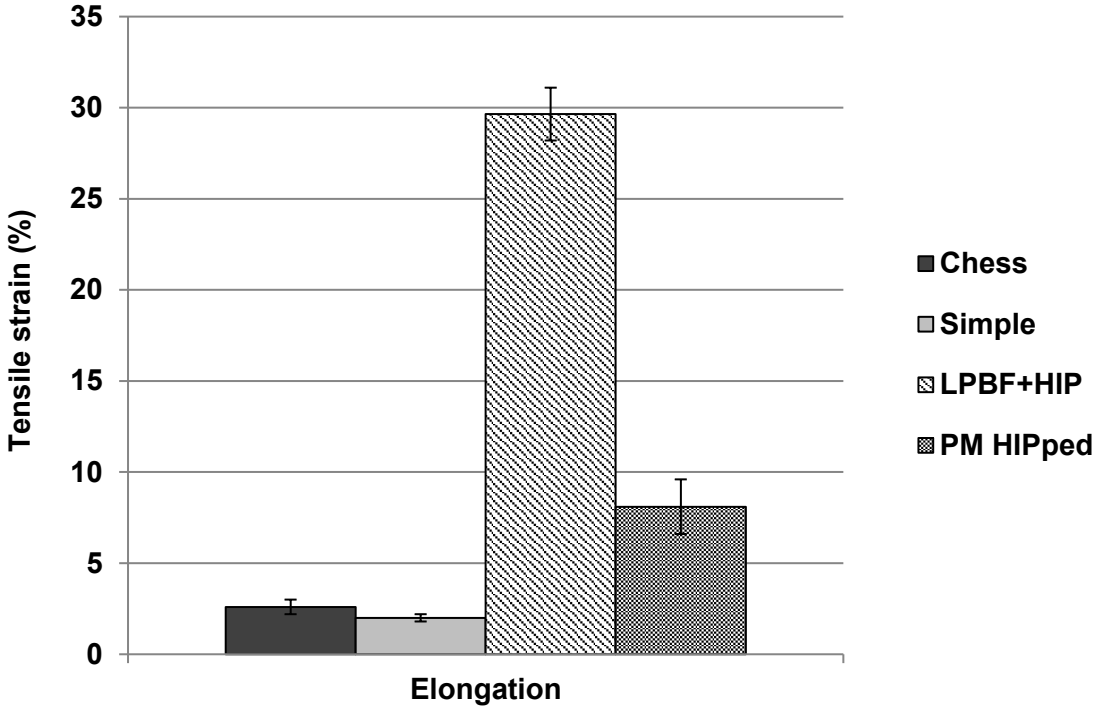

Figure 8-24: RT tensile elongation across the base interface as a function of scanning strategy. Values for PM HIPped material and LPBF+HIP material are provided for comparison.

i. Fractography

Both chess and hatch scan strategy samples fractured in the middle of the gauge (figure 8-25) at the interface. Observations of fracture surfaces for both samples clearly illustrated the laser scanning paths implemented at the SLM stage, with figures 8-26-a and -b showing the hatch scan strategy and chess scan strategy respectively.

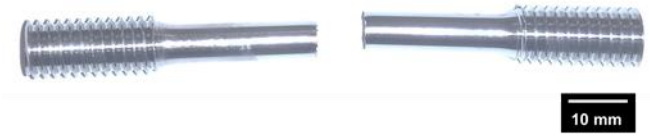

Figure 8-25: Fractured tensile bar. Machined from a cylinder produced by in-situ

shelling with a hatch scan strategy implemented at the LPBF stage.

a) **b)**

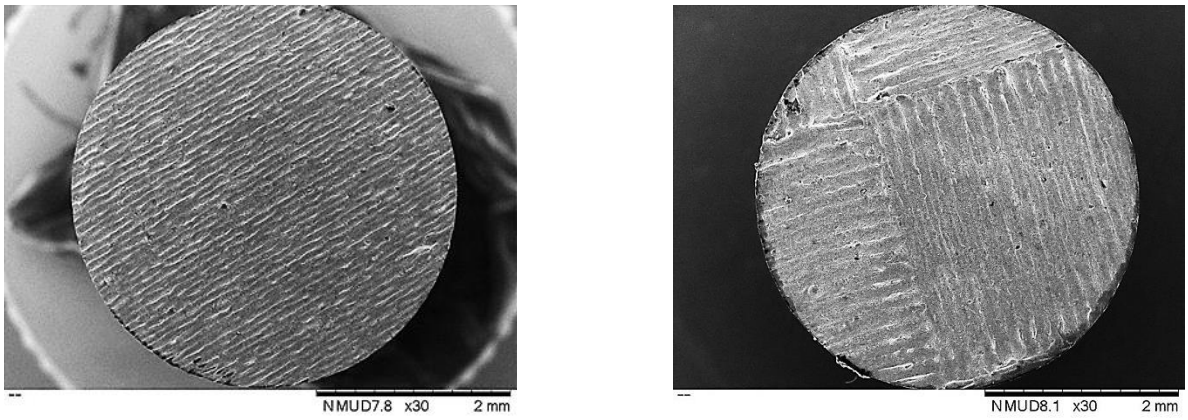

Figure 8-26: SE micrograph of the base interface fracture surfaces of in-situ shelling samples. a) LPBF section manufactured with hatch scan strategy; b) LPBF section manufactured with chess scan strategy.

BSE imaging of fracture surfaces (figure 8-27) revealed a dark striped pattern following the scan tracks. EDS mapping indicates this phase to be Al_2O_3, concurrent with the chemistries measured across the interface prior to testing. The presence of continuous oxides would explain the brittle nature of fracture observed here.

a) **b)**

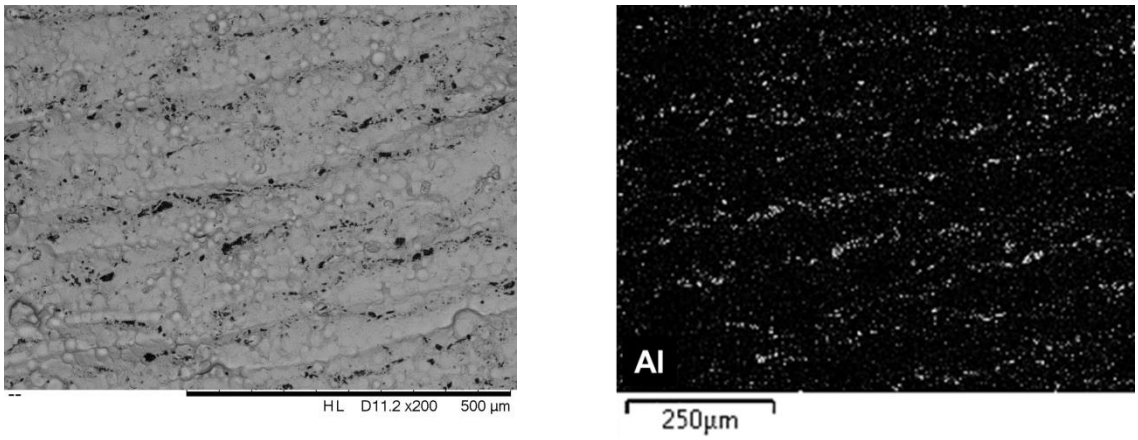

Figure 8-27: a) BSE micrograph of LPBF-PM HIPped fracture surface and b) EDS map highlighting Al distribution at the corresponding surface.

8.7.2 The wall interface

As explained previously only simple scan strategy was used to build in-situ canisters for testing of the wall interface strength. As with tensile testing of the base interface, yield and UTS values were lower than those for LPBF+HIP and PM HIPped materials alone (figure 8-28), indicating the LPBF-PM HIP interface to be the source of specimen failure. Some improvement can be seen in yield and significant improvement is observed in UTS and elongation (figure 8-29) relative to tensile properties across the base interface. This would suggest interlocking between powder particles and the wall of the LPBF canister to have some impact on improving the strength of the interface; however, this added benefit is not sufficient enough to overcome the influence of the oxide film.

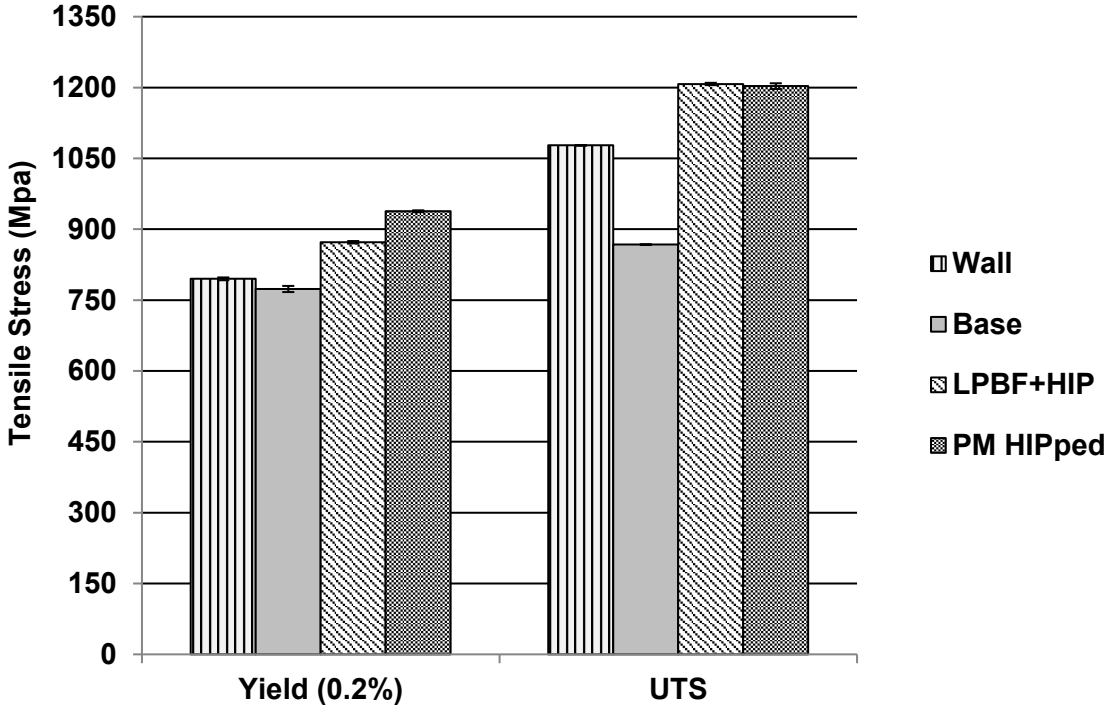

Figure 8-28: RT tensile yield and UTS across the wall and base interface. Values for PM HIPped material and LPBF+HIP material are provided for comparison.

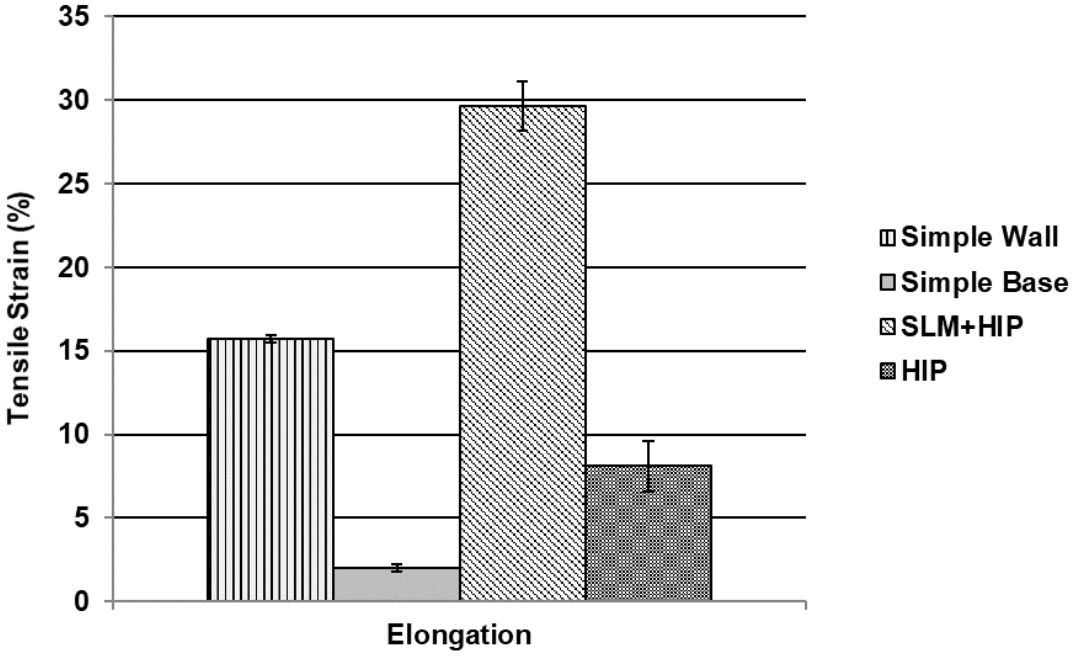

Figure 8-29: RT tensile elongation across the wall interface. Values for PM HIPped material and LPBF+HIP material are provided for comparison.

i. Fractography

Examination of the fracture surface (figure 8-30) shows a distinct void surrounding the central LPBF rod. Closer examination of the two component surfaces (figure 8-31) indicates the LPBF rod to have undergone a more ductile fracture than the PM HIPped powder, with significantly more micro-void coalescence in the LPBF rod relative to the powder. This is in line with the differences in tensile elongation observed between LPBF+HIP material and PM HIPped material alone and would suggest the majority of the tensile stress was bore by the LPBF rod.

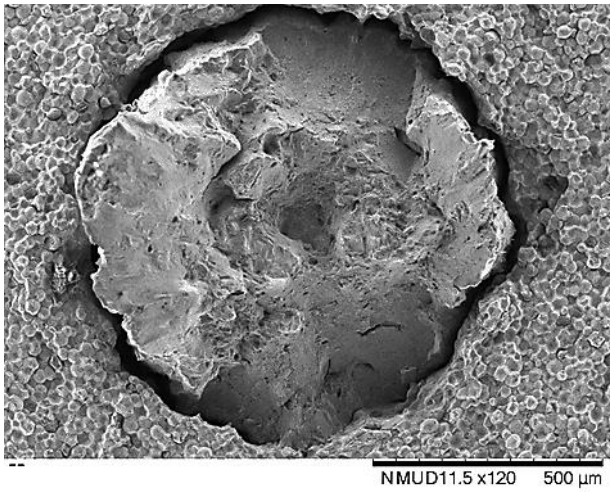

Figure 8-30: SE micrograph of fracture surface of wall interface specimen produced by the in-situ shelling method.

a) **b)**

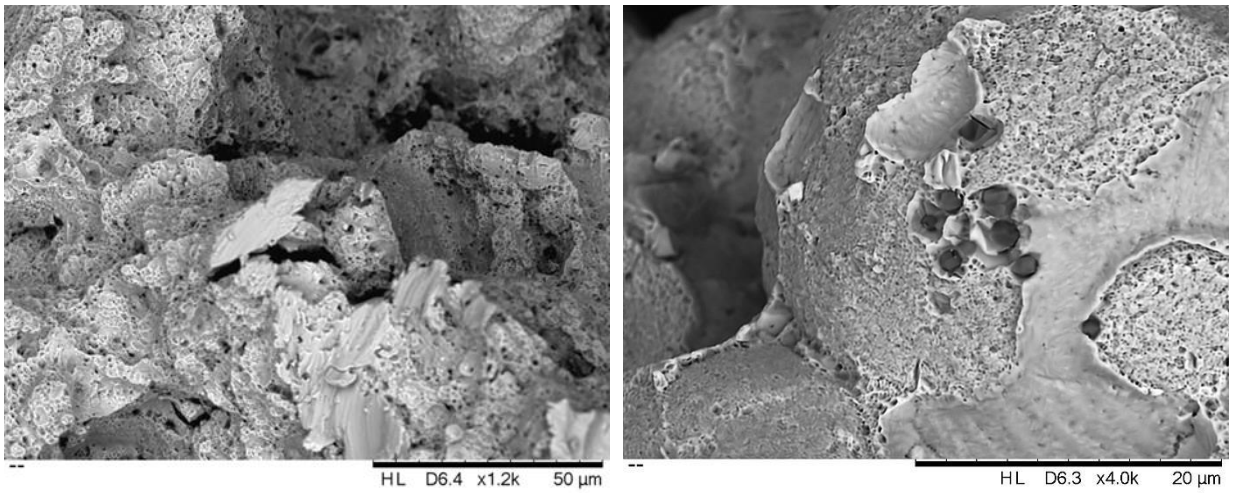

Figure 8-31: BSE micrographs of fracture surface of wall interface: a) LPBF rod and b) PM HIPped material.

8.7.3 The influence of surface features on the strength of the LPBF-PM HIPped interface

BSE imaging, EDS and WDS illustrated the formation of oxide films to be the predominant mechanism impeding grain growth across the LPBF-PM HIPped interface.

Analysis of the interface by high magnification SEM showed several incidents of grain growth across the interface occurring by twin boundary formation and/ or the absence of an oxide film. While the natural interlock between powders and the LPBF canister wall showed some improvement in properties it was not sufficient to overcome the influence of the oxide formed at the interface. An increase in HIPping temperature in these in-situ shelling studies showed little influence over PPB formation and thus it is concluded that prevention of PPBs could only be established by a change in powder. Consequently, the only feasible method by which oxide formation may be minimised at the interface is through modification to the LPBF canister surface. Surface roughness studies showed promise for increasing recrystallisation at the LPBF-PM HIPped interface via increasing the number of contact points, however recrystallisation in these studies was still limited due to the presence of the stable oxide film. Several geometric features aimed at reducing the continuity of oxide films were built onto the surface of LPBF canister bases and central rods for tensile testing. The reasoning behind these geometry selections can be found in chapter 4.

i. Microstructure of the LPBF-PM HIPped interface

Figure 8-32 shows optical micrographs of the LPBF geometric structures in the PM HIPped material. Grains within the LPBF geometries are significantly bigger than those within the PM HIPped material and are coarser than grains observed in as-fabricated LPBF microstructures. As with previous PM HIPped samples, PPBs are prevalent throughout the powder. The most continuous microstructure seems to be that of the powder HIPped around the hemispherical structure; there is no definite line surrounding the LPBF geometry and the difference in grain size between the HIPped powder and LPBF part looks to be smaller than that observed for conical and lattice structures. EBSD was performed for an area surrounding and including one of the LPBF hemispheres, to see if any grain growth could be observed

across the LPBF-PM HIPped interface. Figure 8-33 shows the EBSD map of the area, in which grain growth can be observed across the interface.

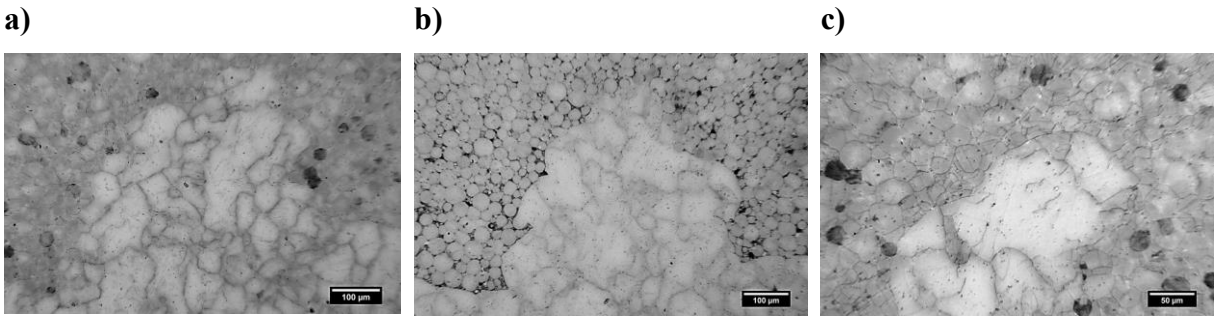

Figure 8-32: Optical micrographs of etched in-situ shelling microstructures with surface features: a) interface at a hemisphere; b) interface at a cone; c) interface at a lattice strut.

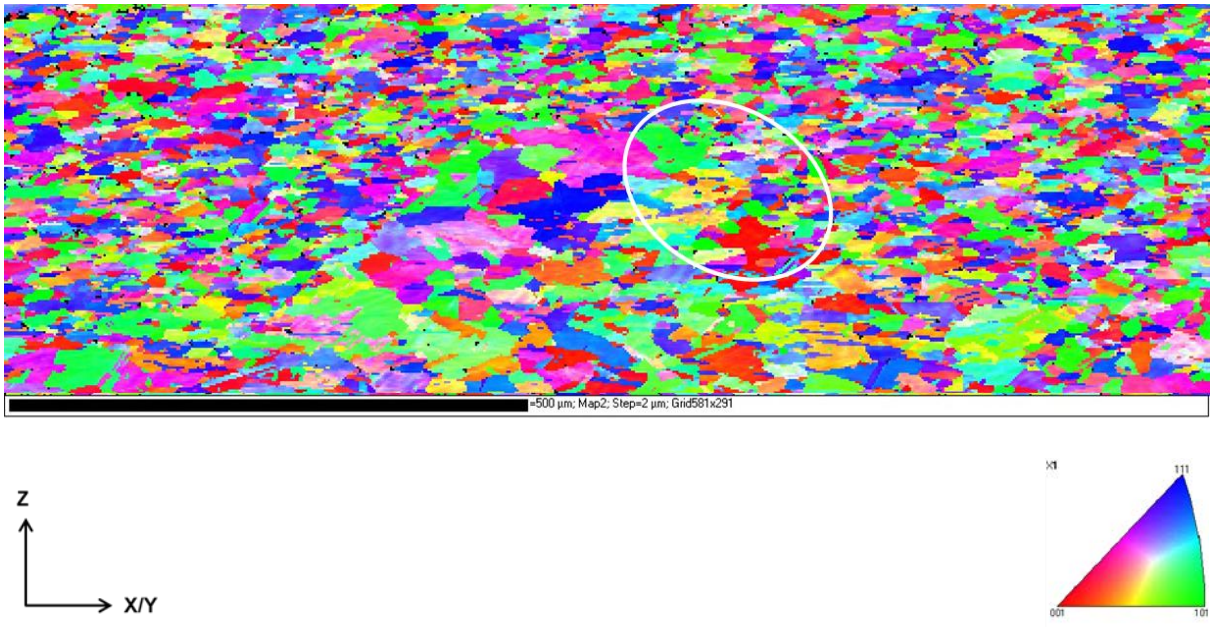

Figure 8-33: EBSD map with IPF colouring of a hemispherical feature at the base of an in-situ shelling canister. Regions of grain growth across he boundary are circled.

ii. Tensile testing across the base interface

Results of the tensile testing for the base interface with surface features can be seen in figures 8-34 and 8-35. None of the three geometries appear to improve the yield strength of the interface, however the hemispherical geometry does produce a very slight improvement in the UTS. All three geometries have significantly improved elongation across the base bond; however, elongation is still not sufficient to match that of the PM-HIPped material. Fracture surfaces for the LPBF half of the bar (figure 8-36) still show the presence of scan tracks between the features, however the tracks are not as well defined as they are without the presence of surface features, suggesting some merit to the idea that breaking the continuous oxide film would result in improved bonding at the interface. Consequently, it is expected that an increase in the quantity of hemispherical features on the LPBF surface would increase bond strength.

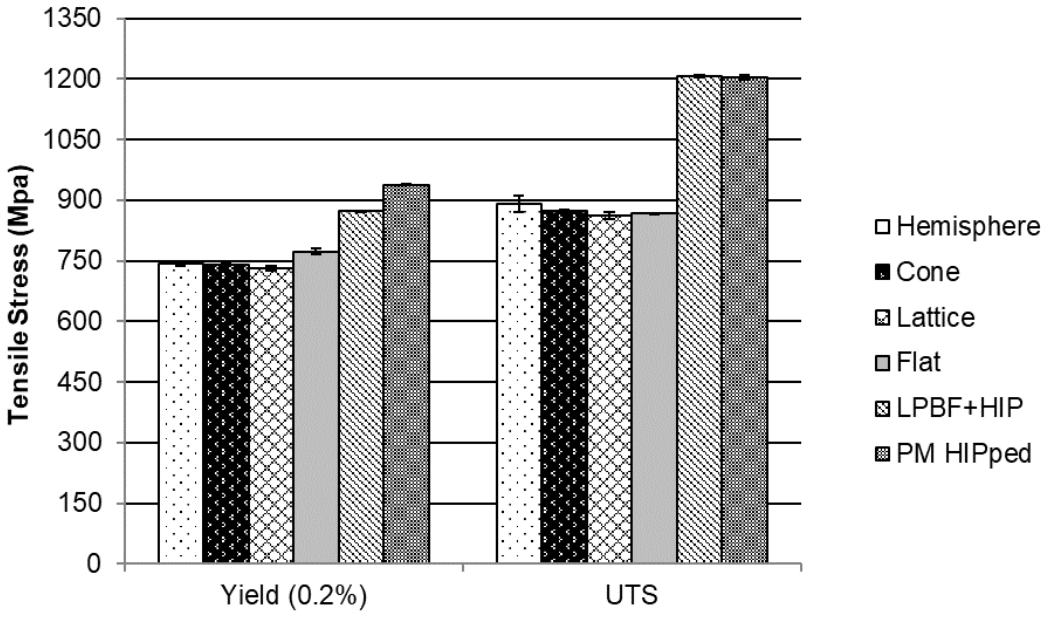

Figure 8-34: Influence of surface features on the yield and UTS across the LPBF-PM HIPped interface. Yield and UTS data are also included for a flat interface, LPBF+HIP and PM HIPped material.

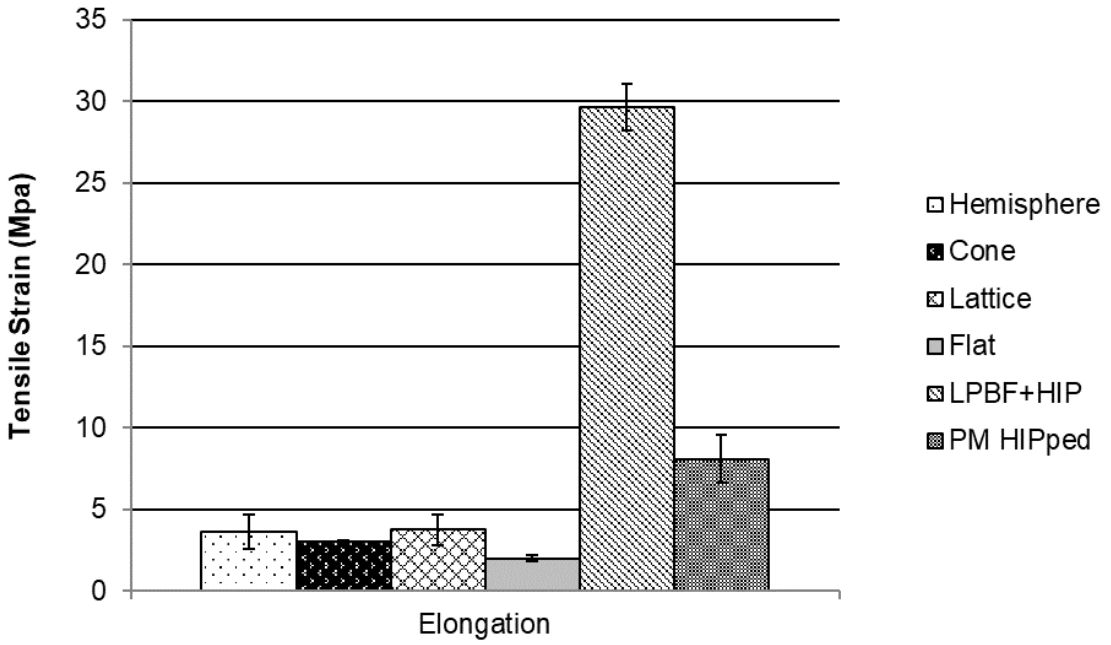

Figure 8-35: Influence of surface features on elongation across the LPBF-PM HIPped base interface. Yield and UTS data are also included for a flat interface, LPBF+HIP and PM HIPped material.

a) **b)** **c)**

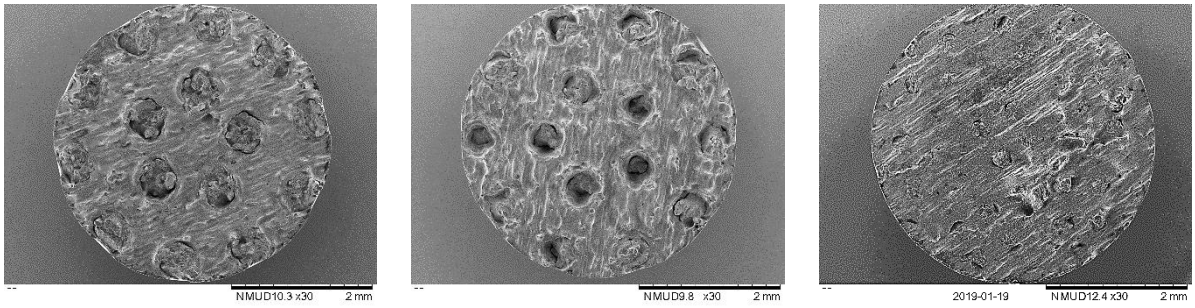

Figure 8-36: Low magnification SE micrographs of the LPBF fracture surface in in-situ shelling canisters produced with different surface geometries: a) hemisphere; b) cone; c) lattice unit.

iii. Tensile testing of the wall interface

Figure 8-37 shows the results of the tensile testing for the wall bond with the addition of surface features. Yield occurs at slightly lower stresses for the wall with surface features compared to a flat wall without. UTS on the other hand, is equivalent for all in-situ shelling specimens, resulting in an increased elongation for the specimens with surface features (figure 8-38). Fractography of the specimens was in agreement with the elongation data, with both fracture surfaces displaying significant evidence of a ductile mode of failure (figure 8-39). Bonding between the LPBF and PM HIPped microstructures appears to be reasonable in the wall with hemispherical features. Failure even seems to have initiated within the LPBF wall rod, with cracking observed in the regions between features and propagating between the central rod and added surface hemisphere.

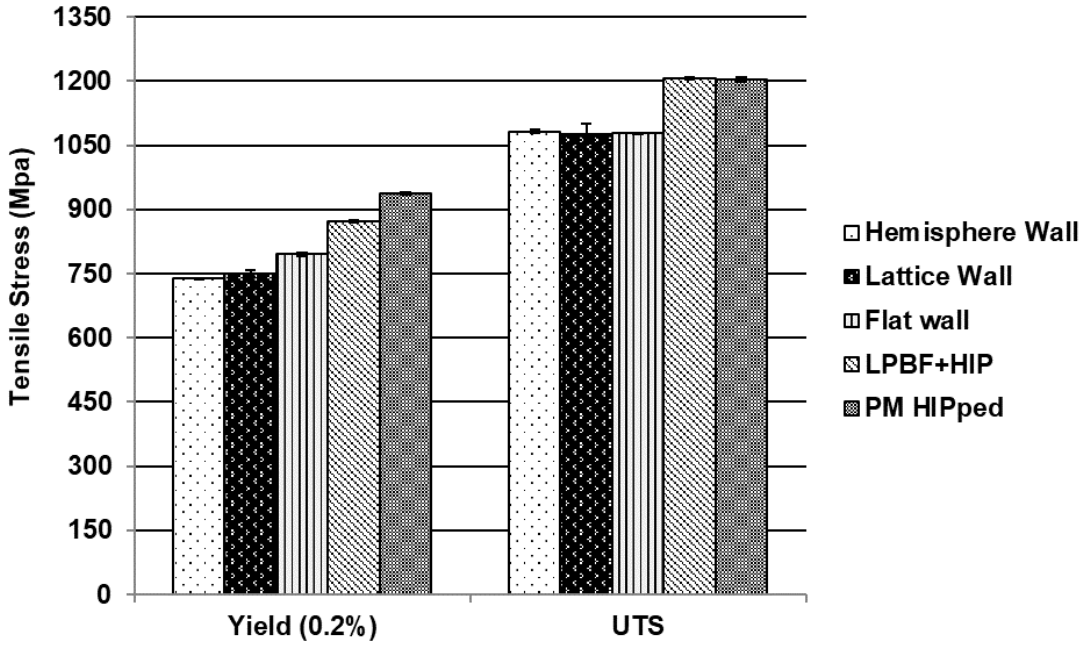

Figure 8-37: Influence of surface features on the yield and UTS across the LPBF-PM HIPped wall interface. Yield and UTS data are also included for a flat interface, LPBF+HIP and PM HIPped material.

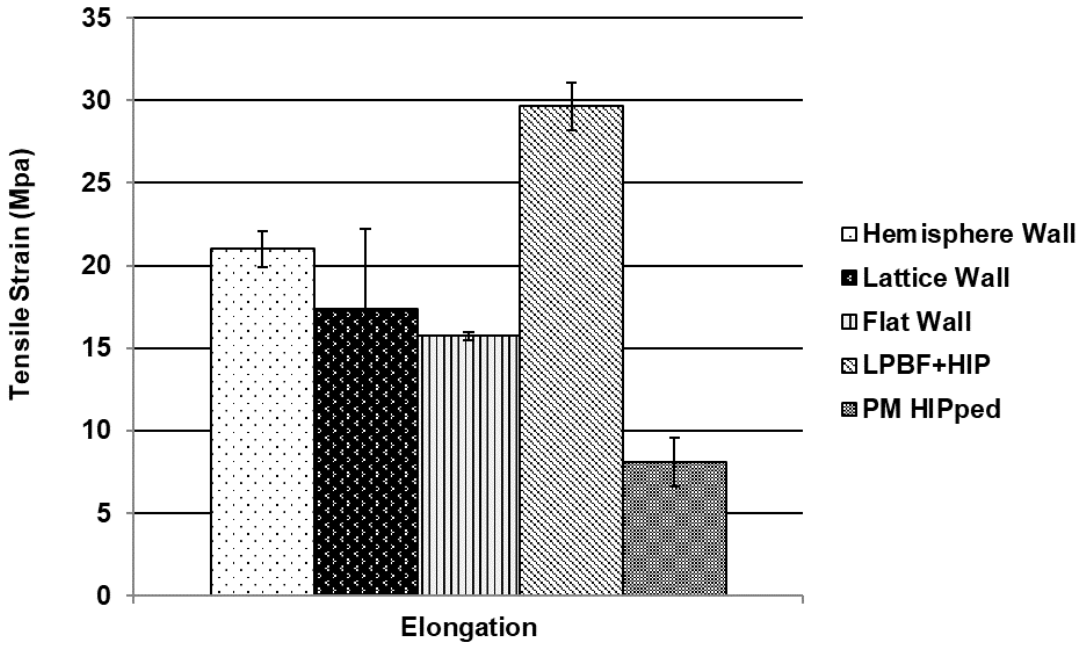

Figure 8-38: Influence of surface features on elongation across the LPBF-PM HIPped wall interface. Yield and UTS data are also included for a flat interface, LPBF+HIP and PM HIPped material.

a) **b)**

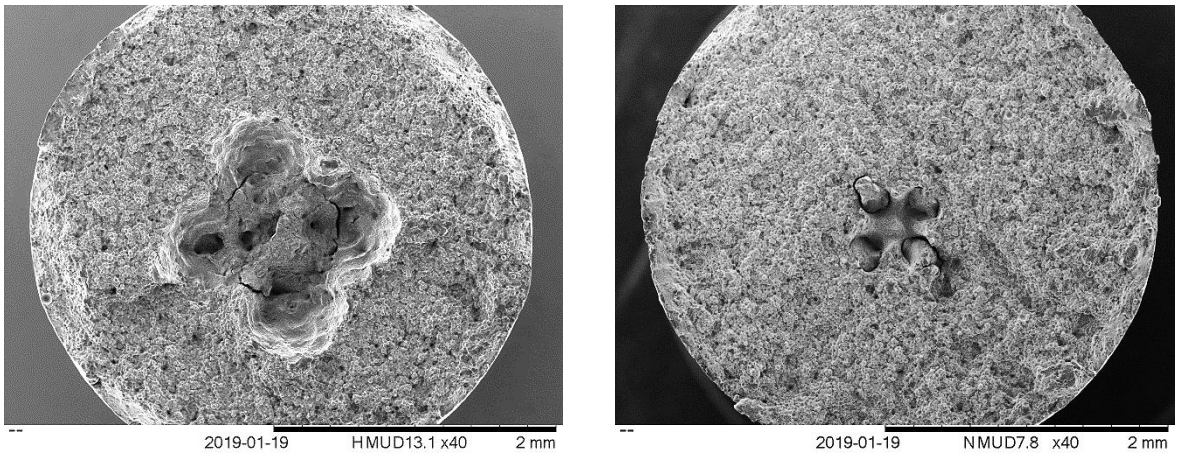

Figure 8-39: Low magnification SE micrographs of the wall interface fracture surfaces with two different geometries: a) hemisphere; b) lattice unit.

8.8 EPBF in-situ shelling

8.8.1 Grain morphology and the EPBF-PM HIPped interface

EPBF in-situ shelling specimens were provided by the industrial sponsor in different wall thicknesses (2-, 3- and 5-mm) for microstructural examination and comparison to the microstructures of LPBF-in-situ shelling specimens. Figure 8-40 shows optical images of the grain structure in the EPBF wall at the middle of the specimen. All wall thicknesses exhibit a trend of having smaller more equiaxed grains at the surface and coarser more columnar grains at the interface with the EPBF PM HIPped powder. Comparing the fine grain structure at the outer edge of EPBF wall, grains in the 2 mm and 3 mm walls appear to have fully recrystallised showing equiaxed grain structure; fine columnar grains however can still be seen in the 5 mm wall. Grain size in the 2 mm wall relative to 3 mm wall is coarser suggesting recrystallisation occurred earlier in the walls with 2 mm thickness. This is concurrent with in-situ shelling literature for Ti-6Al-4V, in which specimens with thinner walls exhibited more shrinkage relative to thicker[16]; increased deformation is favourable for recrystallisation. Across all three wall thickness, the interface between EPBF canister and EPBF PM HIPped powder is made clear by the difference in grain size, however no clean line can be observed suggesting bonding across the interface.

Figure 8-41 shows the base bond for all three wall thicknesses. The interface between EPBF shell and EPBF PM HIPped powder is more defined at the base interface relative to the wall, as is observed in LPBF. Grains in the base show a similar graduating structure to that seen in the walls, grains size increasing closer to the interface.

a)

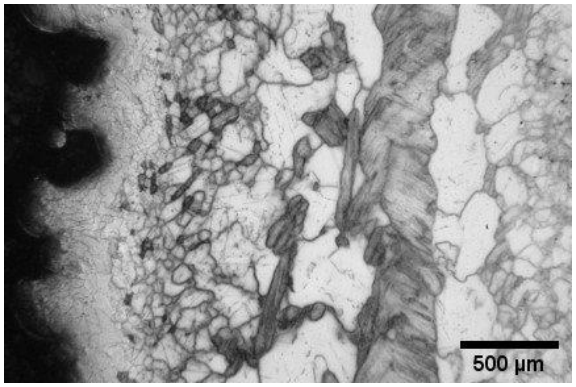

b)

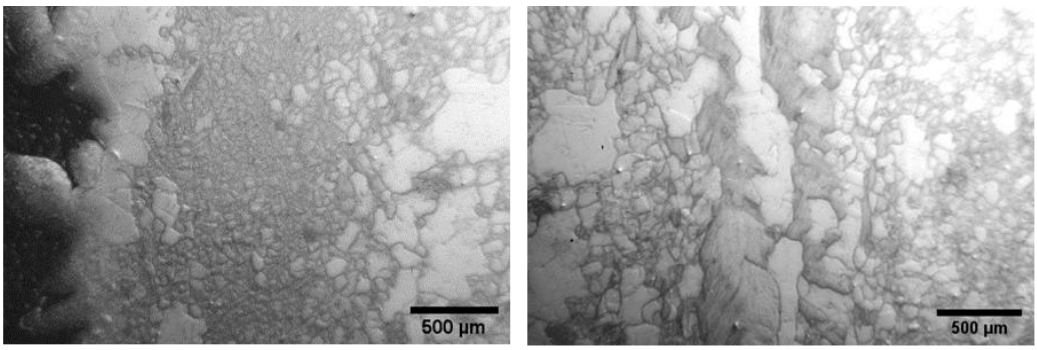

c)

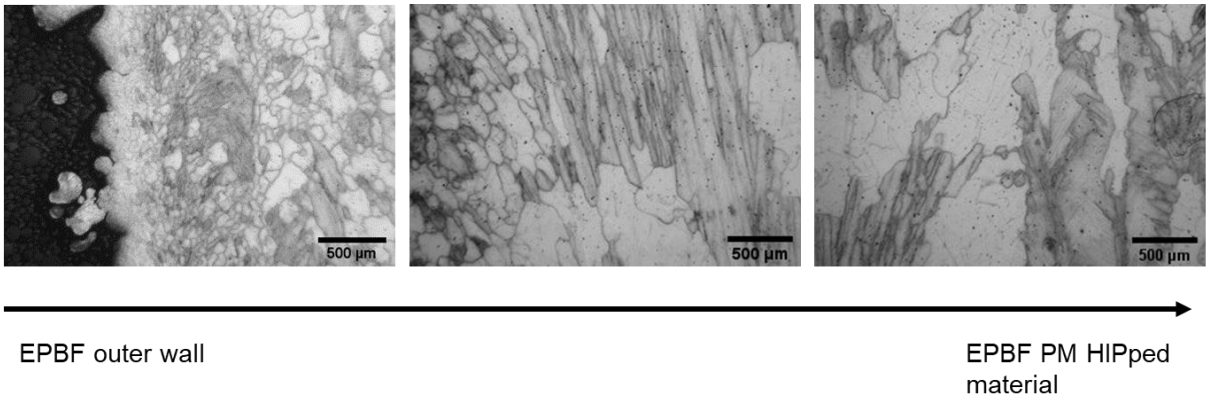

Figure 8-40: Optical micrographs of EPBF canister walls at the mid-point of the wall where the greatest degree of deformation is observed: a) 2 mm thickness; b) 3 mm thickness and c) 5 mm thickness.

a)

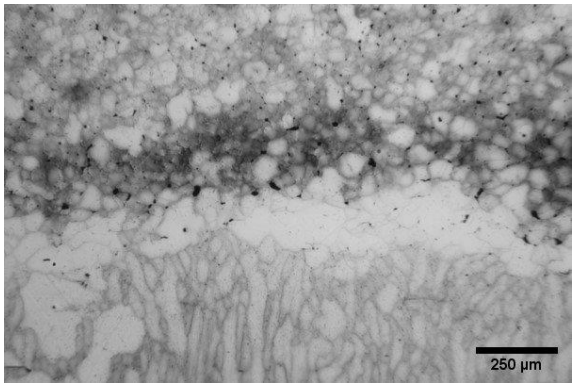

b)

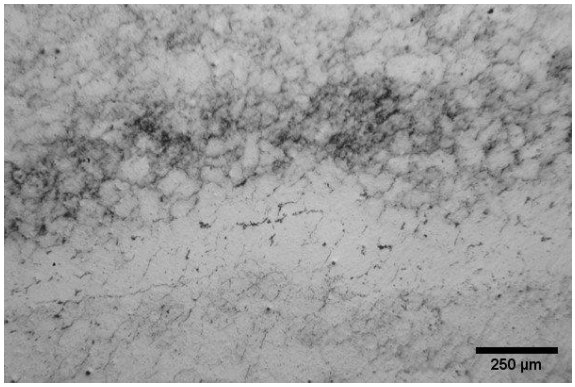

c)

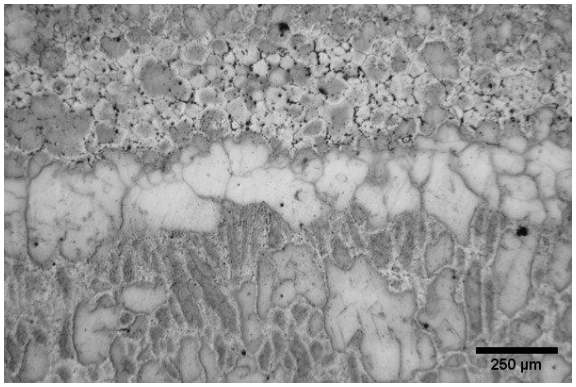

Figure 8-41: Optical micrographs of the EPBF-EPBF PM HIPped interface at the base of in-situ shelling specimens: a) 2 mm wall thickness; b) 3 mm wall thickness and c) 5 mm wall thickness.

BSE imaging was performed along the base and wall interface of each specimen. A film of dark contrasting phase could be observed in regions along the base of all samples (figure 8-42-a) and dark contrasting discrete precipitates observed along the wall interface (figure 8-42-b), believed to be Al oxide. The wall interface was significantly less defined than the base. The continuity of oxide layers in the base was significantly reduced relative to LPBF specimens; likely resulting from the vacuum environment used in EPBF processing. However, it should also be considered that the powder particle size used in EPBF is larger and consequently oxygen concentrations in the virgin EPBF powder are likely to be lower than

those in the LPBF powder leading to a reduction in PPB formation and improved bonding at the interface.

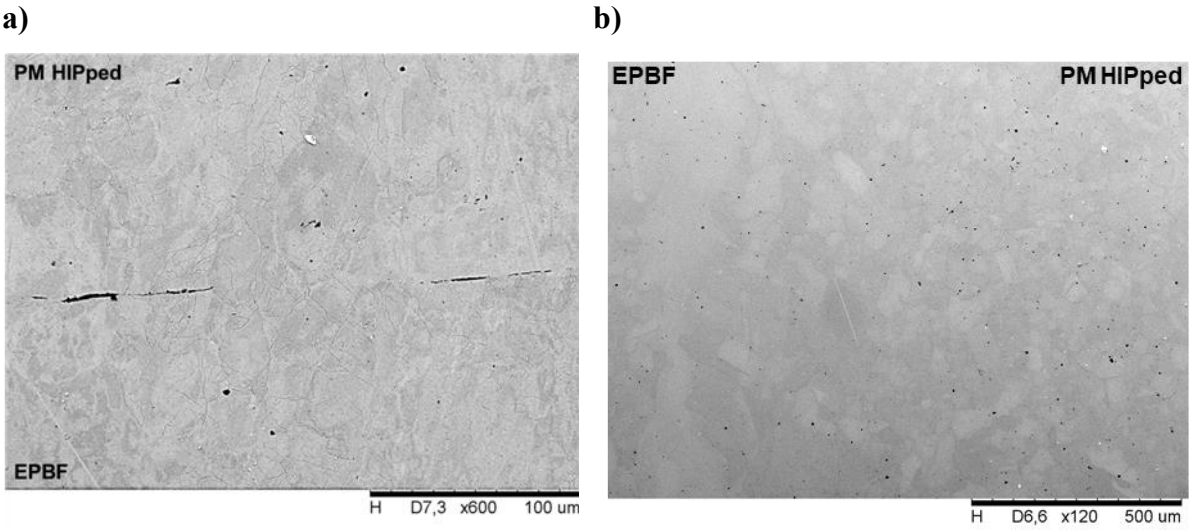

Figure 8-42: BSE images of the interface between EPBF canister and EPBF PM HIPped powder: a) base interface in a 2 mm thick canister and b) wall interface in a 3 mm thick canister

8.8.2 Precipitation

Figure 8-43 shows BSE images of precipitation in the EPBF shell and EPBF PM HIPped powder. In as-fabricated EPBF specimens' precipitation was observed to vary with build height, with significant quantities of coarse δ phase observed in the base and fine NbC carbides observed towards the top of the build. Following HIPping, heterogeneity observed in the as-fabricated samples has disappeared. Precipitates in the EPBF shell consist of a combination of fine NbC carbides and δ. Precipitation in the HIPped powder is dominated by NbC carbides and multi-metal oxy-carbides. HIPping parameters were not disclosed so it is unknown if the precipitation is in line with the thermal history of the specimens.

a) b)

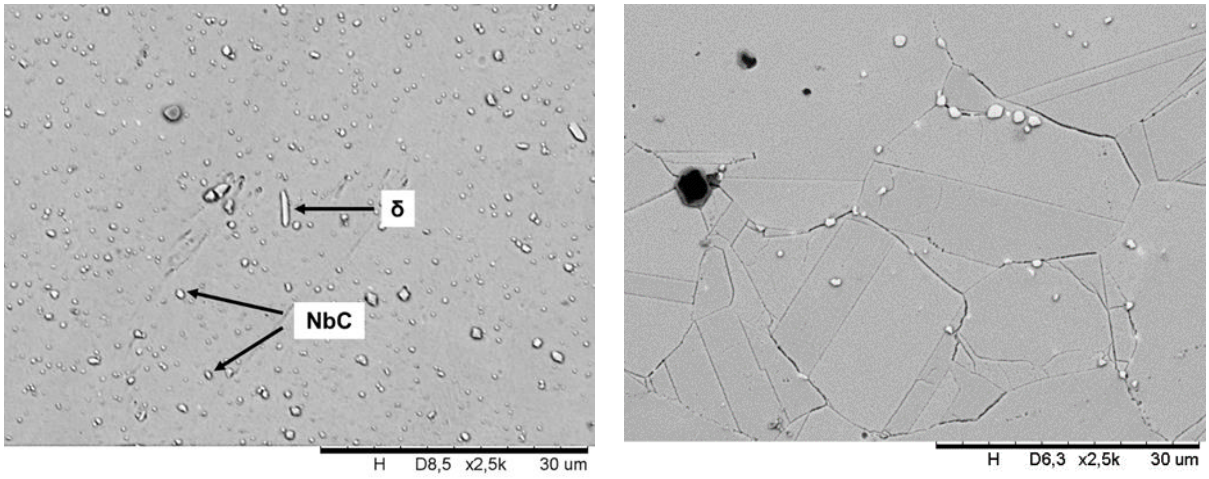

Figure 8-43: BSE micrographs of precipitation in EPBF in-situ shelling sample: a) precipitation in the EPBF canister and b) precipitation in PM HIPped material.

8.9 Summary

The influence of canister wall thickness on shrinkage during HIPping was investigated. Thinner canister walls were shown to result in a slight increase in radial shrinkage relative to thicker walls. The microstructure of EPBF in-situ shelling specimens also suggested thinner walled canisters to result in increased radial shrinkage, with 2 mm walls exhibiting greater quantities of recrystalised grains relative to 3- and 5-mm walls. This is concurrent with previous in-situ shelling studies performed in Ti-6Al-4V.

PPBs were observed in the PM HIPped powder of both successfully HIPped canisters. Relative to state-of-the-art HIPping PPBs were more homogenously distributed, owing to the lack of a diffusion zone in the in-situ shelling samples. PPBs in in-situ shelling canisters also appeared to be more highly decorated with discrete oxides relative to those observed in the

traditional HIPping studies. This was thought to result from the formation of spatter particle in LPBF, which were then incorporated into the canister powders. Spatter particles were also believed to contribute to a lack of fusion in the base of LPBF in-situ shelling canisters.

Bonding across the LPBF-PM HIPped interface was limited resulting from the formation of PPBs and precipitation of Al oxide on the surface of LPBF canisters. A study of influence of LPBF grain structure and surface finish showed surface finish to impact grain growth across the interface, with rougher surfaces resulting in more instances of grain growth. This was thought to be the result of increasing point contacts between powder particles and the LPBF surface leading to increased quantities of recrystallisation.

Tensile testing across the LPBF-PM HIPped interface showed interface bonding to be poor resulting from the formation of Al oxides along the interface. The natural mechanical interlock at the wall and powder interface, improved the strength of bonding, however this was not sufficient to overcome the weakness imparted by the oxide precipitation and lack of grain growth across the interface. Small features were built onto the surface of LPBF canisters with the intention of breaking the continuity of oxide films. This resulted in small but insignificant improvements in UTS values in tensile testing, suggesting a slight increase in grain growth across the LPBF-PM HIPped interface. Given the fracture surfaces observed, potential is shown for using surface features to minimise continuous oxide films, improving bonding between LPBF canister and HIPped powder.

EPBF in-situ shelling specimens showed good bonding across the wall interface, however several regions along the base interface showed an increase in Al O and a consequent reduction in grain growth across the base interface. The increase in bonding in EPBF specimens was attributed to the vacuum environment in which the EPBF build takes place.

Chapter 9

In-situ Shelling for Complex Geometries

9.1 Introduction

One of the key advantages of the in-situ shelling method presented in the work of Das et al.[11], was the ability of the method to improve the production efficiency of both state-of-the-art HIPping and LPBF. It was highlighted in the literature review that this might not be the case for all components and materials but would likely hold true for relatively large and complex structures. With this in mind a feasability study was carried out for an impeller geometry supplied by the industrial sponsor.

9.2 Geometric feasibility

The impeller CAD provided can be seen in figure 9-1. The CAD provided was both solid and shelled (hollow) with a 1 mm wall thickness. Several extreme overhanging features can be identified in the shelled impeller, indicated in figure 9-2-a. The largest overhang being external could be supported with support structures during building. The second largest overhang was chosen for attachment of the outgassing tube; the same conical geometry, with 40° angled walls, used for the simple geometry in-situ shelling canisters was used for the impeller (figure 9-2-b). The smaller internal overhanging features were located at corners; curvature was added to each corner as illustrated in figure 9-2-c, with the hope that these features would be self-supporting.

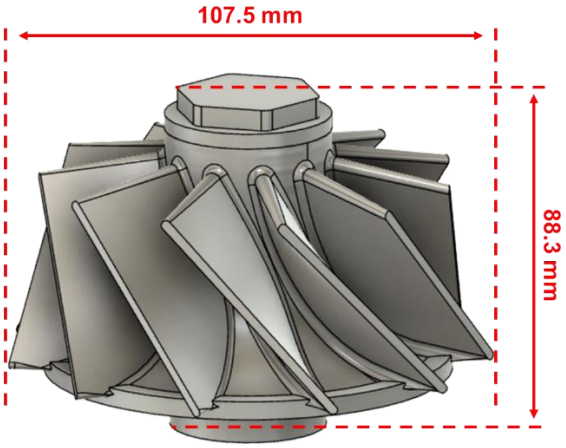

Figure 9-1: 3D illustration of solid impeller CAD.

a)

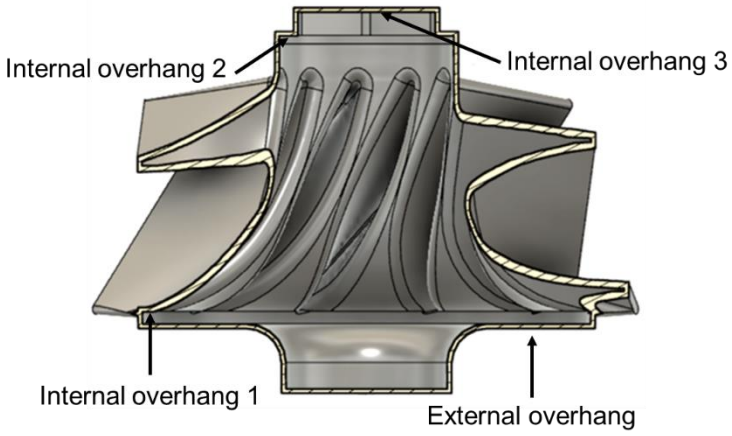

b)

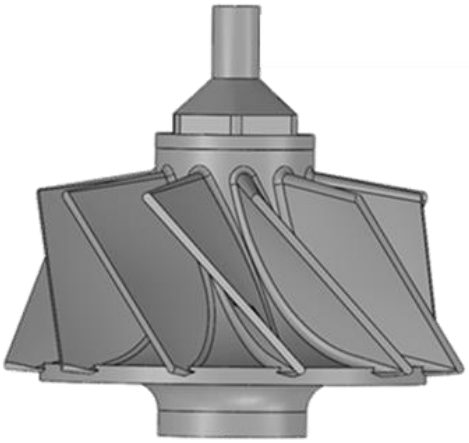

c)

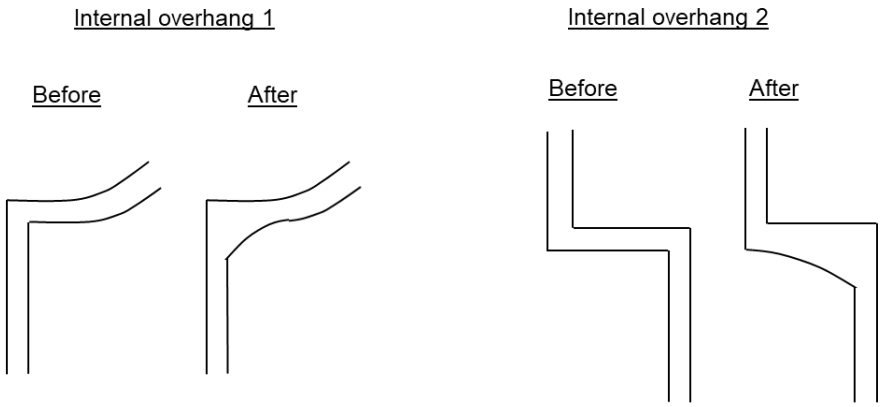

Figure 9-2: Overhanging features in shelled impeller design. a) 3D illustration of cross-section of shelled impeller CAD with overhanging structure identified; b) 3D illustration of shelled impeller CAD with outgassing attachment tube added; c) drawing of internal overhang 1 and 2 (indicated in figure 8-43-a) before and after modification.

Two LPBF builds were attempted for the shelled impeller, however both failed to complete. On both occasions, peeling of the melt layers at internal overhang 1 occurred (figure 9-3), resulting in obstruction of the recoater blade by the protruding metal, and automatic shutdown of the machine. Further modifications were made to the CAD in this region (figure 9-4), with the overhang being eliminated by increasing the wall thickness. It was also deduced that if peeling of material occurred at this small overhang, then peeling was also likely to occur at internal overhang 2. Therefore, it was decided to eliminate the hexagonal structure at the top of the impeller and build the outgassing tube attachment from the circular edge of the impeller hub; with the hexagonal structure being machined from the top material after.

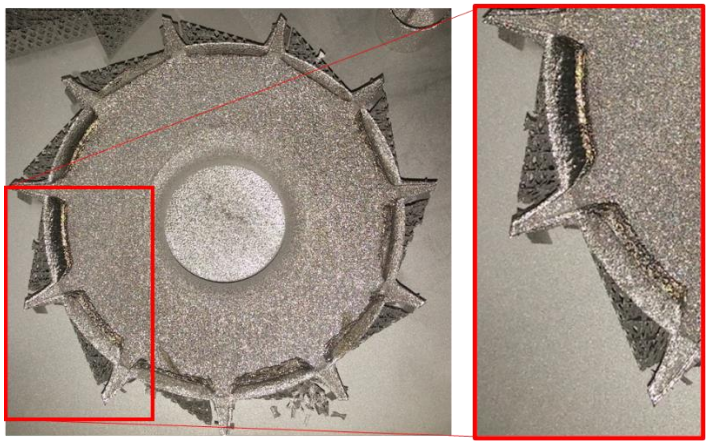

Figure 9-3: Photograph of failed shelled impeller build indicating region of peeling.

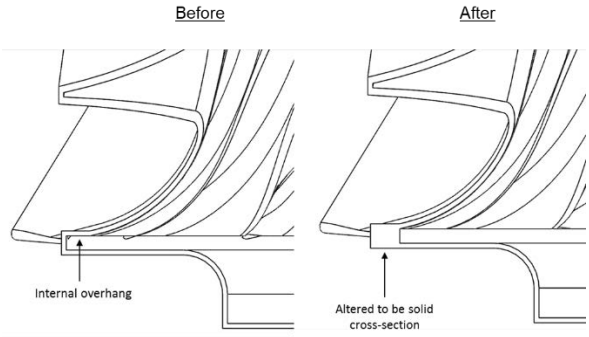

Figure 9-4: Drawing of internal overhang 1 before and after modification.

Figure 9-5 shows the completed impeller build after further CAD modifications. Due to the complex nature of the impeller shell, it was decided that an alternative method of leak testing, in which leak location could be identified, should be used to check for surface connected defects. This involved attaching a compressed air feed to the top tube of the canister and placing the canister in water; small bubbles would then appear in regions where air is escaping from the canister. As the canister was being inserted into water, powders were first emptied from the canister. During leak testing, small bubbles were observed across the entire bottom surface of the impeller, with most occurring in the outer circular plate (indicated in figure 9-5-b). The impeller was produced using a simple scan strategy; given the large diameter of the effected region, it is possible that the input energy was insufficient for the length of scan track. However, given the origins of LoF observed in LPBF and LPBF in-situ shelling canister builds, it is more likely that spatter particle formation is to blame.

a) b)

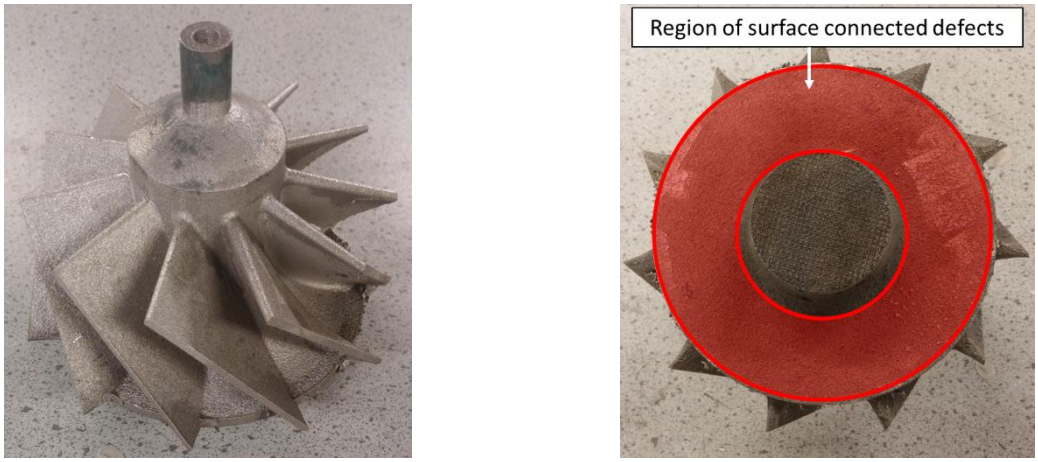

Figure 9-5: Completed LPBF shelled impeller following further CAD modifications: a) front view; b) bottom view with region of surface connected defects highlighted with red shading.

As the impeller component has a significant central solid body, it was decided that it was still economically viable to only HIP the powders in the central portion of the impeller (see section 9.3 table 9-2). The solid impeller was hollowed out and a canister designed to merge with the outer body, as shown in figure 9-6. By doing this, any LoF voids formed in the outer body of the impeller would not impact the integrity of the canister containing loose powders for HIPping. In addition, LoF voids in the outer body, would be reduced in size during HIPping; they would be unlikely to close completely due to the presence of surface oxides and potential entrapment of argon gas during LPBF processing. To avoid porosity formation resulting from having large scan track lengths, the canister was melted separately from the outer body, i.e., scan track length of the canister wall was equivalent to scan track length of the 1 mm simple canister wall successfully produced in earlier studies (section 8.2).

a) **b)**

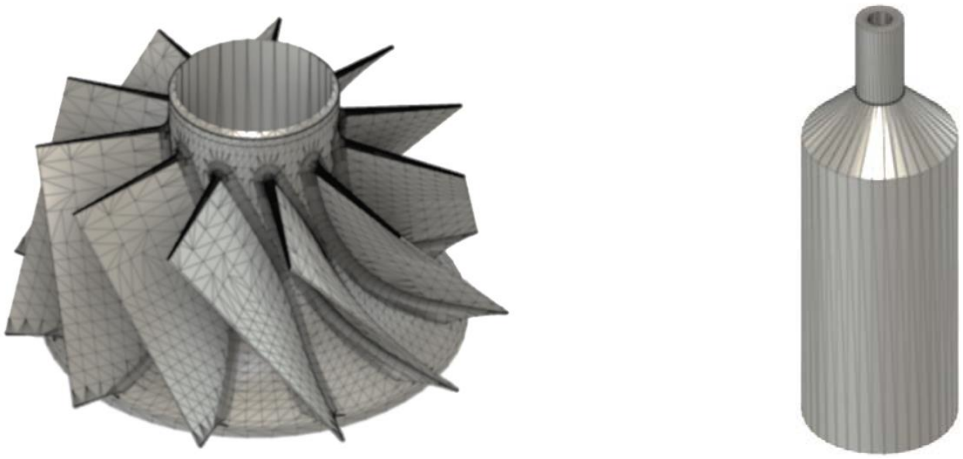

Figure 9-6: a) Solid impeller with centre aspect removed; b) simple canister to replace centre of impeller.

Figure 9-7 shows the LPBF impeller with the external support structures removed. Several seams can be seen on the surface of the impeller, suggesting errors in the STL files generated from the assembly of the inner cylindrical canister and outer impeller hub and blade structure. A step could also be observed along the bottom surface of each blade, again likely to have occurred due to an error in the STL file of the solid impeller. As with the previous impeller, water leak testing was performed to identify regions of surface connected porosity in the central canister. Small bubbles were observed at the seam between the canister and the outer impeller body. As there is not a clean join between the canister and outer body, bubbles observed here could originate from surface connected porosity formed at any point along the top of the canister wall.

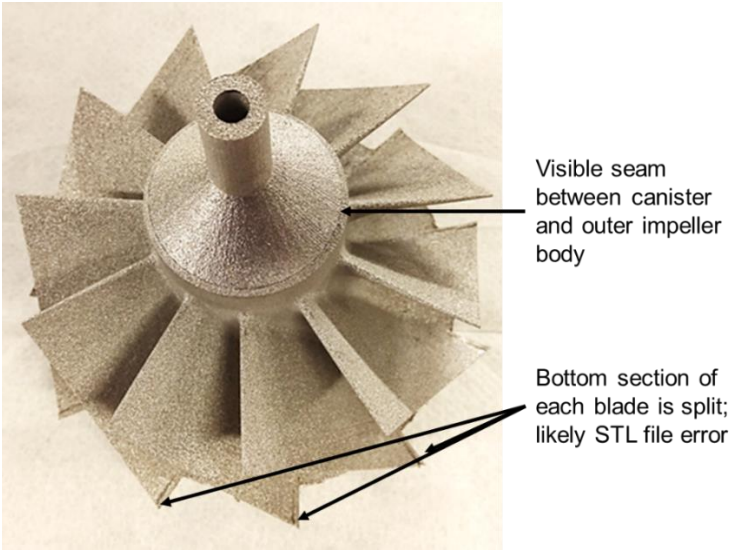

Figure 9-7: Completed LPBF in-situ shelling impeller. STL file errors resulting in poor build are indicated.

Taking into consideration the results of the LPBF wall builds and builds of simple canister geometries, it is reasonable to assume that the process parameters used for melting of the internal canister were suitable for producing high density parts with no surface connected defects. Consequently, it would be safe to assume that LoF porosity formation can be attributed to spatter particle formation as opposed to insufficient energy for melting. As with previous builds, powders reclaimed form the impeller build were examined by BSE SEM. Figure 9-8 shows BSE micrographs of the reclaimed powders. Several types of spatter particle could be observed. While a few singular oversized particles could be seen (figures 9-8-d- and -c) the majority of particles that could be clearly defined as spatter consisted of melt eject attached to virgin powder particles (indicated in figure 9-8-a) and agglomerates (figure 9-8-b). Agglomerates varied in size with some as small as just 20 μm and others as large as 270 μm, consistent with the studies of Gasper et al.[201].

a)

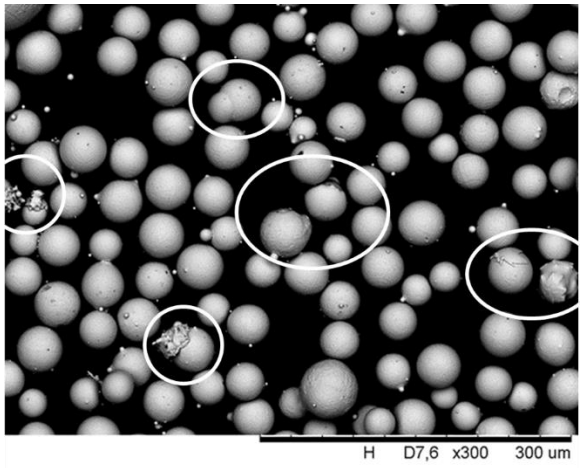

b)

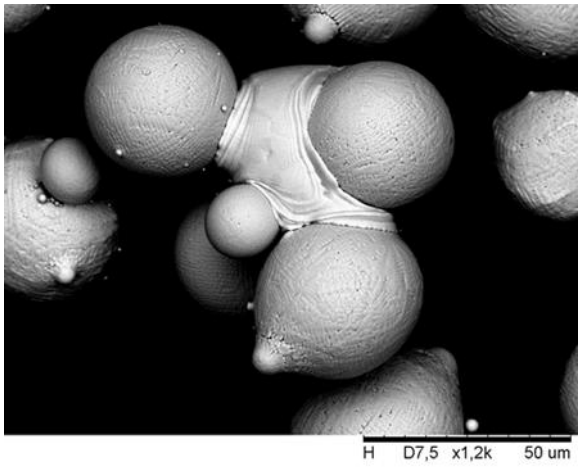

c)

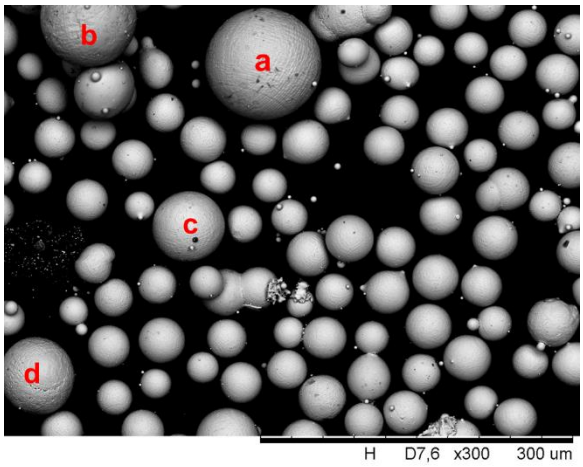

d)

Letter	Powder Diameter (µm)
a	106.96
b	88.73
c	64.56
d	64.37

Figure 9-8: BSE analysis of powder reclaimed from the final impeller build trial: a) low magnification image with clearly defined spatter particles indicated; b) high magnification image of an agglomerate type of spatter particle; c) low magnification image of powder sample containing several large powder particles and d) table of powder diameter measurements corresponding to powder particles in image c.

Given the size of agglomerates observed, it is possible that the laser energy used for melting was not sufficient to remelt these particles into the component, leading to the formation of LoF voids. Comparing the production of simple in-situ shelling canisters with the impeller it is also likely that the impeller build would lead to an increase in the quantity of spatter generated. As the part area is bigger, consisting of more scan tracks, particularly

discontinuous scan tracks, the mechanism by which spatter generation arises (as discussed in chapter 7) occurs more frequently. In addition, on several occasions during building the filtration system -removing particles pulled from the build area by the gas flow- choked, requiring cleaning of the filters. If the filters are full, it is likely to impact the rate of gas flow in the machine as spatter particles begin to build up along the gas inlet pipe. Considering the Concept M2 machine environment, it may be concluded that using an alternative LPBF system would result in more successful builds; consequently, the possibility of using in-situ shelling for producing the impellers should not be completely ruled out.

9.3 Economic feasibility

To truly evaluate the benefits of the in-situ shelling process, the process cost should be considered relative to state-of-the-art HIPping and LPBF. A cost analysis structure was decided by first considering the two main processes involved in the in-situ shelling method and then the associated costs with each process. Table 9-1 summarises the costs considered for the in-situ shelling process. HIP costs are based on a quotation for a HIP run in a HIP vessel similar in size to the EPSI HIP located in AMPLab. All other listed costs are those used to calculate research costs on the M2 Concept machine when budgeting research projects.

Table 9-1: Summary of costs for each stage of the in-situ shelling process.		
Process stage	**Type of cost**	**Unit cost (£)**
HIPping	Lab technician for preparation of the HIP/ argon gas/ power (cost per 3-hour HIP run, in vessel with 400 mm dia.)	950.00
LPBF	File preparation (hourly rate of CAD technician)	22.73
	Machine consumables fixed cost (Ni substrate plate, recoater blade)	53.19
	Machine consumables variable cost (argon gas, machine power per hour)	25.76
	Inconel 718 powder (per Kg)	60.06
	Machine set-up and clean down (hourly rate junior lab technician)	16.23
	Preparation of LPBF built canisters for HIPping- removal of support structures/ welding of outgassing tube/ crimping outgassing tube (hourly rate senior lab technician)	22.73
Post Process	EDM for removal of outgassing tube post HIPping (cost per hour)	50.00

Cost analysis was performed for the impeller component presented in the previous section. Given that the cost of HIPping is dictated by the size of the HIP vessel and length of HIP time, it makes sense to first consider how many components can be fit into a single HIP cycle, and then cost the LPBF accordingly. Three impeller components should be capable of fitting in the HIP vessel costed for in table 9-1. A large build plate in the Concept M2 system is 240 mm by 240 mm and consequently all three impellers could be produced in a single build.

Figures 9-9 and 9-10 summarise the total production time and cost per impeller respectively, for producing impellers via the in-situ shelling method (fully shelled and with a canister as discussed in section 9.2), by LPBF and by state-of-the-art HIPping. Production times presented for LPBF processes were calculated based on the actual experimental time involved in producing the impellers seen in section 9.2. State-of-the-art HIPping time was based on a mock quotation provided by a welding engineer working for TWI Ltd. (see appendix A) and the work presented by Wang et al.[58] on production of multi-material blisks. The quotation provided by the welding engineer was specified for production of 60 impellers shells, as this was the number of shells that could be welded using the quantity of sheet material that could be cut for the minimum chargeable on the laser cutting system. The cost of three impeller was calculated from the information provided for comparison with in-situ and LPBF processes. Comparing production times, the time taken to produce impellers by state-of-the-art HIPping is significantly higher than production time for the in-situ shelling method and LPBF; this is due to the time taken to remove the canister post-HIPping. If canister removal is not considered production times are significantly less than those of the other methods at just 16 hours long. Overall producing the impeller via the in-situ shelling method in a fully shelled state is the fastest production route. In addition to being the fastest production method it is also the cheapest, coming in at approximately £40 cheaper than the next most cost-effective method, state-of-the-art HIPping. It should be noted however that state-of-the-art HIPping costs do not include the cost of the central hub of the impeller as the quote provided assumed the hub was supplied pre-formed and only quotes for the cost of cutting and attaching the blades. Furthermore, the cost of pickling is unknown and has also not been accounted for. Consequently, state-of-the-art HIPping costs may actually be higher than in-situ shelling with a canister and LPBF.

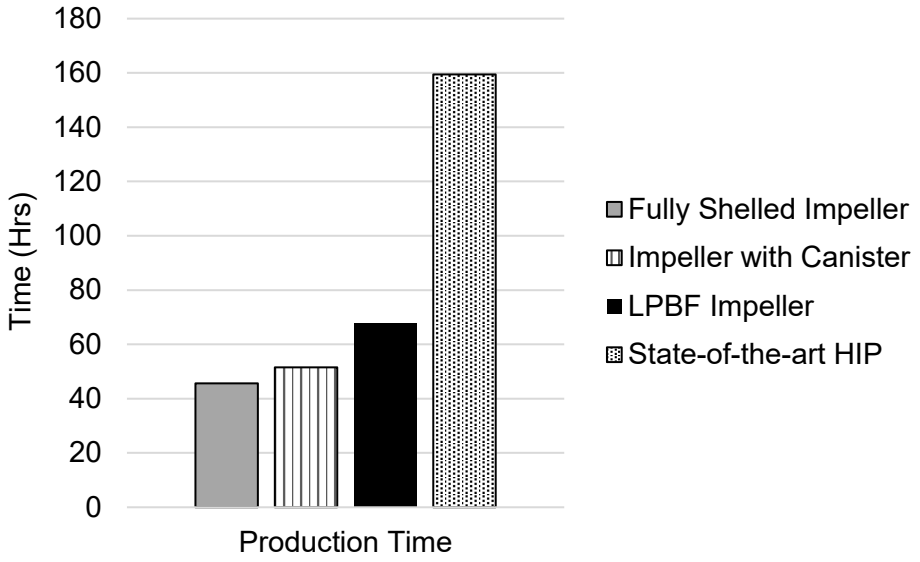

Figure 9-9: Comparison of total production time for three impellers produced by three different processing routes. Times are presented for in-situ shelling for two varying degrees of densification at the LPBF stage, for a solid LPBF impeller and for state-of-the-art HIPping.

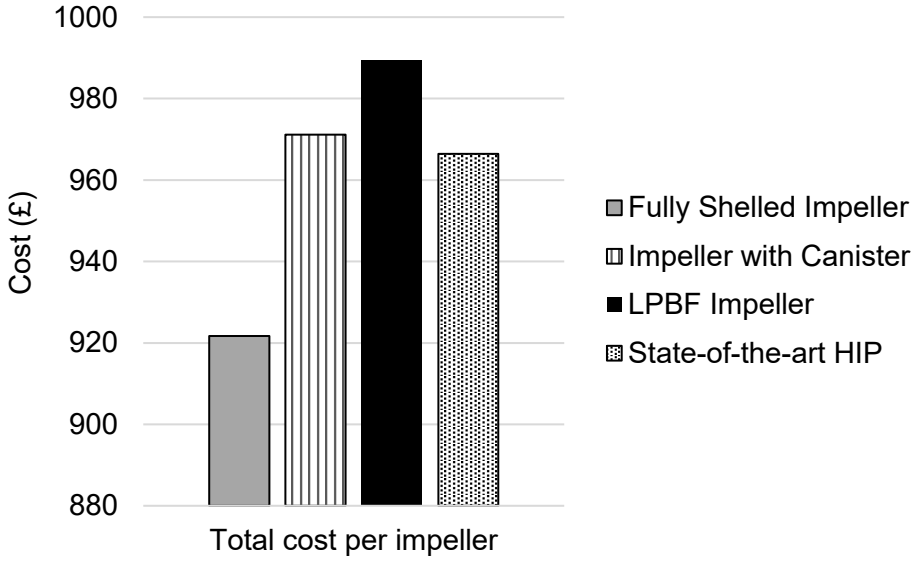

Figure 9-10: Comparison of total cost per impeller for impellers produced by three different processing routes. Times are presented for in-situ shelling for two varying degrees of densification at the LPBF stage, for a solid LPBF impeller and for state-of-the-art HIPping.

Due to the fixed costs associated with producing the impellers by traditional HIPping methods, cost of production by such methods can be significantly reduced by increasing the number of impellers manufactured. However, the production scale of LPBF in-situ shelling impellers could also be scaled up reducing the cost of impeller production; for example, by using a multi-laser LPBF system. Furthermore, the quote provided for welding of the impeller canisters is a hypothetical quote, as in discussions with the welding engineer, it was explained that it would be almost impossible to weld the blades to the canister and have a completely gas tight seal; the distance between each blade restricts access for both the tungsten electrode and filler wire, making precision welding difficult.

9.4 Summary

Geometric and economic feasibility was presented for in-situ shelling of an impeller canister. Production of the canister was unsuccessful due to a number of reasons. In initial trials, canister builds failed owing to a lack of support for over hanging structures which pealed up and away from the build plate. Modifications were made to the canister design resulting in the successful completion of the LPBF build; however, when leak tested the impeller canister was found to not be gas tight, with leak testing indicating porosity across the outer region of the bottom cross-section of the impeller. A further modified design was presented in which the impeller was split into two components, a simple inner canister, and an outer blade attachment. This design was successfully constructed by LPBF however did not pass leak testing. Analysis of powder reclaimed from the impeller builds suggested significant quantities of spatter to have been generated during building. Spatter particles consisted of Al oxide coated powders, melt collision particles and agglomerates. Due to the size of

agglomerates, the laser energy implemented would likely be insufficient for remelting of agglomerates leading to the formation of LoF voids.

Economic feasibility studies showed the in-situ shelling method to be both faster and cheaper for production of complex geometries, relative to LPBF and state-of-the-art HIPping. This was due to the decreased production times at the LPBF stage and significantly less time dedicated to post-processing. While scale up of impeller production for state-of-the-art HIPping would significantly reduce production costs (below that of in-situ shelling), the difficulty in welding canisters of complex geometry, particularly for small features, would mean state-of-the-art HIPping is not a viable production candidate.

Chapter 10

Conclusions and Future Work

10.1 Introduction

This work has presented an alternative PM production method for Inconel 718, the in-situ shelling method. Investigations into the process-microstructure-property relationship have been performed for each PM processing component that makes up the in-situ shelling method. This chapter starts by summarising the main conclusions presented each of these components, PM HIPping and PBF of Inconel 718, discussing the challenges each process presents for the in-situ shelling process. Concluding remarks are then given regarding in-situ shelling trials of simple and complex geometries. Finally, a summary of future work suggested in sections 10.2 through 10.4 is provided.

10.2 PM HIPping

The microstructure and properties of the PM HIPped material was found to be primarily defined by the presence of PPBs. PPBs were found to be decorated with NbC carbides and discrete Al oxides. The formation of these precipitates was attributed to the chemistries of the virgin powder; relatively high levels of oxygen and carbon were observed in the powder as well as segregation of Nb creating favourable conditions for oxide and NbC carbide precipitation.

The formation of PPBs was discussed in the context of powder particle size. Previous studies had conflicting views over the influence of powder particles size on PPBs. Some suggested that irrespective of oxygen content, smaller particles lead to greater recrystallisation[72, 76, 77]

and reduced PPBs, owing to the increased number of point contacts achieved by the higher theoretical powder packing density of finer powders. Other studies however suggested, oxygen concentration had the greatest impact on PPB formation[70, 74]. The work presented here was in agreement with the latter, however this was not solely attributed to the oxygen content of the powder, but instead the composition of the most energetically favourable oxide for Inconel 718 -Al_2O_3. A review of the Ni-base superalloy literature found PPB formation to be unaffected by powder particle size where the preferred oxide was Al_2O_3; yet, when the Ni-base superalloy composition favoured chromia oxide formation, powder particle size had more of an influence on the quantity of PPBs observed. This is not something that has previously been considered and consequently warrants further investigation.

The diffusion zone was shown to influence the distribution of PPBs not only near the canister wall, but also in the centre of the canister. It was suggested that due to the large quantities of NbC type carbides precipitated in the diffusion zone, a concentration gradient for Nb was created drawing Nb away from the centre region of the HIPped powder. While this was beneficial in reducing PPB formation in the centre region, later tensile tests suggested Nb depletion may have resulted in impaired tensile properties, due to a reduction in precipitation of strengthening phases. Consequently, it was concluded that HIPping in a canister of similar material to the powder, or of extremely low carbon content (316L stainless steel) would be beneficial for mechanical properties. In previous studies the impact of the diffusion zone has not been discussed extensively, only to say, that properties within the diffusion zone itself are not favourable and as such the diffusion zone should be removed. It is the view of the author, that an extensive literature review should be performed comparing mechanical properties as a function of diffusion zone depth. This may prompt further experimental work in the field.

10.3 PBF

Extensive LPBF process optimisation studies were conducted for minimising porosity and cracking defect formation in walls. EPBF process optimisation studies were also conducted, but due to machine issues very few samples could be properly assessed. Parameters capable of producing fully dense Inconel 718 walls were identified for building canister in in-situ shelling studies. Microstructures of fully dense LPBF and EPBF specimens were equivalent to those observed in the literature.

Surface studies were also performed so that surface finish could be optimised for in-situ shelling canisters. Parameters shown to influence surface finish included layer thickness, hatch laser power, contour laser power, contour scan speed and number of contours. A range of surface roughness were achieved with minimum average roughness of 4.5 μm and maximum 11.48 μm. While the aim of this study was to maximise surface roughness, an understanding of the process for minimising surface roughness would be beneficial to the AM community, as one of the disadvantages of PBF is that post processing is required to smooth part surfaces reducing possible site of crack initiation. This work and previous work by the author[168] has shown performing double contour scans at relatively low scan speed, placed such that the edge of the contour melt track aligns with the edge of the wall, result in significantly reduced surface roughness. The mechanism by which this occurs has been proposed as follows: in the first scan of the contour, the force of the vapour plume emerging from the melt pool creates a denuded zone around the edge of the wall; in the second contour scan the wall surface -included any attached unmelted powder particles- is remelted smoothing the surface. Due to the denuded zone, there is no availability of powder for attachment to the new melt surface. The mechanisms of surface optimisation should be

studied further through simulation of the melt flow behaviour and observation of melt flow by high frame rate imaging.

Tensile of LPBF as-fabricated specimens showed significant variability in properties. Fractography revealed the presence of a significant number of large spatter particles in samples with poor tensile properties.

10.4 In-situ shelling

Wall thickness studies were performed for the in-situ shelling canisters showing thinner walls to result in slightly higher radial shrinkage relative to thicker walls, consistent with existing literature. PPBs were observed to be more homogeneously distributed in powder HIPped in in-situ shelling canisters relative to state-of-the-art HIPping. However, PPBs were also observed to be more defined relative to state-of-the-art HIPping, with an increase Al oxide decoration. It was suggested that this was due to the incorporation of spatter particles into the powder during the LPBF stage. Consequently, it may be beneficial to empty the LPBF powders from the in-situ shelling canister and replace them with virgin powders unaffected by spatter. The time taken to remove and replace the powders would not result in significant productivity losses; however, for more complex geometries full removal of the spatter affected powder may not be possible.

Clearly defined boundaries were observed between LPBF and PM HIPped material. This was attributed both to PPB formation and oxide precipitation from the LPBF canister surface. Studies on the influence of LPBF grain structure and surface finish showed surface finish to influence bonding across the LPBF-PM HIPped interface, with rougher surfaces resulting in more instances of grain growth. Following analysis of the surface roughness profiles of LPBF specimens, this was attributed to an increase in the number of point contacts between powder

particle and the LPBF specimens, resulting in an increase in recrystallisation at the interface. The influence of surface finish on bonding in in-situ shelling has not previously been considered and may offer a mechanism for improving bond strength in processing of alloys with more stable oxides. As discussed in section 10.2 PPBs in PM HIPped chromia forming Ni-base superalloys may be reduced by encouraging recrystallisation at powder boundaries. Consequently, successful bonding of canister and PM HIPped material maybe achievable in chromia forming Ni-base superalloys by tailoring surface finish to increase point contact with power particles.

Tensile testing was performed across the LPBF-PM HIPped interface. Specimens were observed to fail at the interface owing to a continuous oxide film being deposited along the surfaces of laser scan tracks. Small features of varying geometry were built onto the surfaces of LPBF in-situ tensile specimens, with the purpose of disrupting the precipitation of continuous oxides. Small but insignificant improvements were seen in the tensile properties of specimens. The features were quite far dispersed on the LPBF base surface; increasing the quantity of surface features to eliminate flat LPBF surface entirely may lead to better bonding across the interface.

Economic feasibility studies were conducted showing the in-situ shelling method to be both more productive and cheaper for manufacture of complex geometries. Geometric feasibility studies were not as successful however owing to insufficient gas flow in the concept M2 failing to remove spatter particles. This ultimately led to the formation of LoF voids and impeller canisters were consequently not suitable for HIPping. Future work should consider performing these trials in an alternative machine system with improved gas flow.

10.5 Summary of future work

Below is a summary of future work as discussed in the previous sections. Work is categorised by the processing method to which it applies.

10.5.1 PM HIPping

Future work suggested for the investigation of PM HIPping of Ni-base superalloys is as follows:

1. Investigation of the influence of Ni-base superalloy oxide composition on the recrystallisation mechanisms at powder surface during HIPping.
2. Literature review comparing mechanical properties of PM HIPped Ni-base superalloys as a function of diffusion zone depth.

10.5.2 PBF

Future work suggested for the investigation of PBF of Ni-base superalloys is as follows:

1. Investigation into the mechanisms of the influence of LPBF parameters on surface roughness, included high frame rate imaging of surface melt behaviour during contour scans, and simulation of surface melt flow behaviour.

10.5.3 In-situ shelling

Future work suggested for the investigation of in-situ shelling of Ni-base superalloys is as follows:

1. Investigations into the influence of replacing powders filled in LPBF with virgin powders, on PPB formation and bonding across the LPBF-PM HIPped interface.
2. LPBF in-situ shelling of chromia forming Ni-base superalloys and the influence of surface finish on bonding across the LPBF-PM HIPped interface.
3. Further investigations into the use of surface features to prevent precipitation of continuous oxide films.
4. Further geometric feasibility studies testing the influence of machine system, specifically gas flow system, on spatter formation in large Inconel 718 parts.

Appendix A

Quote for welding of impellers

Please see below a breakdown of equipment and labour costs pertaining to your request. As far as the laser cutting there is a charge of £100 for half a sheet, so for 1 unit this would be the minimum charge payable. However if you were to fill the sheet approx. 60 units worth the charge is £200 for a full sheet making the unit price only £3.40.

This will be TIG welded at a labour cost of £50 per hour using 316L Filler wire. Again the purchase of a pack of wire is £16.62, if you are to batch make it would only cost around £0.30p per unit.

Cost Centre	Material Cost (£)	Per unit (£)
Laser cutting	100	3.4
Welding JIG design and manufacture	500	
Welding filler material 1Kg sif 65 rods	182.82	3.30
Welding labour (3 Hrs.)	150	2.5
Cleaning labour (0.5 Hrs.)	25	0.42
Inspection (0.5 Hrs.)	25	0.42
Total	**6982.82**	**116.38**

References

1. Reed, R.C., *The Superalloys: Fundamentals and Applications*. 2006, Cambridge: Cambridge University Press. 16.

2. Donachie, M.J. and S.J. Donachie, *Superalloys : a technical guide*. 2nd ed. ed. 2002, Materials Park: ASM International.

3. Sims, C. *A HISTORY OF SUPERALLOY METALLURGY FOR SUPERALLOY METALLURGISTS*. in *Superalloys 1984*. 1984. Pennsylvania, USA: Metallurgical Society of AIME.

4. Gilles, R., et al., *Investigations of early stage precipitation in a tungsten-rich nickel-base superalloy using SAXS and SANS.* Journal of Alloys and Compounds. **612**: p. 90-97.

5. Wang-Koh, Y.M., *Understanding the yield behaviour of L12-ordered alloys.* Materials Science and Technology. **33**(8): p. 934-943.

6. Li, X., et al., *Improved plasticity of Inconel 718 superalloy fabricated by selective laser melting through a novel heat treatment process.* Materials & Design. **180**.

7. Devaux, A., et al., *Gamma double prime precipitation kinetic in Alloy 718.* Materials Science & Engineering A, 2008. **486**(1): p. 117-122.

8. Hofer, B. and A. Riou, *Introduction to Hot Isostatic Pressing Technology: A guide for Designers and Engineers*, E.P.M. Association, Editor. 2019.

9. Panwisawas, C., Y.T. Tang, and R.C. Reed, *Metal 3D printing as a disruptive technology for superalloys.* Nat Commun, 2020. **11**(1): p. 2327-2327.

10. Das, S., et al., *Direct Selective Laser SIntering and Containerless Hot Isostatic Pressing for High Performance Metal Components*, in *Solid Freeform Fabrication* D.L. Bourell, Editor. 1997, University of Texas: Austin, Texas, USA. p. 81-90.

11. Das, S., et al., *Producing metal parts with selective laser sintering/hot isostatic pressing.* JOM, 1998. **50**(12): p. 17-20.

12. Qiu, C., et al., *In-situ shelling via selective laser melting: modelling and microstructural characterisation.* 2015.

13. Hassanin, H., et al., *Net-Shape Manufacturing using Hybrid Selective Laser Melting/Hot Isostatic Pressing.* 2017.

14. Cai, C., et al., *A novel hybrid selective laser melting/hot isostatic pressing of near-net shaped Ti-6Al-4V alloy using an in-situ tooling: Interfacial microstructure evolution*

and enhanced mechanical properties. Materials Science and Engineering A, 2018. **717**: p. 95-104.

15. Leicht, A., et al., *As-HIP Microstructure of EBM Fabricated Shell Components*, in *WorldPM 2016*. 2016, European Powder Metallurgy Association (EPMA): Hamburg, Germany.

16. Frisk, K., et al., *Characterisation of EBM-Built Shelled Samples of Ti6Al4V Compacted by HIP*, in *WorldPM 2016*. 2016, European Powder Metallurgy Association (EPMA): Hamburg, Germany.

17. Illston, T.J., *Additive Manufacturing*, T.I.P.O.o.t.U. Kingdom, Editor. 2017, Materials Solutions Limited.

18. Shirzadi, A.A., H. Assadi, and E.R. Wallach, *Interface evolution and bond strength when diffusion bonding materials with stable oxide films.* Surface and interface analysis, 2001. **31**(7): p. 609-618.

19. Shirzadi, A.A. and E. Wallach, *Novel method for diffusion bonding superalloys and aluminium alloys (USA patent 6,669,534 B2, European patent pending).* New Frontiers Of Processing And Engineering In Advanced Materials, 2005. **502**: p. 431-435.

20. Deadmore, D., *Effects of Alloy Composition on Cyclic Flame Hot-Corrosion Attack of Cast Nickel-Base Superalloys at 900°C*. 1984, NASA: Lewis Research Center, Cleveland OH.

21. Gordon, A.P., et al., *Corrosion kinetics of a directionally solidified Ni-base superalloy.* Acta materialia, 2007. **55**(10): p. 3375-3385.

22. Sudbrack, C.K., et al., *Oxidation and the Effects of High Temperature Exposures on Notched Fatigue Life of an Advanced Powder Metallurgy Disk Superalloy*. 2012, Hoboken, NJ, USA: John Wiley & Sons, Inc: Hoboken, NJ, USA. p. 863-872.

23. Jung, J., B. Shollock, and K.-b. Yoo, *Transient Oxidation of a Nickel-Base Superalloy with Varying Oxygen Partial Pressure.* Oxidation of Metals, 2016. **85**(3): p. 221-229.

24. Stott, F.H., *Influence of alloy additions on oxidation.* Materials Science and Technology, 1989. **5**(8): p. 734-740.

25. Ecer, G.M. and G.H. Meier, *Oxidation of high-chromium Ni-Cr alloys.* Oxidation of metals, 1979. **13**(2): p. 119-158.

26. Cruchley, S., H. Evans, and M. Taylor, *An overview of the oxidation of Ni-based superalloys for turbine disc applications: surface condition, applied load and mechanical performance.* Materials at High Temperatures: High Temperature Materials for Aerospace Applications, 2016. **33**(4-5): p. 465-475.

27. Jönsson, B. and A. Westerlund, *Oxidation Comparison of Alumina-Forming and Chromia-Forming Commercial Alloys at 1100 and 1200 °C.* Oxidation of Metals, 2017. **88**(3): p. 315-326.

28. Cruchley, S., et al., *Chromia layer growth on a Ni-based superalloy: Sub-parabolic kinetics and the role of titanium.* Corrosion Science, 2013. **75**.

29. Wood, G.C., *High-temperature oxidation of alloys.* Oxidation of Metals, 1970. **2**(1): p. 11-57.

30. Taylor, M., et al., *The oxidation characteristics of the nickel- based superalloy, RR1000, at temperatures of 700 - 900° C.* Materials at High Temperatures, 2012. **29**(2): p. 145.

31. Brady, M.P., I.G. Wright, and B. Gleeson, *Alloy design strategies for promoting protective oxide-scale formation.* JOM, 2000. **52**(1): p. 16-21.

32. Swadźba, R., et al., *Characterization of Alumina Scales Grown on a 2nd Generation Single Crystal Ni Superalloy During Isothermal Oxidation at 1050, 1100 and 1150 °C.* Oxidation of Metals, 2014. **82**(3): p. 195-208.

33. Evans, J.L., *Effect of Surface Roughness on the Oxidation Behavior of the Ni-Base Superalloy ME3.* Journal of materials engineering and performance, 2010. **19**(7): p. 1001-1004.

34. Pei, H., et al., *Influence of surface roughness on the oxidation behavior of a Ni-4.0Cr-5.7Al single crystal superalloy.* Applied Surface Science, 2018. **440**: p. 790-803.

35. J. Nowak, W., et al., *Consequences of Different Mechanical Surface Preparation of Ni-Base Alloys during High Temperature Oxidation.* Materials, 2020. **13**(16): p. 3529.

36. Naraparaju, R., et al., *Effect of Shot-peening on the Oxidation Behaviour of Boiler Steels.* Oxidation of Metals, 2011. **76**(3): p. 233-245.

37. Evans, H.E., *Cracking and spalling of protective oxide layers.* Materials science & engineering. A, Structural materials : properties, microstructure and processing, 1989. **120**: p. 139-146.

38. Zheng, L., et al., *Investigations on the growing, cracking and spalling of oxide scales of powder metallurgy Rene95 nickel-based superalloy.* Applied Surface Science, 2011(257): p. 6.

39. International, A., *Vacuum Induction*, in *ASM Handbook Volume 15: Casting*. 2008, ASM International.

40. Upadhyaya, A. and G.S. Upadhyaya, *Powder Production*, in *Powder Metallurgy Science, Technology and Materials*, B. Raj, Editor. 2011, Universities Press (India) Private Limited: Hyderabad, India. p. 56.

41. Neikov, O., *Handbook of Non-Ferrous Metal Powders : Technologies and Applications*, S. Naboychenko and I. Mourachova, Editors. 2009, Elsevier.

42. Wheeler, A. *AP&C's Third Plasma Atomization Reactor Put Into Service*. 2015 [cited 2020 September]; Available from: https://new.engineering.com/story/apcs-third-plasma-atomization-reactor-put-into-service.

43. Elliot, A.M., et al. *A Method for Measuring Powder Bed Density in Binder Jet Additive Manufacturing Process and the Powder Feedstock Characteristics Influencing the Powder Bed Density*. in *Solid Freeform Fabrication 2016: Proceedings of the 27th Annual International Solid Freeform Fabrication Symposium*. 2016. Austin, TX, USA: The Minerals, Metals & Materials Society.

44. Schade, C. and J. Dunkley, *Atomization*, in *ASM Handboook, Volume 7, Powder Metallurgy*, P. Samal and J. Newkirk, Editors. 2015, ASM International.

45. Balachandramurthi Ramanathan, A., et al., *Additive Manufacturing of Alloy 718 via Electron Beam Melting: Effect of Post-Treatment on the Microstructure and the Mechanical Properties*. 2018.

46. Chang, I. and Y. Zhao, *Advances in powder metallurgy : properties, processing and applications / edited by Isaac Chang and Yuyuan Zhao*. 2013: Oxford : Woodhead Publishing, 2013.

47. Mostafa, A., et al., *Structure, Texture and Phases in 3D Printed IN718 Alloy Subjected to Homogenization and HIP Treatments.* Metals (Basel), 2017. **7**(6): p. 196.

48. Gruber, H., *Electron Beam Melting of Alloy 718: Powder Recycling and its Effect on Defect Formation*, in *Department of Industrial and Materials Science*. 2019, Chalmers University of Technology.

49. Downing, M., *A New Powder Encapsulation Method And Its Implications On Densification By Hot Isostatic Pressing*, in *School of Industrial and Manufacturing Science*. 1993, Cranfield Institute of Technology.

50. Besson, J. and M. Abouaf, *Behaviour of cylindrical hip containers.* International journal of solids and structures, 1991. **28**(6): p. 691-702.

51. Olevsky, E., et al., *Container influence on shrinkage under hot isostatic pressing - I. shrinkage anisotropy of a cylindrical specimen.* International Journal of Solids and Structures, 1998. **35**(18): p. 2283-2303.

52. Van Nguyen, C., A. Bezold, and C. Broeckmann, *Anisotropic shrinkage during hip of encapsulated powder.* Journal of materials processing technology, 2015. **226**: p. 134-145.

53. Gamil, M., *Lecture #6 Powder Metallurgy Compaction*, in *Hot Isostatic Pressing*. 2016, Bangladesh University: https://bu.edu.eg/portal/uploads/Engineering,%20Shoubra/Mechanical%20Engineering/647/crs-13632/Files/Lecture%206.pdf. p. 15.

54. Qiu, C., *Net-shape hot isostatic pressing of a nickel-based powder superalloy / by Chunlei Qiu*. 2010, Thesis (PhD.)--University of Birmingham, Department of Metallurgy and Materials, College of Engineering and Physical Sciences.

Birmingham : University of Birmingham: Birmingham.

55. Stainless, A., *Handbook for the Pickling and Cleaning of Stainless Steels*. 2002.

56. FisherScientific, *Safety Data Sheet Hydrofluric Acid*. 2010: https://www.fishersci.com/msdsproxy%3FproductName%3DA463500%26productDescription%3DHYDROFLUORIC%2BACID%2BOPTIMA%2B500ML%26catNo%3DA463-500%2B%26vendorId%3DVN00033897%26storeId%3D10652.

57. FisherScientific, *Safety Data Sheet Nitric Acid*. 2009: https://www.fishersci.com/msds?productName=A467250%26productDescription=NITRIC.

58. Wang, X., et al., *Novel hybrid manufacturing process of CM247LC and multi-material blisks.* 2020.

59. Gusarov, A.V., et al., *Contact thermal conductivity of a powder bed in selective laser sintering.* International Journal of Heat and Mass Transfer, 2003. **46**(6): p. 1103-1109.

60. Artz, E., M.F. Ashby, and K.E. Easterling, *Practical Applications of Hot-Isostatic Pressing Diagrams: Four Case Studies.* Metallurgical Transactions A, 1983. **14**(1): p. 11.

61. Radomir, I., V. Geamăn, and M. Stoicănescu, *Densification Mechanisms Made During Creep Techniques Applied to the Hot Isostatic Pressing.* Procedia, social and behavioral sciences, 2012. **62**: p. 779-782.

62. Crompton, J.S. and R.W. Hertzberg, *Analysis of second phase particles in a powder metallurgy HIP nickel-base superalloy.* Journal of Materials Science, 1986. **21**: p. 10.

63. Chang, L., et al., *Influences of hot-isostatic-pressing temperature on microstructure, tensile properties and tensile fracture mode of Inconel 718 powder compact.* Materials Science and Engineering: A, 2014. **599**: p. 186-195.

64. Bai, Q., et al., *Review and Analysis of Powder Prior Boundary (PPB) Formation in Powder Metallurgy Processes for Nickel-based Super Alloys.* Powder Metallurgy & Mining, 2015. **4**(1): p. 6.

65. Adrian, P.M., *22 - Creep of aerospace materials*. 2012, Elsevier Ltd. p. 521-533.

66. Atkinson, H.V. and S. Davies, *Fundamental aspects of hot isostatic pressing: An overview.* Metallurgical and materials transactions. A, Physical metallurgy and materials science, 2000. **31**(12): p. 2981-3000.

67. Mignanelli, P.M., et al., *Microstructural evolution of a delta containing nickel-base superalloy during heat treatment and isothermal forging.* Materials science &

engineering. A, Structural materials : properties, microstructure and processing, 2015. **621**: p. 265-271.

68. Appa Rao, G., M. Srinivas, and D.S. Sarma, *Effect of thermomechanical working on the microstructure and mechanical properties of hot isostatically pressed superalloy Inconel 718.* Materials science & engineering. A, Structural materials : properties, microstructure and processing, 2004. **383**(2): p. 201-212.

69. Guedou, J.Y., J.C. Lautridou, and Y. Honnorat, *N18, Powder metallurgy superalloy for disks: Development and applications.* Journal of materials engineering and performance, 1993. **2**(4): p. 551-556.

70. Rao, G.A., M. Srinivas, and D.S. Sarma, *Effect of oxygen content of powder on microstructure and mechanical properties of hot isostatically pressed superalloy Inconel 718.* Materials science & engineering. A, Structural materials : properties, microstructure and processing, 2006. **435-436**: p. 84-99.

71. Liu, H., et al., *Effect of oxygen content and heat treatment on carbide precipitation behavior in PM Ni-base superalloys.* Int. J. Miner. Metall. Mater., 2012. **19**(9): p. 827-835.

72. Kissinger, R.D., S.V. Nair, and J.K. Tien, *Influence of powder particle size distribution and pressure on the kinetics of hot isostatic pressing (HIP) consolidation of P/M superalloy Rene 95*. 1984, Columbia University: Center for Strategic Materials, Henry Krumb School of Mines.

73. Rao, G.A., M. Srinivas, and D.S. Sarma, *Influence of modified processing on structure and properties of hot isostatically pressed superalloy Inconel 718.* Materials science & engineering. A, Structural materials : properties, microstructure and processing, 2006. **418**(1): p. 282-291.

74. MacDonald, J.E., et al., *Influence of powder characteristics on the microstructure and mechanical properties of HIPped CM247LC Ni superalloy.* Materials & design, 2019. **174**: p. 107796.

75. Huang, X., et al., *Effect of Powder Size on Microstructure and Mechanical Properties of 2A12Al Compacts Fabricated by Hot Isostatic Pressing.* Advances in materials science and engineering, 2018. **2018**: p. 1-7.

76. Irukuvarghula, S., et al., *Effect of powder characteristics and oxygen content on modifications to the microstructural topology during hot isostatic pressing of an austenitic steel.* Acta materialia, 2019. **172**: p. 6-17.

77. Guo, R., et al., *Effect of Powder Size on Fatigue Properties of Ti-6Al-4V Powder Compact Using Hot Isostatic Pressing.* JOM (1989), 2019. **71**(10): p. 3614-3620.

78. Aristizabal, M., et al., *Study of the influence of outgassing parameters, powder particle size and HIP temperature in the mechanical properties of IN718.* 2015.

79. Bassini, E., et al., *Net shape HIPping of Ni-superalloy: Study of the interface between the capsule and the alloy.* Materials science & engineering. A, Structural materials : properties, microstructure and processing, 2017. **695**: p. 55-65.

80. ElRakayby, H. and K. Kim, *Effect of glass container encapsulation on deformation and densification behavior of metal powders during hot isostatic pressing.* International journal of material forming, 2018. **11**(4): p. 517-525.

81. Chang, D.R., D.D. Krueger, and R.A. Sprague. *Superalloy Powder Processing, Properties and Turbine Disk Applications*. in *Superalloys 1984*. 1984. Pennsylvania, USA.

82. Bartos, J.L. and P.S. Mathur. *Development of Hot Isostatically Pressed (As-HIP) Powder Metallurgy Rene' 95 Turbine Hardware*. in *Superalloys 1976*. 1976. Pennsylvania, USA: The Minerals, Metals and Materials Society.

83. Bassini, E., et al., *Study of the Effects of Aging Treatment on Astroloy Processed via Hot Isostatic Pressing.* Materials (Basel), 2019. **12**(9): p. 1517.

84. Appa Rao, G. and D.V.V. Satyanarayana, *Influence of HIP processing on microstructure and mechanical properties of superalloy Udimet 720LI.* Materials science and technology, 2011. **27**(2): p. 478-486.

85. Prasad, K., et al., *High temperature low cycle fatigue behaviour of hot isostatically pressed superalloy Udimet 720 LI.* Materials at high temperatures, 2010. **27**(4): p. 295-300.

86. Couturier, R., et al. *Process development and mechanical properties of alloy U720LI for high temperature turbine disks*. in *Superalloys 2004*. 2004. Pennsylvania, USA: The Minerals, Metals & Materials Society.

87. Moll, J.H. and J.J. Conway. *Characteristics and properties of as-HIP P/M alloy 720*. in *Superalloys 2000*. 2000. Pennsylvania, USA: The Minerals, Metals & Materials Society.

88. Qiu, C., et al., *Influence of heat treatment on microstructure and tensile behavior of a hot isostatically pressed nickel-based superalloy.* Journal of alloys and compounds, 2013. **578**: p. 454-464.

89. May, J.R., et al., *Microstructure and Mechanical Properties of an Advanced Nickel-Based Superalloy in the as-HIP Form.* Advanced Materials Research, 2011. **278**: p. 6.

90. Rao, G.A., et al., *Characterisation of hot isostatically pressed nickel base superalloy Inconel 718.* Materials Science and Technology, 2003. **19**(3): p. 313-321.

91. Chang, L., et al., *Preparation of hot-isostatic-pressed powder metallurgy superalloy Inconel 718 free of prior particle boundaries.* Materials science & engineering. A, Structural materials : properties, microstructure and processing, 2017. **682**: p. 341-344.

92. Chang, S., et al., *Effects of temperature of HIP process on characteristics of Inconel 718 superalloy.* International Journal of Cast Metals Research, 2006. **19**(3): p. 175-180.

93. Yao, C., et al., *Microstructures and Mechanical Properties of Inconel 718 Alloy at Ultralow Temperatures.* Journal of Materials Engineering and Performance, 2018. **27**(5): p. 2060-2069.

94. International, S., *AMS 5662N Nickle Alloy, Corrosion and Heat Resistant, Bars, Forgings, and Rings 52.5Ni 19Cr 3.0Mo 5.1Cb 0.90Ti 0.50Al 18Fe, Consumable Electrode or Vacuum INduction Melted 1775F (968C) Solution Heat Treated, Precipitation Hardenable*. 2016.

95. Adegoke, O., et al., *Review of Laser Powder Bed Fusion of Gamma-Prime-Strengthened Nickel-Based Superalloys.* Metals (Basel), 2020. **10**(8): p. 996.

96. Carter, L., M. Attallah, and R. Reed. *Laser Powder Bed Fabrication of Nickel-Base Superalloys: Influence of Parameters; Characterisation, Quantification and Mitigation of Cracking*. in *Superalloys 2012*. 2012. Champion, Pennsylvania.

97. Magnien, J., et al., *Current surface issues in additive manufacturing.* Plasma processes and polymers, 2019. **17**(1): p. 1900154-n/a.

98. Roidl, B. and T. Fauner *Continuous Improvement in Gas Flow Design*. 2020.

99. Ataee, A., et al., *3 - Metal scaffolds processed by electron beam melting for biomedical applications*. 2017, Elsevier Ltd. p. 83-110.

100. Landau, E., et al., *Thermal characterization of the build chamber in electron beam melting.* Additive manufacturing, 2020. **36**.

101. Masoomi, M., et al. *An Experimental-Numerical Investigation of Heat Transfer during Selective Laser Melting*. in *26th International Solid Freeform Fabrication Symposium*. 2015. Austin, Texas, USA.

102. Edge, E. *Thermal Conductivity of Gases Chart*. 2000 [cited 2020 October]; Available from: https://www.engineersedge.com/heat_transfer/thermal-conductivity-gases.htm.

103. Bidare, P., et al., *Laser powder bed fusion in high-pressure atmospheres.* International journal of advanced manufacturing technology, 2018. **99**(1-4): p. 543-555.

104. Ning, J., et al., *Analytical Modeling of In-Process Temperature in Powder Bed Additive Manufacturing Considering Laser Power Absorption, Latent Heat, Scanning Strategy, and Powder Packing.* Materials (Basel, Switzerland). **12**(5).

105. Field, A.C., et al., *The Effect of Powder Characteristics on Build Quality of High-Purity Tungsten Produced via Laser Powder Bed Fusion (LPBF).* Metallurgical and materials transactions. A, Physical metallurgy and materials science, 2020. **51**(3): p. 1367-1378.

106. Boley, C.D., S.A. Khairallah, and A.M. Rubenchik, *Calculation of laser absorption by metal powders in additive manufacturing.* Appl Opt, 2015. **54**(9): p. 2477-2482.

107. Cloots, M., P.J. Uggowitzer, and K. Wegener, *Investigations on the microstructure and crack formation of IN738LC samples processed by selective laser melting using Gaussian and doughnut profiles.* Materials and Design, 2016. **89**.

108. Körner, C., *Additive manufacturing of metallic components by selective electron beam melting — a review.* International Materials Reviews, 2016. **61**(5): p. 361-377.

109. Cordero, Z.C., et al., *Powder bed charging during electron-beam additive manufacturing.* Acta materialia, 2017. **124**(C): p. 437-445.

110. Merriam-Webster. *Dictionary - permittivity*. 2020 [cited 2020 October].

111. Attallah, M., et al., *Additive manufacturing of Ni-based superalloys: The outstanding issues.* M R S Bulletin, 2016. **41**(10): p. 758-764.

112. Zafer, Y.E., et al., *Encapsulation of Electron Beam Melting Produced Alloy 718 to Reduce Surface Connected Defects by Hot Isostatic Pressing.* Materials (Basel), 2020. **13**(5): p. 1226.

113. Carter, L., et al., *Process Optimisation of Selective Laser Melting using Energy Density Model for Nickel-based Superalloys.* 2015.

114. Gruber, H., et al., *Effect of Powder Recycling on Defect Formation in Electron Beam Melted Alloy 718.* Metallurgical and materials transactions. A, Physical metallurgy and materials science, 2020. **51**(5): p. 2430-2443.

115. Körner, C., E. Attar, and P. Heinl, *Mesoscopic simulation of selective beam melting processes.* Journal of Materials Processing Tech. **211**(6): p. 978-987.

116. Ternovoi, Y.F., et al., *Pore Formation in Atomized Powders.* Poroshkovaya Metallurgiya, 1985. **1**(265): p. 5.

117. Stanciu, E.M., et al., *Mechanism of Keyhole Formation in Laser Welding.* The Romanian Review Precision Mechanics, Optics & Mechatronics, 2010. **20**(38).

118. Berger, P., H. Hugel, and T. Graf, *Understanding Pore Formation in Laser Beam Welding.* Physics Procedia, 2011(12): p. 7.

119. Helmer, H.E., C. Körner, and R.F. Singer, *Additive manufacturing of nickel- based superalloy Inconel 718 by selective electron beam melting: Processing window and microstructure.* Journal of Materials Research, 2014. **29**(17): p. 1987-1996.

120. Zheng, S.T.L.K.N.T.Z.X.Z., *Coarsening Behavior of Gamma Prime Precipitates in a Nickel Based Single Crystal Superalloy.* Journal of Materials Science & Technology, 2016. **32**(2): p. 172-176.

121. Ott, E., J. Groh, and H. Sizek. *Metals Affordability Initiative: Application of Allvac Alloy 718Plus for Aircraft Engine Static Structural Components*. in *TMS*

(Minerals, Metals & Materials Society). 2006. Warrendale, PA, USA.

122. Wang, X., et al., *Defect formation and its mitigation in selective laser melting of high γ′ Ni-base superalloys.* 2016.

123. Carter, L.N., K. Essa, and M.M. Attallah, *Optimisation of selective laser melting for a high temperature Ni-superalloy.* Rapid Prototyping Journal, 2015. **21**(4): p. 423-432.

124. Boswell, J.H., et al., *Cracking during thermal post-processing of laser powder bed fabricated CM247LC Ni-superalloy.* 2019.

125. Cross, C., *On the Origin of Weld Solidification Cracking*, in *Hot Cracking Phenomena in Welds*, T. Böllinghaus and H. Herold, Editors. 2005, Springer: Berlin. p. 3-18.

126. Hermann, R., S.S. Birley, and P. Holdway, *Liquation cracking in aluminium alloy welds.* Materials Science & Engineering A, 1996: p. 247-255.

127. Danis, Y., et al., *Control of Inconel 738LC superalloy microstructure with the aid of precipitate dissolution semi-analytical modelling.* Modelling and Simulation in Materials Science and Engineering, 2010. **18**: p. 1-15.

128. Bi, G. and A. Gasser, *Restoration of Nickel-Base Turbine Blade Knife-Edges with Controlled Laser Aided Additive Manufacturing.* Physics Procedia, 2011. **12**: p. 402-409.

129. Montazeri, M. and F. Ghaini, *The liquation cracking behaviour of IN738LC superalloy during low power Nd:Yag pulsed laser welding.* Materials Characterization, 2012. **67**: p. 65-73.

130. Montazeri, M., F. Ghaini, and O. Ojo, *Heat input and the liquation cracking of laser welded IN738LC superalloy.* Welding Research, 2013. **92**: p. 258-264.

131. Dye, D., O. Hunziker, and R. Reed, *Numerical Analysis of the Weldability of Superalloys.* Acta Materialia, 2001. **49**(4): p. 683-697.

132. Young, G., et al., *The Mechanism of Ductility Dip Cracking in Nickel-Chromium Alloys.* The Welding Journal, 2008. **87**: p. 31-43.

133. Collins, M. and J. Lippold, *An Investigation of Ductility Dip Cracking in Nickel-Based Filler Materials - Part I.* Welding Journal, 2003: p. 8.

134. Collins, M.R., AJ; Lippold, JC, *An Investigation of Ductility Dip Cracking in Nickel-Based Filler Materials - Part II.* Welding Journal, 2003: p. 348-354.

135. Collins, M. and J. Lippold, *An Investigation of Ductility Dip Cracking in Nickel-Based Filler Materials - Part III.* Welding Journal, 2003: p. 11.

136. Lippold, J., *Welding Metallurgy and Weldability*. 2015, Hoboken, New Jersey: John Wiley & Sns, Inc.

137. Nissley, N.E. and J.C. Lippold, *Ductility-Dip Cracking Susceptibility of Nickel-Based Weld Metals Part 1: Strain-to-Fracture Testing.* Welding Research, 2008: p. 257-264.

138. Carter, L., et al., *The influence of the laser scan strategy on grain structure and cracking behaviour in SLM powder-bed fabricated nickel superalloy.* Journal of Alloys and Compounds, 2014. **615**: p. 338-347.

139. Mercelis, P. and J.P. Kruth, *Residual stresses in selective laser sintering and selective laser melting.* Rapid prototyping journal, 2006. **12**(5): p. 254-265.

140. Pant, P., et al., *Mapping of residual stresses in as-built Inconel 718 fabricated by laser powder bed fusion: A neutron diffraction study of build orientation influence on residual stresses.* Additive manufacturing, 2020. **36**: p. 101501.

141. Mughal, M.P., H. Fawad, and R. Mufti, *Finite element prediction of thermal stresses and deformations in layered manufacturing of metallic parts.* Acta mechanica, 2006. **183**(1): p. 61-79.

142. Dai, K. and L. Shaw, *Distortion minimization of laser-processed components through control of laser scanning patterns.* Rapid prototyping journal, 2002. **8**(5): p. 270-276.

143. Beuth, J. and N. Klingbeil, *The role of process variables in laser-based direct metal solid freeform fabrication.* JOM (1989), 2001. **53**(9): p. 36-39.

144. Li, C., et al., *Residual Stress in Metal Additive Manufacturing.* Procedia CIRP, 2018. **71**: p. 348-353.

145. Sochalski-Kolbus, L.M., et al., *Comparison of Residual Stresses in Inconel 718 Simple Parts Made by Electron Beam Melting and Direct Laser Metal Sintering.* Metallurgical and materials transactions. A, Physical metallurgy and materials science, 2015. **46**(3): p. 1419-1432.

146. Rickenbacher, L., T. Etter, and H. Wegener, *High temperature material properties of IN738LC processed by selective laser melting (SLM) technology.* Rapid Prototyping Journal, 2013. **19**(4): p. 282-290.

147. Wan, H.Y., et al., *Effect of scanning strategy on grain structure and crystallographic texture of Inconel 718 processed by selective laser melting.* Journal of materials science & technology, 2018. **34**(10): p. 1799-1804.

148. Wan, H.Y., et al., *Effect of scanning strategy on mechanical properties of selective laser melted Inconel 718.* Materials science & engineering. A, Structural materials : properties, microstructure and processing, 2019. **753**: p. 42-48.

149. Kuo, Y.-L., S. Horikawa, and K. Kakehi, *The effect of interdendritic δ phase on the mechanical properties of Alloy 718 built up by additive manufacturing.* Materials & design, 2017. **116**: p. 411-418.

150. Strößner, J., M. Terock, and U. Glatzel, *Mechanical and Microstructural Investigation of Nickel-Based Superalloy IN718 Manufactured by Selective Laser Melting (SLM.* Advanced Engineering Materials, 2015. **17**(8): p. 1099-1105.

151. Kirka, M.M., et al., *Microstructure Development in Electron Beam-Melted Inconel 718 and Associated Tensile Properties.* JOM (1989), 2016. **68**(3): p. 1012-1020.

152. Xie, X., et al., *TTT Diagram of a newly developed nickel-base superalloy-Allvac718Plud.* Superalloys 718, 625, 706 and Derivatives 2005, 2005.

153. Rasband, W., *ImageJ 1.48V*. National Institutes of Health: USA.

154. SYMPATEC. *HELOS*. 2017; Available from: https://www.sympatec.com/en/particle-measurement/sensors/laser-diffraction/helos/.

155. SympaTEC, *Sucell Wet Dispering Unit*. 2017.

156. SYMPATEC, *Particle Measurement Laser Diffraction*. 2016: https://www.sympatec.com/en/particle-measurement/sensors/laser-diffraction/.

157. International, A., *ASTM B213-17 Standard Test Methods for Flow Rate of Metal Powders Using the Hall Flowmeter Funnel*. 2019.

158. Schulze, D., *Flow Properties of Powders and Bulk Solids*. 2011, Ostfalia University of Applied Sciences: Germany.

159. Technology, F. *Powder Flow Testing with the FT4 Powder Rheometer*. 2020 [cited 2020 September]; Available from: https://www.freemantech.co.uk/powder-testing/ft4-powder-rheometer-powder-flow-tester.

160. FreemanTechnology. *External Variables- The need for versatility*. 2020 [cited 2020 December].

161. Clayton, J. *Pushing for the performance in polymer powders*. tctmagazine, 2019.

162. MacDonald, J.E., *Hot Isostatic Pressing of A High Temperature Ni-Superalloy CM247LC: Processing-Microstructure-Properties*, in *Metallurgy and Materials*. 2016, The University of Birmingahm.

163. Liu, Z.Y., et al., *Energy Consumption in Additive Manufacturing of Metal Parts.* Procedia Manufacturing, 2018.

164. Jia, Q. and D. Gu, *Selective laser melting additive manufacturing of Inconel 718 superalloy parts: Densification, microstructure and properties.* Journal of Alloys and Compounds, 2014. **585**: p. 713-721.

165. Lu, Y., et al., *Study on the microstructure, mechanical property and residual stress of SLM Inconel- 718 alloy manufactured by differing island scanning strategy.* Optics and Laser Technology, 2015. **75**: p. 197-206.

166. Zhang, D., et al., *Effect of standard heat treatment on the microstructure and mechanical properties of selective laser melting manufactured Inconel 718 superalloy.* Materials Science & Engineering A, 2015. **644**: p. 32-40.

167. Amato, K.N., et al., *Microstructures and mechanical behavior of Inconel 718 fabricated by selective laser melting.* Acta Materialia, 2012. **60**(5): p. 2229-2239.

168. Jennings, R.E., R.M. Ward, and M.M. Attallah, *Defect Formation Mapping and Targeted Process Optimisation in Selective Laser Melted IN738LC Ni-Base Superalloy*. 2016: MS&T 2016.

169. Jin, Y., et al., *Annealing twin development during recrystallization and grain growth in pure nickel.* Materials Science and Engineering A, 2014. **597**: p. 9.

170. Additive, G. *Arcam EBM Q20plus*. 2020 [cited 2020 December].

171. Carter, L.N., *Selective laser melting of nickel superalloys for high temperature applications / by Luke Nelson Carter*. 2013, Thesis (PhD)--University of Birmingham, College of Engineering and Physical Sciences, 2013.

Birmingham : University of Birmingham: Birmingham.

172. Sutton, A., et al. *Powders for additive manufacturing processes: characterisation techniques and effects on part properties*. in *Solid Freeform Fabrication 2016*. 2016. Texas, USA: TMS.

173. Cockcroft, S.L., et al. *Inclusion Precipitation in Superalloys*. in *Superalloys 1992*. 1992. Pennsylvania, USA: The Minerals, Metals & Materials Society.

174. Quy Bau, N., et al., *Characteristics of Inconel Powders for Powder-Bed Additive Manufacturing.* Engineering, 2017. **3**(5): p. 695-700.

175. Karunaratne, M.S.A. and R.C. Reed, *Interdiffusion of Niobium and Molybdenum in Nickel between 900 -1300 °C.* Diffusion and defect data. Solid state data. Pt. A, Defect and diffusion forum, 2005. **237-240**: p. 420-425.

176. Connétable, D., B. Ter-Ovanessian, and É. Andrieu, *Diffusion and segregation of niobium in fcc-nickel.* J Phys Condens Matter, 2012. **24**(9): p. 095010-095010.

177. Wang, X., et al., *Investigation on Microsegregation of IN718 Alloy During Additive Manufacturing via Integrated Phase-Field and Finite-Element Modeling.* Journal of materials engineering and performance, 2019. **28**(2): p. 657-665.

178. Vock, S., et al., *Powders for powder bed fusion: a review.* Progress in Additive Manufacturing, 2019. **4**(4): p. 383-397.

179. Lyckfeldt, O. *Powder rheology of steel powders for additive manufacturing*. in *Euro PM2013*. 2013. EPMA.

180. Carr, R.L., *Evaluating Flow Properties of Solids.* Chemical Engineering, 1965. **72**: p. 6.

181. Ricks, R., A. Porter, and R. Ecob, *The growth of gamma-prime precipitates in nickel-base superalloys.* Acta Metallurgica. **31**: p. 43-53.

182. SenteSoftwareLtd., *JMatPro*. 2001.

183. Mitchell, A., et al. *The Precipitation of Primary Carbides in Alloy 718*. in *Superalloys 718, 625, 706 and Various Derivative*. 1994. The Minerals, Metals & Materials Society.

184. Chang, S.-H., et al., *Influences of Soaking Time in Hot Isostatic Pressing on Strength of Inconel 718 Superalloy.* MATERIALS TRANSACTIONS, 2006. **47**(2): p. 426-432.

185. Rosato, et al., *Why the Brazil nuts are on top: Size segregation of particulate matter by shaking.* Physical review letters, 1987. **58**(10): p. 1038-1040.

186. Heeling, T., M. Cloots, and K. Wegener, *Melt pool simulation for the evaluation of process parameters in selective laser melting.* Additive manufacturing, 2017. **14**: p. 116-125.

187. Cheng, B. and K. Chou. *Melt Pool Evolution Study in Selective Laser Melting*. 2015.

188. Popovich, V.A., et al., *Impact of heat treatment on mechanical behaviour of Inconel 718 processed with tailored microstructure by selective laser melting.* Materials & Design. **131**: p. 12-22.

189. Chlebus, E., et al., *Effect of heat treatment on the microstructure and mechanical properties of Inconel 718 processed by selective laser melting.* Materials Science & Engineering A, 2015. **639**: p. 647-655.

190. Tucho, W., et al., *Microstructure and hardness studies of Inconel 718 manufactured by selective laser melting before and after solution heat treatment.* Materials Science & Engineering. A, Structural Materials : Properties, Microstructure and Processing. **689**: p. 220.

191. Ali, H., H. Ghadbeigi, and K. Mumtaz, *Processing Parameter Effects on Residual Stress and Mechanical Properties of Selective Laser Melted Ti6Al4V.* Journal of Materials Engineering and Performance. **27**(8): p. 4059-4068.

192. Kruth, J.-P., et al., *Assessing and comparing influencing factors of residual stresses in selective laser melting using a novel analysis method.* Proceedings of the Institution of Mechanical Engineers, Part B: Journal of Engineering Manufacture. **226**(6): p. 980-991.

193. Qiu, C., et al., *On the role of melt flow into the surface structure and porosity development during selective laser melting.* Acta materialia, 2015. **96**: p. 72-79.

194. Li, R., et al., *Balling behavior of stainless steel and nickel powder during selective laser melting process.* International journal of advanced manufacturing technology, 2011. **59**(9-12): p. 1025-1035.

195. Bidare, P., et al., *Fluid and particle dynamics in laser powder bed fusion.* 2018.

196. David, S.A., S.S. Babu, and J.M. Vitek, *Welding: Solidification and microstructure.* JOM (1989), 2003. **55**(6): p. 14-20.

197. Ali, H., H. Ghadbeigi, and K. Mumtaz, *Effect of scanning strategies on residual stress and mechanical properties of Selective Laser Melted Ti6Al4V.* Materials science & engineering. A, Structural materials : properties, microstructure and processing, 2018. **712**: p. 175-187.

198. Azadian, S., L.-Y. Wei, and R. Warren, *Delta phase precipitation in Inconel 718.* Materials Characterization, 2004. **53**(1): p. 7-16.

199. Ozturk, U., J.M. Cabrera, and J. Calvo, *High-Temperature Deformation of Inconel 718Plus.* Journal of Engineering for Gas Turbines and Power, 2016. **139**(3): p. 7.

200. Agazhanov, A.S., D.A. Samoshkin, and Y.M. Kozlovskii, *Thermophysical properties of Inconel 718 alloy.* Journal of physics. Conference series, 2019. **1382**: p. 12175.

201. Gasper, A.N.D., et al., *Spatter and oxide formation in laser powder bed fusion of Inconel 718.* Additive manufacturing, 2018. **24**: p. 446-456.

202. Khairallah, S.A., et al., *Laser powder-bed fusion additive manufacturing: Physics of complex melt flow and formation mechanisms of pores, spatter, and denudation zones.* Acta materialia, 2016. **108**(C): p. 36-45.

203. Tillmann, W., et al., *Hot isostatic pressing of IN718 components manufactured by selective laser melting.* Additive manufacturing, 2017. **13**: p. 93-102.

204. Lewandowski, J.J. and M. Seifi, *Metal Additive Manufacturing: A Review of Mechanical Properties*. 2016: Annual Review of Materials Research. p. 151-186.

205. Thümmler, F., *An introduction to powder metallurgy / F. Thümmler and R. Oberacker*, R. Oberacker, et al., Editors. 1993, London : Institute of Materials: London.

206. Bozzolo, N. and M. Bernacki, *Viewpoint on the Formation and Evolution of Annealing Twins During Thermomechanical Processing of FCC Metals and Alloys.* Metallurgical and materials transactions. A, Physical metallurgy and materials science, 2020. **51**(6): p. 2665-2684.